UNITED TECHNOLOGIES RESEARCH CENTER
East Hartford, Connecticut 06108

R91-970057-3

The Effects of Reynolds Number, Rotor Incidence Angle and Surface Roughness on the Heat Transfer Distribution in a Large-Scale Turbine Rotor Passage

REPORTED BY M. F. Blair
M. F. Blair

APPROVED BY R. P. Dring
R. P. Dring

DATE November 1991

NO. OF PAGES _____

COPY NO. _____

NASA
National Aeronautics and Space Administration

Report Documentation Page

1. Report No.	2. Government Accession No.	3. Recipient's Catalog No.

4. Title and Subtitle

The Effects of Reynolds Number, Rotor Incidence Angle and Surface Roughness on the Heat Transfer Distribution in a Large-Scale Turbine Rotor Passage

5. Report Date

November 1991

6. Performing Organization Code

7. Author(s)

M. F. Blair

8. Performing Organization Report No.

UTRC R91-970057-3

10. Work Unit No.

9. Performing Organization Name and Address

United Technologies Research Center
Silver Lane
East Hartford, Connecticut 06108

11. Contract or Grant No.

NAS8-38870

13. Type of Report and Period Covered

Contractor Report
Final

12. Sponsoring Agency Name and Address

National Aeronautics and Space Administration
George C. Marshall Space Flight Center
Marshall Space Flight Center, AL 35812

14. Sponsoring Agency Code

15. Supplementary Notes

Technical Contract Monitors, Lisa Griffin and Gil Wilhold
Aerophysics Division
NASA Marshall Space Flight Center, AL 35812

16. Abstract

A combined experimental and computational program was conducted to examine the heat transfer distribution in a turbine rotor passage geometrically similar to the SSME HPFTP. Heat transfer was measured and computed for both the full-span suction and pressure surfaces of the rotor airfoil as well as for the hub endwall surface. The objective of the program was to provide a benchmark-quality data base for the assessment of rotor heat transfer computational procedures.

The experimental portion of the study was conducted previously under NAS8-37351 in a large-scale, ambient temperature, rotating turbine model. Heat transfer data were obtained using thermocouple and liquid-crystal techniques to measure temperature distributions on the thin, electrically-heated skin of the rotor passage model. Test data were obtained for various combinations of Reynolds number, rotor incidence angle and model surface roughness. The data are reported in the form of contour maps of Stanton number. These heat transfer distribution maps revealed numerous local effects produced by the three-dimensional flows within the rotor passage. Of particular importance were regions of local enhancement produced on the airfoil suction surface by the main-passage and tip-leakage vortices and on the hub endwall by the leading-edge horseshoe vortex system. Midspan rotor airfoil results are compared with both smooth-wall and rough-wall finite-difference two-dimensional heat transfer predictions.

The computational portion consisted of the application of a well-posed parabolized Navier-Stokes analysis to the calculation of the three-dimensional viscous flow through ducts simulating a gas turbine passage. These cases include a 90° turning duct, a gas turbine cascade simulating a stator passage, and a gas turbine rotor passage including Coriolis forces. The calculated results have been evaluated using experimental data of the three-dimensional velocity fields, wall static pressures, and wall heat transfer on the suction surface of the turbine airfoil and on the endwall. Particular attention has been paid to an accurate modeling of the passage vortex and to the development of the wall boundary layers including the crossflow. The results of this assessment indicate that the procedure has the potential to predict the aerodynamics and the heat transfer in a gas turbine passage and can be used to develop detailed three-dimensional turbulence models for the prediction of skin friction and heat transfer in complex three-dimensional flow passages.

17. Key Words (Suggested by Author(s))	18. Distribution Statement
Heat Transfer, Turbines, Airfoils, Endwalls	Distribution Unlimited

19. Security Classif. (of this report)	20. Security Classif. (of this page)	21. No. of pages	22. Price
Unclassified	Unclassified		

NASA FORM 1626 OCT 86

The Effects of Reynolds Number, Rotor Incidence Angle and Surface Roughness on the Heat Transfer Distribution in a Large–Scale Turbine Rotor Passage

TABLE OF CONTENTS

LIST OF SYMBOLS

$\vec{A}A_i$	Area on coordinate surfaces
$\vec{b}\ \vec{b}^i\ \vec{b}_i$	Base vectors for potential flow coordinates
Bx	Airfoil axial chord
Cx	Axial flow speed
C_p	Specific heat at constant pressure
Cp	Pressure coefficient, CP = (PTOA–P)/Q_U
$e^{ijk}e_{ijk}$	Permutation symbol
g	Determinate of metric tensor
$Gg^{ij}g_{ij}$	Metric tensor
h_i	Metric scale coefficients
H_T	Total enthalpy
$\vec{K}$	Principal curvature of potential flow streamlines
$\vec{n}$	Inward facing vector at boundary on Y_1 plane
N	Rotor RPM
PP_T	Static pressure – total pressure
$\bar{P}$	Mass flow weighted average total pressure
PTOA	Turbine inlet absolute total pressure
$PrPr_t$	Prandtl number – molecular/turbulent
Q_U	Dynamic pressure based on U
$\vec{r}$	Position vector
$\vec{R}_m$	Relaxation parameters
R	Gas constant
Re	Reynolds number (based on airfoil axial chord and exit flow conditions)
Re_θ	Reynolds number (based on momentum thickness)

LIST OF SYMBOLS (Cont'd)

S	Surface arc length
$\dot{S}$	Source term in continuity equation
$\vec{t}$	Tangent vector at boundary on Y_1 plane
T_T	Mass flow weighted average total temperature
U	Rotor wheel speed at midspan
$\vec{U}_s$	Secondary flow velocity vector
$U_n U_t$	Normal and tangential secondary boundary velocities
$U_1 U_2 U_3$	Contravarient velocity components
$\vec{V}$	Potential flow velocity
W	Mass flow rate
W_O	Inlet mass flow rate
W_t	Relative tangential flow speed
$\vec{X}X_i$	Cartesian coordinates
$\vec{X}_o$	Initial Cartesian coordinates of streamlines
$\vec{yy}_i$	Arc length along potential flow coordinate
$\vec{Y}Y^iY_i$	Potential flow coordinates
α_1	Absolute flow angle from tangential at first stator exit
$\cdot\vec{\alpha}\alpha_i$	Unit vectors in Cartesian coordinates
β_1	Relative flow angle from tangential at the rotor inlet
$\vec{\beta}\beta^i\beta_i$	Unit vectors in potential flow coordinates
γ	Ratio of specific heats
$\mu\mu_t$	Viscosity–molecular/turbulent

LIST OF SYMBOLS (Cont'd)

ρ	Density
Ω	Secondary vorticity
$\dot{\Omega}$	Source term in vorticity equation

THE EFFECTS OF REYNOLDS NUMBER, ROTOR INCIDENCE ANGLE AND SURFACE ROUGHNESS ON THE HEAT TRANSFER DISTRIBUTION IN A LARGE-SCALE TURBINE ROTOR PASSAGE

Michael F. Blair

SUMMARY

A combined experimental and computational program was conducted to examine the heat transfer distribution in a turbine rotor passage geometrically similar to the SSME HPFTP. Heat transfer was measured and computed for both the full–span suction and pressure surfaces of the rotor airfoil as well as for the hub endwall surface. The objective of the program was to provide a benchmark–quality data base for the assessment of rotor passage heat transfer computational procedures.

The experimental portion of the study was conducted in a large–scale, ambient temperature, rotating turbine model. Heat transfer data were obtained using thermocouple and liquid–crystal techniques to measure temperature distributions on the thin, electrically–heated skin of the rotor passage model. Test data were obtained for various combinations of Reynolds number, rotor incidence angle and model surface roughness. The data are reported in the form of contour maps of Stanton number. These heat transfer distribution maps revealed numerous local effects produced by the three–dimensional flows within the rotor passage. Of particular importance were regions of local enhancement produced on the airfoil suction surface by the main–passage and tip–leakage vortices and on the hub endwall by the leading–edge horseshoe vortex system. Comparisons between the present results and midspan results from a previous NASA–HOST funded study are included. Midspan heat transfer distributions for both smooth and rough model surface conditions are compared with predictions of finite–difference two–dimensional boundary layer computation procedures.

The computational portion consisted of the application of a well–posed parabolized Navier–Stokes analysis to the calculation of the three–dimensional viscous flow through ducts simulating a gas turbine passage. These cases include a 90° turning duct, a gas turbine cascade simulating a stator passage, and a gas turbine rotor passage including Coriolis forces. The calculated results have been evaluated using experimental data of the three–dimensional velocity fields, wall static pressures, and wall heat transfer on the suction surface of the turbine airfoil and on the endwall. Particular attention has been paid to an accurate modeling of the passage vortex and to the development of the wall boundary layers including the crossflow. The results of this assessment indicate that the procedure has the potential to predict the aerodynamics and the heat transfer in a gas turbine passage and can be used to develop detailed three–dimensional turbulence models for the prediction of skin friction and heat transfer in complex three–dimensional flow passages.

INTRODUCTION

The aerodynamics and heat transfer occurring in the airfoil–to–airfoil passages of a turbine are strongly three–dimensional in nature. This complexity of the flow is due to both viscous and inviscid flow mechanisms that come into play. Viscous effects in a turbine passage are present on the airfoil surfaces in the form of boundary layers and wakes, with the major contribution to three dimensionality occuring near the endwalls. An idea of the complexity of the three dimensional endwall boundary layers can be obtained by considering the observations of Langston, Nice and Hooper (1977) and/or Sieverding (1985) for large–scale cascades. These studies demonstrated that viscous effects completely dominated the endwall flow. They showed that near the leading edge stagnation point the endwall boundary layer flow was in the upstream direction and that before the flow had reached the passage exit all of the incoming endwall boundary layer had been swept across the endwall from the pressure surface to the suction surface. This cross–passage endwall flow rolled up into a secondary flow vortex leaving an extremely thin endwall boundary layer behind. In addition, their results showed that as the cross–passage flow moved onto the suction surface it radically altered the flow near the airfoil hub and tip.

Inviscid effects are also important in turbine passage flows not only because of the three dimensional nature of the airfoil geometry but also because of the vorticity present in the flow and because of the rotating frame of reference of the rotor. The "relative eddy," an inviscid mechanism produced by the vorticity in the rotating frame of reference, can create significant secondary flow effects on the rotor pressure surface (Dring and Joslyn, 1983).

Considering the highly three dimensional nature of turbine passage aerodynamics it is not surprising that these flows have a powerful impact on the associated heat transfer distributions. As an example, Graziani et al. (1980) presented contours of the airfoil and endwall heat transfer for the same two dimensional cascade used for the aerodynamic study of Langston, Nice and Hooper (1977). These results demonstrated that the flow across the endwall from the pressure to the suction surface had an important impact on both the endwall and suction surface heat transfer distributions. An interesting fact to keep in mind is that the complex three dimensional aerodynamics and heat transfer in this cascade had their origins in the aerodynamics and not in the geometry. The cascade geometry was purely two dimensional.

From the computational perspective, progress toward modeling these flows has been dramatic. This is partly due to more efficient algorithms and partly due to the expansion of computer capabilities and the introduction of supercomputers. As an example, the inviscid aspects of the three dimensional flow in the LSRR rotor have been predicted remarkably well by Holmes and Tong (1984). Not only were the airfoil pressure distributions predicted quite accurately but so also was the effect of the rotating frame of reference in producing the relative eddy.

For at least three reasons, progress in computing the viscous aspects of these flows has been less dramatic. First, the computational modeling of the diffusion terms adds complexity. Second, the calculations are in general far more time consuming. Finally, and perhaps most importantly, the physical models for the turbulent transport processes (for shear and heat flux) are neither very

reliable, nor general, nor accurate. Some relatively recent examples of the calculation of three dimensional viscous flows in turbine airfoil passages can be found in Anderson and Hankins (1981), Anderson (1985), Hah (1983), Kreskovsky, Briley and McDonald (1979) and Moore and Moore (1979). Each of these calculations is based on an elegant formulation of the discretized governing equations and each is based on relatively efficient and accurate computational algorithms. However, all of them suffer from inaccuracy in modelling the turbulent transport. The impact of this shortcoming is frequently inconsequential to the prediction of the global inviscid aspects of the flow, i.e. the pressure distributions. Its impact on the local aerodynamics may be serious but the general qualitative trends can frequently be predicted. The impact of this shortcoming on predicting the heat transfer, however, can be much more serious. The reason for this is that the aerodynamic aspects involve the global flow field and local inaccuracies can be either compensated for or averaged out. Heat transfer, on the other hand, is a local effect and even local inaccuracies in a prediction may obscure strong local gradients and regions with high local heat loads.

Accurate physical models for turbulent heat transfer in the extremely hostile environment of the gas turbine airfoil, e.g. high levels of freestream unsteadiness (both periodic and random), local separations and strong surface curvature still need to be developed for two dimensional flows. It is not unreasonable to expect that even more turbulence–model–development problems will be encountered in the computation of the three dimensional flows of the full–span turbine airfoil and endwall.

Considering the complexity of the aerodynamics and heat transfer present in the full–span flow in a turbine passage, it is essential that any computational procedure aimed at predicting these flows be assessed against a benchmark data base. Such a data base would need to satisfy the following requirements:

(1) The turbine model used in the experiment must be relevant to the turbines for which the computational procedure is intended, having geometric similarity and basically good performance.

(2) The data base should contain a sufficiently detailed description of the turbine and its airfoils so as to provide all the geometry input required by the computation.

(3) All of the conditions upstream of the rotor should be documented and available.

(4) Sufficiently detailed flow visualization data should be available to provide a description of the flow on the airfoil surfaces.

(5) Aerodynamic data downstream of the airfoil sufficient to provide a detailed description of the flow from hub to tip should be available.

(6) Detailed heat transfer data should be provided on the airfoil suction and pressure surfaces as well as on the hub endwall.

Under a previous NASA contract, NAS8–37351, the United Technologies Research Center conducted a program to produce the above benchmark data base. Results from that contract effort were reported by Blair and Anderson (1989). During the conduct of this previous program much more experimental heat transfer data was recorded than was required under the Statement of Work.

Due to cost constraints, however, those extra data sets were not reduced or documented as part of NAS8–37351. This present contract, NAS8–38870, has been forumulated to complete the reduction and analysis of those extra sets of data and to provide thorough documentation (tabulation) of all heat transfer data obtained under NAS8–37351.

For purposes of clarity, the present report is configured as a comprehensive document combining the results of both NAS8–37351 and NAS8–38870. In effect, the present report is a significantly expanded version of Blair and Anderson (1989). For this present report, no distinctions will be made between results produced under the separate contracts. All work will be referred to as if it was conducted under a single, comprehensive study.

As will be discussed in detail in EXPERIMENTAL EQUIPMENT, the turbine model employed in this study was directly relevant to the Space Shuttle Main Engine (SSME) drive turbine (item 1 from the above list of benchmark data base requirements). Items (2) and (3) will provide all the information required to set up and carry out a prediction of the flow and heat transfer. Items (4), (5) and (6) will provide the aerodynamics and heat transfer data required to assess the accuracy of the prediction and to isolate where and why the prediction might fail. The geometric description of the test model is included in EXPERIMENTAL EQUIPMENT (item 2). Items 3, 4 and 5 are available for the design rotor inlet flow angle ($\beta_1 = 40°$) in Joslyn and Dring (1989). Item 4 is available for $\beta_1 = 54°$ in Joslyn and Dring (1983). The primary objective of the present program has been to provide the associated comprehensive set of full–span heat transfer data (item 6) thus fulfilling all requirements for a benchmark–quality data set.

A secondary objective of the program has been to examine the ability of a relatively simplified analysis to capture the major features of a rotating, viscous turbine passage flow. This analytical effort was conducted entirely under NAS8–37351 and reported in Blair and Anderson (1989). The results from this analytical task are included in this present report in order that all work on this study be available in a single, comprehensive document.

The need for this new rotating, viscous analysis arises because of the excessively large computational resource requirements involved if the full Navier–Stokes equations are employed for solution of this problem. Use of the full Navier–Stokes equations results in a problem so large that even modern supercomputers cannot resolve all scales involved in the flow field and currently requires that the problem be solved on a much reduced computational mesh.

Generally this means that one is forced to make a number of approximations concerning the nature of the boundary layer so that the problem is tractable. Unfortunately this means that one can not now completely resolve the scales involved in calculating the flow in the boundary layer. In addition, these approximations are based on our knowledge of two dimensional boundary layers and may be inadequate for three dimensional boundary layers which are different in some important respects. Finally we should note that while there is an established paradigm for the prediction of the forces in the flow field, there is no comparable paradigm for the prediction of the turbulence in the flow field although many models have been suggested. This is particularly important for the prediction of the heat transfer on the turbine airfoils where unsteadiness and transition are important factors. Therefore it would be useful to solve a subset of the Navier–Stokes equations, namely the

parabolized Navier–Stokes (PNS) equations. Although one would be limited in the class of problems one can consider, it does have the advantage of speed so that a detailed mesh can be used to resolve all the scales in the three dimensional flow field and so that the boundary layer can be treated in a more direct manner. Such an algorithm could be used to develop detailed models of turbulence and could also be used to to provide a quick assessment of the flow field for such quantities as heat transfer in the design stage of building a gas turbine. The present study describes one such PNS solution algorithm, applies it to the gas turbine problem, and evaluates the procedure against experimental data for both a rotor and a stator.

The development of the PNS equations and a solution algorithm has two requirements. First it must be shown that the equations are parabolic, and second it must be shown the the problem is well posed. In addition one must face the problem that the solution of a parabolic problem is a function only of the initial conditions and the boundary conditions. It is not a function of the downstream conditions. Therefore some information about the elliptic properties of the flow field must be included in the solution algorithm. Generally speaking,three methods have been used to resolve these problems: 1. parabolized fully viscous methods, 2. reduced Navier–Stokes methods, and 3. fully parabolized Navier–Stokes methods. In the first method, pioneered by Patanker and Spalding (1973), Curetto, Curr, and Spalding (1973), and Briley (1974), these problems are resolved by neglecting the second derivatives in the streamwise direction to parabolize the equations, and using the inviscid streamwise static pressure gradient with some corrections to make the problem well posed and to include the elliptic effects in the algorithm. This unfortunately results in a solution in which the streamwise and crosswise pressure are split and not the same. The second method, developed by Schiff and Steger (1979), Vigneron et al. (1978), and Barnett (1982), again neglects the streamwise second derivatives to parabolize the Navier–Stokes equations but uses a special treatment of the static pressure in the boundary layer to make the problem well posed. This method appears to work well for supersonic flow but it is not clear at the present time that it would work with subsonic flow. The third method, developed by Anderson et al. (1981) involves writing the equations of motion in a potential flow coordinate system in which stream surfaces and potential surfaces are the coordinates. Then Navier–Stokes equations are parabolized by assuming that the crossflow velocities are small following a procedure similar to that used in deriving the boundary layer equations. This procedure results in a set of of equations which are parabolic and the problem is well posed. In addition, the elliptic properties of the flow field are contained in the coordinate system. The price one pays for using this procedure is that one may be limited in the magnitude of the cross flow velocities which may be treated. The detailed procedure is given by Anderson (1989) and is the method contained in the UTRC PATH code which will be evaluated in this report.

The scope of the computational portion of this report is to: 1. describe this analytical procedure, 2. calculate the three dimensional flow fields for a 90° turning duct, a low speed cascade simulating a gas turbine stator, and a gas turbine rotor, and 3. evaluate and assess the method by comparison with experimental data for the three dimensional velocity fields, wall static pressure distributions, and, wall heat transfer.

EXPERIMENTAL EQUIPMENT

1. Turbine Facility

All experimental work for this program was conducted in the United Technologies Research Center Large Scale Rotating Rig (LSRR). This test facility was designed for conducting detailed experimental investigations of flow within turbine and compressor blading. The LSRR facility is of the open circuit type with flow entering through a 12–ft. diameter inlet. A 6 in. thick section of honeycomb is mounted at the inlet face to remove any cross flow effects. The inlet smoothly contracts the cross section to 5 ft. diameter. The flow is then passed through a series of fine mesh screens to reduce the turbulence level. Immediately downstream of the screens is a 7–foot long section which slides axially and permits access to the test section. The test section consists of a series of constant diameter casings enclosing the turbine, compressor, or fan model assemblies. The casings are wholly or partially transparent which facilitates flow visualization and laser–Doppler–velocimeter studies. The rotor shaft is cantilevered from two downstream bearings, thus providing a clean flow path at the model inlet. Axial length of the test section is 36 inches. The rotor is driven or braked by a hydraulic pump and motor system which is capable of maintaining shaft speeds up to 890 rpm. Downstream of the test section flow passes through an annular diffuser into a centrifugal fan and is subsequently exhausted from the rig. A vortex valve is mounted at the fan inlet face for flow rate control.

The general features of the turbine test section geometry are shown in figures 1 through 3. Figure 1 presents a sketch of the test section arranged in the 1 1/2 stage (stator1/rotor/stator2) configuration. As indicated in Fig. 1, the turbine model has 22 first stage stator airfoils, 28 first stage rotor airfoils and 28 second stage stator airfoils. Figure 2 shows a radial view of the first stage airfoils at midspan. A photograph of the facility showing the rotor and second stator rows installed in the test section is presented in Fig. 3.

The turbine model simulates a relatively heavily loaded machine with a hub/tip radius ratio of 0.8. All three airfoil rows have solidities and aspect ratios very near unity. When operating at design conditions the turbine (at midspan) has a rotor inlet flow angle $\beta_1 = 40°$ (a flow coefficient, Cx/U = 0.78) a stage loading coefficient of $\left(\frac{C_p \Delta T}{U^2}\right)$ 2.8 and 34% static pressure reaction ($\Delta Ps_{rotor}/\Delta Ps_{stage}$). The axial spacing between the first stator and the rotor was 50% of the average of the first stage stator and rotor axial chords (Bx). The axial spacing between the rotor and the second stator was 63% Bx. The rotor tip clearance was 0.060 inches or 1% span which is typical for current aircraft engine design.

The LSRR turbine model is shown schematically in Fig. 4 along with the SSME/HPFTP drive turbine. Comparisons of the flow paths and turbine design parameters for the LSRR and the HPFTP are given in Fig. 4 and Table 1. These comparisons indicate that the LSRR and HPFTP are very similar, even in the approach duct and the center body upstream of the turbine. The hub/tip ratios

are quite close (0.83 vs 0.80) while the airfoil aspect ratios (span/axial chord) are within about 15%. Table 1 indicates that the airfoil exit angles (α_2) for the LSRR and the HPFTP are within 1/2 deg. while the inlet flow angles (β_1) can also be brought within 1 deg. by operating the turbine at a flow coefficient (Cx/U) of 0.57 instead of its nominal design value of 0.78. The LSRR has a gap/chord ratio which is about 40% greater than that of the HPFTP. This higher loading is typical of aircraft turbines and is achieved while maintaining good airfoil aerodynamics. Extensive flow visualization tests conducted in the LSRR have confirmed that there is no boundary layer separation on any of the airfoils at Cx/U = 0.78.

2. Turbine Airfoil Coordinates

The surface coordinates (x, y) of the three airfoil rows (stator1/rotor/stator2) are given in Tables 2, 3 and 4, respectively, for the hub, midspan and tip sections.

3. Rotor Passage Heat Transfer Model

Description of the Heat Transfer Technique. Of the numerous phenomena that influence turbine convective heat transfer rates the most important effects (first order effects) are a consequence of local flow conditions. Examples of aerodynamic phenomenon which have extremely large effects on turbine convective heat transfer rates are the transition of a boundary layer from laminar to turbulent flow, separation or reattachment, velocity gradients, and strong secondary flows such as the leading edge horseshoe and main passage vortices. These "first order" heat transfer effects can be experimentally simulated by employing only very small levels of surface heat flux. There is no requirement to reproduce the large temperature differences present in the actual gas turbine environment. These small heat flux levels generate proportionally small fluid temperature gradients (of opposite sign to the actual gas turbine environment) and result in flows of near constant density. For such near–constant density flows the absolute direction of convective heat flux, whether to or from the solid surface, is immaterial. In numerous earlier experiments (e.g. Reynolds, Kay, and Kline, 1958; Ota and Kon, 1974; and Subramanian and Antonia, 1981) electrical resistive heating of surface metal foils has proved to be a highly practical method for generating low levels of uniform surface heat flux. Recently this basic experimental method has been significantly improved through a series of technique development programs at UTRC. Of primary importance has been the development of techniques for using rigid cast urethane foam as the construction material for test aerodynamic models. Rigid urethane has an extremely low thermal conductivity which nearly eliminates errors in heat transfer measurements due to conduction in the airfoil. Techniques have also been developed for attaching metal foil to the urethane foam models using extremely thin layers of adhesive. Use of these new construction techniques results in uniform heat flux test models with negligible (less than 1 percent) back–losses and minimal transverse "smearing" through conduction. Calculations indicate that, even in a region with a lateral gradient of heat transfer coefficient of 100 percent per inch, local heat transfer coefficients can be measured within an accuracy of 5 percent using these construction materials and techniques. Graziani et al.,

1980; Blair, 1983; and Blair, 1984, present examples of the use of these heat transfer measurement techniques.

Instrumented Airfoil Construction Technique. As described in the preceding section, heat transfer measurements were obtained in this study using low conductivity rigid foam castings of the test airfoils. A nearly uniform heat flux was generated on the surface of the foam test airfoils using an electrically heated metal foil skin attached to the model surface. Local heat transfer coefficients around the airfoils were determined using thermocouples and liquid crystal techniques to measure the temperature difference between the heated metal skin and the free stream. A description of the methods used to account for nonuniformities in the current density over the heated metal foil can be found in subsection 7, Foil–Heater Current Nonuniformity Corrections.

Photographs of the first stage rotor airfoil model at various steps of fabrication are presented in Fig. 5, 6 and 7. The first stage of the fabrication process consisted of developing a metal "master airfoil." An aluminum rotor blade, chosen at random from the LSRR rotor, was carefully inspected to determine locations with surface waviness. These slight deviations from a perfectly "developable" surface (a surface with no compound curvature) are an inherent characteristic of the "multiple radial station contour tracing" machining process used to manufacture the aluminum airfoils. Despite the fact that this surface waviness only consists of depressions a few thousandths of an inch deep at their maximum, they do present a problem unique to this method of instrumentation. The metal foil which is to be glued to the exterior surface of the airfoil is extremely intolerant of surface waviness. Even miniscule depressions on the airfoil translate to "wrinkles" or "lumps" on the finished, assembled airfoil surface. For this reason it was necessary that any depressions be filled to produce as nearly a "developable" surface as possible. This filling procedure consisted of a trial–and–error/inspection iteration towards the finished airfoil. An airfoil was accepted as a "master" only after a completely wrinkle–free "test" metal foil could be glued to its entire surface. An inviscid flow computation of the velocity distribution around the finished "master" airfoil indicated that the maximum change in local velocity produced by the surface filling (measured maximum filling thickness) was only 1/4 percent.

A steel skeleton (Fig. 5) was fabricated for each of the test airfoils to ensure adequate strength to endure both the aerodynamic and centrifugal forces of the test environment. The skeleton also provided a secure location to attach the foam airfoil to the rotor hub. The photograph of the steel skeletons presented in Fig. 5 shows the "button" for precisely positioning the steel skeletons. The "button" duplicates the mandril used to position the metal "master airfoil" in the rotor hub. The remaining photographs of Fig. 5 show one of the steel skeletons mounted in a special fixture designed to ensure precise alignment of the steel skeleton in the mold. The curved base plate shown in these photographs duplicates the 24–inch hub radius of the turbine test model and serves as the hub wall of the airfoil mold. The bracket below the curved base plate precisely fits both the mandril "button" on the "metal master" airfoil and the "button" which slides over the mounting post on the steel skeletons.

The next step in the model fabrication process consisted of casting a concrete mold of the master airfoil. Special low shrinkage gypsum cement (USG Hydrocal) was used to produce a

smooth airfoil surface and a precise geometrical reproduction. A photograph of the completed mold is presented in Fig. 6. The final assembly of the steel skeleton, alignment bracket and concrete mold is also shown in Fig. 6 with one wall removed. Photographs of the completed cast foam airfoils showing both the pressure and suction surfaces are also presented in Fig. 6.

Heat transfer measurements were obtained over the entire surface of a rotor passage (rotor endwall and the pressure and suction surfaces of a pair of adjacent rotor airfoils). The rotor airfoil with instrumentation along its pressure surface will henceforth be referred to as the Pressure Surface Airfoil, its adjacent twin as the Suction Surface Airfoil.

Photographs of the Pressure Surface Airfoil at various stages of assembly are given in Fig. 7. The two upper photographs show the airfoil following the attachment of the stainless steel foil to the pressure surface. Miniature thermocouples have been welded to the "backside" of the foil through holes in the airfoil. Thermocouple leads coming from the instrumentation sites were routed in grooves along the airfoil suction surface. The lower–left photograph shows the model with the instrumentation grooves filled to restore the original airfoil contour. Also shown in this photograph are the full span buss bars to which the foil would be attached. The lower right–hand photograph shows the airfoil after the foil was attached to the suction surface and connected to the buss bars. After the groove between the buss bars was filled the airfoil was ready for installation on the rotor hub.

Rotor Hub Endwall Heat Transfer Model. The rotor airfoils in the (LSRR) are mounted on a 48–inch diameter ring (the rotor hub). This hub serves to rigidly support the rotor airfoils and to ensure their precise circumferential and axial locations. Because of the large centrifugal forces associated with the rotating airfoils the rotor hub is, of necessity, a massive device (total weight is approximately 250 pounds).

In order to facilitate the measurement of the hub–endwall heat transfer distributions a new LSRR rotor hub was designed and fabricated as part of the ongoing UTRC Corporate–sponsored program. This new hub differs from earlier models in two ways. First, a deep relief (spanning almost two airfoil pitches) to accommodate the endwall heat transfer model had to be incorporated into the hub. Second, the axial length was greatly increased so that endwall heat transfer data could be obtained upstream and downstream of the airfoil leading and trailing edges. New support rib structures were designed into this hub to prevent out–of–round distortion during rotation.

A photograph of the endwall–heat–transfer hub is presented in Fig. 8. The relieved region in which the hub endwall heat transfer model will be installed can be seen in the upper right of the photo. Also shown in the photo are the radial holes around the circumference of the hub to be used for mounting the airfoils.

As with the airfoil heat transfer models, the hub–endwall model consisted of a block of rigid urethane foam with an electrically heated thin metal foil skin. The endwall foam block was cast to fit into the hub relief region with its exterior surface precisely matching the hub outside diameter. In other words, the endwall casting replaced the relief region cut into the hub.

The heated endwall surface extended axially from 1.50 in. (0.24 Bx) upstream of the rotor leading edge to 1.30 in. (0.21 Bx) downstream of the rotor trailing edge (total axial heated length of 9.15 in.). Circumferentially the heated surface covered the entire endwall between the instrumented airfoils and extended to approximately midway across the endwalls of the two adjacent passages (total circumferential extent of approximately 2 rotor airfoil pitches). Three parallel, 3.05 in wide, circumferentially running metal foil strips were used to generate the uniform heat flux boundary condition on the endwall surface. These three strips were wired in series to assure that precisely the same current passed through each.

With this arrangement the endwall heating foil passed beneath the bases of the two instrumented heat transfer airfoils. Since there would be no gap at the bases of the airfoils and hence no airflow across the bases there would be no exterior convective mechanism to remove the locally generated heat. To alleviate this problem cooled copper plates, shaped to conform to the airfoil profile at the hub, were incorporated into the endwall model. These cooled plates removed the heat generated by the endwall heating foil beneath the base of the heat transfer airfoils.

Photographs showing various views of the endwall model hardware are presented in figure 9. The upper photograph shows the disassembled components including the copper blade root cooling inserts, the power buss bars, and the support frame by which the endwall model is attached to the rotor hub. Note that the copper base plates have cooling tubes soldered to their bottom surfaces. The amount of cooling air passing through the tubes on the backside of the plates was adjusted during operation to achieve the correct thermal boundary conditions. The lower left photograph shows the assembled endwall components viewed from the bottom of the support frame. This view shows the cooling lines, the buss bar power lines, and the access holes for the instrumentation from the rotor blades. The lower right hand photograph shows the assembled endwall model as viewed from the top. Note the instrumentation holes through the copper cooling plates for the rotor blade instrumentation.

Two photographs of the rotor hub/endwall model assembly are presented in Figure 10. The left hand photograph shows the cutout region of the hub, the support bushings for the rotor airfoils and the routing holes for the various power, cooling, and instrumentation lines. The right hand photograph of figure 10 shows the assembled endwall model installed in the hub cutout and ready for the casting of the rigid urethane foam endwall surface.

Rotor Passage Test Configurations. Rotor passage heat transfer data were obtained for two model surface conditions; for an aerodynamically smooth wall and with wall roughness simulating actual SSME hardware. A photograph of the completely assembled rotor passage model in the smooth–wall condition is shown in Fig. 11. For these smooth–wall tests the airfoil and endwall surfaces were prepared for obtaining liquid–crystal data, i.e. they were covered with a black base paint and then coated with encapsulated liquid crystals. The grid lines on the airfoils and endwall were required for interpretation of the photographs of the liquid–crystal temperature patterns. These grid lines were created by masking the unpainted model and provide a very smooth, trip–free finished surface.

Rotor Passage Surface Roughness Measurements. One objective of the present program was to obtain passage heat transfer data for a surface roughness simulating that found in actual SSME hardware. Roughness measurements for actual SSME hardware, obtained with a Dektak Model 3030 profilometer indicated a peak–to–peak roughness height of 3300μ inches which scales (based on chord) to 26,000μ inches for the LSRR model. A screened grit of 26,000μ inches was applied uniformly over the entire rotor model test surface for these rough–wall tests. A photograph of the completed rough–wall model is presented in Figure 12.

The Dektak profilometer was also employed to measure the surface roughness associated with the liquid–crystal coating of the smooth–wall model of the present contract (see Figure 22). These measurements indicated that the liquid–crystal coating had RMS and peak–to–peak roughness heights of 13 and 300μ inches, respectively.

Finally, Dektak profilometer readings were also obtained for the flat–black surface coating used for a previous turbine airfoil heat transfer study conducted in the LSRR (NASA–HOST Contract NAS3–23717, Dring et al., 1986). The RMS and peak–to–peak roughness heights measured for the flat–black coating were 250 and 2000μ inches, respectively.

As part of this report, the rotor–airfoil midspan heat transfer data obtained for both the smooth–wall and rough–wall model configurations will be compared to midspan data measured for the NASA–HOST contract. The profilometer measurements described above indicate that these three sets of heat transfer data encompass a wide range of surface roughness. For the range of Reynolds numbers involved, the liquid–crystal coating of the present tests can be considered to be aerodynamically smooth. The flat–black coating of the NASA–HOST contract was approximately 10 times more rough than the liquid–crystal coating, while the grit–roughened wall was approximately 10 times rougher still than the flat black (100 times rougher than the liquid–crystal coating). For purposes of discussion, these three model surface conditions will be referred to from here forward as smooth (liquid–crystal, present tests), near–smooth (flat–black, the NASA–HOST data) and rough (grit–surface, present tests). The surface roughness values for the various test models are listed in the following table.

Rotor–Model Surface Condition	RMS Roughness Height (μ inches)	Peak–to–Peak Roughness Height (μ inches)
Smooth (Liquid–Crystal)	13	300
Near Smooth (Flat–Black)	250	2,000
Rough (Grit)	Not Measured	26,000

4. Rig and Turbine Model Assembly

Slipring–Rotary Union Assembly. Thermocouple and electrical power leads for the rotor airfoils and endwall model were all connected through a Wendon Co. 212 slipring unit. Leads from the rotating models passed through a hollow arbor which also served to support the slipring unit. Photographs of the slipring unit and arbor are presented in Figure 13.

Coolant air for the copper baseplates (mounted beneath the rotor airfoils) is also passed through this hollow arbor. The stationary/rotating connection for this coolant air is made through a rotary union mounted on the extreme end of the arbor. The rotary union can be seen in the upper photograph of Figure 13 in which the components are shown disassembled. The high pressure flexible hoses shown in this disassembled view were connected to the rotating face of the union, passed through the arbor and were connected to a bank of 6 remotely controlled needle valves (not shown). The coolant flowrates in the passages in the copper baseplates were controlled by these needle valves. The assembled slip ring/rotary union is shown in the lower photograph of Figure 13.

Hardware and Model Assembly. As part of the installation of the new rotor hub into the rig it was necessary to fabricate and fit a pneumatic seal between the first–stage stator and the rotor hub. This seal consists of an abradable ring on the forward face of the rotor hub which was custom–fit to a set of knife–edges aft of the stator support ring. This custom–fitting process consisted of a series of step–by–step engagements of the stator knife edges into the abradable rotor seal with the LSRR operating at very low speed. With each successive step the knife edges wear grooves of increasing depth into the abradable material. The end result of this procedure is a precision–fit rotating seal which prevents leakage of air from the inner rig cavity to the gas path.

Installation of the test hardware into the LSRR consisted of the following tasks: (1) The 28 rotor airfoils (2 heat transfer airfoils and 26 solid aluminum airfoils) were installed into the rotor hub. (2) The first stator and rotor passage throats were set precisely to assure uniform, periodic

blade–to–blade flow through the stage. (3) The blade tip gaps were adjusted to assure equal tip/rotor–casing clearance for all airfoils. (4) All power and instrumentation wiring and all cooling lines were routed to the slipring/rotary union. (5) The completed hub–assembly was dynamically balanced at 320 RPM.

A photograph of the partially completed assembly is presented in Figure 14. Shown in the photo are the 6 remote controlled needle valves, the cooling lines running to the rotor blade baseplates, and the instrumentation wiring routed to the rig centerline. Figure 15 shows the rotor at the next stage of assembly. In this photograph the instrumentation wiring has been routed through the slipring. Note the completed heat transfer model mounted on the rotor hub.

5. Thermocouple Data Acquisition System

Thermocouple leads from the rotor passage model were connected through the previously described Wendon Co. slipring unit. Figure 13 shows an important feature of this slipring unit, the stationary and rotating connection points are in close proximity in order to minimize any secondary voltages generated at these connections. Leads from the stationary terminals of the slipring unit were connected to Uniform Temperature Reference (UTR) blocks (Kaye Instruments, UTR–48N). Data were recorded using a Hewlett–Packard 300 channel data acquisition unit (3497A/3498A), and an ice point reference (Kaye Instruments, K140–4). Reduction of the thermocouple signals to temperature and engineering heat transfer units was accomplished using an IBM PC.

The Wendon Co. slipring unit employed for these tests was a low–noise, multi–wiper, carbon/silver model. Secondary thermoelectric sources produced by frictional heating at the slipring/wiper contacts was minimized through air cooling of the Wendon unit. The remaining spurious (frictional) signal generated at each channel of the air–cooled slipring was determined in–situ through a series (ten rotational speeds) of adiabatic model tests. These tests consisted of the measurement of the rotor passage model temperatures with the model unheated (for a zero spurious slipring signal the thermocouples would have indicated the relative–frame adiabatic recovery temperature). These measurements established that the spurious slipring–generated signals were small, highly repeatable, and linearly dependent on the rotational speed. An individual "slipring correction factor" was determined for each slipring (typical value – 0.008 deg. C/rpm) and was used to correct temperature data recorded for the heat transfer tests.

The combination of the precision thermocouple signal recording system and the above slipring corrections provided the capability to obtain highly accurate thermocouple temperature measurements on the rotor passage model. It is estimated that surface temperatures on the rotating model were measured within +1/2 deg. C.

6. Thermocouple Instrumentation Coordinates

For the present program, detailed heat transfer distribution data were obtained over the hub endwall and on both the suction and pressure surfaces of the rotor airfoil. A special rotor surface

instrumentation coordinate system was developed to accommodate the complex three–dimensional geometry of the rotor airfoil. This instrumentation coordinate system fulfilled two purposes: (1) it provided a technique to accurately position heat transfer measurement sites (thermocouples), and (2) it provided a system for transmittal of the measured heat transfer distributions. The coordinate system uniquely identifies a position on the rotor airfoil surface (1) radially in terms of percent span, and (2) chordwise in terms of percent distance along the respective (pressure or suction) surface. Surface distances along the airfoil were measured between reference S=0% and 100% locii, the definitions of which are illustrated in Fig. 16. The geometric "zero" at a given spanwise location was defined as the point on the leading edge circle tangent to a straight line which was also tangent to the trailing edge circle (S=100%). The tip, midspan and hub tangencies are illustrated in Fig. 16. The locii of the tangency points at all spanwise locations formed the S=0% and S=100% lines. As shown in Fig. 16, the distance "S" is defined as increasing positive along the suction surface and increasing negative along the pressure surface.

A full–scale coordinate–system rotor airfoil model was constructed to facilitate the production of a template in the above % span vs. % S coordinates. This template was later employed for locating thermocouples during the instrumentation of the heat transfer models. First, the span on one of the original 28 metal airfoils from the LSRR rotor was extended by 1% (the tip clearance for the rotor model) to provide a "100%–span" geometric model. Second, the entire airfoil surface was covered with a sheet of Vellum drafting paper. Third, the S=0% and 100% locii as well as locii of constant % span (in 5% increments) were drawn onto the Vellum. Finally, straight lines were generated, from hub to tip, connecting points of equal % surface arc length (in 5% increments). The resulting pattern on the Vellum sheet, then, consisted of lines of constant % span and % S in 5% increments.

Four views of the assembled coordinate system model are presented in Fig. 17. Also shown in Fig. 17 are the locations of the adjacent airfoils on the rotor stage. It should be pointed out that the locii of constant % span correspond to surfaces of constant radius from the turbine axis of rotation but that the locii of constant % S are not radial and do not correspond to lines of constant axial position.

The thermocouple instrumentation arrays for the pressure and suction surface heat transfer airfoils are presented in Figures 18 and 19 respectively. Note that each airfoil thermocouple site is located at the juncture of a grid line of fixed % span and a grid line of constant % surface distance. The lines marked LE in Figs. 18 and 19 correspond to the airfoil leading edge (S=0). Both the spanwise and surface length grid lines are in increments of 5%. For both Figs. 18 and 19, the airfoil root (0% span) is located at the bottom. Following is an example of determining a thermocouple location: for Fig. 19, thermocouple number 24 is located 8 grid increments from the root (40% span) and 2 grid increments from the leading edge (10% S).

For the pressure surface airfoil there were 89 thermocouples installed on the test (pressure) surface and 7 thermocouples on the reverse side. For the suction surface airfoil there were 124 test (suction) surface thermocouples and 6 on the backside. The locations of the power buss bars are also shown in each figure.

A diagram of the thermocouple pattern for the endwall model is presented in Figure 20. The endwall instrumentation extends from 0.12 Bx upstream of the leading edge plane to 0.14 Bx downstream of the trailing edge plane. As indicated in Fig. 20, there were 101 thermocouples installed on the endwall surface.

7. Foil–Heater Current Nonuniformity Corrections

As described in Section 3 above, numerous earlier heat transfer experiments have employed thin–foil, electrical resistive heating as a means of generating a surface heat flux. Heater foils employed for these earlier experiments have been high–aspect–ratio rectangles with electrical buss bars attached at the ends. With this configuration, provided that the buss bars are in uniformly good contact over the entire width of the foil strip and provided that the foil has spatially uniform resistivity, the electrical current (and heat generation) will be uniformly distributed everywhere on the foil.

Rotor Airfoil Models. One objective of the present program was to obtain heat transfer data over the entire surface of the test rotor passage. To achieve this end it was necessary that the heater foil attached to the surface of the rotor airfoils cover the entire airfoil surface, from root to tip (0 to 100% span). The surface heater foils attached to the pressure–surface and suction–surface rotor heat transfer models were the precise shape of the "unwrapped" surfaces shown in figures 18 and 19, respectively. The buss bar attachment sites are also indicated. As can be seen from an examination of Figure 18 and 19, these heater foils were not simple rectangles but rather complex shapes.

Nonuniformity of the electrical current over the complex heater foil was determined using a finite–difference two–dimensional Laplace equation solver configured for use as a thermal conduction solution. The solutions could be applied to the present problem because the Laplace equations govern the potential flow of both heat and electrical current. There is a direct analogy between the temperature and voltage potential fields and between the resulting flow distribution of heat and electrical current. The analysis was performed to determine local heat (current) fluxes at the thermocouple sites on the airfoil surfaces. A temperature (voltage) potential difference was imposed between the buss bar attachment sites and the resulting heat (current) fluxes were determined. The ratio of local heat (current) flux to the average flux on each surface was calculated and used as the foil–heater current nonuniformity correction.

The computer program used to determine the corrections (ANSYS–PC/THERMAL 4.3) is one of a family of ANSYS products developed for structural and thermal analysis. (Anon., 1988). This program uses a finite element method in which the surface to be analyzed is divided into discrete pieces, called elements, that are connected together at a finite number of points or nodes. Each node has a degree of freedom which is the temperature at the node. A conductivity matrix, which relates the nodal temperatures of an element, is a combination of the temperature function and material properties of the element. By imposing a heat balance at every node, the individual conductivity element matrices are assembled into a set of linear simultaneous equations. This equation set is solved for the nodal temperatures from which quantities such as thermal gradients can be found.

The grids for the thermocouple placement shown in Figs. 18 and 19 were also used for the thermal analysis. Nodes were placed at 10% intervals in the spanwise direction and at 5% intervals from –5% to 105% along the surface arc length. Therefore, each element had dimensions of 10% of span by 5% of surface arc length. The ANSYS program provided the nodal temperatures and the heat fluxes at the centroid of each element. The fluxes for each set of ten spanwise elements were summed to determine the total flux passing through the airfoil at a particular surface arc length. Each total was compared to the average of the totals as a check on the internal consistency of the calculation procedure. The largest deviation from the mean was 1.5% on the suction surface and 0.7% on the pressure side.

The deviation of the flux for each element from the average flux was used to determine the current nonuniformity correction. For each node (thermocouple location) which was the common point of four elements, the correction applied was the average of the flux deviations for the four elements. For those nodes which were at the common midpoint of two elements, the correction was the average flux deviation for those two elements.

Typical current density corrections at the various thermocouple sites on the foil surfaces were ±4% from the mean. The largest corrections were –10% at T.C. site #10 and +10% at T.C. site #18, both on the suction surface (see Figure 19). Corrections within the spanwise zone covering ±10% from midspan were within ±3% for both the pressure and suction surfaces.

Endwall Model. This same procedure was applied to the endwall region to determine corrections at the thermocouple sites there. Despite the fact that the endwall heater foil consisted of simple rectangular strips, a current nonuniformity analysis was required to account for the effect of several access holes cut through the foil beneath the rotor bases. These holes, which can be seen located in the blade–base cooling plates of Figure 9, were employed to pass the power and thermocouple leads from the instrumented rotor airfoils through the hub to the slipring. All of the holes were located way from the actual heated endwall test surface.

Implementation of the ANSYS solver was considerably more complex for the endwall problem than for the airfoil power strips. Because of the extreme distortion of the current flow paths near the holes, it was necessary to employ a more closely packed mesh of elements in their immediate vicinity. However, since the holes through the foil were located several hole diameters away from thermocouple sites it was possible to employ a uniform grid over the regions where the thermocouples were located. Because of this, the same procedure employed to determine the correction factors from the airfoil surface heat fluxes was applicable to the endwall problem.

Current density corrections on the endwall were less than those required for the airfoil surfaces. Over 90% of the thermocouple sites required corrections of +3% or less. The larges single correction (+4.9%) required was for T.C. #17H (see Fig. 20).

8. Liquid Crystal Temperature Measurements

Liquid–crystal techniques were used in conjuction with data from the model thermocouple arrays to determine the heat transfer distributions on the airfoil and endwall surfaces. The objective

of employing liquid–crystals in addition to the thermocouple arrays was to obtain more detailed information in regions of strong spatial variations of the passage heat transfer distributions. All liquid crystals employed in this investigation consisted of a mixture of Hallcrest encapsulated Chiralnematic slurries. The mixture contained 8 slurries, each with a different color–band temperature. The width of each color band, however, was 2 deg. F for all of the individual slurries. The nominal color–change (begin–red) temperatures for the 8 slurries were 50, 60, 70, 80, 90, 100, 106 and 116 deg. F. The accuracy of each color band was within 1 deg. F as determined in water calibration tests. Application of the liquid–crystal mixture on the passage surface was accomplished by spraying over a Hallcrest–supplied black base coat (see Fig. 14).

The liquid–crystal illumination was accomplished with a General Radio Model 1540 Strobolume synchronized to the passing of the rotor model. A Xenon bulb with a flash duration of 12 μsec. and a power of 1.8 Joules/flash was employed. Photographs were obtained with a Cannon 35 mm. SLR with a 35–105 mm zoom lens and 200 ASA color print film. Typical exposure settings were approximately f5.6. The camera viewed the rotor passage through a plexiglass window at the rotor axial station. The arrangement provided near–normal viewing angles to most of the rotor airfoil and endwall surfaces.

TEST CONDITIONS

1. Flowpath Aerodynamic Documentation

The aerodynamic characteristics of the LSRR 1 1/2 stage turbine model have been thoroughly documented in previous investigations, most of which were conducted at the design rotor inlet flow angle ($\beta_1 = 40°$). All of these aerodynamic data are available either in the form of UTRC reports, Government Contract reports or as open literature publications.

The most exhaustive documentation of the aerodynamics of the turbine model is presented by Joslyn and Dring (1989). Some of the most important results from this document will be presented here as an indication of the nature of the aerodynamic data available for this model.

Joslyn and Dring (1989) present a comprehensive set of rotor airfoil aerodynamic data including measurements of the total pressure, static pressure, flow velocity and flow direction both upstream and downstream of the rotor. These measurements were obtained through the use of inter–airfoil–row traversing instrumentation. Both stationary and rotating instrumentation were employed. All of the traverse and rake probes utilized in this study were standard United Sensor products. Ammonia–Ozalid paper surface flow visualization techniques were employed on the turbine airfoil surfaces.

The highly three–dimensional nature of the flow through the rotor passage is demonstrated by the flow visualization results of Fig. 21. The suction surface results clearly show the flow convergence produced by the hub and tip secondary flow vortices (endwall cross–passage flow moving onto the suction surface). The suction surface view also shows how the path taken by the

tip leakage flow varied along the chord. The dominant feature on the rotor pressure surface was the radial flow toward the tip due to the relative eddy. This is an inviscid mechanism due to the vorticity in the rotating frame of reference. Its effect was strongest on the forward portion of the pressure surface because the surface flow speed was lowest there (Dring and Joslyn, 1983). The surface streamlines turned away from the radial direction as the flow accelerated toward the trailing edge. The hub endwall flow visualization (not shown) revealed strong over–turning due to secondary flow.

Comparisons of the measured and computed static pressure distributions for the first stage stator and rotor are shown in Fig. 22 for the 2%, 50% and 98% span locations. The curves are the time–averaged computed results and the symbols are the measured results.

The measured rotor pressure distribution data are shown as pairs of symbols at the 2% and 50% locations. These two symbols represent the range of the measurements that have been taken on the rotor during the various experiments that have been conducted between 1977 and 1988. A similar comparison for the first stator showed that the range of measurements for this airfoil was within the size of the symbols.

The computed results are by Rai (1987). This comparison was made in spite of the fact that the rotor aspect ratio in the computation was low (by the factor 11/14) and in spite of the fact that the tip clearance was too small (0.4% vs. 1% span). The results by Madavan et al. (1989), however, showed that the impact of the rotor aspect ratio on the rotor pressure distribution was relatively small. The same can not necessarily be said for the effect of the rotor tip clearance, especially at the 98% span location. This question remains to be answered (Rai, 1989a).

In general, the agreement between the measured and computed pressure distribution results was excellent. Agreement at the hub was reasonably good and the results of Madavan et al. (1989) show that the suction surface agreement gets better when the correct aspect ratio and a finer computational grid were used. At the rotor midspan agreement was excellent. At the tip, however, there was a difference between the measured and computed results on the aft portion of the rotor suction surface. This discrepancy may well have been due to the small tip clearance used in the Rai (1987) calculation.

Total pressure contours measured in the flow downstream of the first stator are shown in Fig. 23a. These data were obtained at a plane located 17% aft of the stator trailing edge. The contours show the migration toward the hub of the low total pressure fluid in the hub and tip secondary flows. The maximum local losses $\left(\frac{\Delta P}{QU_m}\right)$ for the tip secondary flow (near 65% span) and hub secondary flow (near 13% span) were about 1.5 and 2.5 respectively. These results indicate a thicker endwall boundary layer at the tip than at the hub, a result due to the thicker tip boundary layer at the stator inlet.

The measured secondary flow vectors downstream of the first stator are shown in Fig. 23b. The radial component of each vector is proportional to the radial velocity component. The tangential component of each vector is proportional to the difference between the actual tangential velocity

component and the tangential velocity component corresponding to the actual axial velocity component and the area averaged velocity components at midspan. This corresponds to looking upstream at the velocity vectors from the direction of the averaged yaw angle at midspan.

Each vector in Fig. 23b represents a measurement location. It can be seen that the data density was highest in the airfoil wakes and near the end walls. These results demonstrate the radial transport (toward the hub) in the stator wake due to the strong radial static pressure gradient at this plane. This was the mechanism that moved the tip and hub secondary flows toward the hub (Fig.23a). Note the vortical motion in the hub secondary flow.

The spanwise distribution of the measured relative yaw angles (from axial) aft of the first stator are shown in Fig. 24. As for Fig. 23 these data were obtained at a station 17% aft of the trailing edge. The two outermost measured points demonstrate the problem of under–turning near the tip.

Contours of rotary total pressure aft of the rotor are shown in Fig. 25a. Here, as with Fig. 23, the traverse data were acquired over two pitches. Since there were 22 first stator airfoils and 28 rotor airfoils the circumferential width of Fig. 25 was reduced by a factor of 11/14 relative to Fig. 23. The contours of Fig. 25a indicate that there was a large low total pressure region downstream of the rotor centered at about 60% span. This was produced by the hub and tip endwall flows impacting the rotor suction surface and then moving toward the midspan region. Note that at this station the hub and tip secondary flows had merged into a single low total pressure region. The effect of the rotor tip leakage flow can be seen in the regions of low rotary total pressure between 80% span and the tip. Recall that the rotor tip clearance was 1% span.

The secondary flow velocity vectors in the flow aft of the rotor are shown in Fig. 25b. This plot was generated in the same manner as Fig. 23b for the flow aft of the first stator. Here also the viewing angle was the averaged relative yaw angle at midspan. Two distinct counter–rotating vortices are clearly evident in the flow downstream of each rotor airfoil passage. These are the hub and tip secondary flow vortices. The region of low rotary total pressure for Fig 25a was coincident with the tip secondary flow vortex at about 60% span.

The final figure demonstrating aerodynamic documentation of the LSRR turbine model presents the spanwise distribution of the rotor relative exit flow angle (Fig. 26). These results can be employed to demonstrate the relationship between turning and axial velocity. A comparison of these turning angle distributions with their respective axial velocity distribution measurements revealed that regions of high angle (over–turning) correspond to regions of low axial velocity, and vice–versa.

2. Compendium of Available LSRR Aerodynamic Data

The results presented in Figs. 21 through 26 represent only a small fraction of the total volume of aerodynamic data available for the LSRR turbine model. This facility has been in operation since 1974 and, since that time, a large number of experimental programs have been conducted in it. Following is a list of these programs in chronological order.

(1) The turbine model was operated in the LSRR with the intent to examine endwall and other secondary flows occurring in the stationary vane and rotor passages (Joslyn, Dring and Camarata, 1976). Several experiments were conducted to improve and expand the capability to obtain meaningful measurements on board a moving rotor (Joslyn, Dring and Camarata, 1977).

(2) A study of film cooling on a turbine rotor blade was conducted under contract to AFAPL, Contract No. F33615–77–C–2068 (Dring, 1977 and Dring, Blair and Joslyn, 1980). This study demonstrated the insensitivity of film effectiveness to centrifugal effects and also demonstrated that the coolant trajectory had an unexpectedly strong radial component on the blade pressure surface.

(3) A study of the three–dimensional nature of the flow over an axial turbine rotor blade was documented by Dring and Joslyn (1981). This study examined a wide variety of flow features and, particularly, the radial flow on the rotor pressure surface and the effects of secondary flow and the tip leakage flow on the nature of the rotor exit flow field.

(4) The turbine model was used to study unsteady and three–dimensional effects. This program utilized multi–element hot–film probes and the on–line phase–lock–averaging capabilities of the LSRR data system. Complete radial–circumferential arrays of the instantaneous and phase–lock–averaged velocity vector were acquired downstream of each of the three airfoil rows. A very small portion of the 10^9 measurements in this program were presented by Joslyn, Dring and Sharma (1982).

(5) A study of turbine rotor–stator interaction and turbine negative incidence stall was conducted under AFWAL Contract No.F33615–80–C–2008 (Dring et al., 1981 and Dring et al. 1982). This work demonstrated that extremely large fluctuations of the rotor and stator pressure distributions occur at typical rotor–stator axial gaps. As part of this study it was also demonstrated that the relative eddy present in the rotor passage was responsible for the strong radial flows on the rotor pressure surface (Dring and Joslyn, 1983). The impact of rotor negative incidence stall on the rotor full–span pressure distribution and surface flow visualization was also investigated. The onset of the pressure surface stall separation bubble, its impact on the pressure distribution and the radial flow within it were all demonstrated (Joslyn and Dring, 1983).

(6) A study of the effects of inlet turbulence and rotor–stator interactions on the aerodynamics (and heat transfer) of the turbine model was conducted under NASA Contract NAS3–23717. Aerodynamic measurements obtained in the program include distributions of the mean and fluctuating velocities at the turbine inlet and, for each airfoil row, midspan airfoil surface pressures and circumferential distributions of the downstream steady state pressures and fluctuating velocities. (Dring et al., 1986 and Blair, Dring and Joslyn, 1989).

(7) In addition to the above experimental studies conducted in the LSRR, the following analytical programs have dealt with the prediction of the flow through this same turbine geometry: (a) Rai, 1987, (b) Rai and Dring, 1987, (c) Rai and Madavan, 1988, and (d) Madavan, Rai and Gavali, 1989.

3. Test Matrix

Rotor passage heat transfer distributions were obtained over a range of Reynolds numbers and rotor inlet flow angles, the variations produced by changing rotor rotational speed and turbine throughflow velocity. A map of the various operating conditions for which heat transfer data were obtained is presented in Fig. 27. An examination of Fig. 27 reveals that data sets A, through E correspond to $\beta_1 = 40°$ (Cx/U = 0.78), set F corresponds to $\beta_1 = 45°$ (Cx/U = 0.68) and sets G through I, and F correspond to $\beta_1 = 54°$ (Cx/U = 0.57). Heat transfer data were obtained for all nine conditions with both the smooth–wall model and the rough–wall model for a total of eighteen (18) data sets.

EXPERIMENTAL RESULTS

As previously discussed, heat transfer data were obtained using both liquid–crystal thermography techniques and arrays of surface thermocouples. The data will be presented in the following order: (1) Samples of the liquid–crystal data will be presented and discussed. The purpose of introducing these particular data first is that they provide a convenient method to discuss a number of general, qualitative features of the passage heat transfer distributions. (2) Next, the quantitative measurements of the passage heat transfer distributions (determined using both the thermocouple and liquid–crystal data) will be presented in the form of contour maps of Stanton number on the airfoil and hub endwall surfaces. (3) The streamwise distributions of the airfoil midspan heat transfer will be compared to the other test cases and to similar data obtained previously under NASA–HOST funding. (4) Finally, the streamwise distributions of the airfoil midspan heat transfer will be compared to data obtained for the same airfoil section in a 2–dimensional cascade.

1. Sample Liquid Crystal Data

Photographs of rotor–passage liquid–crystal temperature patterns were recorded for all nine (9) combinations of incidence and Reynolds number (see Fig. 27). These liquid–crystal data were obtained for the smooth–wall model only since color–temperature patterns were not discernable on the roughened surfaces. The liquid–crystal data acquisition procedure consisted of setting the LSRR to a particular inlet flow angle and Reynolds number combination and then adjusting the rotor–model power to produce a multi–color–band system of temperature contours. After allowing the heated model to reach thermal equilibrium, photographs of the temperature contours and scans of the model thermocouple array were simultaneously recorded.

Multiple photographs covering a range of film exposures and camera viewing angles were obtained for each test condition. In total, there were approximately 200 print–film and 100 slide–film photographs recorded for this program. Fourteen (14) print photographs have been selected for presentation in this report. These fourteen (14) photographs were selected to demonstrate all the important qualitative features of the passage heat transfer distributions revealed in these liquid–crystal tests.

Color–temperature contours recorded on the rotor pressure surface for a range of Reynolds numbers (from 2.3 to 5.8 x 10^5) but a fixed inlet flow angle of $\beta_1 = 40°$ (Cx/U=0.78) are presented

in Fig. 28. Figure 28a was obtained for the highest test Reynolds number (Re = 5.8 x 10^5) and illustrates two important features of the pressure surface heat transfer. First, near the leading edge, for the outer 60% of the span, the heat transfer pattern was nearly two-dimensional. There were three closely-spaced, monotonically increasing in temperature, isotherms roughly parallel to the leading edge line. These lines are marked by the (A) in Fig. 28a. This pattern indicates that, for $\beta_1 = 40°$, the leading edge flow was attached (no separation bubble). Second, near the endwall, Fig. 28a shows a wedge-shaped region of relatively high heat transfer ((B) marker). One isotherm of this wedge pattern extended out to about 25% span. The next-higher-temperature isotherm, though showing a less distinct wedge shape, extended to nearly midspan. This phenomenon is thought to be produced by the secondary flows emerging from the first-stage stator. The first stator generates passage vortices near the hub and tip which enter the blade row as regions of intense turbulence and secondary flow (see Fig. 23). It is reasonable to expect that an enhancement of the heat transfer near the hub and tip would be produced as the rotor cuts through these regions of intense secondary flows. The tip region was not visible through the viewing window so it was not possible to determine if a similar effect occurred at the outer part of the span.

Figure 28b shows the liquid-crystal data for the next lower Reynolds number (Re = 5.2 x 10^5). Although the general features of this photograph are similar to those of Fig. 28a, there are two additional effects shown here that merit discussion. First, there was a small region of reatively high temperature (low heat transfer) indicated by the (C) marker. This max-temperature isotherm delineates the region of minimum heat transfer for the entire pressure surface at this inlet flow angle. As expected, this minimum heat transfer occurred near the end of the region of minimum flow speed on the pressure surface. It is interesting to note, however, that because of secondary flow effects the absolute-minimum heat transfer only existed in a small patch near midspan.

The photograph of the rotor passage model presented in Fig 28b captured a relatively clear view of the hub and revealed a feature of the hub-endwall heat transfer pattern. An endwall isotherm can be seen running from the pressure-surface/hub intersection at about 25% Bx, and across the hub at about 25% gap ((D) marker). The region enclosed by this isotherm corresponded to the zone of minimum hub endwall heat transfer. This region of relatively low hub heat transfer near the hub/pressure-surface intersection was common to all the $\beta_1 = 40°$ cases.

Figure 28c also shows an important feature of the endwall heat transfer. A zone of significantly increased heat transfer can be clearly seen near the hub/leading-edge intersection ((E) marker). This region of enhanced heat transfer is a product of the leading-edge (horseshoe) vortex system. Interactions between the horseshoe vortex system, the near-hub secondary flows from the upstream stator and the airfoil surface boundary layer may also be involved in the "wedge-shaped" pattern on the pressure surface near the endwall ((B) marker).

Notice that all four photographs of Fig. 28 show a local cold spot on the endwall near the pressure-surface junction and about 1/2 inch downstream of the first spanwise running grid line ((F) marker on Fig. 28c for example). This cold spot is not associated with the flow in the passage but arose solely because of a nearby hole through the heater foil. This hole was beneath the airfoil and was required to allow the main support rod for the airfoil to attach to the hub (see Figs. 6 and

9). As described in EXPERIMENTAL EQUIPMENT, corrections for the localized non–uniformity in heater–foil current which arose from this hole were incorporated into the reduction of the endwall data.

Finally, Figure 28d also shows the small patch of minimum heat transfer near midspan similar to that indicated by the (C) marker of Fig. 28b.

Liquid–crystal temperature patterns for the airfoil pressure surface are also presented in Fig. 29. For this figure color–temperature patterns are shown for a range of both inlet flow angles and Reynolds numbers. Figure 29a shows the temperature distribution for $Re = 5.1 \times 10^5$ and $\beta_1 = 45°$. The temperature pattern near the leading edge was significantly different at this inlet flow angle than for all the cases of $\beta_1 = 40°$ shown in Fig. 28. At midspan the color pattern shows, moving downstream from the leading edge, that the temperature first increased then decreased and then increased again. This pattern indicates that there was a separation bubble near the leading edge overspeed site for this inlet flow angle. The local separation produced low heat transfer beneath the bubble followed by higher heat transfer at reattachment. The location and extent of the separation bubble probably coincide quite accurately with the fully closed isotherm indicated by the (G) marker.

Changing inlet flow angle from $\beta_1 = 40°$ to 45° also had an impact on the previously discussed "wedge–shaped" region of enhancement near the pressure–surface/endwall intersection. At $\beta_1 = 45°$ the near–endwall enhancement region merged with the midspan–region of enhancement associated with the reattachment of the separation bubble. For this incidence, then, a band of relatively high heat transfer, indicated by the (H) marker, extended across the entire span.

The remaining three photographs of Fig. 29 show color patterns recorded for $\beta_1 = 54°$ for a range of Reynolds numbers from 2.4 to 4.2×10^5. All three photographs show a narrow band of low heat transfer near the leading edge corresponding to a leading–edge–overspeed separation bubble. All three photographs also show that downstream of the separation bubble a band of relatively high heat transfer extended across the entire span.

To review, the effects of changing inlet flow angle on the leading–edge region heat transfer distribution can be seen by comparing Figs. 28b, 29a and 29d which were all recorded for roughly equal Reynolds numbers. For Fig 28a ($\beta_1 = 40°$) the flow was attached, but as the inlet flow angle was increased to $\beta_1 = 45°$ (Fig. 29a) and then to $\beta_1 = 54°$ (Fig. 29d) the leading–edge overspeed produced a local separation bubble. The strength and streamwise extent of the bubble reattachment zone increased with increasing β_1.

Notice, also, that Figs. 29a, b and c all show the enhancement of heat transfer produced by the horseshoe vortex system at the leading–edge/endwall junction. This effect is shown particularly clearly in Figs. 29b and c where two color bands (the second band is indicated by the (I) marker in Fig. 29c) were photographed in the leading edge region.

Suction–surface color–temperature patterns, obtained for a range of Reynolds numbers and inlet flow angles, are presented in Fig. 30. The effects on the temperature patterns produced by changing flow conditions (Re and β_1) were much less on the suction surface than for the pressure surface. In fact, the general characteristics of the various temperature patterns for the

suction–surface were so similar that they can be discussed most easily as a group. All four photographs of Fig. 30 show a pattern of isotherms originating near the front of the suction surface at either the hub or tip and converging near midspan at around 70% Bx (e.g. the isotherms marked (J) for Fig. 30a). The order of the color bands indicates that the heat transfer was progressively higher moving from midspan towards the hub or tip. This temperature pattern, which was common to all the smooth–wall, suction surface test conditions, was almost certainly produced by the passage hub and tip secondary flows (see Figs 21a and 25b).

The endwall boundary layers, having been swept across the endwall towards the suction surface by the cross–passage static pressure gradient, roll up into a pair of vortices located near the suction–surface–tip/endwall and the suction–surface–hub/endwall corners. This pair of passage secondary flows has the effect of producing a streamwise–converging flow pattern in the suction–surface boundary layer. Flow visualization data of Langston et al., 1977 and Joslyn and Dring, 1989 and many others showed that this converging pattern corresponded to a pair of suction–surface separation lines. These separation lines divide the streamwise flow in the midspan region from the hub and tip regions which are dominated by the secondary passage flows. The effect on the suction–surface heat transfer produced by these secondary flows is to enhance the local Stanton number. The shape of the color–temperature patterns correspond directly with the shape of the lines of "three–dimensional" separation deduced from the flow visualization results presented in Fig. 21a.

All four photographs of Fig. 30 also show a region of intense heat transfer near the tip for the downstream 70% of the chord (e.g. (K) marker, Fig. 30a). This local enhancement was produced by the tip–leakage flow which rolls into a tip–leakage vortex in that region (see Fig. 21). Also, all four photographs of Fig. 30 show a region of enhanced heat transfer on the endwall just downstream of the airfoil leading edge (e.g. (L) marker, Fig. 30b). This enhancement is probably produced by the suction–surface leg of the leading–edge horseshoe vortex.

Finally, Fig. 31 presents close–up views of the color–temperature patterns on the airfoil trailing edge. Both photographs are for the same flow condition and merely give different views of the same color pattern. Apparently the trailing–edge heat transfer rates were much higher near the tip than for the remainder of the span. The (M) marker of Fig. 31a indicates three color lines between the midspan and tip regions.

2. Data Format

The heat transfer distributions measured on the airfoil and hub endwall surfaces are presented in the form of contour maps of equal Stanton number. These contour maps were created in a three–step process. First, a commercially available topographical plotting routine (SURFER–Golden Software, Inc.) was employed to create contour maps from the thermocouple–array data. Second, these thermocouple–based contour maps were compared with the liquid–crystal temperature contours to assure compatibility with these supportive measurements. And finally, the liquid–crystal results were used to supplement the thermocouple

data in regions where extremely localized effects were beyond the resolution of the thermocouple array, e.g. the leading–edge separation bubbles fell between rows of thermocouples.

The shape of the rotor airfoil surface, unwrapped and flattened on a plane, is complex (see Figs. 18 and 19). In order to alleviate the complexities involved with generating contours in this form a coordinate system, illustrated in Fig. 32, was developed to project the complex airfoil–surface shape onto rectangles with the same span/arc–length ratio. The left–hand portion of Fig. 32 compares a number of coordinate scales on a rectangle. The horizontal axis is straightforward with the span percentage equal to the radial distance from the hub divided by the total airfoil span of 6.0 inches. The vertical scale running up the center of the rectangle shows the surface arc length (inches), measured at midspan, with S = 0 defined as in Fig. 16. The central–vertical and the horizontal scales are consistent in that 1 inch of span = 1 inch of arc–length. The right–hand vertical scale was constructed by non–dimensionalizing the surface distance by the total–arc–length for the respective (suction or pressure) surface. Although this scale has the advantage of ending at $\pm$ 100% (the trailing edge line) the inequality beween the suction and pressure scales was considered to be cumbersome. To eliminate this problem it was decided to non–dimensionalize all arc–length distances by the span, thus making grid increments equal for the horizontal and for both the pressure and suction portions of the vertical scale. The disadvantage of this, of course, is that the trailing–edge lines coincide with values $\neq$ 100%. For the suction surface the trailing–edge line falls at 185% while for the pressure surface it falls at 132%.

The airfoil surface, though having a constant span, was not rectangular when unwrapped because the total surface–arc–length (on both surfaces) was a function of span. Rectangular projections were acheived by plotting off–midspan data at surface distances proportionally scaled by the ratio of midspan/local arc length. The mathematical definition of S* is given at the top of Fig. 32.

The right–hand portion of Fig. 32 shows a sample set of airfoil surface heat transfer contours plotted in these % span vs. % S* coordinates.

3. Heat Transfer Contours for the Smooth–Wall Model

Contour maps of the rotor passage heat transfer distributions (smooth–wall model) are presented in Figs. 33 through 41 for the various combinations of Reynolds number and inlet flow angle. Each data set is presented in three forms: a. – an overall view of both the endwall and airfoil heat transfer distributions, b. – expanded, separate views of the airfoil suction and pressure surface distributions and, c. – an expanded view of the hub endwall distribution .

For all of the contour map figures the inlet flow angle (β_1), rotor RPM (N) and the test Reynolds number (Re) are given at the top. Contour keys indicate that the solid contours were constructed from the thermocouple data, the dash–dot contours were inferred from the liquid–crystal data and the dashed contours show finer increments of Stanton number (0.0001) for the pressure surface. The physical scales of the airfoil surface and hub endwall plots are identical for figures in which both

appear (a-type figures) That is, spanwise, surface-arc-length, and the chordwise and gapwise dimensions are all consistent. The scales of the b & c type figures were chosen to fill the page and are not consistent.

Following the case designation format of Figure 27, the various data sets are presented in the following order: (1) Sets A through E, all of which were obtained at $\beta_1 = 40°$, are presented in order of increasing Reynolds number in Figures 33 through 37. (2) Set F, the singular set obtained at $\beta_1 = 45°$, is presented in Figure 38. and (3) Sets G, H, and I, all of which were obtained at $\beta_1 = 54°$, are presented in order of increasing Reynolds number in Figures 39 through 41.

Tabulations of the data used to generate the heat transfer contour maps are given in the APPENDIX of this report. These data are also available from the author in ASCII format on 5 1/4 inch floppy disks.

General Discussion of a Sample Data Set. The first data set presented (Figs. 33a, b, and c) was obtained at $\beta_1 = 40°$ and $Re = 2.37 \times 10^5$. The airfoil surface views (33a and 33b), consistent with the previously discussed liquid-crystal results, indicate that three-dimensional flow effects had a much stronger influence on the suction surface than on the pressure surface. The influences of the passage vortices on the suction-surface heat transfer are apparent for $S^* > 50\%$ at both the hub and tip. Note that the shape of the lines of constant suction-surface Stanton number shown on Figs. 33a and b agree with the shape of the lines of constant temperature for the suction-surface liquid-crystal photographs of Fig. 30. The absolute level of the Stanton number contours within the zones dominated by secondary flow was higher than observed at any streamwise station at midspan (downstream of the immediate vicinity of the leading edge). The highest heat transfer rates on the suction surface were recorded near the tip for $70\% < S^* < 130\%$. The peak Stanton numbers were observed very near the tip for $100 < S^* < 120$ where the heat transfer was more than 100% greater than the midspan value. This local enhancement, as discussed in the previous section, was produced by the tip-leakage vortex.

Another region of locally enhanced heat transfer on the suction surface can be observed in the region $0\% < S^* < 20\%$ near the hub (from 0 to 40% span). A remarkably similar heat transfer pattern was observed by Graziani et al. (1980) where the full-span heat transfer data were acquired for the midspan rotor airfoil geometry mounted in a two-dimensional cascade. No similar region of enhancement was evident near the tip at this streamwise location for the present rotating model tests. The fact that similar patterns were observed for the cascade tests and near the hub (but not the tip) of the rotating tests indicates that the phenomenon is related to leading edge/endwall interaction effects (the horseshoe vortex system). The aerodynamic effects produced at the hub/leading-edge junction were similar to those produced at the endwall/leading-edge junction in the stationary cascade since, in both cases, there was no relative motion between the airfoil and the endwall. At the tip, however, the tip leakage and the tip/casing relative motion must certainly produce an entirely different secondary flow pattern. Unfortunately, at this time interpretation of the near-tip heat transfer patterns is limited by a lack of existing data for secondary flows generated near moving-tip/casing junctures. The results of the present program, however, do indicate that

enhancement of the airfoil heat transfer by leading–edge/endwall interaction effects is limited to the hub region.

The pressure–surface results can be discussed most easily using Fig. 33b which shows contours of Stanton number with finer increments than 33a. This figure shows the "wedge–shaped" enhancement region near the hub at S* = 20% and the minimum–heat–transfer patch at about 60% span and 30% S*. Both of these features, as previously discussed, can be seen in the liquid–crystal photographs of Fig. 28. Note, also, that in the trailing–edge region the heat transfer rates were slightly higher near the tip than at the hub. This was probably a result of the tip–leakage flow. Because of the flow across the tip from the pressure surface the near–tip pressure–surface boundary layer is thinned relative the rest of the span. Somewhat higher heat transfer rates result for this near–tip region of reduced Re_θ boundary layers.

The hub endwall heat transfer distribution is presented in expanded scale in fig. 33c. This figure clearly shows the regions of intense heat transfer near the rotor–leading–edge/endwall junction. This effect, a product of the leading–edge horseshoe vortex system was also visible in the photographs of Figs. 28 and 29. The heat transfer beneath the leading–edge vortices was the maximum observed anywhere on the endwall. Notice that the region of enhanced heat transfer near the leading edge is not symmetrical about the stagnation streamline but extends considerably further towards the suction surface. This result is almost certainly related to the previously discussed near–hub region of enhancement on the airfoil suction surface for 0% < S* <20%. The lowest heat transfer on the endwall occurred near the pressure–surface corner. Again, this effect was demonstrated in a liquid–crystal photograph in Fig. 28b.

Effects of Increasing Re for Fixed $\beta 1 = 40°$. The following observations are based on an examination of Figures 33 through 37 which correspond to Data Sets A–E of the test matrix (Figure 27). These observations will be discussed in the following order: (1) airfoil suction surface effects, (2) airfoil pressure surface effects, and (3) endwall effects.

(1) – Suction Surface: Effects on the suction surface heat transfer distributions produced by increasing the Reynolds number can best be seen through examination of the suction–surface detail maps of Figures 33b–37b. These contour maps show that there is an orderly and progressive system of changes in the distributions produced by the increase in Re. First, an examination of the near–midspan region at 140% < S* < 170% reveals a continuous drop in the Stanton number with increasing Re. The boundary layer in this portion of the suction surface is fully turbulent and the heat transfer is simply reflecting the well–known decrease in wall transport associated with the thickening of equilibrium shear layers. It will be demonstrated in a later section that the aft–chord/midspan heat transfer can be accurately described by $St \propto Re^{-0.2}$, the well–known equilibrium turbulent boundary layer relationship.

At S* = 60%, again near midspan, the suction surface contour maps reveal effects associated with transition of the suction surface boundary layer. If Figures 33b–37b are examined in order of increasing Re, it can be seen that the Stanton number first decreases, reaches a minimum, and then increases again. The decrease in St for the three lowest Re is associated with a thickening laminar boundary layer. Somewhere in the range $4.4 \lesssim Re \lesssim 5 \times 10^5$, however, the boundary layer began

to pass through transition upstream of S* ≅ 60%. For the two highest Re, therefore, we observe the direct increase in St with Re associated with transitional flows.

Consistent trends with increasing Re can also be observed in the regions of enchanced heat transfer near the suction surface tip and root (70% < S* < 130%). These enhanced zones show a continuous and progressive decrease in St with increasing Re for the full range of test Re. This results confirms the conclusion reached earlier from the liquid–crystal data, that the flow in these regions was fully turbulent.

(2) – Pressure Surface: As with the suction surface, effects on the pressure surface heat transfer distributions can best be seen through examination of the pressure–surface maps of Figures 33b–37b. Interpretation of the pressure surface results is considerably simpler than for the suction surface because the flow over the entire pressure surface is turbulent. At midspan the Stanton number decreased everywhere with increasing Re. For example, at S* = –80% St decreased progressively from 0.0021 to 0.0015 over the range of test Re. The same trend can be seen at S* = –120% where St decreased from 0.0024 to 0.0019. A third example can be observed at an off–midspan location, 20% span and S* = –20%. Here St dropped from 0.0025 to 0.0018 over the test Re range. All of these examples reflect the presence, for this inlet flow angle, of turbulent boundary layer flow over the entire pressure surface.

(3) – Endwall Surface: Effects directly attributable to changes of Re were smaller on the endwall than on the airfoil surfaces. Slight decreases in St with increasing Re can be observed across the entire gap in the trailing–edge region and in the midchord region near the pressure surface.

Effects of Increasing Re for Fixed $\beta_1 = 54°$. The following observations are based on an examination of Figures 39 through 41 which correspond to Data Sets G–I of the test matrix (Figure 27).

Heat transfer distribution data were obtained for only three Re settings for $\beta_1 = 54°$ compared to the five values of Re examined for $\beta_1 = 40°$. Nevertheless, the same trends observed at $\beta_1 = 40°$ on the suction, pressure and endwall surfaces can be seen for the $\beta_1 = 54°$ cases. The transitional behavior on the fore–chord (0% < S* < 100%) suction surface is clearly evident while for all locations where the flow was fully turbulent St decreased progressively with increasing Re.

Effects of Increasing β_1 for Fixed Re. Comparisons within this section will be made between data sets obtained at the same rotor exit Reynolds number but different inlet relative flow angle (β_1). Changes to β_1 were achieved experimentally by operating the facility at a fixed throughflow velocity and altering the rotor rotation speed. An increased β_1 for a fixed exit Re corresponds to a decreased relative inlet velocity (reduced velocity in the forechord with stronger acceleration to reach the same exit velocity). The effect of increasing β_1 above its design value of 40° (negative incidence) is to shift the stagnation line away from the pressure surface and towards the suction surface. This shift strengthens the overspeed at the leading–edge/pressure surface juncture and produces a relatively stronger favorable pressure gradient at the leading–edge/suction surface juncture.

Comparisons in this section will be made between the following pairs of data sets:

Figure Nos.	Re	β_1
36 vs. 38	5.1×10^5	40° vs. 45°
35 vs. 41	4.3×10^5	40° vs. 54°
34 vs. 40	3.2×10^5	40° vs. 54°
33 vs. 39	2.4×10^5	40° vs. 54°

(1) – Suction Surface: Comparisons beween the suction surface heat transfer distributions indicates that for all four of the above pairs of data sets, increases in β_1 produced decreased heat transfer in the fore–chord region ($0\% < S^* < 100\%$). Note that for all the suction surface plots at increased β_1, the laminar–flow region in which $St < 0.002$ (centered around 60% span) expanded considerably compared to the respective design inlet flow angle data. In addition, the turbulent–flow regions of the fore–chord (near the blade root) also show reduced heat transfer for increased β_1. This general reduction in fore–chord heat transfer is primarily the result of the reduction in relative inlet velocity associated with increased β_1. Since the suction surface boundary layer is still laminar in the midspan/fore–chord region, the increase in β_1 also reduces the heat transfer through a pressure gradient effect. The increased favorable pressure gradients in the forechord tend to inhibit boundary layer transition and permit the region of laminar flow to extend further onto the suction surface. It is worth commenting that the presence of laminar flow anywhere on the rotor is quite surprising, given the high level of turbulence in the wakes from the upstream stators.

(2) – Pressure Surface: For all four data sets obtained at negative incidence (Sets F–I, Fig. 27), a narrow band of reduced heat transfer was observed at $S^* = -5\%$. Downstream of this narrow band of low heat transfer, the Stanton number increased rapidly and then gradually decreased for $S^* > -20\%$. In order to illustrate this effect in another format, plots of the streamwise distributions of the Stanton number at midspan are given in Figs. 38b through 41b. These plots show the rapid fall, the subsequent rise and then the gradual fall of Stanton number with increasing S^*. This heat transfer pattern indicates that, for the negative incidence cases, a short separation bubble resulted at the pressure surface leading–edge overspeed. The low heat transfer resulted directly beneath the bubble while the rapid rise to a much higher level was associated with reattachment. The gradual decline of the Stanton number downstream of reattachment coincided with the streamwise growth of the pressure–surface boundary layer. A comparison of the four sets of negative incidence data reveals that the separation bubble was much weaker for the $\beta_1 = 45°$ case than for the three cases at $\beta_1 = 54°$.

(3) – Endwall Surface: The most important effects of the change in incidence on the hub endwall heat transfer distribution were found in the forechord region. Comparisons between the various sets of fixed exit Re data reveal that increased β_1 produced reductions in heat transfer both at midgap and beneath the horseshoe vortex patterns. As discussed with respect to the rotor airfoil forechord, these decreases in heat transfer almost certainly resulted from the decrease in relative inlet velocity.

Effects of negative incidence operation were very small for the mid and aft chord regions of the endwall. Slight decreases in heat transfer, relative to design incidence, were observed in the

midchord region near the suction surface corner. Slight increases in heat transfer, again relative to design incidence, were recorded across the entire gap in the trailing edge region and in the midchord region near the pressure surface corner. All of these small adjustments to the endwall heat transfer probably resulted from the redistribution of the rotor–passage acceleration produced by the incidence change.

4. Heat Transfer Contours for the Rough–Wall Model

Contour maps of the rotor passage heat transfer distributions for the rough–wall model are presented in Figs. 42 through 50 for the same combinations of Reynolds numbers and inlet flow angles as given for the smooth–wall cases. Again, each data set is presented in three forms: a. – an overall view of both the endwall and airfoil heat transfer distributions, b. – expanded, separate views of the airfoil suction and pressure surface distributions and, c. – an expanded view of the hub endwall distribution. As previously discussed, no liquid–crystal data are incorporated into these rough–wall data sets.

General Discussion of Roughness Effects. Comparison of any of the rough–wall and smooth–wall data sets obtained at the same operating conditions reveals that the surface roughness significantly increased the heat transfer rates at all locations. The largest relative changes (> 100%) occurred in the fore–chord, suction surface region for all cases. For the smooth–wall tests the boundary layer in this region was laminar/transitional while for the rough–wall cases it was apparently fully turbulent. The heat transfer data indicates that the surface roughness tripped the suction–surface boundary layer very near the stagnation line. This produced a low Re_θ turbulent boundary layer with very high levels of heat transfer.

It is interesting to note that the local regions of augmented heat transfer, e.g. the leading–edge/endwall junction and the mid–chord, near–tip region of the suction surface, were still present on the rough–wall model. This result indicates that surface roughness had important augmentation effects even in regions with extremely thin, skewed, non–equilibrium boundary layers.

Effects of Increased Reynolds Number for All β_1 Settings. The following observations are based on comparisons of Figs. 42 through 46 (β_1 fixed at 40°) and comparisons of Figs. 47 through 50 (β_1 fixed at 54°). Examination of these data sets reveals that for both the airfoil and endwall surfaces local heat transfer rates were highly insensitive to changes in the Reynolds number. This result is not unexpected, considering the extremely coarse grit used to roughen the passage surfaces. It is well established that for extremely rough surfaces both the skin friction coefficient and the heat transfer coefficient become independent of Reynolds number.

Effects of Negative Incidence Operation. Comparisons in this section will be made between the following pairs of data sets:

Figure Nos.	Re	β_1
45 vs. 47	4.9×10^5	40° vs. 45°
44 vs. 50	4.1×10^5	40° vs. 54°

43 vs. 49	3.0×10^5	40° vs. 54°
42 vs. 48	2.2×10^5	40° vs. 54°

For the rough–wall test conditions, the effects of negative incidence operation were almost exclusively confined to the forechord region of the rotor passage. Decreases in heat transfer, relative to design incidence operation, were observed in the forechord region of both the rotor airfoil and endwall surfaces. As discussed previously in Section 3, this effect results from the decrease in relative inlet velocity associated with increased relative inlet flow angles.

5. Midspan Heat Transfer Distributions

Midspan Heat Transfer Data for the Smooth–Wall Model. In the previous two sections rotor–passage heat transfer contour maps were presented for various inlet flow angles and Reynolds numbers. These maps displayed the streamwise and spanwise variations in the heat transfer on the airfoil surfaces as well as revealing highly localized heat transfer effects on the endwall.

Another useful format for the presentation of the rotor heat transfer data consists of plots of the streamwise variation of the Stanton number at the airfoil midspan. In this form the data obtained in the present study can be compared to midspan heat transfer data obtained previously for this same turbine airfoil under NASA–HOST Contract NAS3–23717 (Dring et al., 1986). In addition, since three–dimensional flow effects are less near the midspan than they are nearer the hub or tip, the midspan is the most relevant position at which comparisons can be made between the data and two–dimensional heat transfer predictions.

Midspan heat transfer distributions measured at Cx/U = 0.78 (β_1 = 40°) at seven Reynolds numbers (Re = 5.80, 5.15, 4.40, 3.20 & 2.30×10^5) are presented in Figures 51 a&b. Data from the present study are given for the smooth–wall cases, compared with NASA–HOST data for the same flow conditions. Also included are predictions from a two–dimensional, fully turbulent boundary layer computation procedure (Edwards et al., 1981, 1982). Each of the data sets of Figs. 51a&b are shown compared to two–dimensional boundary layer predictions for that specific test condition. Predictions for laminar boundary layer flow on the suction surface are labled L. Predictions for both suction and pressure surfaces for fully turbulent flow (labled T) employed the algebraic turbulence model of Cebeci and Smith (1974).

An examination of the data and predictions on the suction surface reveals a continuous trend with increasing Reynolds number. At $Re=2.30 \times 10^5$ the Stanton number distribution indicates that the heat transfer was laminar from the leading edge to approximately S/Bx= 0.5. Downstream of this location, the boundary layer passed through transition as indicated by the streamwise increase in the measured heat transfer. Boundary layer transition appears to near completion around S/Bx = 1.2 where the measured heat transfer and fully–turbulent predictions agree. This same sequence can be observed for all five test conditions with the onset of transition moving upstream progressively with increasing Reynolds number. As the Reynolds number was increased the region of laminar flow in the fore–chord decreased. Simultaneously, in the aftchord region, the length of the fully turbulent zone is seen to progressively increase.

An examination of the data measured on the suction surface indicates that, for the three highest Reynolds numbers, there was extremely close agreement between the results from the present study and those from the NASA–HOST Contract. At the two lowest Reynolds numbers there is some evidence that transition of the suction surface boundary layer began somewhat earlier for the NASA–HOST data. For these two Reynolds numbers, at about S/Bx = 0.5, the heat transfer for the NASA–HOST model increased towards the fully–turbulent prediction at a steeper slope than did the smoother–surface data. This difference in transition location was probably caused by the difference in surface roughness between the two rotor models. Recall that the model for the present tests was coated with liquid–crystal paint (300μ in. peak–to–peak roughness) while the NASA–HOST model was coated with flat–black paint (2000μ in. peak–to–peak roughness).

An examination of the pressure surface results indicates that, for the three lowest Reynolds numbers, there was quite good agreement between the two–dimensional predictions and both sets of experimental data. For the downstream half of the pressure surface at the two highest Reynolds numbers the heat transfer rates for the present study were as much as 25% less than those recorded under the NASA–HOST program. This difference is examined in detail in the following section where, like the previously discussed suction–surface transition shift, it is demonstrated to be a result of the difference in surface roughness of the test models.

There are two general conclusions that can be reached from the results shown in Figs. 51 a&b. First, that the data obtained at all five Reynolds numbers for the present study form an orderly, systematically behaved set. Second, that the midspan, nominally smooth wall data obtained under the present contract are in excellent agreement with similar results measured for the earlier NASA–HOST contract.

The midspan heat transfer (present program) distributions for at all five test conditions of Fig. 51 are replotted in two more formats in Fig. 52. The upper figure shows the Stanton number distributions for all five cases plotted on a common set of axes. The lower figure again shows all five cases plotted in coordinates of surface distance vs. the product St x $Re^{0.2}$. In the upper format it is easy to discern the range of Stanton numbers associated with the range of test Reynolds numbers. The lower format demonstrates that the aft chord data on both the suction and pressure surfaces can be collapsed to a narrow band when scaled by $Re^{0.2}$. This collapse indicates that the aft chord flows on both airfoil surfaces are behaving as classic equilibrium, fully turbulent, smooth–wall boundary layers.

Midspan Heat Transfer Data for the Rough–Wall Model. Midspan heat transfer distributions for all three test–model surface roughness conditions (present test smooth and rough and NASA–HOST near smooth) are presented in Fig. 53 for $\beta_1 = 40°$ and two test Reynolds numbers. Also included in Fig. 52 are fully turbulent predictions from the previously described two–dimensional boundary layer computation procedure (Edwards et al., 1981, 1982).

Differences between the results for the present smooth–wall data and the near–smooth–wall data of NASA–HOST were discussed in the previous section. The significant feature of Fig. 52 is the profound impact that the rough–wall condition had on the heat transfer rates relative to the smooth– and near–smooth wall conditions. The effect of the surface roughness was to increase the

heat transfer everywhere on the airfoil surface with the largest increase (approximately 100%) in the fore–chord region of the suction surface. Note that the furthest–downstream point on the (rough–wall) pressure surface registered a local decrease in Stanton number for both Reynolds numbers. This effect may be the result of one of the roughness grains sitting directly on a thermocouple site and is probably not a "real" phenomenon.

Rough–surface heat transfer data for all five test Reynolds numbers and design inlet flow angle ($\beta_1 = 40°$) are given in two formats in Fig. 54. These same formats were previously used to examine the smooth–wall results in Fig. 52. Figure 54 reveals that for the rough–wall data the midspan Stanton number distributions were nearly identical for all Reynolds numbers. Unlike the smooth–wall data, $Re^{0.2}$ scaling failed to provide a collapse of the various data sets. This result indicates that these rough–wall data are representative of "fully–rough" conditions, i.e. surface roughness so extreme that the Stanton number (and skin friction coefficient) become independent of velocity.

Comparison of Midspan Rough–Wall Data with Predictions. The following section presents comparisons of the midspan rough–wall data with various analytical rough–wall heat transfer predictive techniques.

Much of the literature related to rough–surface boundary layer flows employs the roughness Reynolds number $k+ = kU_\tau/\nu$ to characterize the degree of roughness of a surface. Here U_τ is the friction velocity and k is the height of the roughness elements. There is widespread agreement that turbulent boundary layer flow over rough surfaces can be grouped into three categories:

(1) hydraulically smooth $\quad 0 < k^+ < 5$

(2) transitionally rough $\quad 5 < k^+ < 55–70$

(3) fully rough $\quad k^+ > 70$

In 1985 Han produced a carefully constructed model for analysis and calculation of rough surface turbulent boundary layers. Han's analysis is based upon a modification of the mixing–length turbulence model in which the mixing length is multiplied by an appropriate amplification factor. He conclusively demonstrated that his mathematical formulation satisfactorily reproduced experimentally documented rough–surface turbulent boundary layer velocity profiles. Specifically, he demonstrated that he could mathematically reproduce the ΔU^+ shift (in U+ vs. Y^+ coordinates) relative to smooth–wall profiles experimentally observed for turbulent boundary layers over roughened surfaces. Han also produced an empirical model to link the type and degree of roughness with the amplification factor required for the mixing–length model. Han presented results from his predictive model in the form of charts of skin friction coefficient plotted as a function of Re_x and a roughness parameter $Re_k = Uk/\nu$. For the present study, Han's zero–pressure–gradient results were employed to estimate the skin friction distribution along the rotor midspan by using the local velocity to compute the local Reynolds numbers. The roughness parameter was computed from the local velocity and the grit size (0.026 in.) while Re_x was based upon the surface distance along the airfoil measured from the stagnation line.

The skin friction coefficient distributions computed by the technique of Han were used to determine the k^+ distributions along the rotor midspan for the rough-wall condition. These calculations indicated that for $Re_{Bx} = 5.8x10^5$ the entire suction surface and the downstream half of the pressure surface were in the fully rough regime. The upstream half of the pressure surface fell into the transitionally rough regime.

The results of a large number of studies of rough-wall heat transfer have been published in the open literature. These studies have mostly been limited to zero-pressure-gradient flows but have included examinations of a wide variety of types and degree of surface roughness. All of these studies have produced proposed correlative equations to predict the heat transfer given the local Reynolds number, Prandtl number, some roughness parameter and the skin friction coefficient. Comparisons will be presented here between four of these correlation-based predictions and the present rough-wall midspan data. The previously described skin friction distribution computed by the method of Han was used as a common input to all the rough-surface heat transfer correlations to be described below.

The following heat transfer correlations for prediction of roughwall heat transfer were examined:

(1) Dippery and Sabersky (1963)-based on flow through rough tubes

$$St = \frac{C_f/2}{1 + [g(k^+) - 8.48]C_f/2}$$

where $g(k^+)$ is a function of the molecular Prandtl number and the Roughness Reynolds number.

(2) Kadar and Yaglom (1972)-based on flat-plate data

$$St = \frac{\sqrt{C_f}\,Pr^{-1}}{4.3 \ln (Re_x C_f) + 3.8}$$

(3) Seidman (1978)- based on supersonic exterior flows

$$St = C_f/2\,[1 + 0.52\,(C_f/2)^{0.725}\,(Re_k)^{0.45}\,Pr^{0.8}]^{-1} + 0.0002$$

(4) Han and Delpassand (1990) – an analytical model

St is determined from plotted computational results $St = St(Re_x, Re_k)$

The above four analyses were used to compute the heat transfer distributions for the rotor airfoil midspan. The results of these computations are compared with the experimental data in Figure 55 for both the smooth wall (k = 0) and rough wall (k = 0.026 in.) conditions for $Re = 5.8x10^5$. An examination of Fig. 55 reveals that for the smooth-wall condition all four predicted distributions are in fairly good agreement with the measurements for both the suction and pressure surfaces. For the rough-wall condition, however, all of the methods over-predict the suction surface rates and

seriously under–predict the pressure surface rates. The model of Seidman is seen to most nearly predict the suction surface data while the model of Han and Delpassand was slightly more successful than the others along the pressure surface.

The STAN–5 Deck (Crawford and Kays, 1976) is a widely available, two–dimensional boundary layer prediction procedure. The Pratt and Whitney Division of UTC has recently incorporated a new roughness model into their version of STAN–5 and has made this code available for use in this present contract. This new roughness model has also been implemented into the Rai ROTOR Code (Rai, 1987, 1988) as part of NASA Marshall Contract NAS8–36950, "3–D Turbopump Flowfield Analysis" by Dr. Om Sharma of Pratt and Whitney.

The roughness model incorporated into STAN–5 by Pratt & Whitney was originally proposed by van Driest (1956). According to this model surface roughness erodes the effect of viscous damping near the wall causing an increase in mixing length in the inner part of the boundary layer. The modified damping function due to surface roughness is given as:

$$D = D_s + D_r$$

D = damping term for modifying mixing lengths

D_s = damping term for smooth surfaces

D_r = damping term for rough surfaces

$$D_r = -60y^+/k^+A^+$$

$$y^+ = yU_\tau/\nu$$

$$k^+ = kU_\tau/\nu$$

A^+ = constant

k = roughness height

Midspan rotor airfoil Stanton number distributions predicted with the Pratt and Whitney version of STAN–5 are given in Fig. 55. Predictions are presented for both a smooth wall and for a wall roughness equal to the size of the grit on the rough–wall model. The STAN–5 predictions are seen to be significantly superior to any of the correlation based predictions, both for the smooth–wall and rough–wall cases. It is significant that The STAN–5 calculations predict both the absolute levels and the streamwise distributions of the measured heat transfer. The superiority of the STAN–5 code in this regard results from the fact that, as a finite–difference boundary layer flow solution, it reflects the impact of the flow history (velocity distribution) along the airfoil surface. The correlation–based equations, on the other hand, were based upon zero–pressure–gradient data and only represent a prediction of a local Stanton number at some point on a constant–velocity surface.

It should be pointed out that the STAN–5 predictions for the smooth–wall case are in very good agreement with the predictions from the Edwards et al. 2–D code for this same Reynolds number (see Fig. 51a).

Results from a more detailed examination of predictions from the Pratt and Whitney version of STAN–5 are presented in Fig. 56. All of the predictions and data presented in Fig. 56 are for the flow condition of Cx/U = 0.78 (β_1 = 40°) and Re = 5.8x10^5. Measured heat transfer results are given for the smooth–wall and rough–wall cases of the present program and for the near–smooth–wall case of the NASA–Host program. Predictions from the STAN–5 code are given for surface roughness values ranging from 0 to 30,000μ in. As discussed in Fig. 55 above, the smooth–wall predictions are seen to agree very well with the present smooth–wall data (the measured peak–to–peak roughnes of 300μ in. corresponds to a range of k^+ from 0.6 to 2 over the airfoil). Agreement is excellent for the entire pressure surface and for the post–transitional portion of the suction surface. The predictions for k = 2,500μ in. and data for the NASA–HOST case (measured peak–to–peak roughness = 2000μ in. 4 < k^+ < 15) are also in excellent agreement. Finally, predictions for k = 30,000μ in. and the present roughwall data (grit size = 26,000μ in. 50 < k^+ < 200) are excellent for the entire suction surface and reasonably good for the pressure surface. The conclusion reached from the results of Fig. 56 is that the van Driest roughness model produced quite accurate rough–surface heat transfer distribution predictions for a very wide range of surface roughness heights. It is important to note that successful predictions for the various surface conditions were produced using the peak–to–peak roughness values as input (k) to the van Driest model. This result suggests that the extremes of the roughness distribution may be much more important than the mean roughness height in determining the enhancement of heat transfer.

Effects of Incidence on the Midspan Heat Transfer Distributions of the Rough–Wall Model. Midspan heat transfer distributions for Re = 2.3 and 4.2 x 10^5 at β_1 = 54° are given in Figure 57. Although there were data obtained at this β_1 under the NASA–HOST program none were obtained at these Reynolds numbers. For this reason Fig. 57 shows only a comparison of the respective rough and smooth wall cases from the present program. As with the data of Figure 53, these results indicate that the surface roughness produced a very significant increase in the heat transfer. Again, increases were particularly large in the fore–chord of the suction surface.

Figure 58 shows comparisons of the smooth (upper figure) and rough (lower figure) wall data obtained at the same Reynolds number Re = 4.2 x 10^5 but different inlet flow angles. The effects were well behaved for the smooth–wall cases. Lowering the flow coefficient (increasing the inlet flow angle) increased and decreased heat transfer in the fore–chord regions of the pressure and suction surfaces respectively. Note that for the smooth–wall cases the trailing–edge–region heat transfer for the two flow coefficients were equal for both the suction and pressure surfaces. This is the expected result because the passage exit velocity (Reynolds number) was nearly identical for these two cases.

Results for the rough wall cases were less clear. Inlet flow angle had little effect on either the pressure or suction surface heat transfer. This was probably because the surface roughness tripped the boundary layer eliminating any leading–edge overspeed/separation–bubble effects.

6. Comparison of Present Results with Cascade Data

Midspan heat transfer distribution data were obtained in an earlier investigation in a cascade with the same rotor airfoil geometry used in this present program. The earlier data were measured in a large–scale, plane cascade and were published by Graziani et al. (1980). In brief, the cascade test airfoils had an axial chord of 11.08 inches and an aspect ratio and solidity near unity. The cascade inlet flow angle was 44.6° so the airfoil incidence was nearly identical to the case in the present program with $\beta_1 = 45°$. The cascade heat transfer data were obtained for an exit Reynolds number of 8.8×10^5 and for two values of endwall boundary layer thickness. The heat transfer data of the cascade study were measured using an electrically–heated–wall/thermocouple system similar in principal to that used for the present study. Only a very limited number of data points were obtained in the leading edge region of the cascade.

A comparison of the heat transfer distribution measured in the cascade (thin endwall boundary layers) with the data of the present study is presented in Figure 59. Note that the two data sets were obtained at somewhat different Reynolds numbers. Predictions from a 2–D boundary layer computation procedure (Edwards et al., 1981, 1982) are also given for the two test Reynolds numbers. An examination of Figure 59 indicates that, on the suction surface, transition was slightly earlier for the rotating case than for the cascade. This result is not surprising as the disturbance level for the rotating blade was considerably higher than the 1 percent turbulence level at the entrance of the cascade. For the post–transitional region of flow on the suction surface ($S/B_x > 1$), the measured data are seen to be in excellent agreement with the respective fully–turbulent predictions.

There was, however, a significant difference between the heat transfer distributions measured on the pressure surface with the cascade data falling below the set from the rotating blade. This difference was probably also caused by the higher disturbance level in the rotating blade row. Previous studies (e.g. Blair, 1983) have conclusively demonstrated that freestream turbulence can enhance turbulent heat transfer rates. In addition, turbine airfoil heat transfer studies (e.g. Blair et al., 1989) have indicated that freestream turbulence may have considerably larger effects along pressure (concave) surfaces than along flat or convex surfaces. The difference shown in Figure 59 along the pressure surface was probably a result of this phenomenon.

In summary, the cascade results are seen to be consistent with the present data when the differences in Reynolds numbers and inlet disturbance level (turbulence) are accounted for. The major difference between the rotating and non–rotating airfoil midspan heat transfer distributions was the considerably higher levels on the pressure surface of the rotating airfoil. There is no evidence in the present results that this difference is directly attributable to the effects of rotation (e.g. Coriolis or centrifugal effects).

COMPUTATIONAL PROGRAM

1. Analysis

Generalized Potential Flow Coordinates

The basic equations of motion are derived in a potential flow coordinate system Y_1, Y_2, Y_3 using the general vector relations derived by Owczarek (1964). This potential flow coordinate system can be constructed from any potential flow solution using the potential surfaces as one coordinate (streamwise coordinate Y_1) and two mutually independent sets of stream surfaces (Y_2, Y_3) satisfying the Pfaffian differential equations described by Karamcheti (1980). This coordinate system has the particular advantages that it is body conforming and that the Y_1 surfaces are orthogonal to the Y_2 and Y_3 surfaces reducing the number of metrics that must be stored. The general procedure for constructing a coordinate system is described by Anderson (1989).

Construction of Duct Passage and Coordinates

The first step is to construct a duct passage simulating the gas turbine passage. With the blades and inlet conditions given, the UTRC CASPOF code was used to obtain the potential flow solution of the mid plane blade section yielding the upstream and downstream stagnation streamlines. In using the CASPOF code the downstream flow angle was adjusted until the pressure distribution matched the experimental pressure distribution. Then using the stagnation streamlines and the blade shape, a duct was constructed using these as boundaries. A two dimensional grid was then obtained using the UTRC CODUCT code which is an analysis based on the Schwarz–Christoffel transformation (Anderson et al., 1982). This grid is a potential flow solution for the flow through the simulated turbine passage in which the streamlines and potential lines form the coordinate grid. The UTRC Path code (Anderson, 1989) then constructs a three dimensional grid by extension in the radial direction calculating all the metrics as well as the transformation tensor from Cartesian coordinates to the calculation coordinates.

Equations of Motion

The basic equations of motion are derived in the potential flow coordinate system using the general vector equations derived by Owczarek (1964). Since it is intended to use the secondary vorticity Ω_1 as a dependent variable, the two transverse momentum equations are replaced by the corresponding Y_2 and Y_3 components of Poisson's dynamical equations (see Owczarek, 1964) and the Y_1 component of the vorticity transport equation. These equations are first derived in a general coordinate system using the metric coefficients of Warsi (1981). Then using the properties of the potential flow coordinate system, it is assumed that the cross flow velocities U_2 and U_3 are small compared the the streamwise velocity U_1 and the secondary vorticity Ω_1 is small compared to the primary vorticities Ω_2 and Ω_3.

$$\frac{\Omega_1}{\Omega_2} = \frac{\Omega_1}{\Omega_3} = O(\epsilon) \tag{1.1}$$

The equations of motion are then parabolized by neglecting terms of O (ε^2). It is noted that in in equations listed below, the distinction between covariant and contravariant vectors is dropped except for the metric coefficients.

Continuity Equation

$$\frac{\partial}{\partial Y_1}\left[\frac{\sqrt{g}}{h_1}\rho U_1\right] + \frac{\partial}{\partial Y_2}\left[\frac{\sqrt{g}}{h_2}\rho U_2\right] + \frac{\partial}{\partial Y_3}\left[\frac{\sqrt{g}}{h_3}\rho U_3\right] = 0.0 \tag{1.2}$$

Streamwise Momentum Equation

$$\frac{\partial}{\partial Y_1}\left[\frac{\sqrt{g}}{h_1}\rho U_1 U_1\right] + \frac{\partial}{\partial Y_2}\left[\frac{\sqrt{g}}{h_2}\rho U_2 U_1\right] + \frac{\partial}{\partial Y_3}\left[\frac{\sqrt{g}}{h_3}\rho U_3 U_1\right] + \frac{\sqrt{g}}{h_1}\frac{\partial P}{\partial Y_1}$$

$$-\sqrt{g}g^{22}\frac{\partial}{\partial Y_2}\left[\mu_t\frac{\partial U_1}{\partial Y_2}\right] - \sqrt{g}g^{23}\frac{\partial}{\partial Y_2}\left[\mu_t\frac{\partial U_1}{\partial Y_3}\right]$$

$$-\sqrt{g}g^{32}\frac{\partial}{\partial Y_3}\left[\mu_t\frac{\partial U_1}{\partial Y_2}\right] - \sqrt{g}g^{33}\frac{\partial}{\partial Y_3}\left[\mu_t\frac{\partial U_1}{\partial Y_3}\right] = 0.0 \tag{1.3}$$

Transverse Pressure Equation

$$\frac{\partial}{\partial Y_2}\left[\sqrt{g}\left(g^{22}\frac{\partial P}{\partial Y_2} + g^{23}\frac{\partial P}{\partial Y_3}\right)\right] + \frac{\partial}{\partial Y_3}\left[\sqrt{g}\left(g^{23}\frac{\partial P}{\partial Y_2} + g^{33}\frac{\partial P}{\partial Y_3}\right)\right]$$

$$+\frac{\partial}{\partial Y_2}\left[\frac{\sqrt{g}}{h_2}K_2\rho U_1^2\right] + \frac{\partial}{\partial Y_3}\left[\frac{\sqrt{g}}{h_3}K_3\rho U_1^2\right] + C_r\frac{\partial}{\partial Y_3}\left[\frac{\sqrt{g}}{h_3}\rho\frac{U_\phi^2}{r}\right] = 0.0 \tag{1.4}$$

Energy Equation

$$\frac{\partial}{\partial Y_1}\left[\frac{\sqrt{g}}{h_1}\rho U_1 H_T\right] + \frac{\partial}{\partial Y_2}\left[\frac{\sqrt{g}}{h_2}\rho U_2 H_T\right] + \frac{\partial}{\partial Y_3}\left[\frac{\sqrt{g}}{h_3}\rho U_3 H_T\right] -$$

$$-\frac{1}{Pr_t}\sqrt{g}g^{22}\frac{\partial}{\partial Y_2}\left[\mu_t\frac{\partial H_T}{\partial Y_2}\right] - \frac{1}{Pr_t}\sqrt{g}g^{23}\frac{\partial}{\partial Y_2}\left[\mu_t\frac{\partial H_T}{\partial Y_3}\right]$$

$$-\frac{1}{Pr_t}\sqrt{g}g^{32}\frac{\partial}{\partial Y_3}\left[\mu_t\frac{\partial H_T}{\partial Y_2}\right] - \frac{1}{Pr_t}\sqrt{g}g^{33}\frac{\partial}{\partial Y_3}\left[\mu_t\frac{\partial H_T}{\partial Y_3}\right]$$

$$-\frac{Pr_t-1}{2Pr_t}\sqrt{g}g^{22}\frac{\partial}{\partial Y_2}\left[\mu_t\frac{\partial U_1^2}{\partial Y_2}\right] - \frac{Pr_t-1}{2Pr_t}\sqrt{g}g^{23}\frac{\partial}{\partial Y_2}\left[\mu_t\frac{\partial U_1^2}{\partial Y_3}\right]$$

$$-\frac{Pr_t-1}{2Pr_t}\sqrt{g}g^{32}\frac{\partial}{\partial Y_3}\left[\mu_t\frac{\partial U_1^2}{\partial Y_2}\right] - \frac{Pr_t-1}{2Pr_t}\sqrt{g}g^{33}\frac{\partial}{\partial Y_3}\left[\mu_t\frac{\partial U_1^2}{\partial Y_3}\right] = 0.0 \tag{1.5}$$

Vorticity Equation

$$\frac{\partial}{\partial Y_2}\left[\frac{g_{23}}{h_2}U_2 + h_3U_3\right] - \frac{\partial}{\partial Y_3}\left[h_2U_2 + \frac{g_{23}}{h_3}U_3\right] - \frac{\sqrt{g}}{h_1}\Omega = 0.0 \tag{1.6}$$

Vorticity Transport Equation

$$\frac{\partial}{\partial Y_1}\left[\frac{\sqrt{g}}{h_1}\rho U_1\Omega\right] + \frac{\partial}{\partial Y_2}\left[\frac{\sqrt{g}}{h_2}\rho U_2\Omega\right] + \frac{\partial}{\partial Y_3}\left[\frac{\sqrt{g}}{h_3}\rho U_3\Omega\right] - \frac{\sqrt{g}}{h_1}\Omega\frac{\partial}{\partial Y_1}\left[\rho U_1\right]$$

$$-(h_1h_2K_2)\frac{\partial}{\partial Y_3}\left[\rho U_1^2\right] + (h_1h_3K_3)\frac{\partial}{\partial Y_2}\left[\rho U_1^2\right]$$

$$-\sqrt{g}g^{22}\frac{\partial^2}{\partial Y_2^2}\left[\mu_t\Omega\right] - 2\sqrt{g}g^{23}\frac{\partial^2}{\partial Y_2Y_3}\left[\mu_t\Omega\right] - \sqrt{g}g^{33}\frac{\partial^2}{\partial Y_3^2}\left[\mu_t\Omega\right] + C_r2V_2\frac{1}{h_1}\frac{\partial}{\partial Y_1}\left[\frac{\sqrt{g}}{h_1}\rho U_1\right] = 0.0 \quad (1.7)$$

In these equations, the two first order momentum equations have been replaced by the vorticity transport equation and a transverse pressure equation. The vorticity transport equation is used in the manner of Briley and McDonald (1974) to explicitly calculate the secondary vorticity. The transverse pressure equation is obtained by differentiating the first order momentum equations (Poisson's dynamical equations) and adding together in the manner of Ghia (1979). It should be noted that some curvature terms (derivatives of the metrics in the stress tensor) have been neglected based on the experience of Anderson (1980) in that streamline curvature is much more important in the turbulence modeling than in the momentum equations. It is also noted that there is a significant residual benefit to using the potential flow coordinate system. The pressure gradient may be separated into two components; the streamwise pressure gradient determined by duct area and flow blockage, and the transverse pressure gradient determined by the principal streamline curvature. As can be seen by the transverse pressure equation, (Eq. 1.4), the transverse pressure is determined exclusively by the principal curvature components K_2 and K_3.

Auxiliary Equations

These equations of motion are closed using the following auxiliary relations.

$$P = \rho RT \quad (1.8)$$

$$H_T = C_pT + \frac{U^2}{2} - C_r\frac{V^2}{2} \quad (1.9)$$

In addition it is noted that the magnitude of the velocity is given by

$$U^2 = U_1^2 + U_2^2 + U_3^2 + \frac{2g_{23}}{h_2h_3}U_2U_3 \quad (1.10)$$

Stationary/Rotating Coordinates

The Constant C_r takes on the value of 0.0 for stationary coordinates and the value of 1.0 for rotating coordinates. In rotating coordinates, the terms having C_r as a coefficient are the Coriolis terms. All the dependent variables U_1, U_2, U_3, H_t, Ω are the values in the rotating coordinating system. H_T becomes the rothalpy in the rotating coordinate system, but U_ϕ remains the tangential

velocity in the stationary coordinate system. These Coriolis forces are assumed to be written in a coordinate system where the coordinate Y_3 is assumed to be aligned width the radial direction. These Coriolis forces are easily identified. In the transverse pressure equation Eq. 1.4, the term is essentially the centrifugal force. In the vorticity transport Eq. 1.7, it is the component of coordinate rotation added to the relative vorticity after the manner of (Dring and Joslyn, 1983).

Global Conditions and Boundary Conditions

The solution to these equations requires boundary conditions for six equations and six unknowns. These boundary conditions are

$$U_1 = 0 \tag{1.11}$$

$$U_2 = 0 \tag{1.12}$$

$$U_3 = 0 \tag{1.13}$$

for the no slip boundary condition. For adiabatic walls we have,

$$\frac{\partial H_T}{\partial Y_2} = 0.0 \tag{1.14}$$

$$\frac{\partial H_T}{\partial Y_3} = 0.0 \tag{1.15}$$

and for prescribed wall temperature (heat transfer) we have,

$$H_T = H_{TW} \tag{1.16}$$

On the vorticity we have,

$$\frac{\sqrt{g}}{h_1}\Omega = \frac{\partial}{\partial Y_2}\left[\frac{g_{23}}{h_2}U_2 + h_3 U_3\right]$$

$$\frac{\sqrt{g}}{h_1}\Omega = -\frac{\partial}{\partial Y_3}\left[h_2 U_2 + \frac{g_{23}}{h_3}U_3\right] \tag{1.17}$$

Finally for the transverse static pressure equation we may have either of two boundary conditions.

$$\frac{\partial P}{\partial Y_2} = 0.0$$

$$\frac{\partial P}{\partial Y_3} = 0.0 \tag{1.18}$$

$$\frac{\partial P}{\partial Y_2} = -\frac{\sqrt{g}}{h_1 h_3^2}\frac{\partial(\mu_t \Omega)}{\partial Y_3}$$

$$\frac{\partial P}{\partial Y_3} = \frac{\sqrt{g}}{h_1 h_2^2} \frac{\partial(\mu_t \Omega)}{\partial Y_2} \tag{1.19}$$

depending on the wall. The first boundary condition 1.18 is consistent with the approximations used to simplify the equations of motion namely that the cross flow is small. The second set of boundary conditions (1.19) is required when the cross flow is moderately large. Substitution of the definition of vorticity into this equation results in

$$\frac{\partial P}{\partial Y_2} = -\frac{\sqrt{g}}{h_1 h_3^2} \frac{\partial}{\partial Y_3} \left(\mu_t \frac{\partial U_2}{dY_3} \right) \tag{1.20}$$

which is easily recognized from the boundary layer equations as the pressure gradient in the crossflow direction. The second boundary conditions is implemented by integrating Eqs. 1.19 around the boundary to obtain the static pressure to within an additative constant. These conditions on the pressure and their consequence will be discussed in more detail later in the discussion section.

In addition we note according to Brandt that two global conditions must be satisfied.

$$\int \dot{S} dY_2 dY_3 = \oint h_1 \rho \vec{U} \circ \vec{n} dy \tag{1.21}$$

and

$$\int \dot{\Omega} dY_2 dY_3 = \oint \vec{U} \circ d\vec{y} = \Gamma \tag{1.22}$$

where

$$\dot{S} = -\frac{\partial}{\partial Y_1} \left[\frac{\sqrt{g}}{h_1} \rho U_1 \right] \tag{1.23}$$

$$\dot{\Omega} = \frac{\sqrt{g}}{h_1} \Omega \tag{1.24}$$

Eq. 1.21 states that the rate of change of mass flow crossing the computational area is equal to the net mass flow entering at the boundaries. Eq. 1.22 is recognized as Stokes theorem which states that the integral of the secondary vorticity over the crossectional area is equal to the circulation. We note that either Eq. 1.18 or Eq. 1.19 satisfies the boundary condition only to within an additive constant. This additive constant is obtained by satisfying the global mass flow constraint Eq. 1.21. The second constraint, Eq. 1.22, is necessary to insure convergence of the secondary flow field (i.e., U_2, U_3). It can be seen from Stokes theorem that for flows in ducts, the circulation over a crossection is always zero. The algorithm for solving these equations with the given boundary conditions is given in Anderson (1989).

Algebraic Turbulence Modeling

The problem associated with implementing an algebraic turbulence model for a turbulent boundary layer is the determination of a turbulent length scale such as the boundary layer thickness, boundary layer displacement thickness, or as with the Baldwin–Lomax model a length scale based

on vorticity. In complex three dimensional flows such as occur in turbine vane passages, this length scale is often ambiguous and difficult to determine. Thus as an example, three dimensional flows have no region in the free stream where the vorticity is zero so that the Baldwin–Lomax vorticity function which was fitted to a simple flat plate boundary may loose some of its meaning. However although boundary layer displacement thickness is ambiguous in passage flows, blockage is not. Therefore an algebraic eddy viscosity model based on blockage, which is an extension of the model used in Anderson (1980), was developed.

This model is a two layer model where the outer portion of the boundary and the free stream is described with a constant eddy viscosity based on the blockage and the inner layer near the wall is described by the van Driest's model. In the outer region we have an effective displacement thickness δ^* given by,

$$\delta^* = \frac{A}{l}\left[1 - \frac{W}{A(\rho U_1)_{max}}\right] \tag{1.25}$$

where A is the passage area, W is the mass flow, l is the wall perimeter, and ρU_1 is the mass flux. As can be seen from the definition, δ^* is defined by global parameters which are unambiguous. The eddy viscosity in the outer layer is then given by,

$$\mu_t = \mu + \chi_c(\rho U_1)_{max}\delta^* \tag{1.26}$$

The van Driest eddy viscosity distribution is given by;

$$\mu_t = \mu + \frac{2\mu_w(\kappa DY^+)^2}{1 + \sqrt{1 + 4(\kappa DY^+)^2}} \tag{1.27}$$

where the van Driest damping is given by,

$$D = 1 - exp\left(\frac{-Y^+}{A^+}\right) \tag{1.28}$$

In a corner two walls affect the mixing length Y^+. Therefore it was assumed that

$$\frac{1}{(Y^+)^2} = \frac{1}{(Y_1^+)^2} + \frac{1}{(Y_2^+)^2} \tag{1.29}$$

where the subscripts refer to the closest and next closest walls. It may be observed that far from the second wall, the mixing length reduces to that for a two dimensional boundary layer.

2. Results and Discussion

Turbulent Flow in a Square Curved Duct

The laminar and turbulent flow in a square curved duct with small radius of curvature was measured by Taylor et al. (1981) and a solution for the turbulent flow field was first given by Kreskovsky et al. (1979) using an approximate solution for the turbulent sublayer. This flow field presents a particularly difficult test for the analysis because of the large secondary flows which are generated in the plane normal to the mean flow direction. Thus the assumption of small secondary flow velocities, which was used to derive the equations of motion, is severely tested.

The potential flow solution used for the coordinate system was calculated using the analysis given by Anderson et al. (1982) where the computational grid consists of 100 streamwise stations with a crossplane grid of 49 x 49 mesh points. Figure 60 shows, for clarity, the coordinate grid with only 17 uniformly spaced streamlines and 50 streamwise stations (potential planes). The actual grid consists of 49 streamlines nonuniformly spaced to resolve the boundary layer flow accurately. The inlet conditions were measured at approximately streamwise station I = 20 (i.e. I = 10 on Fig. 60) which is just upstream of the turn. The measured conditions were used to start the calculation at this station. The exit station just downstream from the turn occurs at approximately I = 72 (i.e. I = 36 on Fig. 60).

The flow conditions given in Taylor et al. (1981) indicate a Reynolds number based on hydraulic diameter as 40,000 in water which is turbulent and incompressible. Thus the mean inlet flow velocity was chosen at 100 ft/sec to eliminate compressibility effects and the molecular viscosity adjusted to match the Reynolds number. Initial conditions specified uniform flow with a boundary layer thickness about 10 per cent of the height of the duct corresponding to a Reynolds number based on momentum thickness of about 400 which is quite low.

Data was obtained at angular distances of θ = 30., 60., and 90. degs. At θ = 90. degs, the secondary flow field is shown on Fig. 61. The center of the passage vortex is clearly seen centered near the ID wall. Maximum velocities in the end wall boundary layer reach 40 ft/sec which is a significant fraction of the free stream velocity (100 ft/sec) and which severely test the assumptions made in the analysis. The streamwise velocity profile in the boundary layer in universal coordinates is shown on Fig. 62 where it is compared to the law of the wall and and a laminar sublayer curve of $U^+ = Y^+$. This profile was taken at θ = 90. degs on the end wall and in the mid channel. It can be seen from this figure that the law of the wall is satisfied using the algebraic turbulence model developed for this analysis. Details of the boundary layer at this same location are shown in Fig. 63. The U_1 and U_2 components were resolved into the free stream direction U_s, and the cross flow direction U_c. However since the boundary layer Reynolds number is so low, power law curve fits such as the empirical correlation of Mager (1952) are not useful.

Figs. 64 through 69 show a comparison of the calculated streamwise and cross flow velocities with the measurements for planes at θ = 30., 60. and 90. degs. It can be seen from these figures that the results are quite good indicating that the analysis can provide a quite accurate calculation even

when the cross flow velocity is quite large. A closer inspection indicates that the secondary U_2 is predicted very well. At $r^* = .1$ and .9, the traverses are within the side wall boundary layers large velocity gradients and so are quite sensitive to location of the traverse relative to the boundary layer thickness. In the core flow region, the predictions are also good. The overall boundary layer thickness is also predicted very well. In addition one notes that the flow (U_1 velocity) at $\theta = 60.$ and 90. degs has a significant depression on the ID wall near the mid span. This phenomena is also predicted, but the extent of the region is under predicted. It is also interesting that the analysis correctly predicts that the U_1 velocity peaks on the OD (pressure) side of the duct. This peaking of the velocity on the pressure side of the duct is a consequence of the secondary flow mixing which appears to be reasonably well modeled by the analysis.

LSRR Gas Turbine Cascade

The UTRC Low Speed Rotating Rig (LSRR) tests used a rotor mid plane section identical to earlier tests performed in a cascade by Graziani et al. (1980). These tests included static pressure distributions at several spanwise sections, and heat transfer measurements on the blade surfaces and the end wall. Since these tests are in stationary coordinates, they may be thought of as representative of heat transfer on a gas turbine stator, and can be used to verify the analysis and the computational procedure.

Construction of Duct Passage & Computational Grid

The coordinate system for the gas turbine cascade was constructed using the procedure described in the analysis section. The grid obtained in this manner is shown on Fig. 70 with the turbine blades superimposed. It has 100 x 49 x 49 mesh (Y_1, Y_2, Y_3 directions respectively) points and will be used as a reference grid for all the figures which follow. The actual calculation was made on a 200 x 49 x 49 where the intermediate streamwise grid planes were interpolated.

As was noted in the analysis section, this grid is obtained from the potential flow solution for the flow through the simulated gas turbine passage. Thus the computational coordinates are the potential lines Y_1 coordinate and the streamlines Y_2 coordinate. Therefor the potential flow static pressure distribution can be obtained from the metric h_1 of the coordinates. In terms of the metrics, the pressure coefficient C_p is given by,

By comparing the calculated inviscid static pressure distribution with the measured static pressure distribution, one can evaluate how well the simulated gas turbine passage represents the the blade. This comparison is shown on Fig. 71 and indicates that the coordinates are a reasonable approximation of the turbine cascade passage.

In addition to constructing the mesh, one must consider the distribution of mesh points. Thus in order to clearly resolve the boundary layers down into the sublayer rather than using wall function or other approximations near the wall a large number of mesh points must be devoted to defining the boundary layer. This may be done by distorting the mesh and crowding mesh points near the wall.

The distribution of mesh points was determined by requiring at least fifteen to twenty mesh points to define the boundary layer as shown in the detail of the boundary layer shown on Fig. 72.

Verification of Aerodynamic Predictions

Since the LSRR gas turbine cascade is simulated by a duct passage, it is very important that the duct passage produce a static pressure distribution which closely approximates the pressure distribution on the cascade blades. Measurements of the static pressure distributions at three locations on the cascade blade were taken by Camarata et al. (1975) which can be used as a baseline comparison with the calculated pressure distributions. The calculations were made with the pressure boundary condition Eq. 1.18 which specifies a zero normal pressure at he walls. The comparisons between the calculated and measured wall pressure distributions are shown on Figs. 73, 74 and 75. As can be seen on these figures. the predictions are quite good for the mid span and quarter span pressure distributions but fail to predict the unloading of the blade near the hub. When one examines the equations of motion, it is seen that a pressure gradient can only be produced by the streamline curvature of the potential flow as expressed by Eq. 1.4. For this case, the potential flow has no spanwise pressure distribution and therefor there is no spanwise pressure distribution calculated. However if one uses the boundary condition given by Eq. 1.19, a spanwise pressure distribution will be created by the secondary flow. Attempts to implement this second boundary condition have not been successful.

Verification of the Turbulence Model

The algebraic eddy viscosity model was used for this calculation is an extension to three dimensions of the model used by Anderson (1980) and is described in the analysis section. It is a two layer model satisfying the law of the wake and the law of the wall. Since detailed boundary layer profile data are not available for this case, verification consists of making sure that the law of the wall is satisfied. Figures 76 and 77 show the developing streamwise velocity profiles in universal turbulent coordinates compared to the law of the wall and laminar sublayer along the end wall and along the suction surface of the duct. As can be seen from these comparisons, the law of the wall is accurately captured. Note also the number of points in the sublayer which is accurately captured as well. Near the inlet (i = 10), the wake region of the boundary layer is much like any two dimensional boundary layer. However as the flow progresses downstream, the wake region changes considerably. At the present time, this effect can not be evaluated without detailed boundary layer data.

Detailed boundary layer data is not available for this case. However detailed boundary layer data was obtained by Vermeulen (1971) for a rectangular duct turning 60 deg. If one compares two stations on the end wall with the same amount of turning, the principal features of the boundary layer should be similar. At the selected point in the flow field, the the edge of the boundary, the magnitude of the free stream velocity U_e, and the flow direction were determined. Then the velocity components were resolved into the streamwise direction U_s and the normal (crosswise) direction U_c. Using the friction velocity U_τ, the two components of velocity can be calculated in universal

coordinates. Fig. 78 shows the boundary layer profiles in universal coordinates calculated for the LSRR turbine cascade passage, and Fig. 79 shows the results measured by Vermuelen (1971). Although a one on one comparison can not be made, the principal features of the boundary layer flow are similar. The U_s^+ velocity component closely follows the law of the wall in both cases. The cross flow component U_c^+ reaches a maximum at about $Y^+ = 30$ for the calculated flow and at about $Y^+ = 50$ for the measured flow. The calculated flow shows a slightly higher maximum crossflow velocity. Overall it may be concluded that the principal features of the boundary layer flow on the end wall are captured.

Development of the Passage Vortex

It is well know that gas turbine passages develop a passage vortex which generally ends up near the suction surface at the exit. This passage vortex plays an important roll in the heat transfer. Thus an accurate capturing of the passage vortex is essential for the prediction of the heat transfer. The development of this vortex is shown on Fig. 80. As shown on this figure, the secondary flow on the end wall is just starting at (i = 20) which is near the leading edge of the blades. Near the mid chord (i = 30), a clear vortex pattern has developed which appears centered on the end wall. The center of this vortex moves along the end wall from the pressure to the suction side of the passage until near the trailing edge at (i = 60) it is in the corner of the passage. Then the vortex moves up the suction surface at the trailing edge as shown at (i = 80). The location of this vortex is close to where it is observed experimentally in turbine passages. The mechanism by which the vorticity generated by the end wall boundary layer is swept up into a vortex is clearly captured. In addition we note that the vortex follows streamlines as the vorticity transport theorem predicts.

A detail of the flow in the suction surface/end wall corner is shown on Fig. 81 where the gapwise velocity (U_2) distribution is clearly plotted. This velocity decreases as it approaches the suction surface and turns the corner. Then on the suction surface, the spanwise velocity increases as it leaves the end wall. One can see clearly that the peak crossflow is very close to the wall. The development of the crossflow velocity along the end wall on a coordinate line midway along the gap (j = 25) is shown on Fig. 82. Peak gapwise velocities reach a value of 89.0 ft/sec at a about (i = 42) and then decrease slowly. This peak velocity thus approaches the inlet streamwise velocity which is 93.0 ft/sec. Some interesting observations may be made about the secondary vorticity distribution (streamwise component of vorticity) which drives the secondary flow. Since the derivative (dU_2/dY_3) is the vorticity near the end wall, the vorticity must change sign at the peak velocity. Hence we see from Fig. 82 that the vorticity distribution consists of a very large region of small vorticity in the middle of the duct and a very thin region of very large vorticity along the walls. In fact these two regions must just cancel since by Stokes theorem the circulation on a crossplane must be zero. The vorticity in the core flow is the classical (inviscid) secondary vorticity, while the vorticity near the wall is that generated by the boundary layer and which slowly diffuses inward.

The passage vortex has a profound effect on the wall streamlines. Since the limiting streamlines are tangent to the skin friction vectors, a plot of these vectors shows the direction of these streamlines. These vectors are shown on Figs. 83 and 84. On the end wall one observes very large

crossflow from the pressure side to the suction side of the passage. This crossflow, as observed above, approaches the inlet streamwise velocity of 93.0 ft/sec. On the suction surface, one observes the flow moving from the end walls in towards the midspan. These spanwise velocities are not quite as large as the gapwise velocities, but do approach approximately 60.0 ft/sec compared to the 93.0 ft/sec of the inlet streamwise velocity. The effect of the passage vortex is to sweep flow from the end wall up on to the suction surface.

Evaluation of Heat Transfer Predictions

A comparison of the calculated heat transfer with experimental data Graziani et al. (1980) for the end wall and suction surfaces is shown on Figs. 85 through 90. It should be noted that since the cascade passage is treated as a duct, the complex flow on the end wall surrounding the leading edge can not be rigorously treated as well as the flow on the leading edge of the blade. However, in spite of this, the general features and level of the heat transfer on the end wall are captured. Thus we note that a small peak in heat transfer near the leading edge ($S_t = 3.0 \times 10^3$) is predicted. The heat transfer then drops off especially near the pressure surface (note $S_t = 1.0 \times 10^3$ contour). Finally the heat transfer reaches a peak near the trailing edge of ($S_t = 4.0 \times 10^3$) compared to the maximum measured heat transfer of ($S_t = 4.0 \times 10^3$). The comparison of the suction surface heat transfer shown on Figs. 86 and 87 is not quite as good. The calculation shows peak heat transfer near the midspan (note $S_t = 3.5 \times 10^3$ contour) where the measured peak heat transfer is close to the end walls. However, it should be noted that the boundary layer on the suction surface was a transitional boundary layer (Sharma and Graziani, 1983) and transition was not modeled. These observations are also seen in Figs. 89 and 90 which compare the calculated S_t on the end wall and suction surface with the measurements of Graziani et al. (1980). In both cases it appears that the general level of the heat transfer is predicted as well as the high and low points although the location of these points are not that well predicted.

LSRR Gas Turbine Rotor

Construction of Duct Passage & Computational Grid

The gas turbine blade sections designed for the LSRR tests are shown stacked on Fig. 91. It has a constant axial chord with a slight twist and a considerable change in the thickness distribution. The gap to chord and span to chord are approximately 1.0. At the present time, the PATH code does not have the capability of constructing a coordinate system for this blade passage. Therefore an approximate blade passage was constructed using the midspan blade section and assuming a constant blade section. The midspan section is the same as that used in the cascade tests by Graziani et al. (1980) and Langston et al. (1977). The procedure for obtaining the coordinate system is described in the analysis section and leads to a coordinate system shown on Fig. 70. The calculations then will not show any effects due to blade twist or blade thickness distribution.

Evaluation of Heat Transfer Predictions

A comparison between the calculated and measured heat transfer is shown on Figs. 92 through 95 for the end wall and suction surfaces. The comparison for the end wall Figs. 92 and 93 generally shows lower predicted heat transfer than was measured although the code does predict a qualitative increase in heat transfer near the trailing edge of the blade similar to that which was measured and a low rate of heat transfer near the pressure surface. The distribution of end wall heat transfer is qualitatively similar to that predicted for the cascade (stator) passage. The comparison for the suction surface is shown on Figs. 94 and 95. Again we note higher rates of measured heat transfer than was calculated and in addition we note that the distribution of heat transfer is quite different. The calculated heat transfer is again more similar to that calculated for cascade (stator). A major difference can of course be attributed to the fact that the twist a thickness distribution effects were not simulated although a final conclusion can not be made until the calculation is repeated with these effects included. Since the calculations used the mid span blade shape to construct the coordinate system, heat transfer on the mid span may be better predicted. A comparison of the calculated and measured mid span heat transfer on the suction surface is shown on Fig. 96. One can see that the predictions are quite good accept near the leading edge where one may expect differences since a duct passage was used to simulate the turbine passage so that the leading edge effects were neglected.

Comparison of Stator/Rotor Coriolis Effects

The calculations for both the cascade (stator) and the rotor were run on the same coordinates and with the same inlet conditions. The only difference being that the rotor had the Coriolis forces included whereas the stator did not. Therefore these calculations can be used to estimate the effect of Coriolis forces alone on the heat transfer. Figure 97 shows the effect of Coriolis forces on the behavior of the passage vortex by comparing the location of the passage vortex for the stator and rotor at the same location in the turbine passage. This figure appears to indicate that the Coriolis effect alone on the location of the vortex is quite small. Figures 98 and 99 show the effect of Coriolis forces on the endwall and suction heat transfer. It appears that the Coriolis forces have very little effect on the mid span suction surface heat transfer and a significant effect on the end wall heat transfer. A second observation may also be made in that the blade thickness distribution and twist have a major effect on the suction surface heat transfer as indicated by Figs. 78 and 79.

CONCLUDING COMMENTS

A combined experimental and computational program has been conducted to examine the heat transfer distribution in a turbine rotor passage. Heat transfer was measured and computed for both the full–span suction and pressure surfaces of the rotor airfoil as well as for the hub endwall surface. The effects of the following variables on the rotor passage heat transfer were documented:

* Reynolds number

* Rotor inlet flow angle (flow coefficient)

* Surface roughness

1. Conclusions

(1) The results of this program have demonstrated that secondary flows within the rotor–passage flow produced localized regions with significantly enhanced heat transfer rates. The largest enhancement on the airfoil surface was observed near the tip on the suction surface for 100%<S*<120% where the local Stanton number was more than 100% greater than the midspan value. This region of enhancement was produced by the tip–leakage vortex. The largest enhancements on the endwall surface, with local Stanton numbers 90% greater than at the leading–edge midgap , were observed near the rotor–leading–edge/endwall junction. This enhancement was produced by the leading–edge horseshoe vortex system (see Fig. 33a).

(2) Increased surface roughness significantly increased heat transfer rates relative to the smooth–wall test cases for all locations within the rotor passage (e.g. compare Fig. 33a and 42a). The largest relative changes produced by the wall roughness (> 100%) occurred in the fore–chord (0<S/Bx<0.7) , suction surface region for β_1= 40° (Fig. 53). For the smooth–wall test cases the boundary layer in this region was laminar/transitional while for the rough–wall test cases it was apparently fully turbulent. Local regions of augumented heat transfer that were observed for the smooth–wall test cases were also present for the rough–wall cases, e.g. the leading–edge/endwall junction and the tip–leakage vortex site (compare Figs. 33a and 42a). This result indicates that surface roughness had important augmentation effects even in regions with extremely thin, skewed, nonequilibrium boundary layers.

(3) Comparisons between the present rough–wall data, the nearsmooth wall data of the NASA–HOST contract and predictions of the Pratt & Whitney version of the STAN–5 boundary layer code showed excellent agreement (Fig. 56). Use of the vanDreist "modified mixing–length" turbulence model with peak–to–peak surface roughness values produced excellent heat transfer predictions over a factor–of–ten range in surface roughness.

2. Observations – Design–Inlet Flow Angle Test Cases

(1) The heat transfer data indicate that the flow was everywhere attached at design inlet flow angle; there was no evidence of separation bubbles on either the airfoil or endwall surfaces (e.g. Figs. 33–37).

(2) Three–dimensional flow effects associated with the mainpassage vortices had a much stronger influence on the heat transfer on the suction than on the pressure surface. In the aft–chord region, near both the hub and tip, these secondary flows increased the local heat transfer as much as 60% above midspan rates.

(3) Increasing the Reynolds number produced the expected reduction of local Stanton number for all locations in the rotor passage where the boundary layers were turbulent. Increasing the Reynolds number also hastened the transition process in regions where the boundary layer was laminar/transitional (e.g. Fig 51).

(4) The largest enhancement on the airfoil surface was observed near the tip on the suction surface for 100%<S*<120% where the local Stanton number was more than 100% greater than the midspan value. This region of enhancement was produced by the tip–leakage vortex (e.g. see Figs. 33b–37b).

(5) The secondary flows produced by the first stage stator increased the heat transfer near the hub and tip of the forechord region of the rotor airfoil (e.g. Fig. 28a–marker B and Fig. 33b).

(6) The minimum heat transfer on the pressure surface occurred near the downstream end of the minimum–speed region. This area of minimum heat transfer occurred near midspan (e.g. Fig. 28b–marker C and Fig. 33b).

(7) Heat transfer rates in the aft–chord region of the pressure surface were slightly (approximately 10%) higher near the tip than for the remainder of the span (e.g. Fig. 33b). This resulted because the tip–leakage flow reduced the pressure surface boundary layer thickness near the tip.

(8) Comparisons of the present smooth–wall midspan heat transfer distributions with midspan data previously obtained for this same airfoil section (NASA–HOST) show very good agreement (Fig. 53).

(9) The leading edge horseshoe vortex system produced a region of greatly enhanced heat transfer on the endwall at the leading–edge/endwall junction (90% greater than at the leading edge midgap) (e.g. Fig. 28c–marker E and Fig. 33c). The maximum endwall heat transfer rates were observed in this region.

(10) The minimum heat transfer on the hub endwall occurred in the mid–chord region near the endwall/pressure–surface corner (e.g. Fig. 28b–marker D and Fig. 33c).

3. Observations – Off–Design–Incidence Test Cases

(1) Increasing the rotor inlet flow angle from $\beta 1 = 40°$ to 54° produced a full–span separation bubble (approximate streamwise length of 2% S*) near the streamwise location of the pressuresurface leading edge overspeed. Reattachment downstream of this bubble produced a narrow, full–span band of relatively high heat transfer with Stanton numbers approximately 60% greater than for that streamwise location with attached flow (e.g. Fig. 29d and Figs. 39–41).

(2) Increasing the rotor inlet flow angle increased the heat transfer in the fore–chord region of the pressure surface and simultaneously decreased the heat transfer in the fore–chord region of the suction surface. As expected, trailing–edge region heat transfer rates for both the pressure and suction surfaces were unchanged by changing incidence (Fig. 58).

(3) The fore–chord region of the endwall showed a decrease in heat transfer with increased inlet flow angle, an effect produced directly by the decrease in relative inlet velocity (e.g. compare Fig. 33c and 39).

4. Observations – Passage Analysis Program

(1) An assessment of the analytical and computational procedure indicates that the PATH code can predict reasonably well the aerodynamic properties of the three dimensional flow field, the wall skin friction, and the wall heat transfer in a gas turbine passage.

(2) Use of the vorticity equation and vorticity transport equation rather than the two transverse momentum equations insures that the passage vortex is accurately captured with little numerical diffusion as indicated by the results shown of the development of the passage vortex.

(3) The results indicate that (a) the development of the three dimensional boundary layers on the end wall and airfoil surfaces conform accurately to the law of the wall and (b) that the sublayer and crossflow can be accurately captured with an appropriate computational mesh and (c) that the small length scales in the boundary layer can be resolved.

(4) The present analysis can be improved significantly if the alternative boundary condition on the static pressure can be used since it would account for crosswise pressure gradients on surfaces where there is no pressure gradients in the potential flow solution.

(5) Although not explicitly examined in this report, it is possible to significantly improve the computational time by adding a multi–grid capability to part of the algorithm. For the rotor case, as an example, it took 9854 iterations to converge the primary flow solution but 35979 iterations to resolve the secondary flow solution. Since the solution of the secondary flow involves the classical generalized Cauchy–Rieman problem, it is possible that a multi–grid procedure may significantly improve the computational time.

ACKNOWLEDGEMENT

The author gratefully acknowledges the numerous contributions of others to the conduct of this project. The technical contract monitors for the work were Dr. Helen V. McConnaughey and Ms. Lisa W. Griffin, National Aeronautics and Space Administration (NASA), George C. Marshall Space Flight Center. The passage analysis presented in this report was conducted and reported entirely by Dr. Olaf L. Anderson (since retired from UTRC) under NAS8–37351. The STAN–5 computations presented herein were conducted by Dr. Om Sharma (Pratt & Whitney, Commercial Engine Business) and Mr. Joel H. Wagner. The ANSYS–PC/THERMAL computations were performed by Mr. Richard Roback. The experimental models were constructed by Mr. Richard C. Adamonis, Ms. Susanne L. Orr prepared the figures and tables and employed the SURFER contour routine to construct the heat transfer maps and Ms. Doris A. Zimmer typed the manuscript. Finally, the author acknowledges the contributions of Dr. Robert P. Dring who provided invaluable guidance throughout the project.

REFERENCES

Anderson, O. L., 1980, "Calculation of Internal Viscous Flows in Axisymmetric Ducts at Moderate to High Reynolds Numbers", Intl. J. Computers and Fluids, Vol. 8, No. 4, pp. 391–411.

Anderson, O. L. and Hankins, G. B., 1981, "Development of a Parabolic Finite Difference Method for 3–D Viscous Internal Flows", ASME Winter Meeting – Computers in Flow Predictions and Fluid Dynamic Experiments.

Anderson, O. L., Davis, R. T., Hankins, G. B. and Edwards, D. E., 1982, "Solution of Viscous Internal Flows on Curvilinear Grids Generated by the Schwarz–Christoffel Transformation", Numerical Grid Generation, J. F. Thompson editor, Elsevier Science Publishing Co., Inc.

Anderson, O. L., 1985, "Assessment of a 3–D Boundary Layer Code to Predict Heat Transfer and Flow Field in a Turbine Passage", UTRC Report R85–956834–2.

Anderson, O. L., 1989, "A Parabolic Analysis of a Three Dimensional Compressible Viscous Flow Solution Based on Potential Flow Coordinates", UTRC Report, December 1989.

Anon., (1988): ANASYS–PC.THERMAL 4.3 Reference Manual. Swanson Analysis Systems, Inc., Houston, PA.

Barnett, M., 1982, "The Solution of the Parabolized Navier–Stokes Equations by a Fully Implicit Method", AIAA 20th Aerospace Sciences Meeting, AIAA–82–0415.

Blair, M. F., 1983, "Influence of Free–Stream Turbulence on Turbulent Boundary Layer Heat Transfer and Mean Profile Development", ASME Journal of Heat Transfer, Vol. 105, pp. 33–47.

Blair, M. F., 1985, "Heat Transfer in the Vicinity of a LargeScale Obstruction in a Turbulent Boundary Layer", AIAA Journal of Propulsion and Power, Vol. 1, No. 2, pp. 158–160.

Blair, M. F., Dring, R. P. and Joslyn, H. D., 1989, "The Effects of Turbulence and Stator/Rotor Interactions on Turbine Heat Transfer, Part–I, Design Operating Conditions, Part–II, Effects of Reynolds Number and Incidence", ASME Journal of Turbomachinery, Vol. 111, No. 1, pp. 87–103.

Blair, M. F. and Anderson, O. L.: "The Effects of Reynolds Number, Rotor Incidence Angle and Surface Roughness on the Heat Transfer Distribution in a Large–Scale Turbine Rotor Passage", UTRC Report R89–957852–24, November 1989.

Blair, M.F. and Anderson, O.L., 1989, "The Effects of Reynolds Number, Rotor Incidence Angle and Surface Roughness on the Heat Transfer Distribution in a Large–Scale Turbine Rotor Passage", UTRC Report R89–957852–24.

Brandt, A., "Multi–Grid Solutions to Elliptic Flow Problems", Dept. of Applied Mathematics, The Weizmann Institute of Science, Rehovot, Israel.

Briley, W. R., 1974, "Numerical Methods for Predicting Three Dimensional Steady Viscous Flow in Ducts", J. Comp. Physics, Vol. 14, pp. 8–28.

Briley, W. R. and McDonald, H., 1979, "Analysis and Computation of Viscous Subsonic Primary and Secondary Flows", AIAA Computational Fluid Dynamics Conference, AIAA paper No. 79–1453.

Camarata, F. J., Hooper, R. M. and Nice, M. L., 1975, "Experimental Investigation of Passage Flow in a Baseline Build of a Large Scale Turbine Cascade", UTRC Report R75–212632.

Caretto, L. B., Curr, R.M. and Spalding, D. B., 1973, "Two Numerical Methods for Three Dimensional Boundary Layers", Comp. Methods in Applied Mechanics and Engineering, Vol. 1, pp. 1.

Carter, J.E., Edwards, D.E. and Werle, M.J., 1982, "Coordinate Transformation for Laminar and Turbulent Boundary Layers", AIAA Journal, Vol. 20, No. 2, pp. 282–284.

Cebeci, T. and Smith, A.M.O., 1974, Analysis of Turbulent Boundary Layers, Academic Press.

Crawford, M.E. and Kays, W.M., 1976, "STAN–5 Program for Calculation of Two–Dimensional Internal and External Boundary Layer Flows", NASA CR–2742

Dippery, R.B. and Sabersky, R.H., 1963, "Heat and Mass Transfer in Smooth and Rough Tubes at Various Prandtl Numbers", Int. J. Heat and Mass Transfer, Vol. 6, pp. 329–353.

Dring, R. P., Blair, M. F. and Joslyn, H. D., 1980, "An Experimental Investigation of Film Cooling on a Turbine Rotor Blade", ASME Journal of Engr. for Power, Vol. 102, No. 1, pp. 81–87.

Dring, R. P. and Joslyn, H. D., 1981, "Measurement of Turbine Rotor Blade Flows", ASME Journal of Engr. for Power, Vol. 103, No. 2, pp. 400–405.

Dring, R. P., Joslyn, H. D., Hardin, L. W. and Wagner, J. H., 1982, "Turbine Rotor–Stator Interaction", ASME Journal of Engr. for Power, Vol. 104, No. 4, pp. 729–742.

Dring, R. P. and Joslyn, H. D., 1983, "The Relative Eddy in Axial Turbine Rotor Passages", ASME paper number 83–GT–22.

Dring, R. P., Blair, M. F., Joslyn, H. D., Power, G. D. and Verdon, J. M., 1986, "The Effects of Inlet Turbulence and Rotor/Stator Interactions on the Aerodynamics and Heat Transfer of a Large Scale Rotating Turbine Model", Vol. I, Final Report, NASA Contractor Report 4079.

Edwards, D.E., Carter, J.E., and Werle, M.J., 1981, "Analysis of the Boundary Layer Equations Including a Coordinate Transformation" – The ABLE Code, UTRC81–30.

Ghia, K. N. and Sokhey, J. S., 1979, "Laminar Incompressible Viscous Flow in Curved Ducts of Regular Crossection", ASME J. of Fluids Engr., Vol. 99, pp. 640–648.

Graziani, R. A., Blair, M. F., Taylor, J. R. and Mayle, R. E., 1980, "An Experimental Study of Endwall and Airfoil Surface Heat Transfer in a Large Scale Turbine Blade Cascade", ASME Journal of Engr. for Power, Vol. 102, pp. 257–267.

Hah, C., 1983, "A Navier–Stokes Analysis of Three–Dimensional Turbulent Flows Inside Turbine Blade Rows at Design and Off Design Conditions", ASME paper number 83–GT–40.

Han, L.S., 1985, "Turbulent Flow Over Rough Turbine Airfoils", AFWAL–TR–85–2056, Final Contractor Report, The Ohio State University.

Han, L.S. and Delpassand, M., 1990, "A Heat Transfer Analysis for Rough Turbine Airfoils", WRDC–TR–89–2135, Final Contractor Report, The Ohio State University.

Holmes, D. G. and Tong, J. S., 1984, "A Three–Dimensional Euler Solver for Turbomachinery Blade Rows", ASME paper number 84–GT–69.

Joslyn, H. D., Dring, R. P. and Camarata, F. J., 1977, "Some Experiments Pertinent to Relative Frame Data Acquisition in the UTRC Large Scale Rotating Rig" UTRC Report UTRC77–12.

Joslyn, H. D. and Dring, R. P., 1977, "Final Results of the 1976 PWA Turbine Program in the UTRC Large Scale Rotating Rig", UTRC Report R77–217020.

Joslyn, H. D., Dring, R. P. and Sharma, O. P., 1983, "Unsteady Three–Dimensional Turbine Aerodynamics", ASME Journal of Engr. for Power, Vol. 105, pp. 322–331.

Joslyn H. D. and Dring, R. P., 1983, "Turbine Rotor Negative Incidence Stall", ASME paper number 83–GT–23.

Joslyn, H. D. and Dring, R. P., 1989, "Three Dimensional Flow and Temperature Profile Attenuation in an Axial Flow Turbine", Final Report under AFOSR Contract F49620–86–C–0020, UTRC Report R89–957334–1.

Kadar, B.A. and Yaglom, A.M., 1972, "Heat and Mass Transfer Laws for Fully Turbulent Wall Flows", Int. J. Heat and Mass Transfer, Vol. 15, pp. 2329–2351.

Karamcheti, K., 1980, Principals of Ideal Fluid Mechanics, Robert E. Krieger Publishing Company, Malabar, Florida.

Kreskovsky, J. P., Briley, W. R., and McDonald, H., 1979, "Analysis and Computation of Three–Dimensional Flow in Strongly Curved Ducts", ASME Annual Winter Meeting–Flow in Primary, Non–Rotating Passages in Turbomachines.

Langston, L.S., Nice, M. S. and Hooper, R. M., 1977, "ThreeDimensional Flow Within a Turbine Cascade Passage", ASME Journal of Engr. for Power, Vol. 99.

Madavan, N. K., Rai, M. M. and Gavali, S., 1989, "Grid Refinement Studies of Turbine Rotor–Stator Interaction", AIAA paper AIAA–89–0325.

Mager, A., Mahoney, J. J. and Budinger, R. E., 1952, "Discussion of Boundary Layer Characteristics Near the Wall of an Axial Flow Compressor", NACA Report 1085.

Moore, J. and Moore, J. G., 1979, "A Calculation Procedure for Three–Dimensional, Viscous, Compressible Duct Flow", ASME Winter Annual Meeting–Flow in Primary, Non–Rotating Passages in Turbomachines.

Owczarek, J. A., 1964, Fundamentals of Gas Dynamics, International Textbook Co., Scranton, Pennsylvania.

Patankar, S. V. and Spalding, D. B., 1972, "A Calculation Procedure for Heat, Mass, and Momentum Transfer in Three Dimensional Parabolic Flows", Int. J. Heat and Mass Transfer, Vol. 15, pp. 1787–1805.

Rai, M. M., 1987, "Unsteady Three–Dimensional Navier–Stokes Simulations of Turbine Rotor–Stator Interaction Including Tip Effects", AIAA paper number AIAA–87–2058.

Rai, M. M. and Dring, R. P., 1987, "Navier–Stokes Analysis of the Redistribution of Inlet Temperature Distortions in a Turbine", AIAA paper number AIAA–87–2146.

Rai, M. M. and Madavan, N. K., 1988, "Multi–Airfoil Navier–Stokes Simulations of Turbine Rotor–Stator Interaction", AIAA paper number AIAA–88–0361.

Rai, M. M., 1989, Private communication regarding a turbine stage calculation at NASA/Ames with the same rotor aspect ratio and tip clearance as in the experiment. January 12, 1989.

Rai, M.M., 1987, "Unsteady Three–Dimensional Navier–Stokes Simulations of Turbine Rotor–Stator Interaction Including Tip Effects," AIAA paper number AIAA–87–2058, presented at the Joint Propulsion Conference, San Diego, CA.

Rai, M.M. and Madavan, N.K., 1988, "Multi–Airfoil Navier–Stokes Simulations of Turbine Rotor–Stator Interaction," AIAA paper number AIAA–88–0361, AIAA 26th Aerospace Sciences Meeting, Reno, Nevada.

Reynolds, W. C., Kays, W. M. and Kline, S. J., 1958, "Heat Transfer in the Turbulent Incompressible Boundary Layer, III Arbitrary Wall Temperature and Heat Flux, NASA Memo 12–3–58w.

Schiff, L. B. and Steger, J. L., 1979, "Numerical Simulation of Steady Supersonic Viscous Flows", 17th Aerospace Sciences Meeting, AIAA paper 79–0130.

Seidman, M.H., 1978, "Rough Wall Heat Transfer in a Compressible Turbulent Boundary Layer", AIAA Paper No. 78–163 presented at the AIAA 16th Aerospace Sciences Meeting, Huntsville, Al.

Sharma, O. P. and Graziani, R. A., 1983, "Influence of End Wall Flow on Airfoil Suction Surface Midheight Boundary Layer Development in a Turbine Cascade", ASME J. Engr. for Power, Vol. 105, pp. 147–155.

Sieverding, C. H., 1985, "Recent Progress in the Understanding of Basic Aspects of Secondary Flows in Turbine Blade Passages", ASME Journal of Engr. for Gas Turbines and Power, Vol. 107, No. 2, pp. 248–257.

Subramanian, C. S. and Antonia, R. A., 1981, "Effect of Reynolds Number on a Slightly Heated Turbulent Boundary Layer", Int. Journal of Heat and Mass Transfer, Vol. 24, No. 11, pp. 1833–1846.

Taylor, A. M. K. P., Whitelaw, J. H. and Yianneskis, M., 1981, "Measurements of Laminar and Turbulent Flow in a Curved Duct With Thin Inlet Boundary Layers", NASA Contractor Report 3367.

van Driest. E.R., 1956, "On Turbulent Flow Near a Wall," J. Aeronautical Sci., Vol. 23, pp. 1007–1011.

Vermeulen, A. J., 1971, "Measurements of Three Dimensional Turbulent Boundary Layers", Phd. Dissertation, University College, Cambridge.

Vigneron, Y. C., Rakich, J. V. and Tannehill, J. C., 1978, "Calculation of Supersonic Viscous Flows Over Delta Wings with Sharp Supersonic Leading Edges", NASA TM–78500.

Warsi, Z. U. A., Tensors and Differential Geometry Applied to Analytic and Numerical Coordinate Generation, Mississippi State University, MSSU–EIRS–81–1.

Table 1
Comparison of the UTRC/LSRR with the SSME Turbopump Drive Turbines

Parameter	HPFTP	LSRR	HPOTP
D_T (ins)	11.1	60.0	
N (rpm)	38000	410 (520)	
Hub/Tip	0.83	0.80	0.88
Stator 1			
(S/B_x) avg	0.84	1.01	
(τ/B_x) avg	0.75	1.30	
α_1	90.0°	90.0°	90.0°
α_2	22.5°	22.0°	16.0°
Rotor 1			
(S/B_x)	1.20	0.95	
(τ/B_x)	0.69	0.96	
β_1	53.4°	40.0° (54.2°)	25.8°
β_2	25.5°	25.0°	24.0°
Stator 2			
(S/B_x)	0.94	0.93	
(τ/B_x)	0.79	0.94	
α_1	69.0°	50.0° (68.7°)	32.4°
α_2	23.5°	25.0°	24.0°
Rotor 2			
(S/B_x)	1.29		
(τ/B_x)	0.71		
α_1	54.4°		32.4°
α_2	29.5°		24.0°
$\phi = (C_x/U_m)$	0.61	0.78 (0.57)	

B_x - Airfoil axial chord
C_x - Axial flow speed
D_T - Tip diameter
N - Rotor speed
S - Airfoil span
U_m - Midspan wheel speed
α_1 - Stator inlet flow angle
α_2 - Stator exit flow angle
β_1 - Rotor inlet flow angle
β_2 - Rotor exit flow angle
τ - Airfoil pitch

Table 2a
Airfoil Geometry

AIRFOIL: FIRST STATOR (HUB)
PITCH (ins.): 6.88865

	LEADING EDGE	TRAILING EDGE
RADIUS (ins.)	0.44485	0.10988
METAL ANGLE (degr.)	90.00395	22.44246
WEDGE ANGLE (degr.)	31.79000	6.85000

	X(ins.)	Y_L(ins.)	Y_U(ins.)
1	0.00000	5.98844	5.98844
2	0.05932	5.76650	6.21038
3	0.11864	5.68598	6.29089
4	0.17796	5.63254	6.34433
5	0.23728	5.59498	6.38189
6	0.29660	5.56902	6.40786
7	0.35592	5.55114	6.42556
8	0.41524	5.53364	6.44182
9	0.47456	5.51555	6.45743
10	0.53388	5.49688	6.47239
11	0.59320	5.47760	6.48668
12	0.74150	5.42681	6.51919
13	0.88980	5.37219	6.54678
14	1.03810	5.31366	6.56894
15	1.18640	5.25111	6.58508
16	1.33470	5.18440	6.59454
17	1.48300	5.11341	6.59667
18	1.63130	5.03800	6.59063
19	1.77960	4.95798	6.57559
20	1.92790	4.87318	6.55065
21	2.07620	4.78339	6.51481
22	2.22450	4.68839	6.46704
23	2.37280	4.58791	6.40627
24	2.52110	4.48160	6.33143
25	2.66940	4.36922	6.24143
26	2.81770	4.25033	6.13530
27	2.96600	4.12450	6.01210
28	3.11430	3.99119	5.87111
29	3.26260	3.84973	5.71175
30	3.41090	3.69938	5.53366
31	3.55920	3.53930	5.33677
32	3.70750	3.36863	5.12118
33	3.85580	3.18656	4.88723
34	4.00410	2.99229	4.63534
35	4.15240	2.78525	4.36603
36	4.30070	2.56517	4.07986
37	4.44900	2.33245	3.77749
38	4.59730	2.08792	3.45958
39	4.74560	1.83271	3.12684
40	4.89390	1.56797	2.78000
41	5.04220	1.29464	2.41981
42	5.19050	1.01365	2.04697
43	5.33880	0.72592	1.66229
44	5.39812	0.60905	1.50524
45	5.45744	0.49120	1.34645
46	5.51676	0.37243	1.18596
47	5.57608	0.25271	1.02380
48	5.63540	0.13213	0.86004
49	5.69472	0.01077	0.69471
50	5.75404	-0.08624	0.52783
51	5.81336	-0.10952	0.35947
52	5.87268	-0.09755	0.18966
53	5.93200	0.00001	0.00001

Table 2b
Airfoil Geometry

AIRFOIL: FIRST STATOR (MIDSPAN)
PITCH (ins.): 7.71118

	LEADING EDGE	TRAILING EDGE
RADIUS (ins.)	0.44484	0.10987
METAL ANGLE (degr.)	90.00000	21.42000
WEDGE ANGLE (degr.)	31.80000	6.84000

	X(ins.)	Y_L(ins.)	Y_U(ins.)
1	0.00000	6.80766	6.80766
2	0.05932	6.44830	7.15365
3	0.11864	6.43405	7.17319
4	0.17796	6.41912	7.19210
5	0.23728	6.40354	7.21034
6	0.29660	6.38729	7.22791
7	0.35592	6.37035	7.24476
8	0.41524	6.35273	7.26089
9	0.47456	6.33441	7.27624
10	0.53388	6.31540	7.29080
11	0.59320	6.29568	7.30453
12	0.74150	6.24325	7.33502
13	0.88980	6.18623	7.35957
14	1.03810	6.12447	7.37758
15	1.18640	6.05781	7.38835
16	1.33470	5.98603	7.39114
17	1.48300	5.90896	7.38513
18	1.63130	5.82633	7.36940
19	1.77960	5.73787	7.34300
20	1.92790	5.64326	7.30490
21	2.07620	5.54212	7.25403
22	2.22450	5.43404	7.18927
23	2.37280	5.31852	7.10949
24	2.52110	5.19498	7.01363
25	2.66940	5.06273	6.90066
26	2.81770	4.92096	6.76967
27	2.96600	4.76873	6.61989
28	3.11430	4.60490	6.45078
29	3.26260	4.42825	6.26202
30	3.41090	4.23771	6.05354
31	3.55920	4.03254	5.82550
32	3.70750	3.81279	5.57826
33	3.85580	3.57948	5.31230
34	4.00410	3.33397	5.02816
35	4.15240	3.07798	4.72650
36	4.30070	2.81269	4.40803
37	4.44900	2.53937	4.07350
38	4.59730	2.25873	3.72369
39	4.74560	1.97172	3.35942
40	4.89390	1.67884	2.98147
41	5.04220	1.38062	2.59066
42	5.19050	1.07737	2.18773
43	5.33880	0.76951	1.77352
44	5.39812	0.64517	1.60482
45	5.45744	0.52020	1.43448
46	5.51676	0.39451	1.26252
47	5.57608	0.26816	1.08901
48	5.63540	0.14117	0.91397
49	5.69472	0.01364	0.73745
50	5.75404	-0.11456	0.55950
51	5.81336	-0.24329	0.38014
52	5.87268	-0.37263	0.19943
53	5.93200	0.00000	0.00000

Table 2c
Airfoil Geometry

AIRFOIL: FIRST STATOR (TIP)
PITCH (ins.): 8.53371

	LEADING EDGE	TRAILING EDGE
RADIUS (ins.)	0.44487	0.10986
METAL ANGLE (degr.)	90.00401	20.25751
WEDGE ANGLE (degr.)	31.79000	6.79000

	X(ins.)	Y_L(ins.)	Y_U(ins.)
1	0.00000	7.57702	7.57702
2	0.05932	7.35507	7.79897
3	0.11864	7.27456	7.87949
4	0.17796	7.22112	7.93293
5	0.23728	7.18355	7.97049
6	0.29660	7.15759	7.99646
7	0.35592	7.13967	8.01409
8	0.41524	7.12193	8.02987
9	0.47456	7.10338	8.04449
10	0.53388	7.08402	8.05803
11	0.59320	7.06383	8.07044
12	0.74150	7.00967	8.09615
13	0.88980	6.95010	8.11406
14	1.03810	6.88487	8.12374
15	1.18640	6.81377	8.12465
16	1.33470	6.73650	8.11627
17	1.48300	6.65274	8.09803
18	1.63130	6.56207	8.06935
19	1.77960	6.46407	8.02955
20	1.92790	6.35817	7.97793
21	2.07620	6.24376	7.91381
22	2.22450	6.12004	7.83635
23	2.37280	5.98609	7.74477
24	2.52110	5.84072	7.63818
25	2.66940	5.68263	7.51566
26	2.81770	5.51023	7.37624
27	2.96600	5.32200	7.21892
28	3.11430	5.11693	7.04264
29	3.26260	4.89526	6.84631
30	3.41090	4.65850	6.62883
31	3.55920	4.40859	6.38910
32	3.70750	4.14741	6.12648
33	3.85580	3.87650	5.84072
34	4.00410	3.59714	5.53208
35	4.15240	3.31031	5.20125
36	4.30070	3.01688	4.84935
37	4.44900	2.71730	4.47775
38	4.59730	2.41223	4.08802
39	4.74560	2.10214	3.68183
40	4.89390	1.78726	3.26080
41	5.04220	1.46798	2.82654
42	5.19050	1.14458	2.38047
43	5.33880	0.81723	1.92403
44	5.39812	0.68529	1.73880
45	5.45744	0.55272	1.55219
46	5.51676	0.41958	1.36422
47	5.57608	0.28587	1.17502
48	5.63540	0.15177	0.98458
49	5.69472	0.01698	0.79299
50	5.75404	-0.08620	0.60033
51	5.81336	-0.10950	0.40661
52	5.87268	-0.09754	0.21192
53	5.93200	0.00001	0.00001

Table 3a
Airfoil Geometry

AIRFOIL: FIRST ROTOR (HUB)
PITCH (ins.): 5.41251

	LEADING EDGE	TRAILING EDGE
RADIUS (ins.)	0.34867	0.19000
METAL ANGLE (degr.)	39.56323	25.97078
WEDGE ANGLE (degr.)	31.19000	5.31000

	X(ins.)	Y_L(ins.)	Y_U(ins.)
1	0.00000	2.86604	2.86604
2	0.06341	2.66555	3.08102
3	0.12682	2.59706	3.21151
4	0.19023	2.55545	3.33187
5	0.25364	2.53057	3.44343
6	0.31705	2.51881	3.54722
7	0.38046	2.51882	3.64406
8	0.44387	2.53062	3.73464
9	0.50728	2.55553	3.81950
10	0.57069	2.59558	3.89912
11	0.63410	2.63747	3.97388
12	0.79262	2.73147	4.14166
13	0.95115	2.81137	4.28528
14	1.10967	2.87832	4.40773
15	1.26820	2.93322	4.51126
16	1.42672	2.97676	4.59755
17	1.58525	3.00948	4.66791
18	1.74377	3.03180	4.72339
19	1.90230	3.04408	4.76477
20	2.06082	3.04653	4.79267
21	2.21935	3.03939	4.80757
22	2.37787	3.02278	4.80981
23	2.53640	2.99681	4.79963
24	2.69492	2.96157	4.77715
25	2.85345	2.91708	4.74242
26	3.01197	2.86339	4.69537
27	3.17050	2.80050	4.63584
28	3.32902	2.72831	4.56359
29	3.48755	2.64670	4.47823
30	3.64607	2.55547	4.37924
31	3.80460	2.45445	4.26599
32	3.96312	2.34348	4.13761
33	4.12165	2.22234	3.99304
34	4.28017	2.09081	3.83080
35	4.43870	1.94860	3.64903
36	4.59722	1.79535	3.44572
37	4.75575	1.63070	3.21968
38	4.91427	1.45405	2.97070
39	5.07280	1.26487	2.69996
40	5.23132	1.06245	2.40938
41	5.38985	0.84595	2.10143
42	5.54837	0.61435	1.77875
43	5.70690	0.36649	1.44378
44	5.77031	0.26245	1.30685
45	5.83372	0.15541	1.16841
46	5.89713	0.04543	1.02861
47	5.96054	-0.06777	0.88753
48	6.02395	-0.16117	0.74527
49	6.08736	-0.19892	0.60194
50	6.15077	-0.20989	0.45759
51	6.21418	-0.19908	0.31233
52	6.27759	-0.16158	0.16622
53	6.34100	-0.01989	-0.01989

Table 3b
Airfoil Geometry

AIRFOIL: FIRST ROTOR (MIDSPAN)
PITCH (ins.): 6.05879

	LEADING EDGE	TRAILING EDGE
RADIUS (ins.)	0.34872	0.19000
METAL ANGLE (degr.)	42.18646	25.97093
WEDGE ANGLE (degr.)	31.24000	5.31000

	X(ins.)	Y_L(ins.)	Y_U(ins.)
1	0.00000	3.41970	3.41970
2	0.06341	3.21919	3.62774
3	0.12682	3.15069	3.74347
4	0.19023	3.10908	3.84906
5	0.25364	3.08419	3.94593
6	0.31705	3.07242	4.03518
7	0.38046	3.07243	4.11769
8	0.44387	3.08422	4.19414
9	0.50728	3.10912	4.26511
10	0.57069	3.14694	4.33106
11	0.63410	3.18401	4.39238
12	0.79262	3.26583	4.52752
13	0.95115	3.33349	4.63984
14	1.10967	3.38822	4.73220
15	1.26820	3.43094	4.80674
16	1.42672	3.46228	4.86506
17	1.58525	3.48271	4.90837
18	1.74377	3.49248	4.93760
19	1.90230	3.49176	4.95347
20	2.06082	3.48053	4.95652
21	2.21935	3.45868	4.94712
22	2.37787	3.42596	4.92555
23	2.53640	3.38201	4.89193
24	2.69492	3.32633	4.84632
25	2.85345	3.25830	4.78863
26	3.01197	3.17735	4.71868
27	3.17050	3.08283	4.63616
28	3.32902	2.97433	4.54063
29	3.48755	2.85162	4.43151
30	3.64607	2.71488	4.30799
31	3.80460	2.56463	4.16905
32	3.96312	2.40136	4.01334
33	4.12165	2.22577	3.83912
34	4.28017	2.03852	3.64406
35	4.43870	1.84022	3.42595
36	4.59722	1.63139	3.18387
37	4.75575	1.41252	2.91861
38	4.91427	1.18402	2.63221
39	5.07280	0.94623	2.32774
40	5.23132	0.69955	2.00832
41	5.38985	0.44403	1.67680
42	5.54837	0.18008	1.33571
43	5.70690	-0.09214	0.98699
44	5.77031	-0.20337	0.84573
45	5.83372	-0.31578	0.70359
46	5.89713	-0.42949	0.56065
47	5.96054	-0.54448	0.41698
48	6.02395	-0.63800	0.27261
49	6.08736	-0.67575	0.12765
50	6.15077	-0.68673	-0.01791
51	6.21418	-0.67591	-0.16397
52	6.27759	-0.63841	-0.31052
53	6.34100	-0.49672	-0.49672

Table 3c
Airfoil Geometry

AIRFOIL: FIRST ROTOR (TIP)
PITCH (ins.): 6.70506

	LEADING EDGE	TRAILING EDGE
RADIUS (ins.)	0.34881	0.19000
METAL ANGLE (degr.)	46.66805	25.96767
WEDGE ANGLE (degr.)	31.26000	5.31000

	X(ins.)	Y_L(ins.)	Y_U(ins.)
1	0.00000	3.97348	3.97348
2	0.06341	3.77294	4.17548
3	0.12682	3.70443	4.27381
4	0.19023	3.66280	4.36353
5	0.25364	3.63790	4.44573
6	0.31705	3.62612	4.52127
7	0.38046	3.62611	4.59084
8	0.44387	3.63787	4.65499
9	0.50728	3.66275	4.71419
10	0.57069	3.69488	4.76883
11	0.63410	3.72462	4.81924
12	0.79262	3.78887	4.92848
13	0.95115	3.83974	5.01637
14	1.10967	3.87814	5.08539
15	1.26820	3.90472	5.13737
16	1.42672	3.91989	5.17369
17	1.58525	3.92388	5.19537
18	1.74377	3.91674	5.20321
19	1.90230	3.89838	5.19778
20	2.06082	3.86851	5.17950
21	2.21935	3.82665	5.14862
22	2.37787	3.77210	5.10529
23	2.53640	3.70385	5.04954
24	2.69492	3.62049	4.98122
25	2.85345	3.52015	4.90012
26	3.01197	3.40033	4.80585
27	3.17050	3.25903	4.69788
28	3.32902	3.09581	4.57543
29	3.48755	2.91352	4.43757
30	3.64607	2.71577	4.28296
31	3.80460	2.50562	4.10990
32	3.96312	2.28505	3.91608
33	4.12165	2.05587	3.69853
34	4.28017	1.81890	3.45544
35	4.43870	1.57520	3.18730
36	4.59722	1.32521	2.89675
37	4.75575	1.06966	2.58780
38	4.91427	0.80884	2.26420
39	5.07280	0.54319	1.92951
40	5.23132	0.27306	1.58629
41	5.38985	-0.00136	1.23664
42	5.54837	-0.27975	0.88207
43	5.70690	-0.56201	0.52368
44	5.77031	-0.67597	0.37945
45	5.83372	-0.79046	0.23478
46	5.89713	-0.90562	0.08974
47	5.96054	-1.02119	-0.05569
48	6.02395	-1.11481	-0.20147
49	6.08736	-1.15257	-0.34753
50	6.15077	-1.16355	-0.49387
51	6.21418	-1.15274	-0.64045
52	6.27759	-1.11524	-0.78728
53	6.34100	-0.97355	-0.97355

Table 4a
Airfoil Geometry

AIRFOIL: SECOND STATOR (HUB)
PITCH (ins.): 5.41251

	LEADING EDGE	TRAILING EDGE
RADIUS (ins.)	0.34999	0.19000
METAL ANGLE (degr.)	41.01068	24.98619
WEDGE ANGLE (degr.)	29.91000	8.91000

	X(ins.)	Y_L(ins.)	Y_U(ins.)
1	0.00000	3.68263	3.68263
2	0.06452	3.48015	3.89472
3	0.12904	3.41120	4.01869
4	0.19356	3.36955	4.13494
5	0.25808	3.34493	4.24410
6	0.32260	3.33372	4.34672
7	0.38712	3.33462	4.44324
8	0.45164	3.34773	4.53408
9	0.51616	3.37461	4.61958
10	0.58068	3.41583	4.70006
11	0.64520	3.45739	4.77578
12	0.80650	3.55269	4.94580
13	0.96780	3.63560	5.09069
14	1.12910	3.70599	5.21287
15	1.29040	3.76376	5.31424
16	1.45170	3.80880	5.39634
17	1.61300	3.84106	5.46037
18	1.77430	3.86048	5.50735
19	1.93560	3.86704	5.53806
20	2.09690	3.86072	5.55317
21	2.25820	3.84153	5.55319
22	2.41950	3.80950	5.53852
23	2.58080	3.76468	5.50948
24	2.74210	3.70714	5.46629
25	2.90340	3.63698	5.40908
26	3.06470	3.55430	5.33790
27	3.22600	3.45921	5.25273
28	3.38730	3.35188	5.15348
29	3.54860	3.23245	5.03995
30	3.70990	3.10111	4.91189
31	3.87120	2.95802	4.76892
32	4.03250	2.80339	4.61058
33	4.19380	2.63745	4.43628
34	4.35510	2.46037	4.24527
35	4.51640	2.27244	4.03662
36	4.67770	2.07384	3.80928
37	4.83900	1.86483	3.56222
38	5.00030	1.64569	3.29479
39	5.16160	1.41663	3.00662
40	5.32290	1.17789	2.69784
41	5.48420	0.92975	2.36890
42	5.64550	0.67246	2.02068
43	5.80680	0.40629	1.65431
44	5.87132	0.29738	1.50296
45	5.93584	0.18710	1.34900
46	6.00036	0.07548	1.19252
47	6.06488	-0.03748	1.03361
48	6.12940	-0.13608	0.87238
49	6.19392	-0.17738	0.70890
50	6.25844	-0.18997	0.54327
51	6.32296	-0.17996	0.37560
52	6.38748	-0.14267	0.20595
53	6.45200	0.00000	0.00000

Table 4b
Airfoil Geometry

AIRFOIL: SECOND STATOR (MIDSPAN)
PITCH (ins.): 6.05879

	LEADING EDGE	TRAILING EDGE
RADIUS (ins.)	0.34999	0.19000
METAL ANGLE (degr.)	45.66800	25.00000
WEDGE ANGLE (degr.)	27.50000	6.50000

	X(ins.)	Y_L(ins.)	Y_U(ins.)
1	0.00000	4.10291	4.10291
2	0.06452	3.47786	4.30650
3	0.12904	3.52885	4.40610
4	0.19356	3.57793	4.50013
5	0.25808	3.62510	4.58895
6	0.32260	3.67035	4.67285
7	0.38712	3.71368	4.75210
8	0.45164	3.75508	4.82695
9	0.51616	3.79454	4.89760
10	0.58068	3.83206	4.96425
11	0.64520	3.86762	5.02707
12	0.80650	3.94796	5.16834
13	0.96780	4.01599	5.28865
14	1.12910	4.07162	5.38963
15	1.29040	4.11482	5.47259
16	1.45170	4.14552	5.53859
17	1.61300	4.16371	5.58849
18	1.77430	4.16934	5.62296
19	1.93560	4.16244	5.64258
20	2.09690	4.14298	5.64778
21	2.25820	4.11101	5.63888
22	2.41950	4.06655	5.61615
23	2.58080	4.00965	5.57973
24	2.74210	3.94037	5.52972
25	2.90340	3.85879	5.46611
26	3.06470	3.76498	5.38882
27	3.22600	3.65906	5.29771
28	3.38730	3.54111	5.19255
29	3.54860	3.41127	5.07300
30	3.70990	3.26967	4.93863
31	3.87120	3.11644	4.78891
32	4.03250	2.95172	4.62316
33	4.19380	2.77568	4.44053
34	4.35510	2.58849	4.24001
35	4.51640	2.39030	4.02052
36	4.67770	2.18130	3.78134
37	4.83900	1.96166	3.52218
38	5.00030	1.73160	3.24330
39	5.16160	1.49128	2.94535
40	5.32290	1.24090	2.62941
41	5.48420	0.98064	2.29682
42	5.64550	0.71074	1.94914
43	5.80680	0.43141	1.58790
44	5.87132	0.31707	1.43996
45	5.93584	0.20126	1.29018
46	6.00036	0.08400	1.13867
47	6.06488	-0.03471	0.98552
48	6.12940	-0.15484	0.83080
49	6.19392	-0.27639	0.67459
50	6.25844	-0.39934	0.51699
51	6.32296	-0.52368	0.35805
52	6.38748	-0.64939	0.19786
53	6.45200	0.00000	0.00000

Table 4c
Airfoil Geometry

AIRFOIL: SECOND STATOR (TIP)
PITCH (ins.): 6.70506

	LEADING EDGE	TRAILING EDGE
RADIUS (ins.)	0.35006	0.19000
METAL ANGLE (degr.)	50.49115	24.98778
WEDGE ANGLE (degr.)	25.12000	4.09000

	X(ins.)	Y_L(ins.)	Y_U(ins.)
1	0.00000	4.53429	4.53429
2	0.06452	4.33178	4.73679
3	0.12904	4.26282	4.81836
4	0.19356	4.22116	4.89463
5	0.25808	4.19652	4.96641
6	0.32260	4.18530	5.03396
7	0.38712	4.18619	5.09751
8	0.45164	4.19929	5.15728
9	0.51616	4.22602	5.21343
10	0.58068	4.25762	5.26613
11	0.64520	4.28729	5.31552
12	0.80650	4.35297	5.42538
13	0.96780	4.40647	5.51708
14	1.12910	4.44777	5.59199
15	1.29040	4.47683	5.65117
16	1.45170	4.49364	5.69551
17	1.61300	4.49819	5.72567
18	1.77430	4.49045	5.74219
19	1.93560	4.47047	5.74550
20	2.09690	4.43822	5.73590
21	2.25820	4.39375	5.71360
22	2.41950	4.33706	5.67874
23	2.58080	4.26823	5.63135
24	2.74210	4.18728	5.57140
25	2.90340	4.09426	5.49876
26	3.06470	3.98924	5.41323
27	3.22600	3.87229	5.31449
28	3.38730	3.74348	5.20215
29	3.54860	3.60289	5.07566
30	3.70990	3.45062	4.93435
31	3.87120	3.28675	4.77738
32	4.03250	3.11139	4.60366
33	4.19380	2.92465	4.41196
34	4.35510	2.72666	4.20118
35	4.51640	2.51749	3.97077
36	4.67770	2.29731	3.72077
37	4.83900	2.06620	3.45177
38	5.00030	1.82436	3.16495
39	5.16160	1.57187	2.86176
40	5.32290	1.30889	2.54389
41	5.48420	1.03553	2.21304
42	5.64550	0.75199	1.87091
43	5.80680	0.45841	1.51902
44	5.87132	0.33818	1.37585
45	5.93584	0.21639	1.23140
46	6.00036	0.09302	1.08577
47	6.06488	-0.03190	0.93902
48	6.12940	-0.13607	0.79122
49	6.19392	-0.17738	0.64244
50	6.25844	-0.18996	0.49272
51	6.32296	-0.17995	0.34214
52	6.38748	-0.14267	0.19073
53	6.45200	0.00000	0.00000

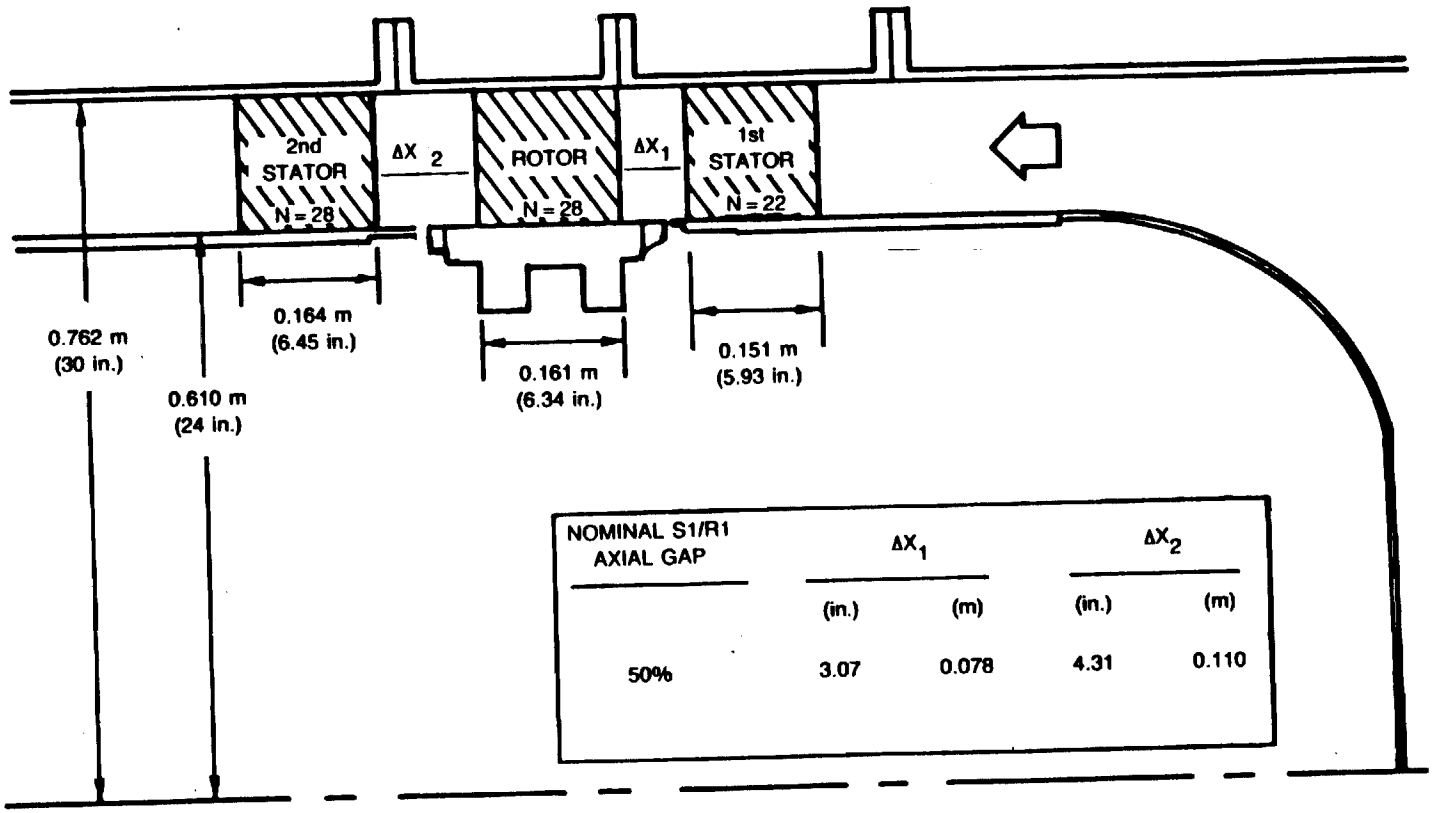

NOMINAL S1/R1 AXIAL GAP	ΔX_1		ΔX_2	
	(in.)	(m)	(in.)	(m)
50%	3.07	0.078	4.31	0.110

Figure 1 United Technologies Research Center Large Scale Rotating Rig

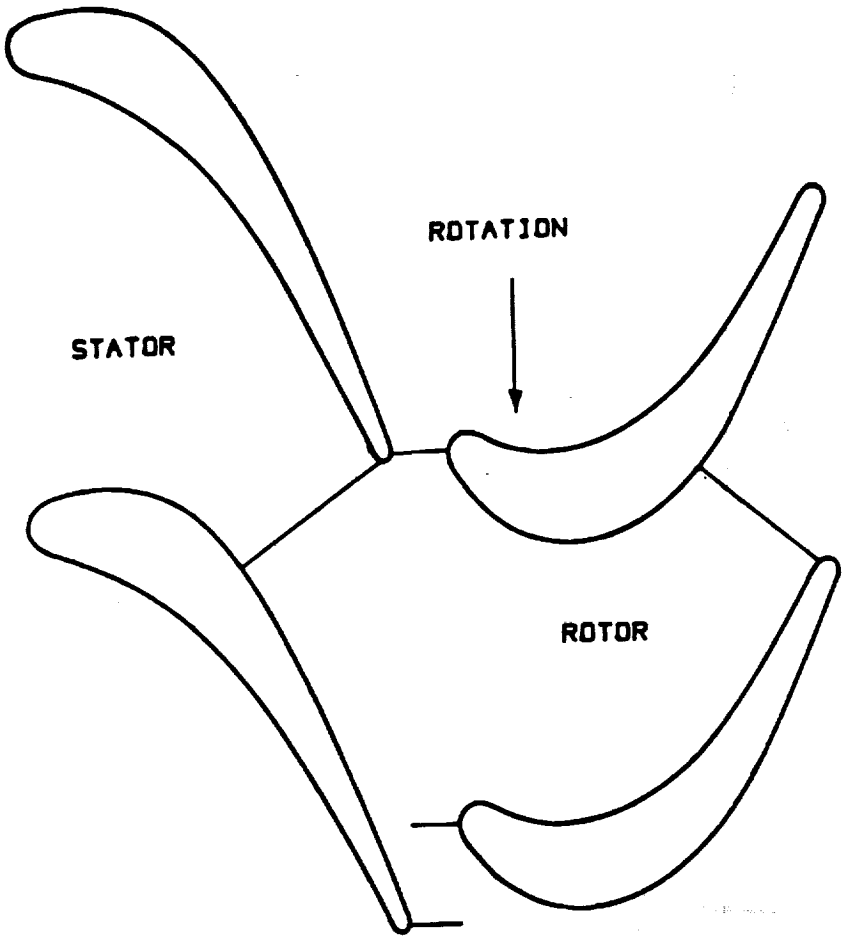

Figure 2 Turbine Stage at Mid Span

ORIGINAL PAGE
BLACK AND WHITE PHOTOGRAPH

(First Vane and Rotor Case Removed)

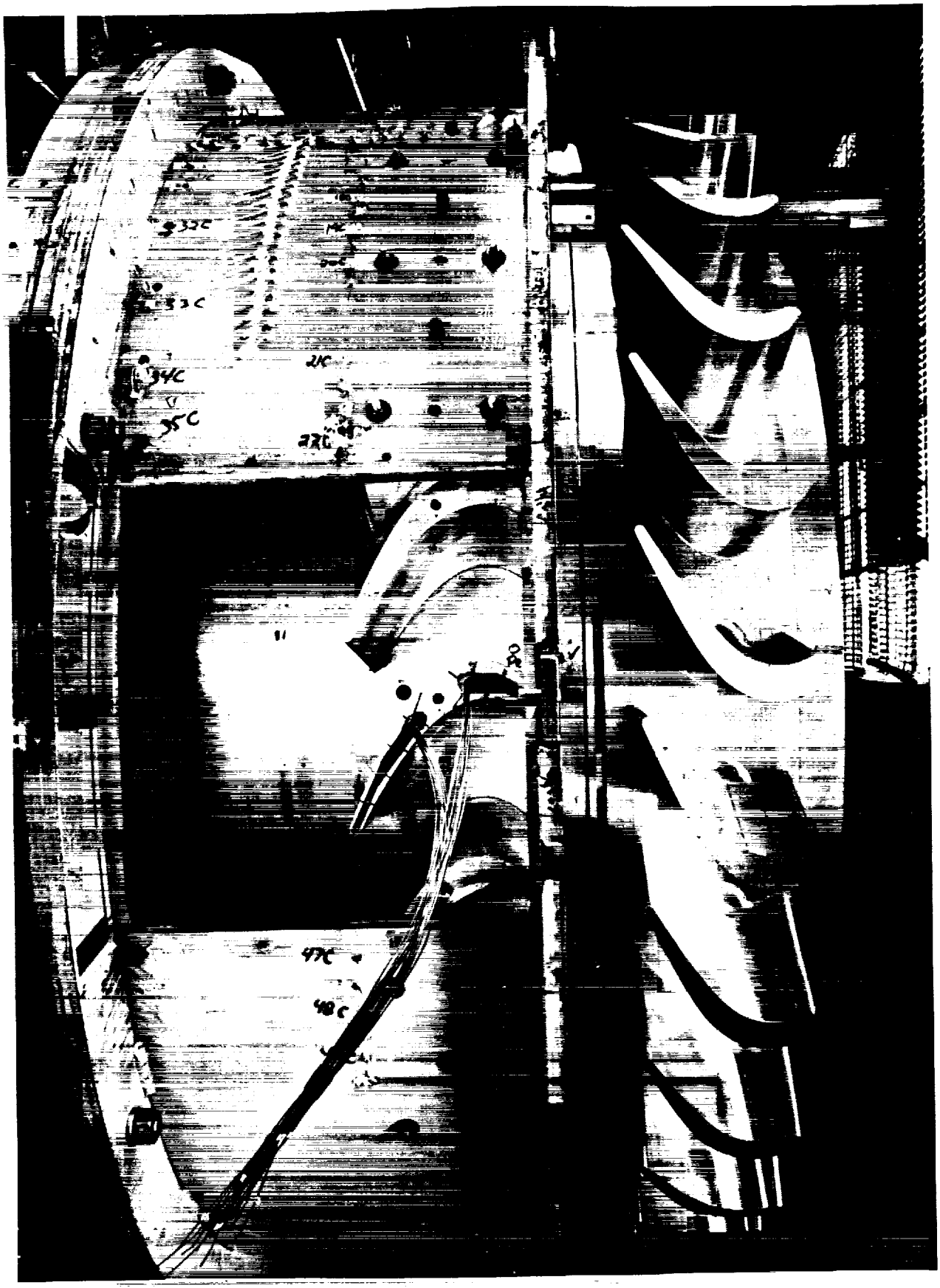

Figure 3 Large Scale Rotating Rig 1 1/2 Stage Turbine Configuration

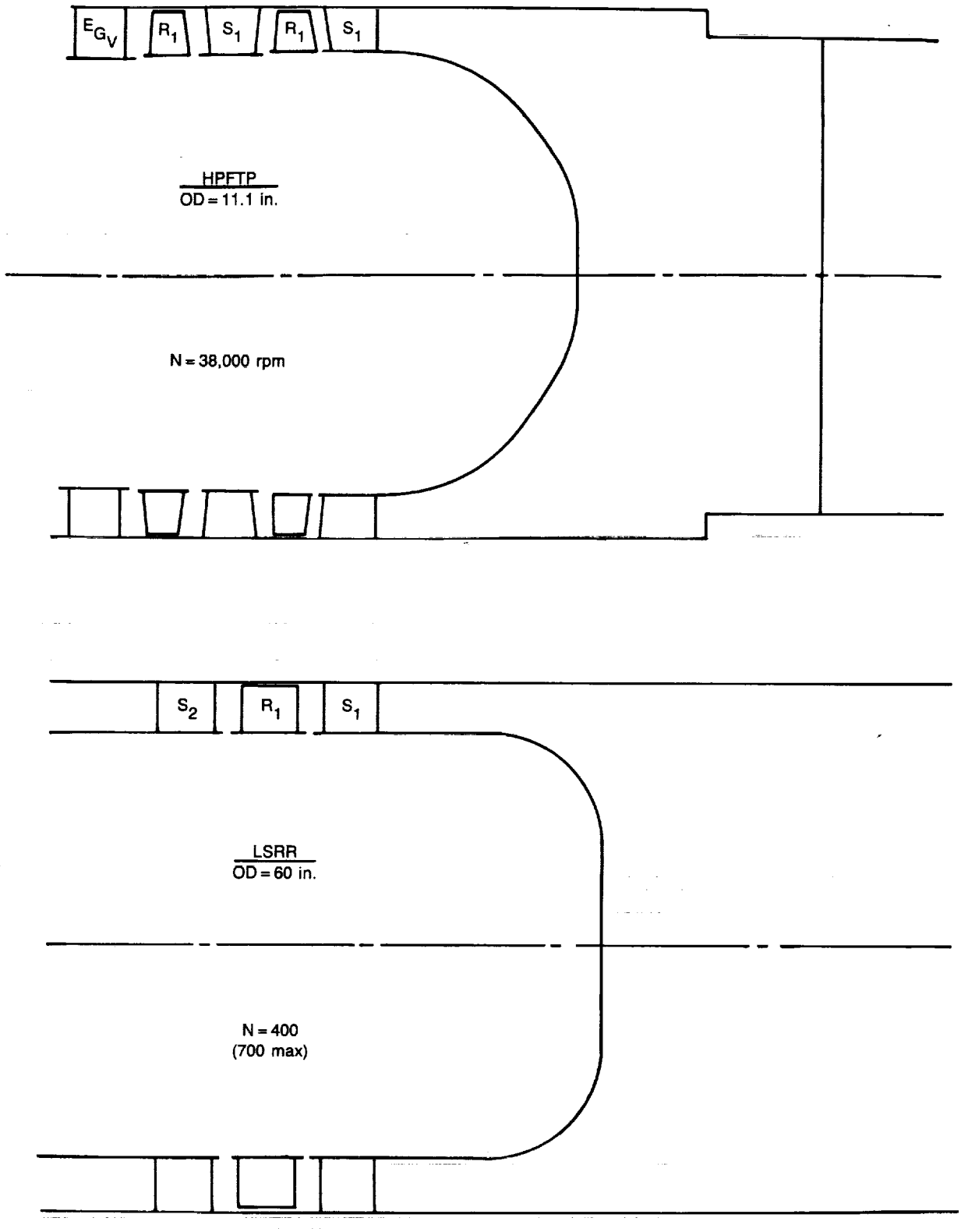

Figure 4 Comparison of the UTRC/LSRR and the SSME/HPFTP Drive Turbine

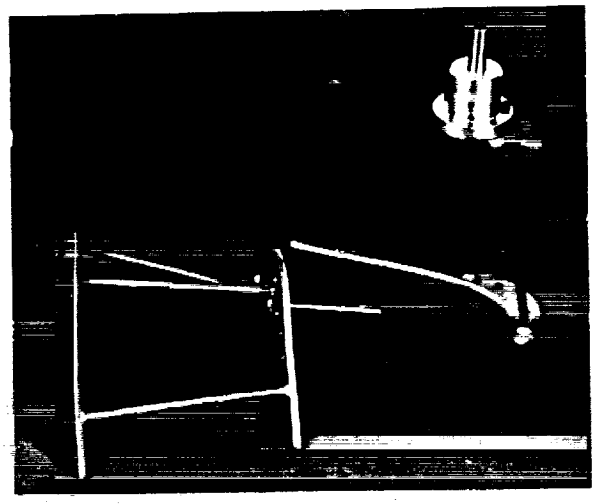

STEEL SKELETONS

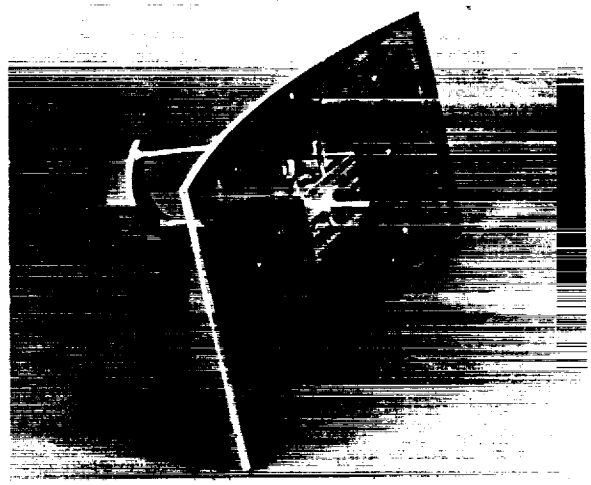

SKELETON MOUNTED IN ALIGNMENT BRACKET (VIEW FROM ROOT)

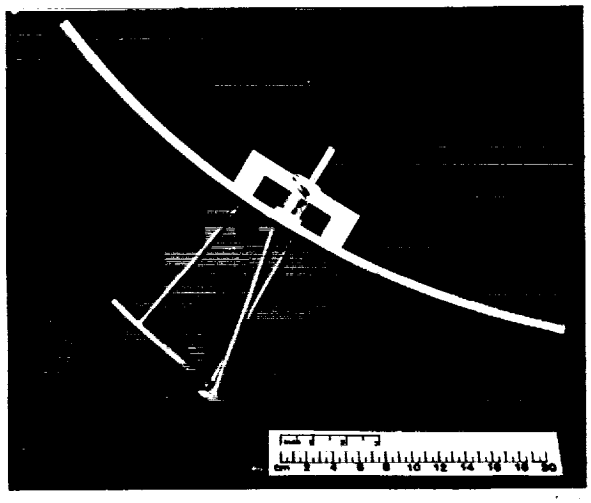

SKELETON MOUNTED IN ALIGNMENT BRACKET (VIEW FROM LEADING EDGE)

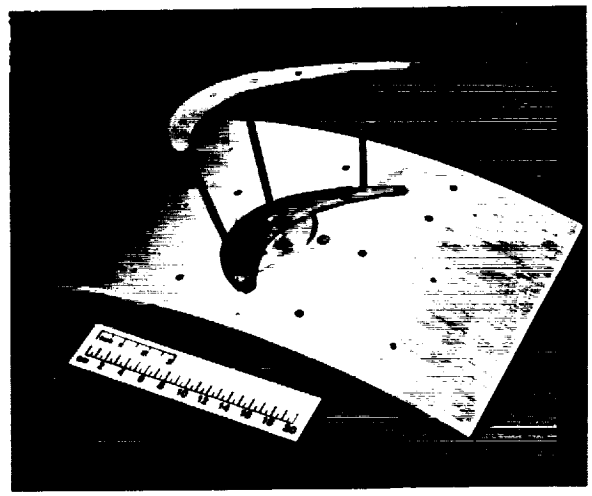

SKELETON MOUNTED IN ALIGNMENT BRACKET (VIEW FROM TIP)

Figure 5 Stages of Rotor Airfoil Fabrication

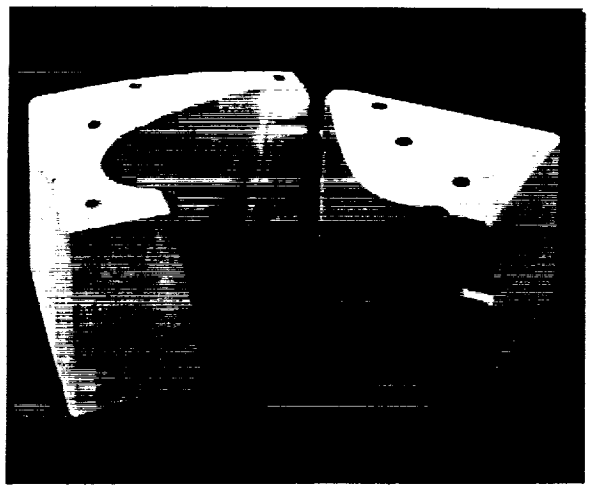

ROTOR AIRFOIL MOLD

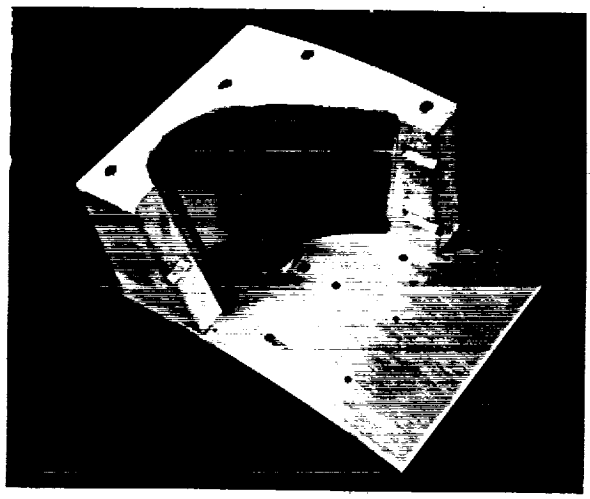

STEEL SKELETON – MOLD ASSEMBLY

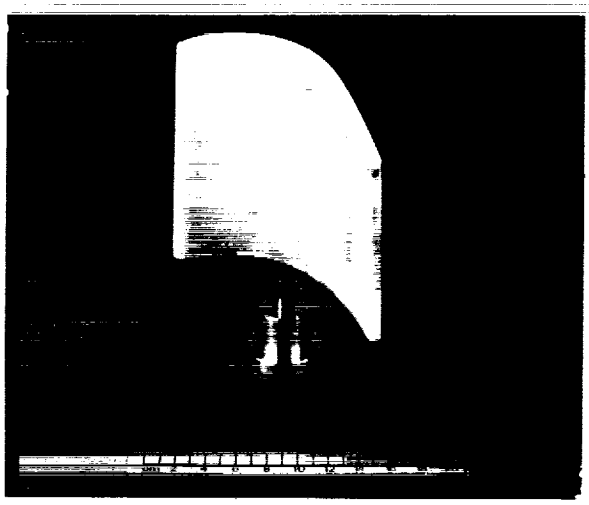

CAST FOAM AIRFOIL (VIEW FROM PRESSURE SURFACE)

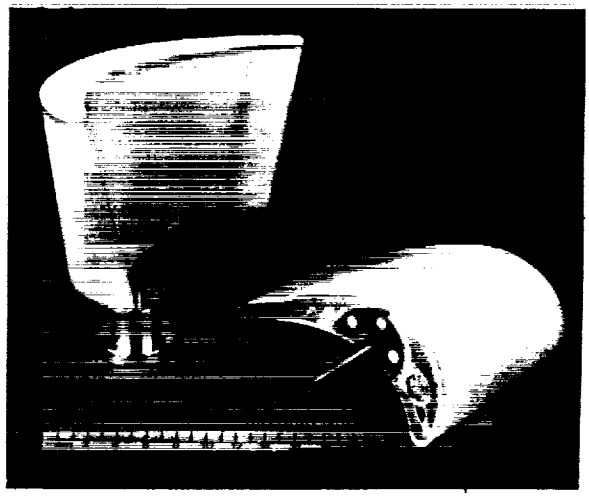

CAST FOAM AIRFOILS

Figure 6 Stages of Rotor Airfoil Fabrication

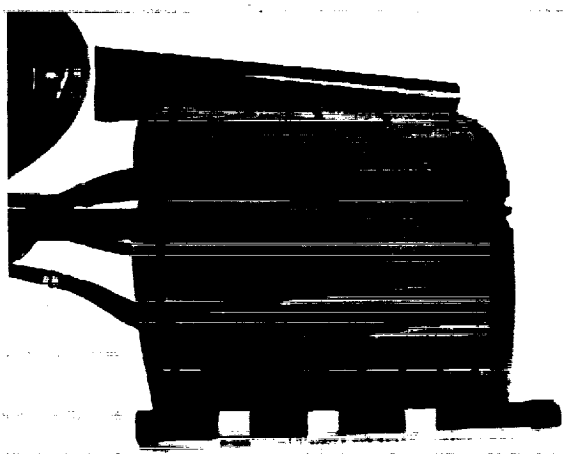

VIEW OF FORE-CHORD
INSTRUMENTATION ROUTING

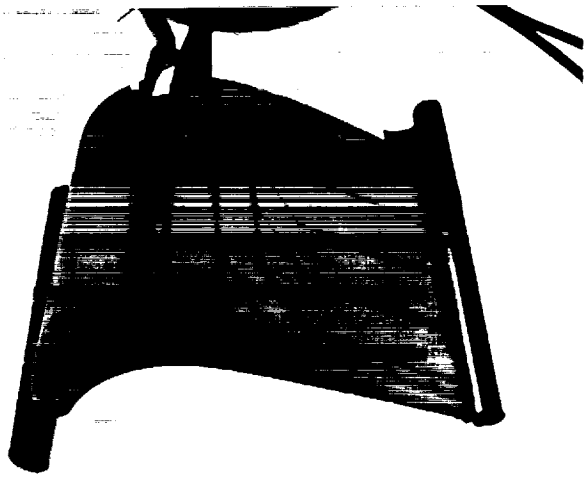

VIEW OF AFT-CHORD
INSTRUMENTATION ROUTING

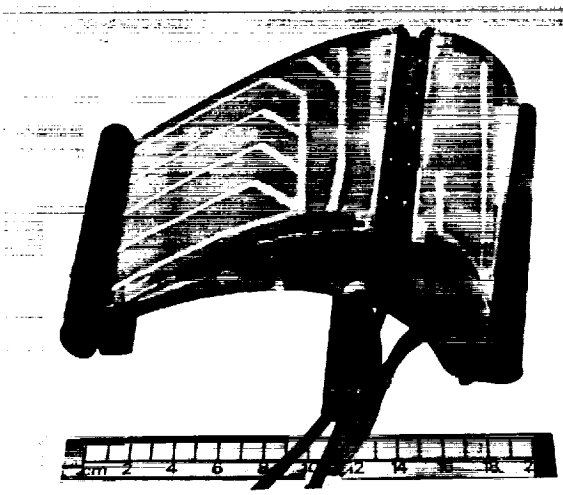

AIRFOIL MODEL WITH INSTRUMENTATION
ROUTING FILLED

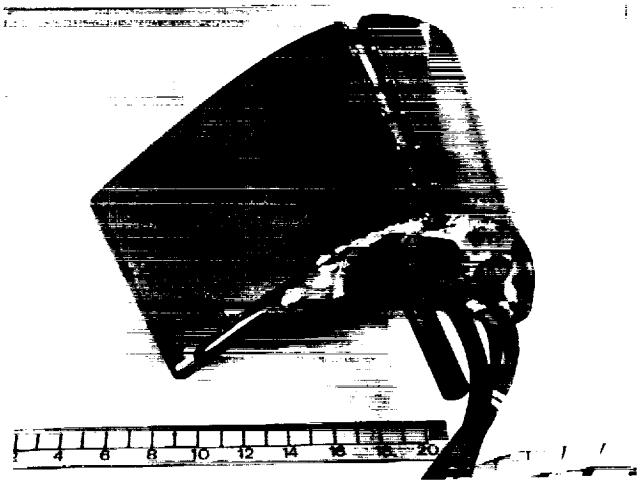

AIRFOIL MODEL WITH COMPLETED
FOIL INSTALLATION

Figure 7 Stages of Pressure Surface Airfoil Instrumentation

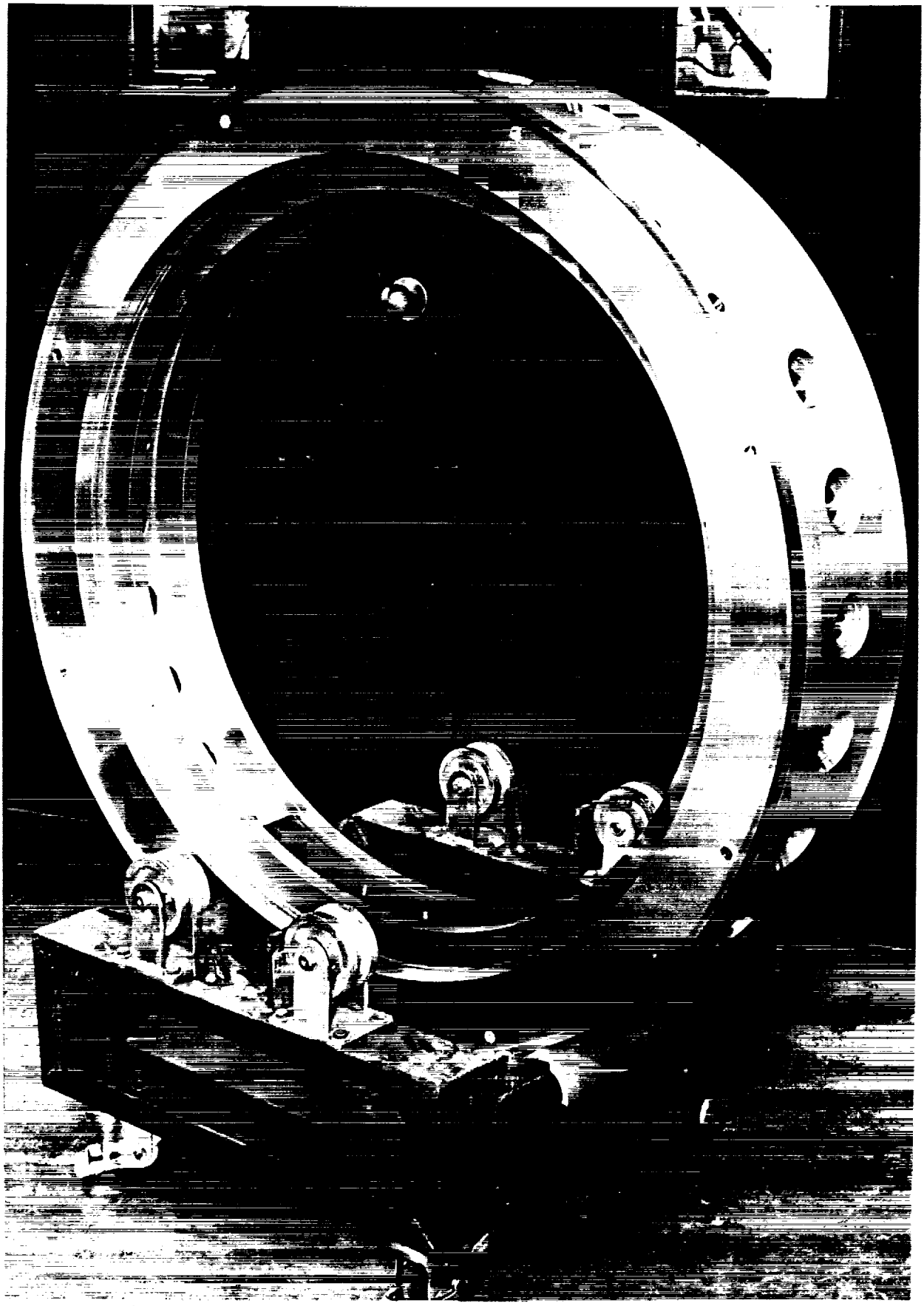

Figure 8 Rotor Hub Showing Endwall Heat Transfer Region

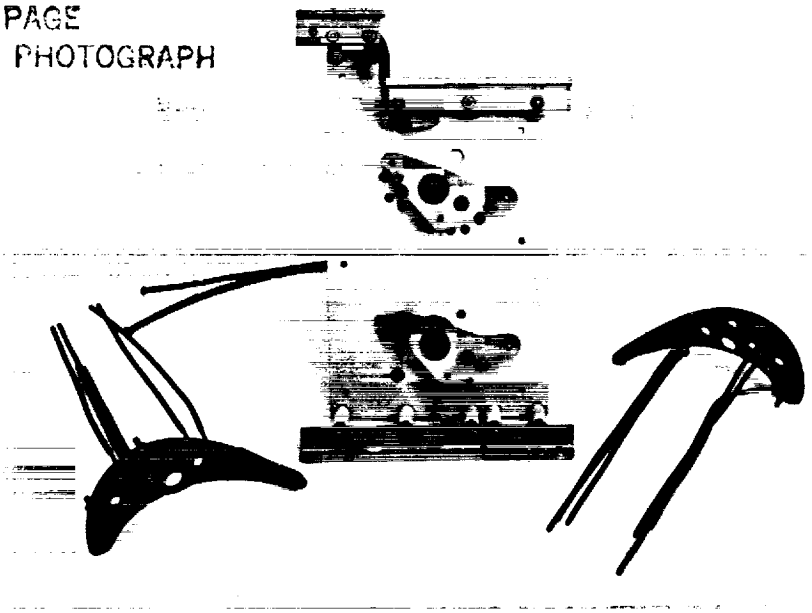

ENDWALL MODEL COMPONENTS

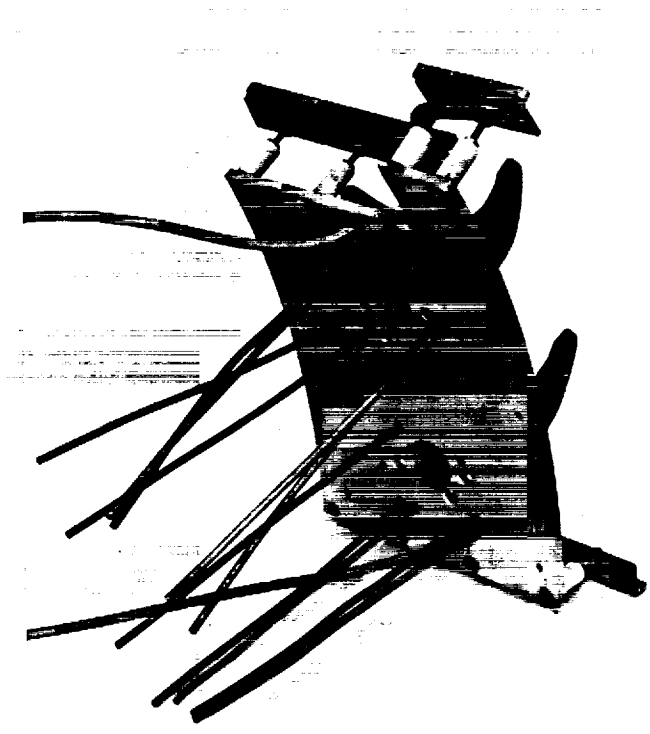

ENDWALL MODEL ASSEMBLY
BOTTOM VIEW

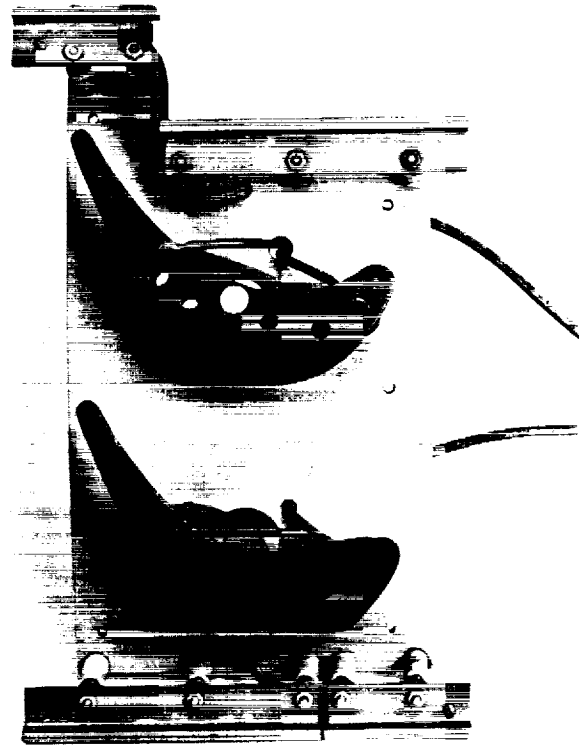

ENDWALL MODEL ASSEMBLY
TOP VIEW

Figure 9 Endwall Model Assembly Prior to Casting

88-268B
88-268C
88-268A

88-7-14-1

ORIGINAL PAGE
BLACK AND WHITE PHOTOGRAPH

CUTOUT REGION OF ROTOR HUB

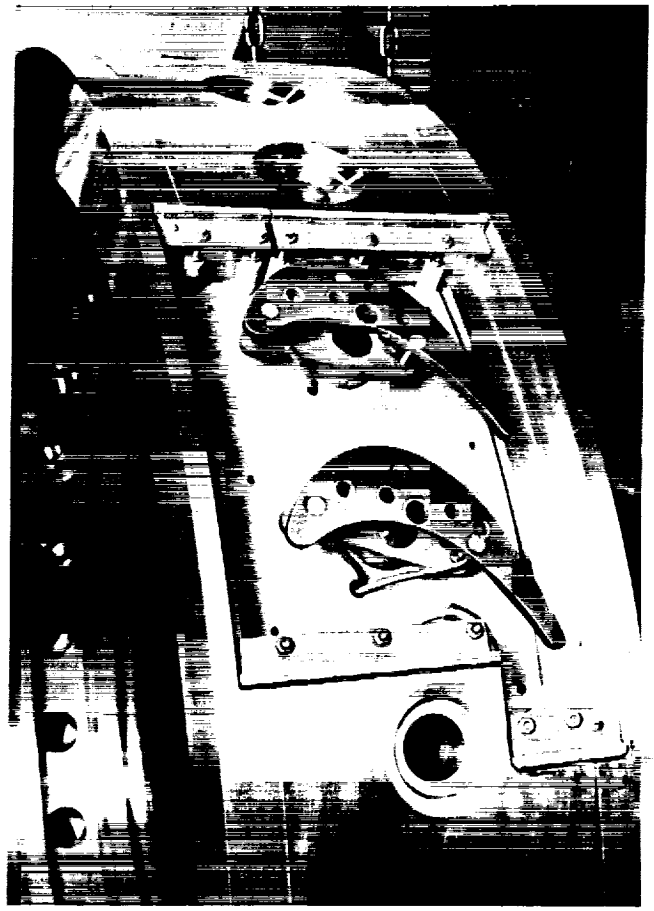

ENDWALL MODEL ASSEMBLY
INSTALLED IN HUB CUTOUT

Figure 10 Endwall Model Installation In Rotor Hub

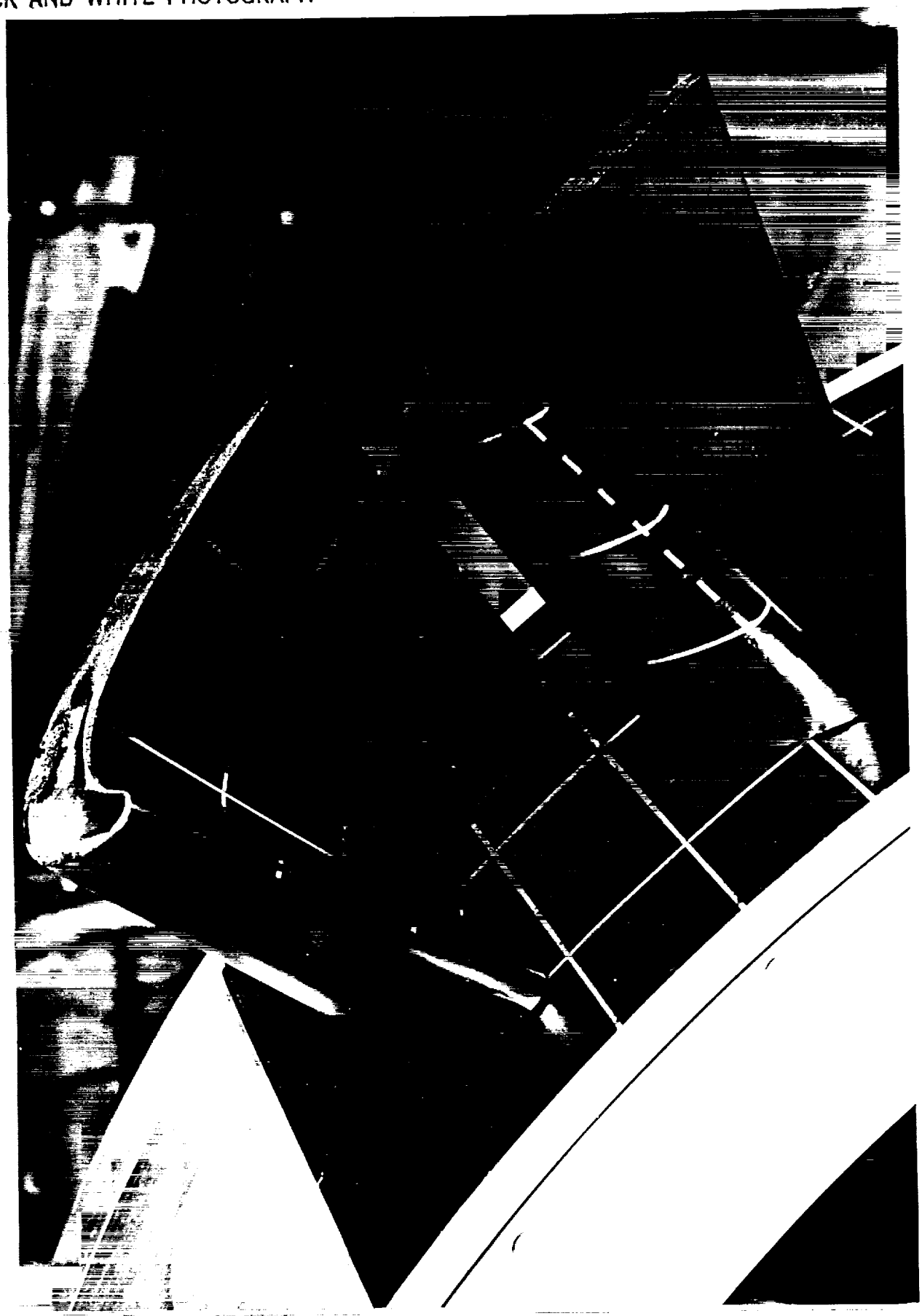

Figure 11 Airfoil and Endwall Heat Transfer Models Installed in Rotor Hub — the Bench-Test Model for Evaluating Liquid-Crystal Techniques

Figure 12 Rotor Passage Heat Transfer Model with Surface Roughness Grit

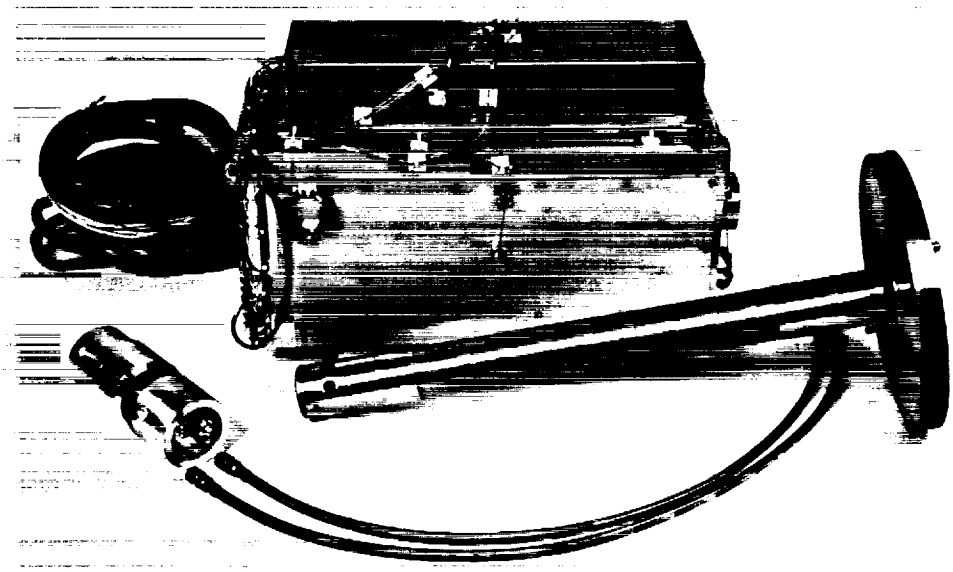

SLIP RING, MOUNTING ARBOR AND ROTARY UNION

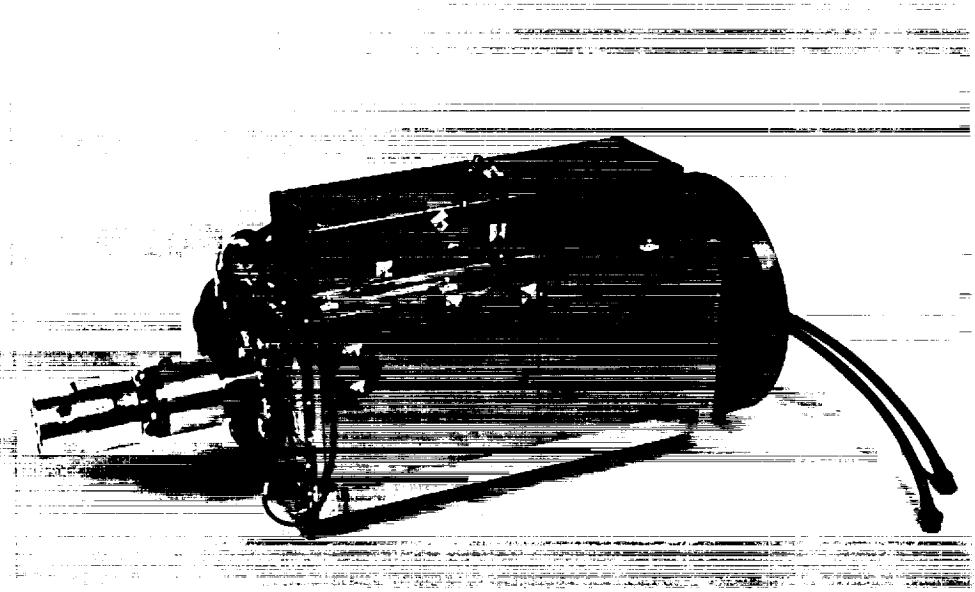

ASSEMBLED UNIT READY FOR INSTALLATION INTO LSRR

Figure 13 Slip Ring — Rotary Union Assembly

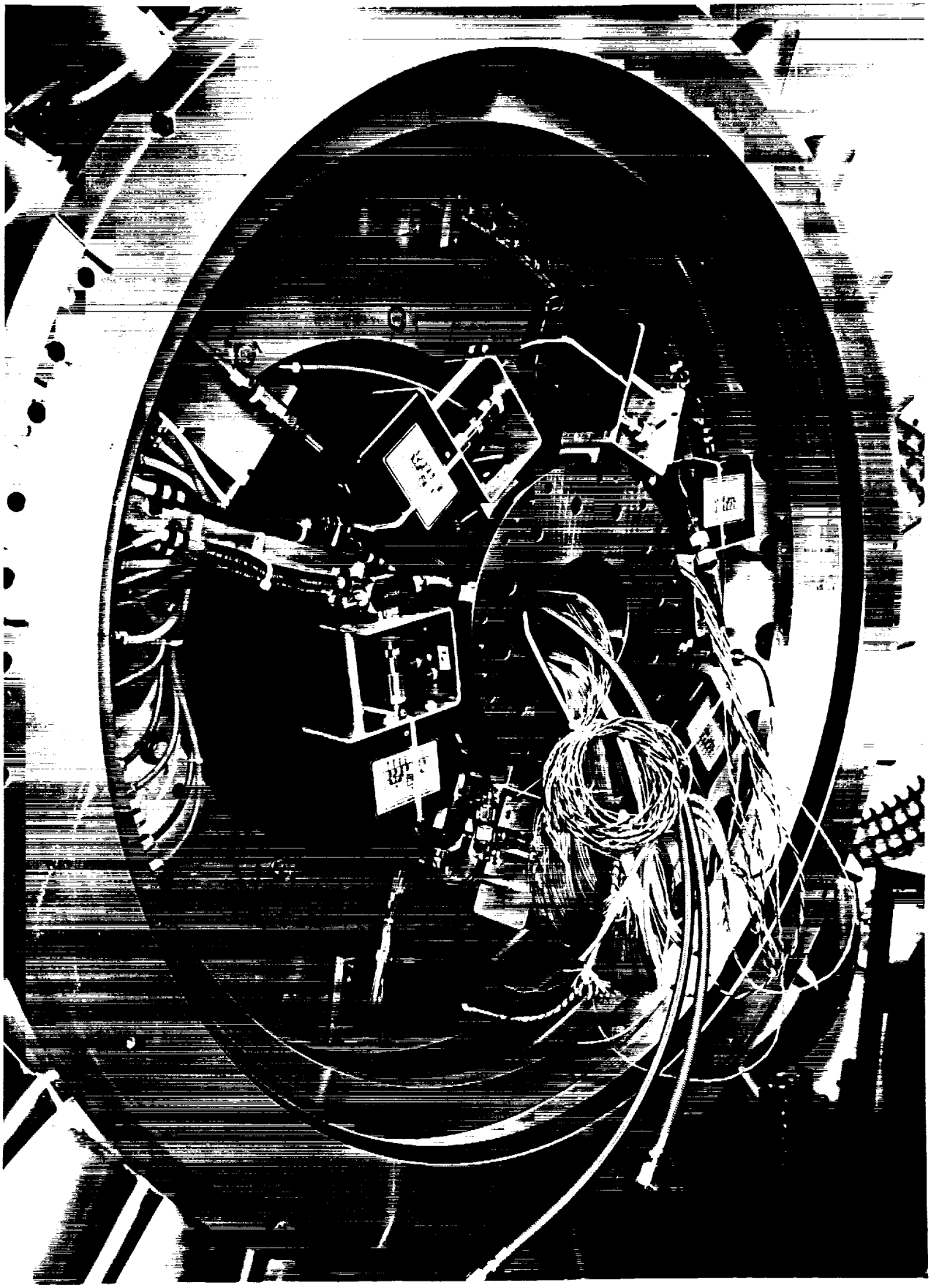

Figure 14 Rotor Instrumentation Prior to Installation of Slip-ring - Note Remote Control Valves and Heat Transfer Model Wiring

89-37-7

89-2-20-1

ORIGINAL PAGE
BLACK AND WHITE PHOTOGRAPH

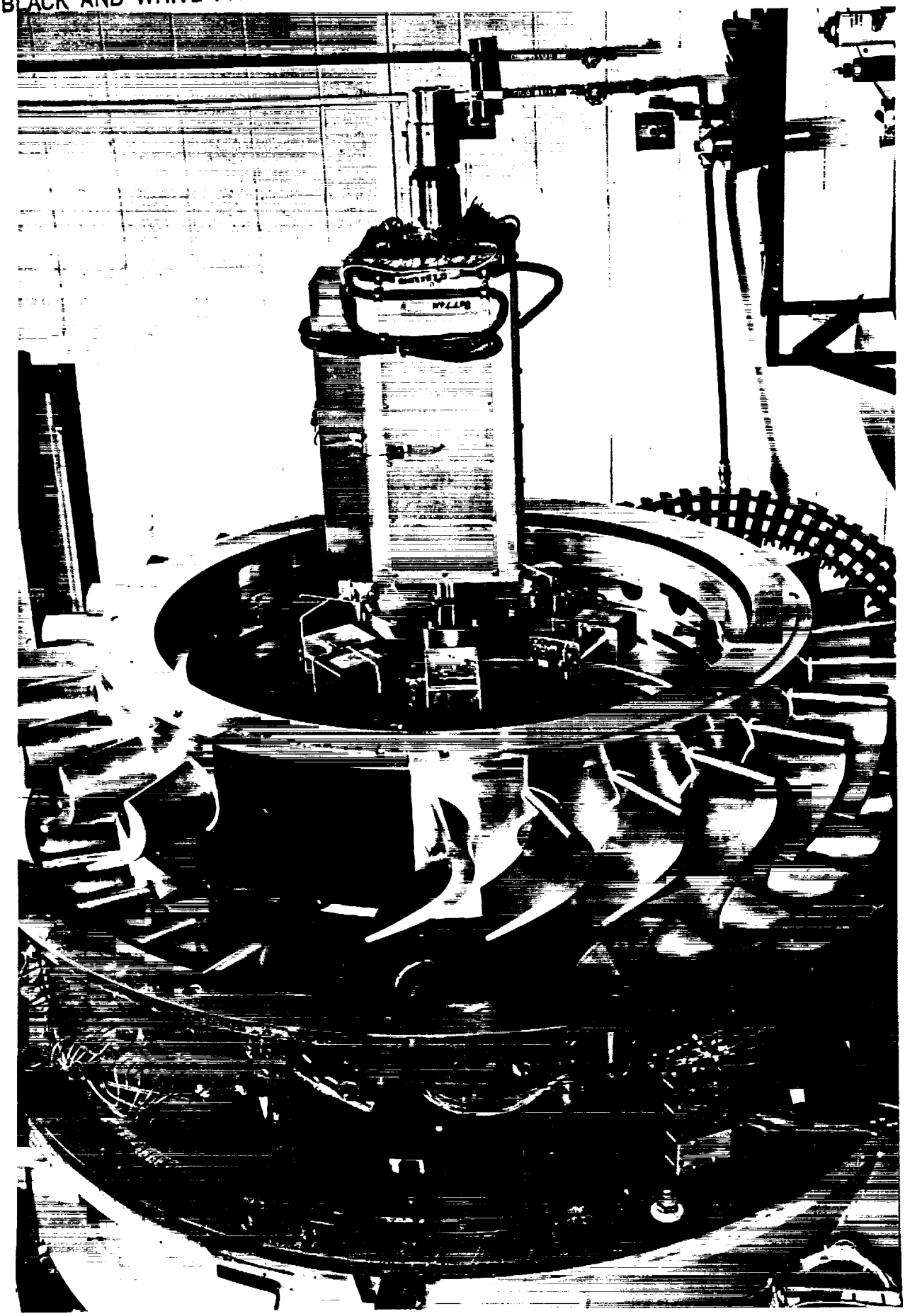

89-37B-10

Figure 15 LSRR Rotor with Case Removed -- Slip-ring Installed - Note Heat Transfer Model Installed

89-2-20-2

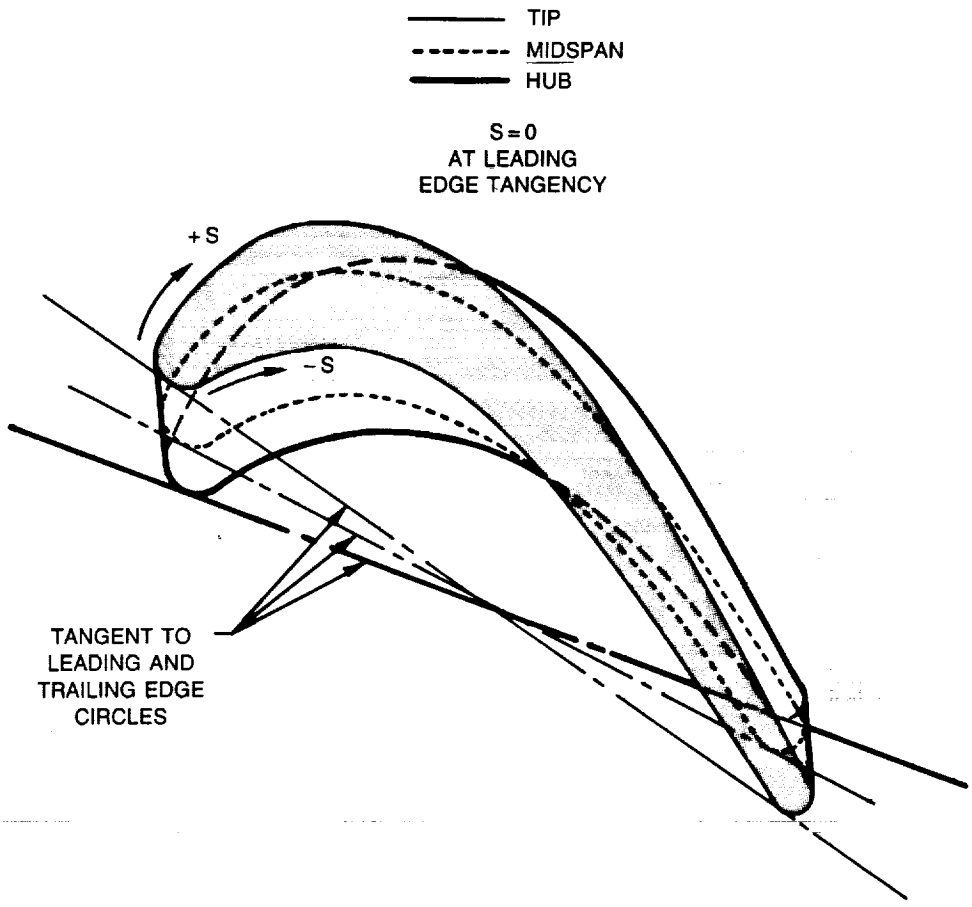

Figure 16 Diagram of Surface Distance (s) Nomenclature

LEADING EDGE-PRESSURE
SURFACE VIEW

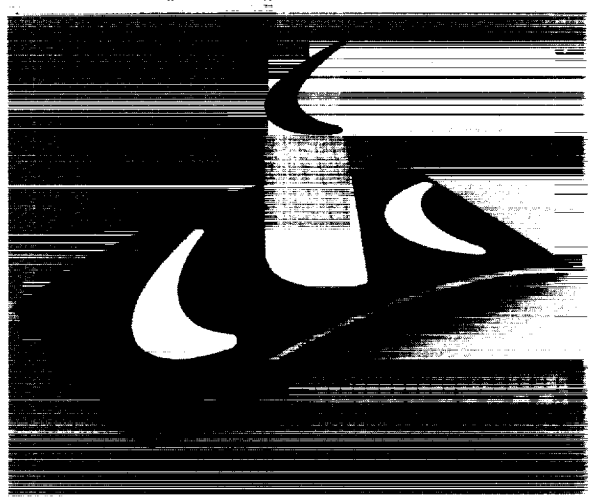

LEADING EDGE-SUCTION
SURFACE VIEW

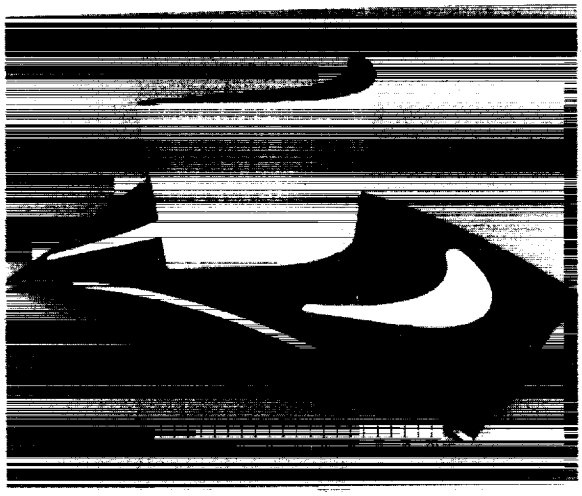

TRAILING EDGE-SUCTION
SURFACE VIEW

TRAILING EDGE-PRESSURE
SURFACE VIEW

Figure 17 Rotor Airfoil Instrumentation Coordinate System

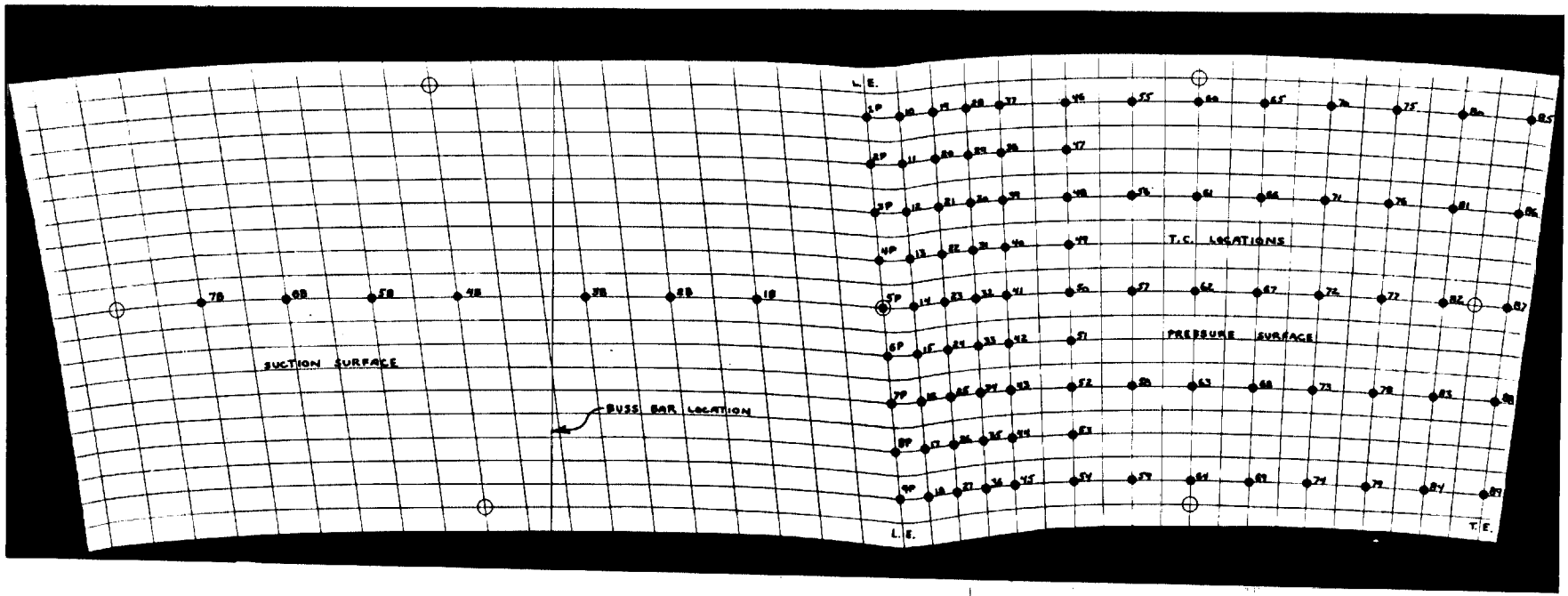

Figure 18 Pressure Surface Thermocouple Instrumentation Array

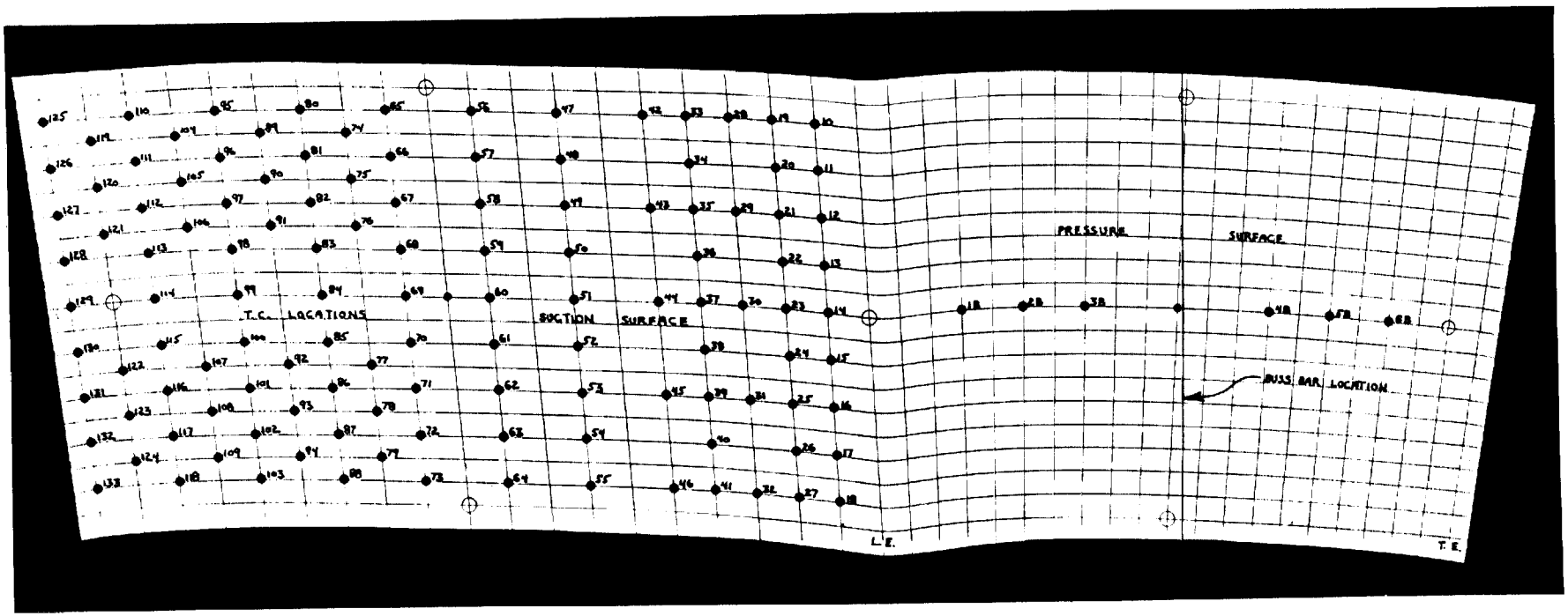

Figure 19 Suction Surface Thermocouple Instrumentation Array

Figure 20 Endwall Thermocouple Instrumentation Array

88—8—12—1

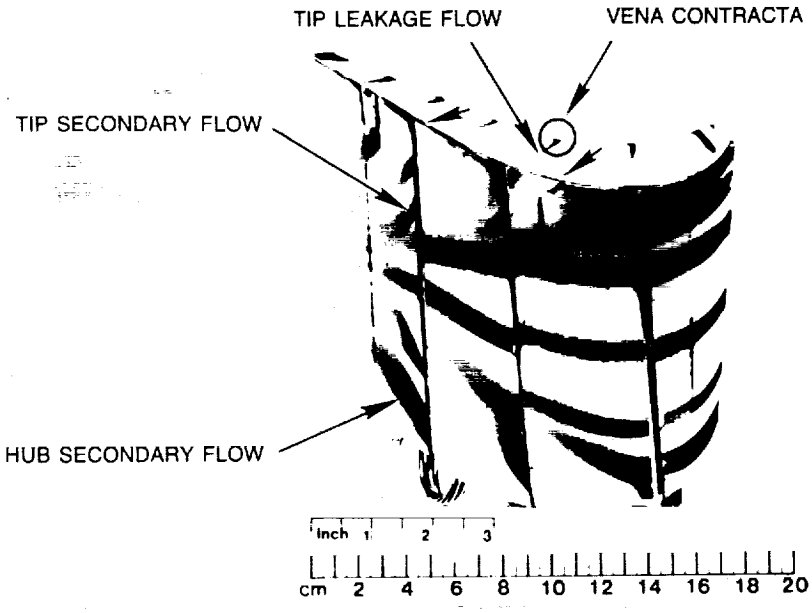

a) SUCTION SURFACE AND TIP

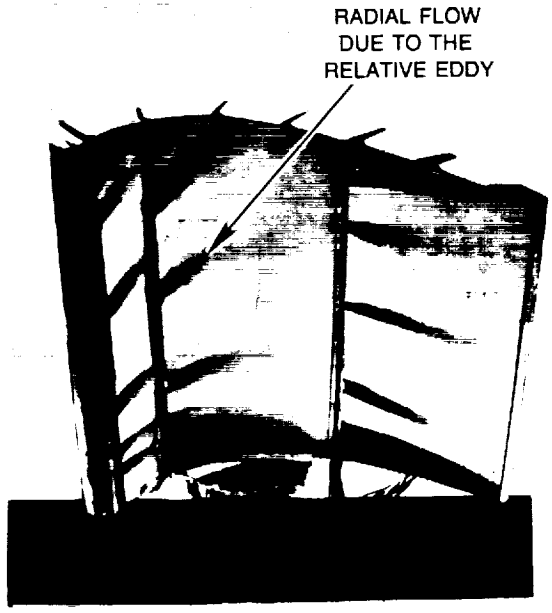

b) PRESSURE SURFACE AND TIP

Fig. 21 Rotor Surface Flow Visualization, Showing Hub and Tip Secondary Flow, Tip Leakage and Effect of Relative Eddy

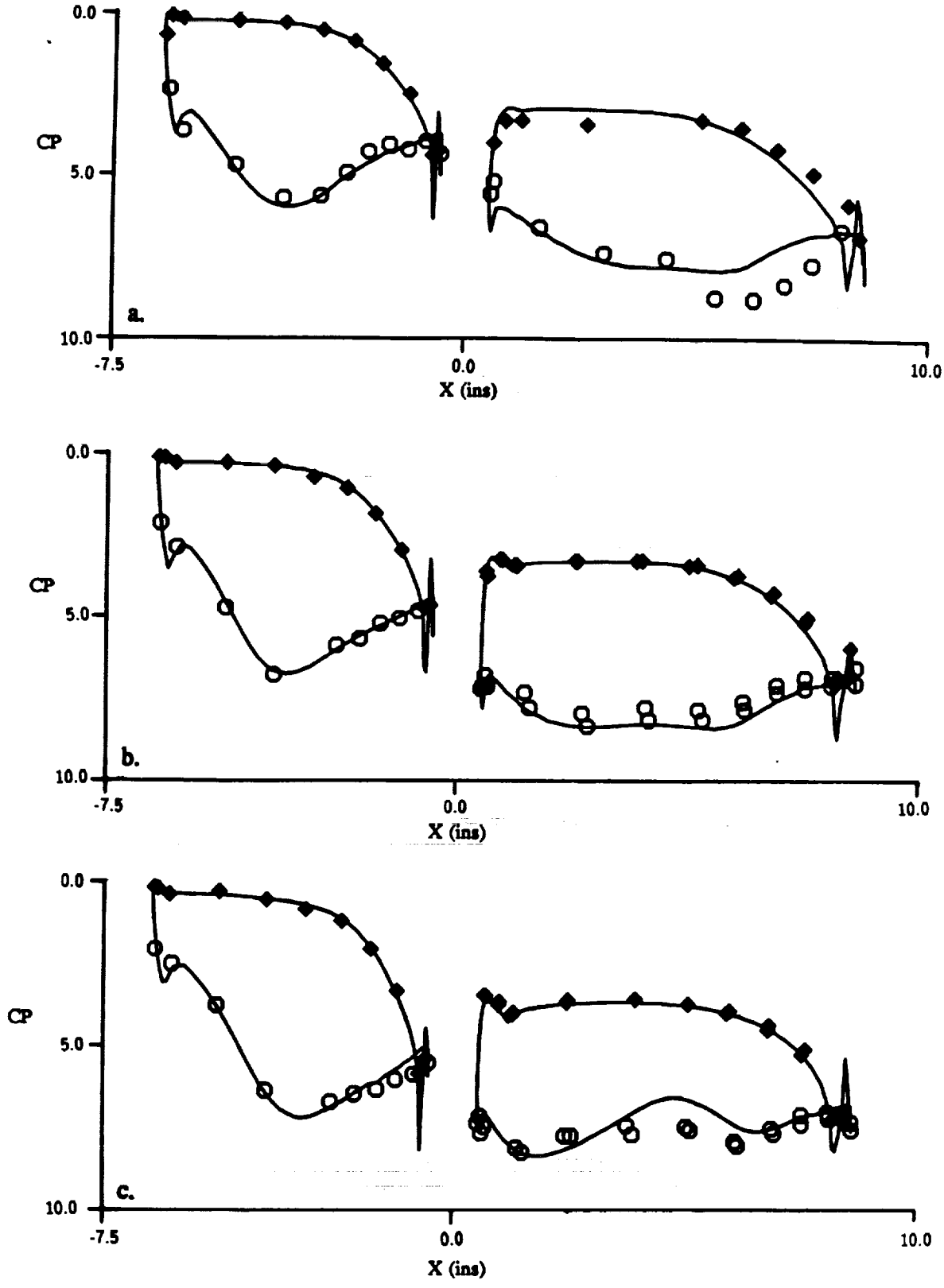

Figure 22 First Stator and Rotor Fullspan Pressure Distributions
a. 98% Span
b. 50% Span
c. 2% Span

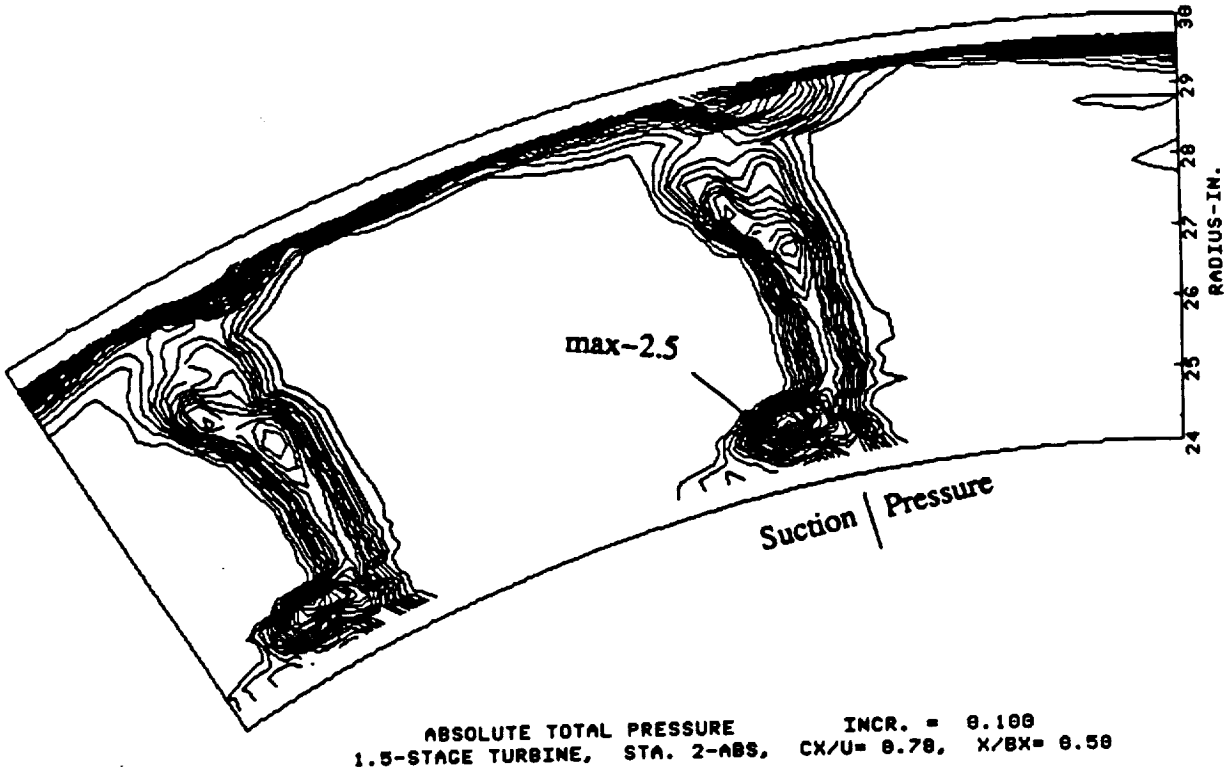

Figure 23a First Stator Exit Results, Plane 2-Absolute, Measured 17% Aft, Absolute Total Pressure Contours, ΔCPTABS=0. 10

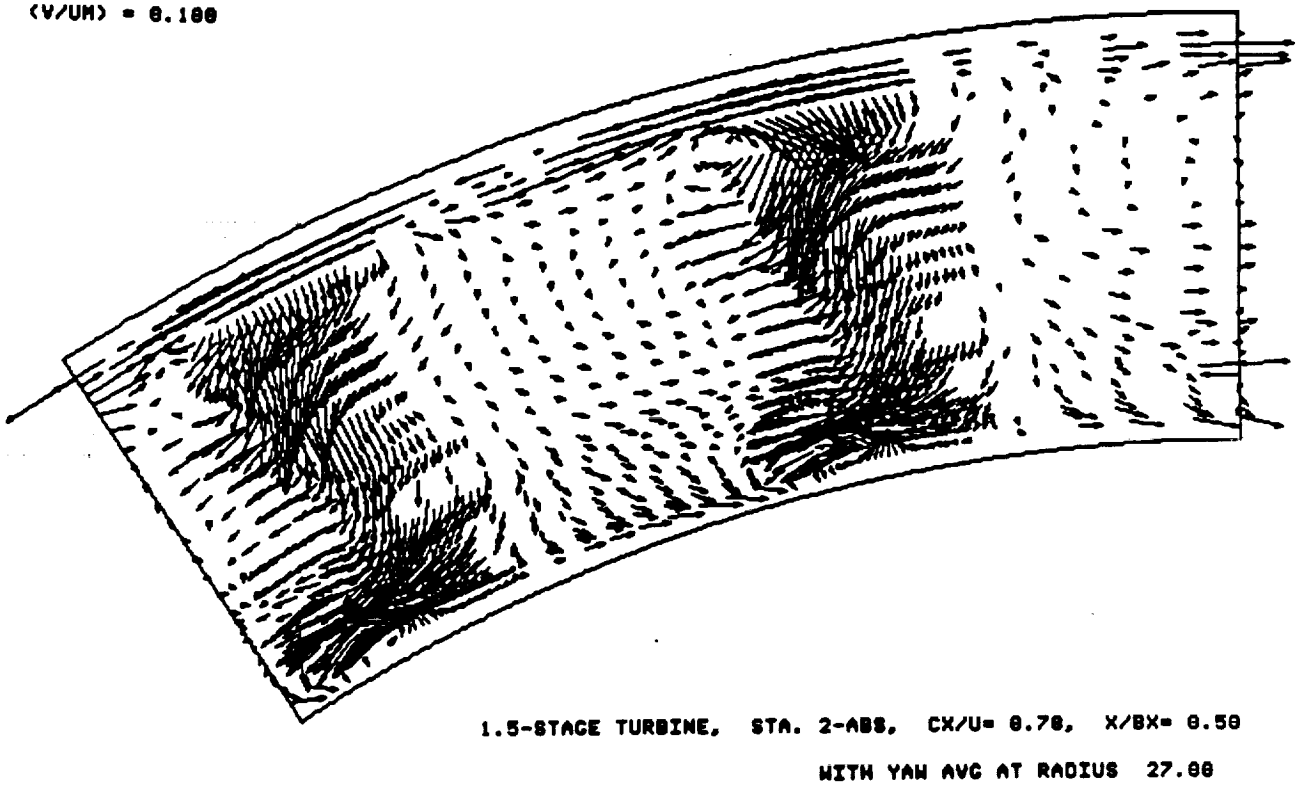

Figure 23b First Stator Exit Results, Plane 2-Absolute, Measured 17% Aft, Secondary Flow with Average Yaw (Absolute) at 50% Span

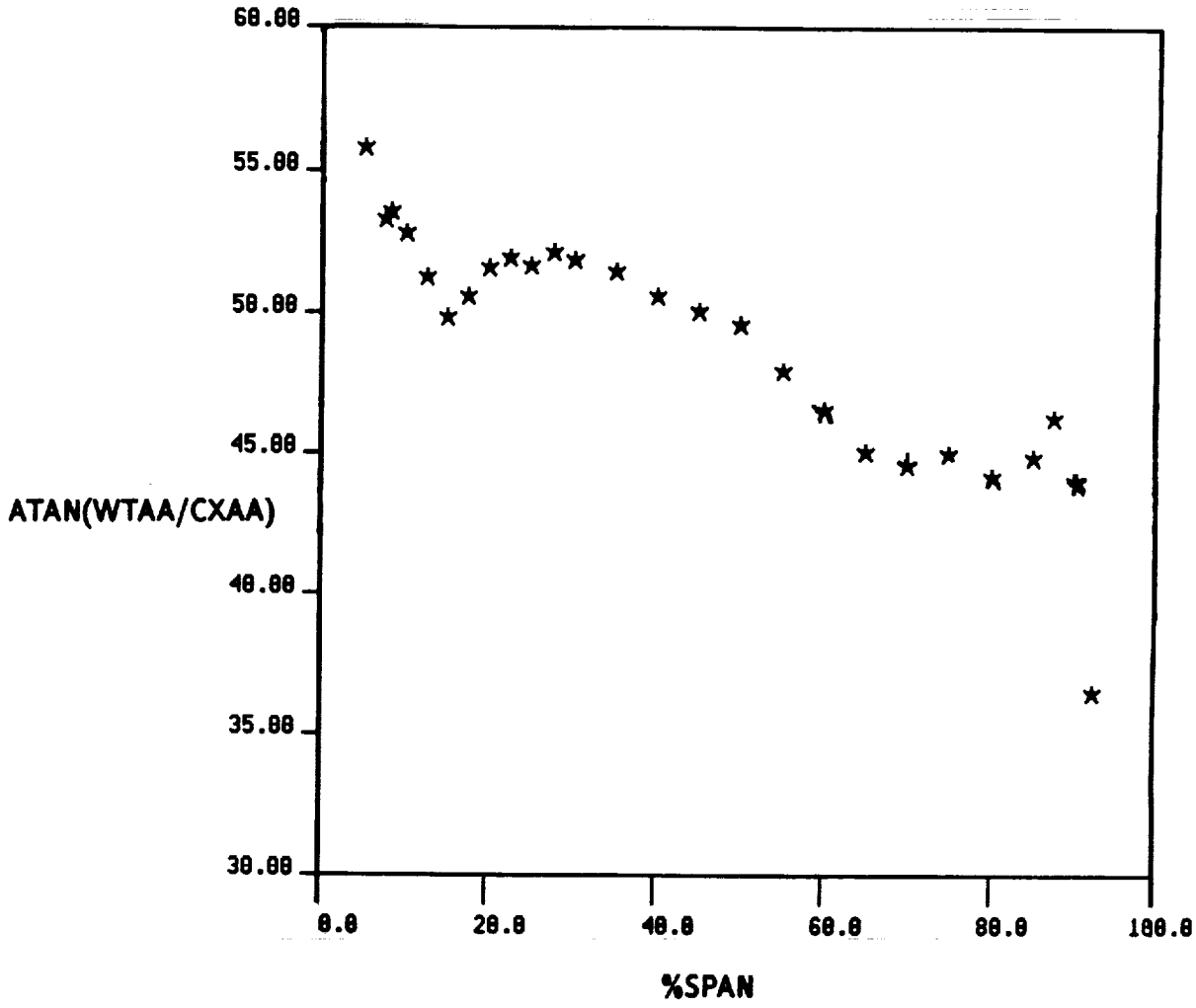

Figure 24 First Stator Exit Results, Plane 2-Absolute, Measured 17% Aft, and Computed 9% Aft, Relative Flow Angle (Arctan [WTAA/CXAA])

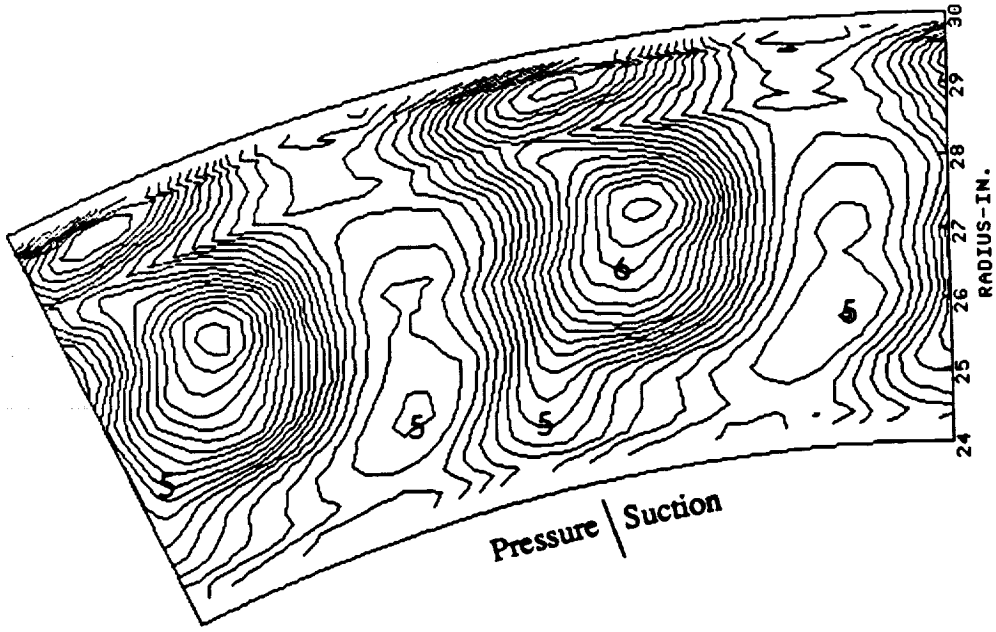

ROTARY TOTAL PRESSURE INCR. = 0.100
1.5-STAGE TURBINE, STA. 3-REL, CX/U= 0.78, X/BX= 0.50

Figure 25a Rotor Exit Results, Plane 3-Relative, Measured 36% Aft, Rotary Total Pressure Contours, ΔCPTROT=0.10

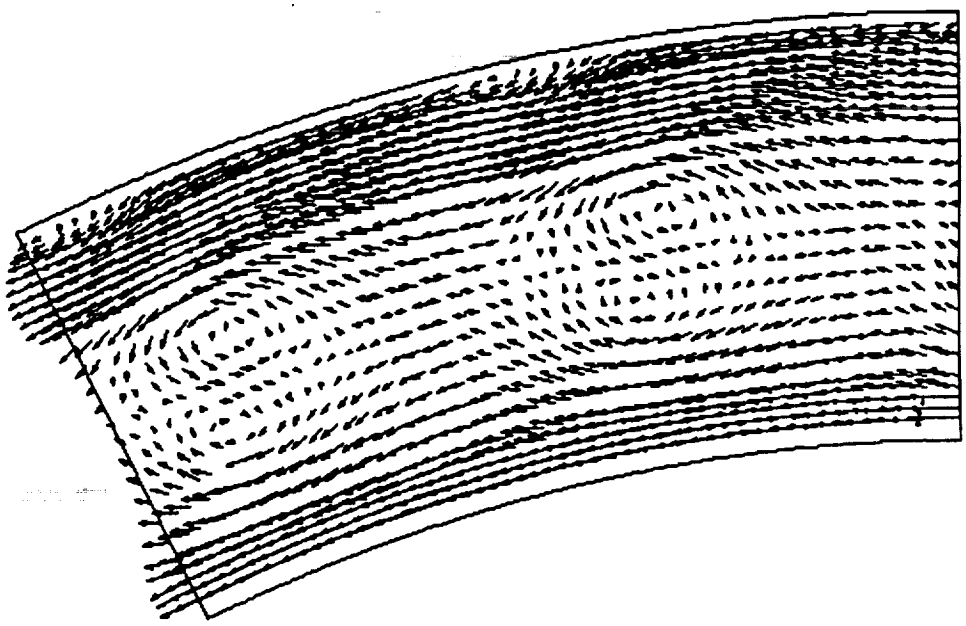

1.5-STAGE TURBINE, STA. 3-REL, CX/U= 0.78, X/BX= 0.50
WITH YAW AVG AT RADIUS 27.00

Figure 25b Rotor Exit Results, 3-Relative, Measured 36% Aft, Secondary Flow with Average Yaw (Relative) at 50% Span

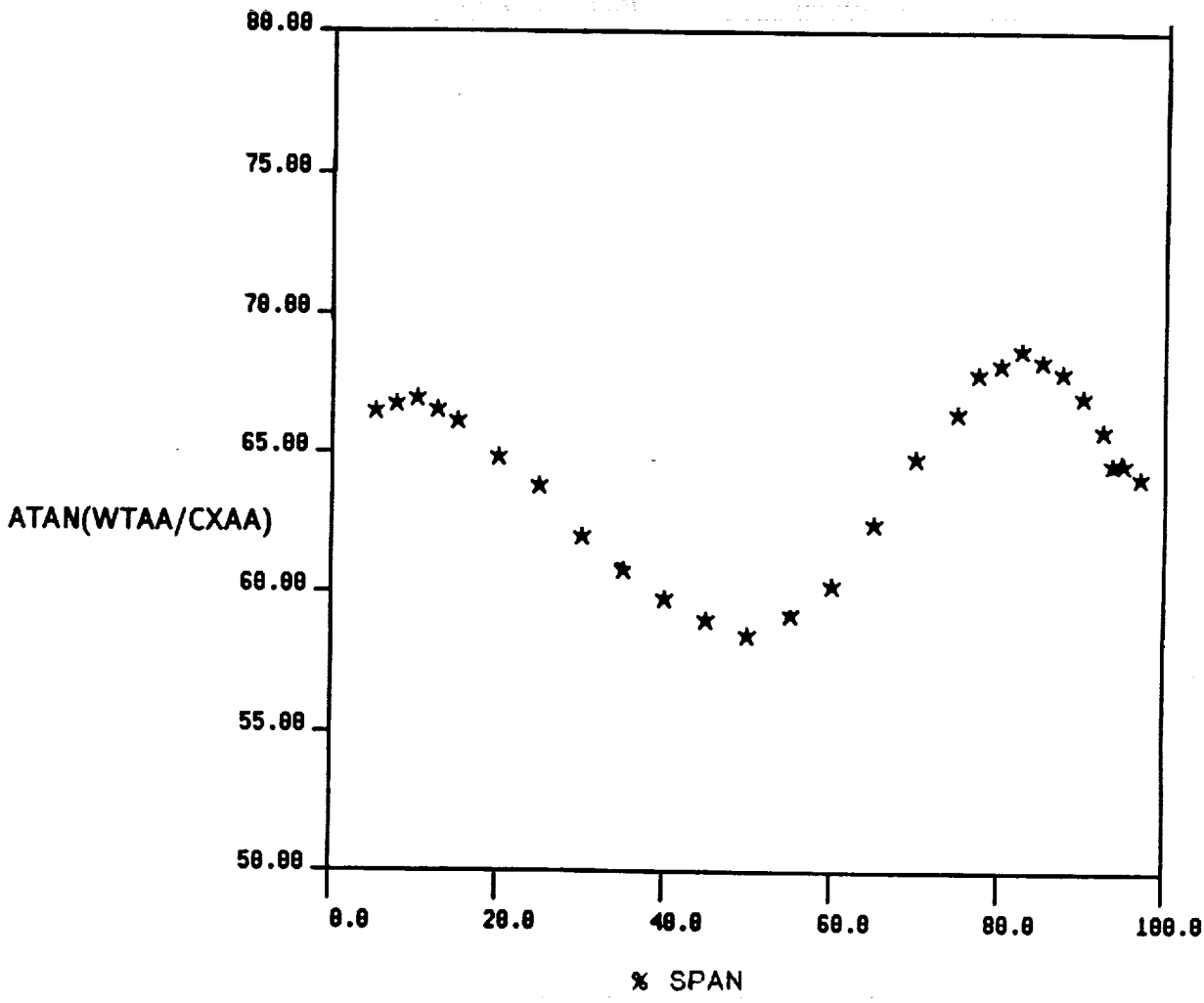

Figure 26 Rotor Exit Results, Plane 3-Relative, Measured 36% Aft, Relative Flow Angle (Arctan [WTAA/CXAA])

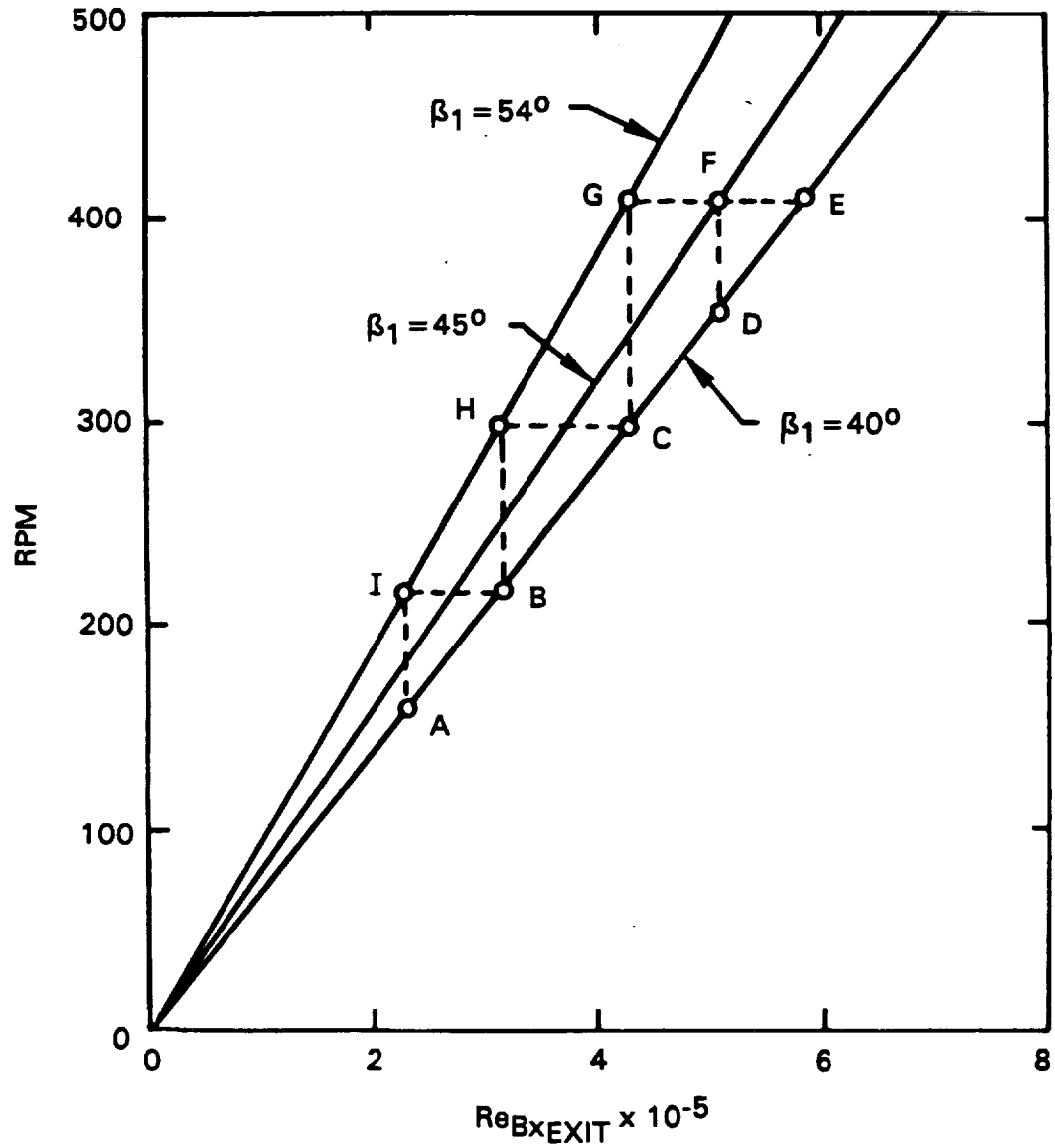

Figure 27 Matrix of Test Data Obtained for the Present Program

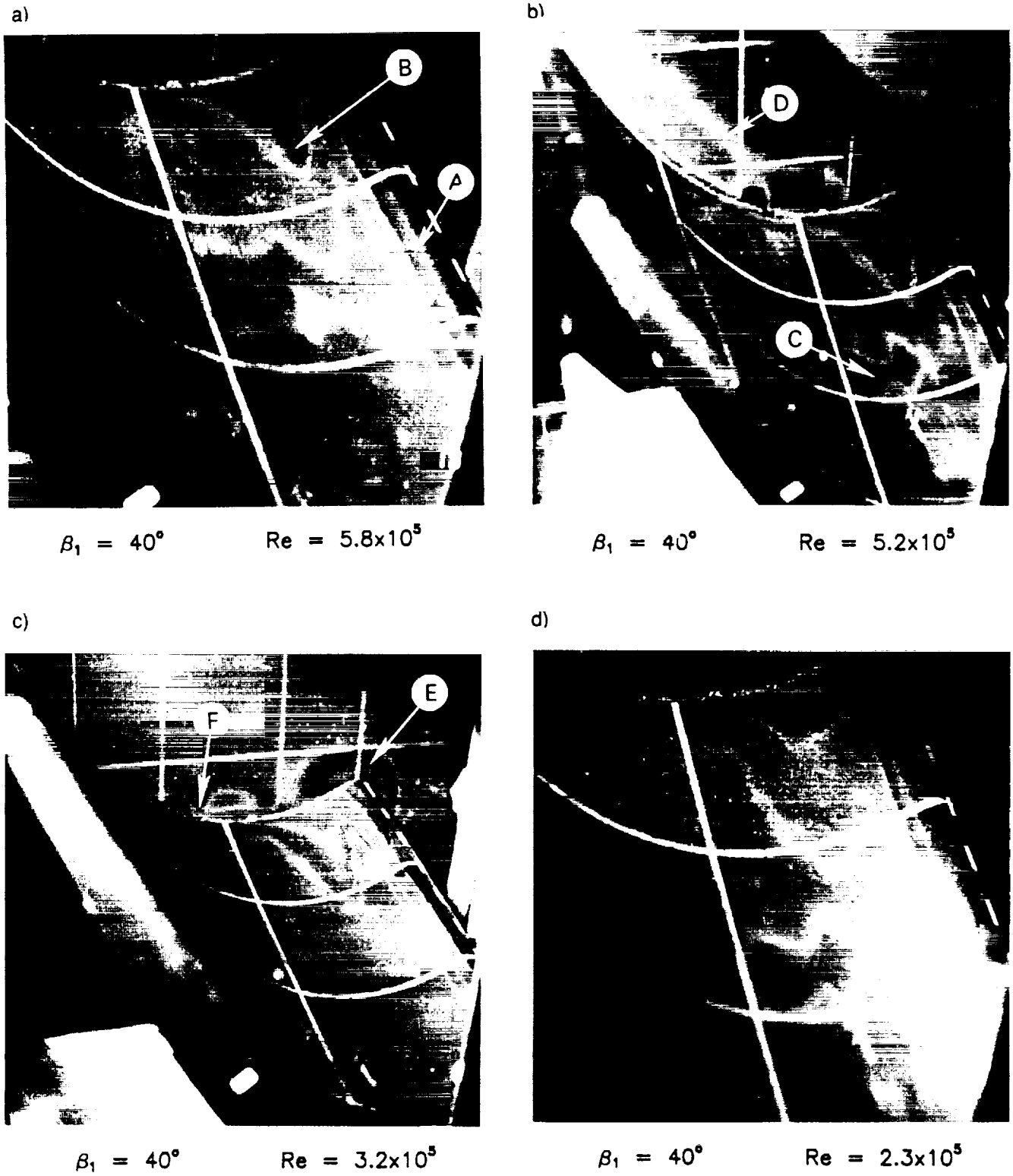

Figure 28 Liquid-Crystal Temperature Contours on the Rotor Pressure Surface for a Range of Reynolds Numbers at β_1=40°

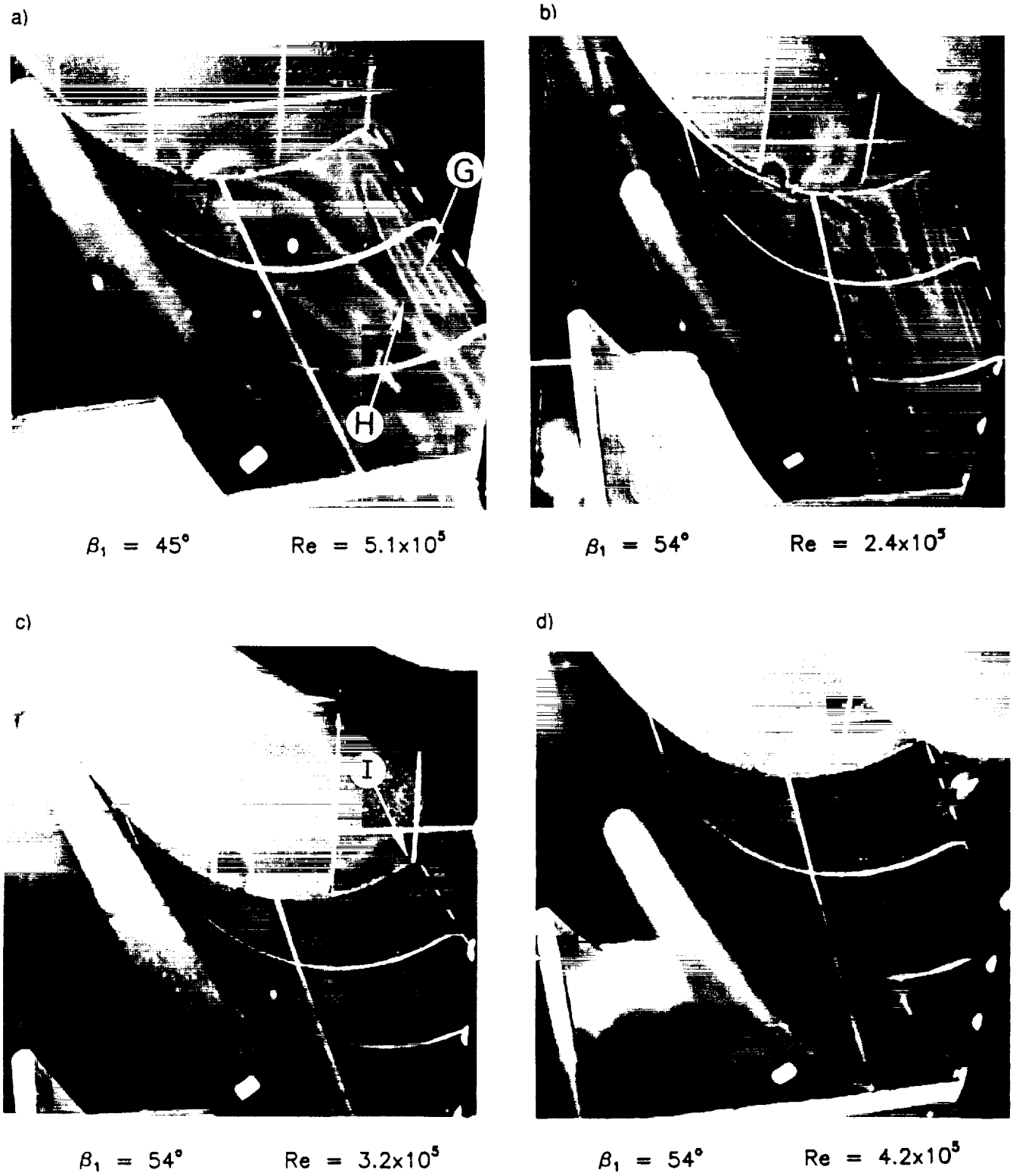

Figure 29 Liquid-Crystal Temperature Contours on the Rotor Pressure Surface for a Range of Incidence Angles and Reynolds Numbers

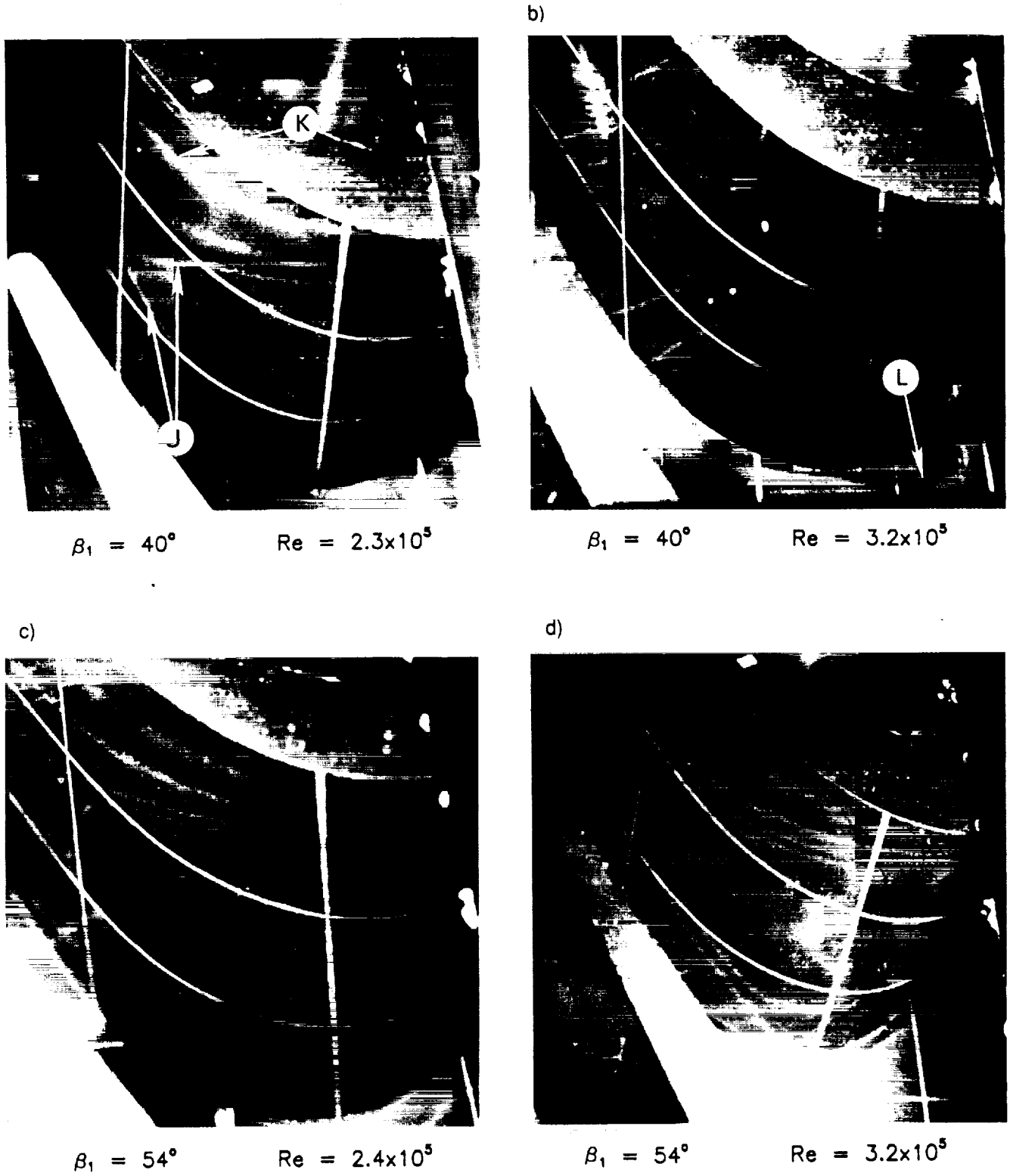

Figure 30 Liquid-Crystal Temperature Contours on the Rotor Suction Angle Surface for a Range of Incidence Angles and Reynolds Numbers

a)

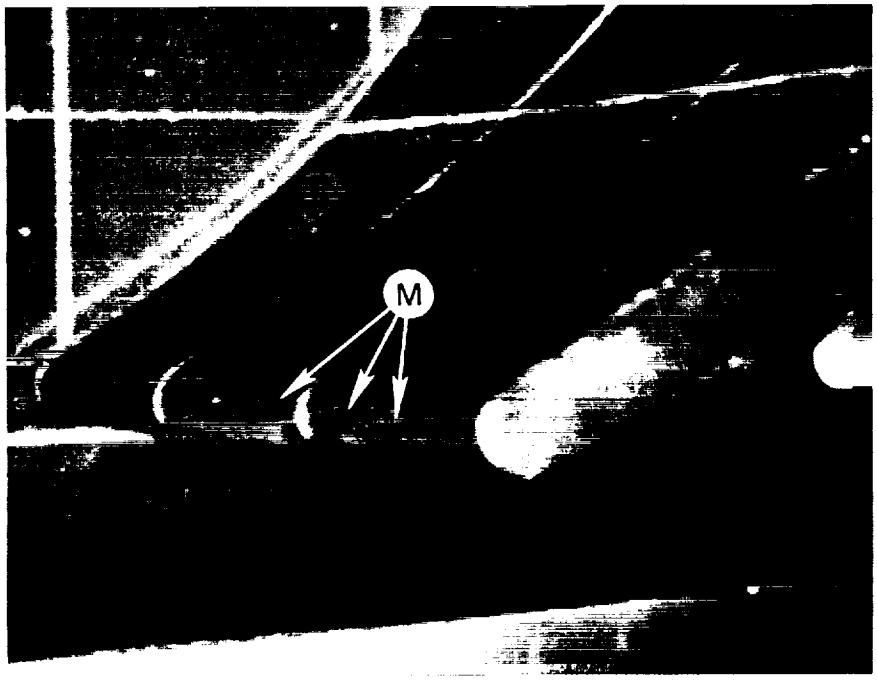

β_1 = 54° Re = 4.2×10^5

b)

β_1 = 54° Re = 4.2×10^5

Figure 31 Close-up Photographs of the Liquid-Crystal Temperature Contours on the Airfoil Trailing Edge for β_1=54° and Re=4.2×10^5

$$S^* = \frac{S}{S_{tot(r)}} \quad \frac{S_{tot(midspan)}}{SPAN}$$

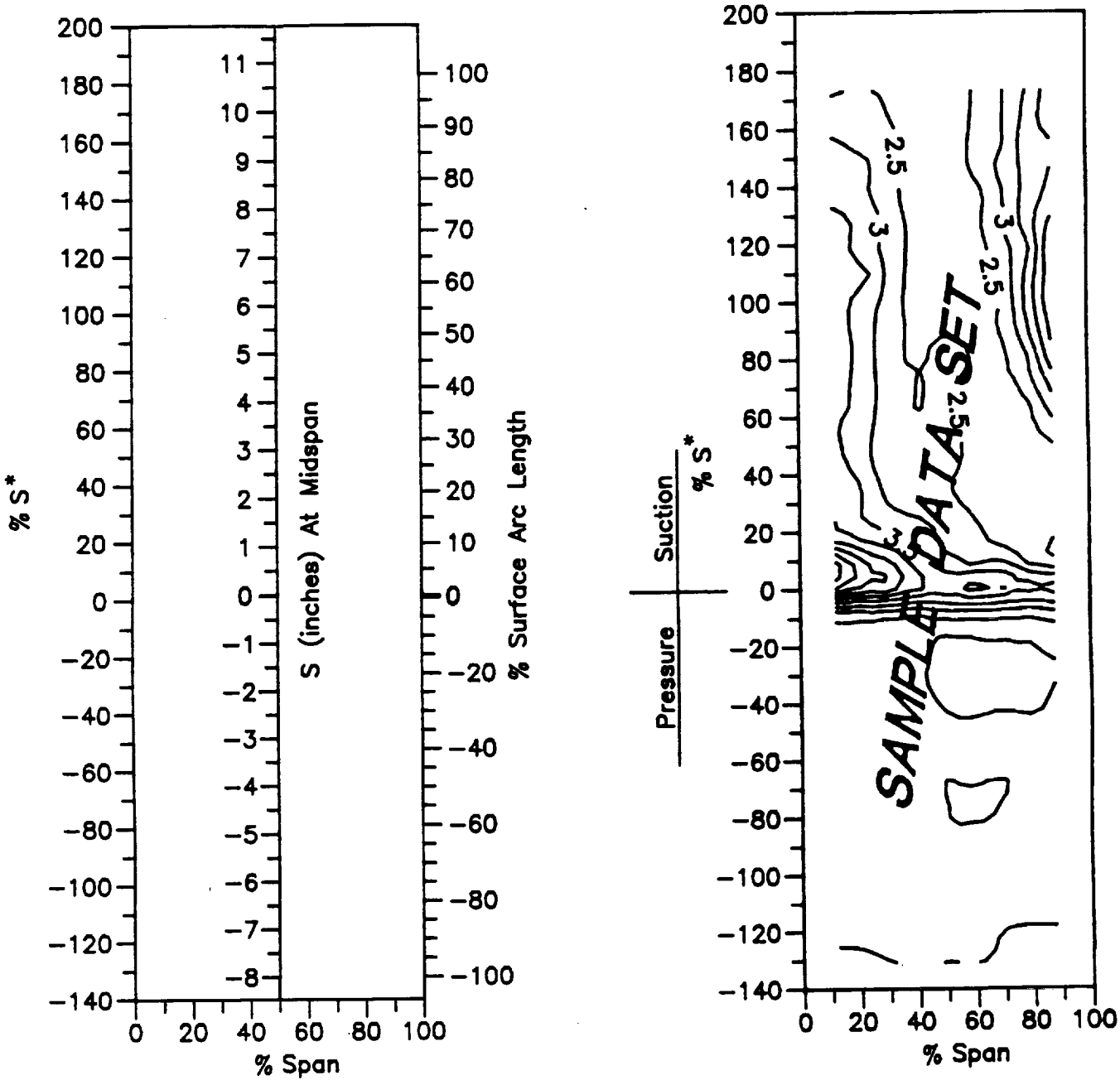

Figure 32 Coordinates for Presentation of the Airfoil Surface Contours of Stanton Number

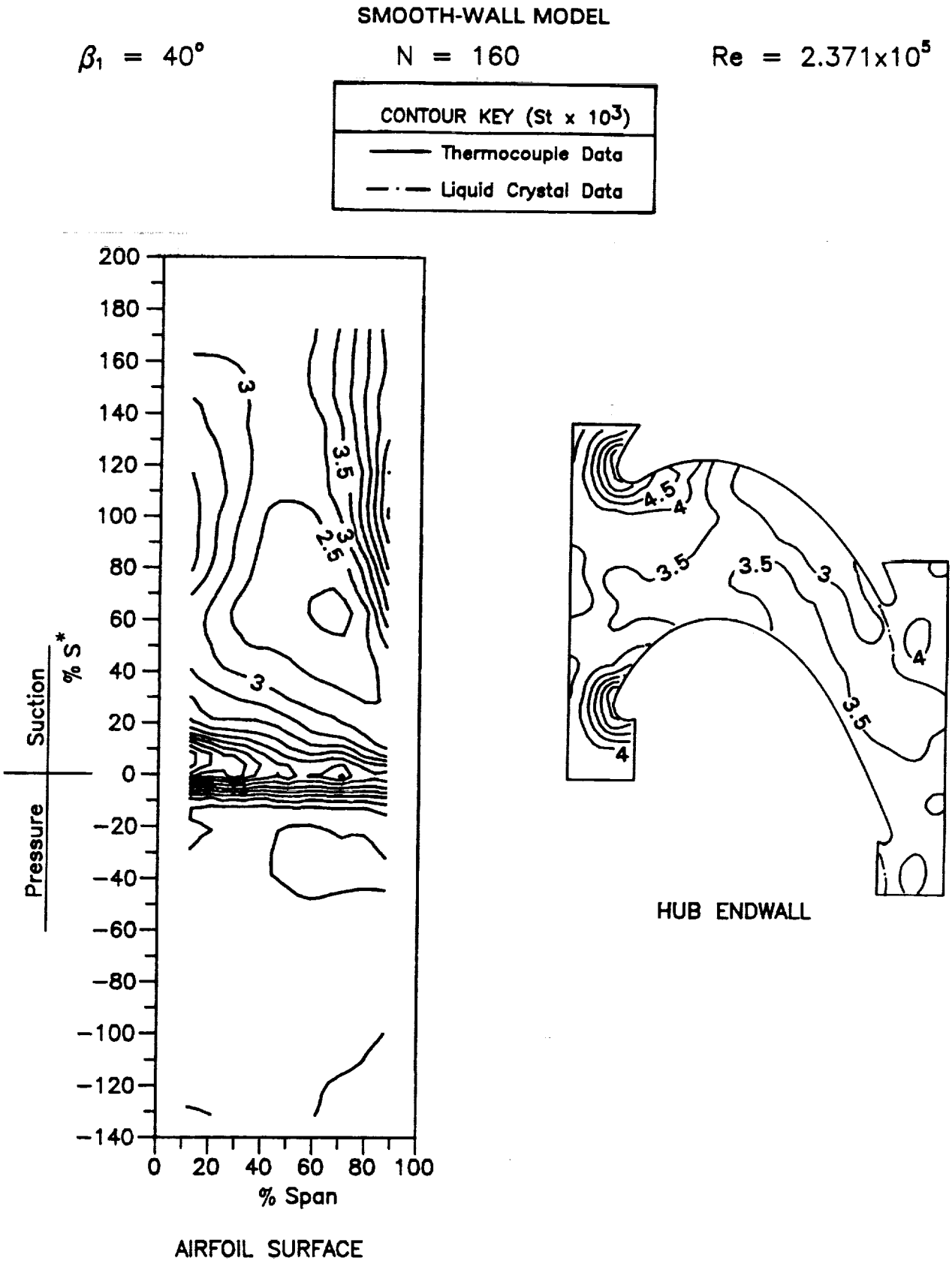

Figure 33a Stanton Number Contours on the Airfoil and Hub Endwall Surfaces

SMOOTH-WALL MODEL

β_1 = 40° N = 160 Re = 2.371×10^5

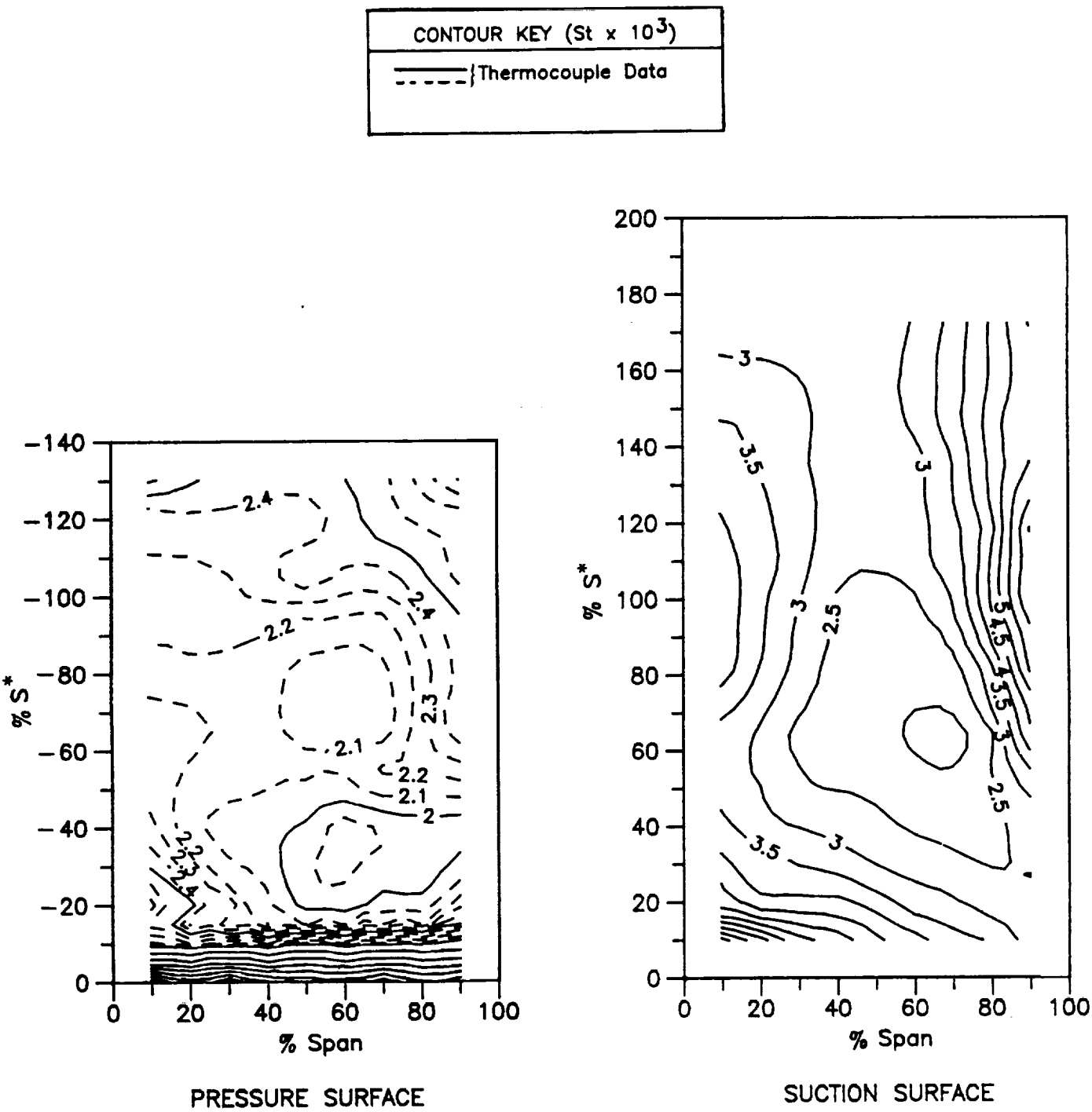

Figure 33b Details of the Stanton Number Contours on the Airfoil Suction and Pressure Surfaces

SMOOTH-WALL MODEL

$\beta_1 = 40°$ N = 160 Re = 2.371×10^5

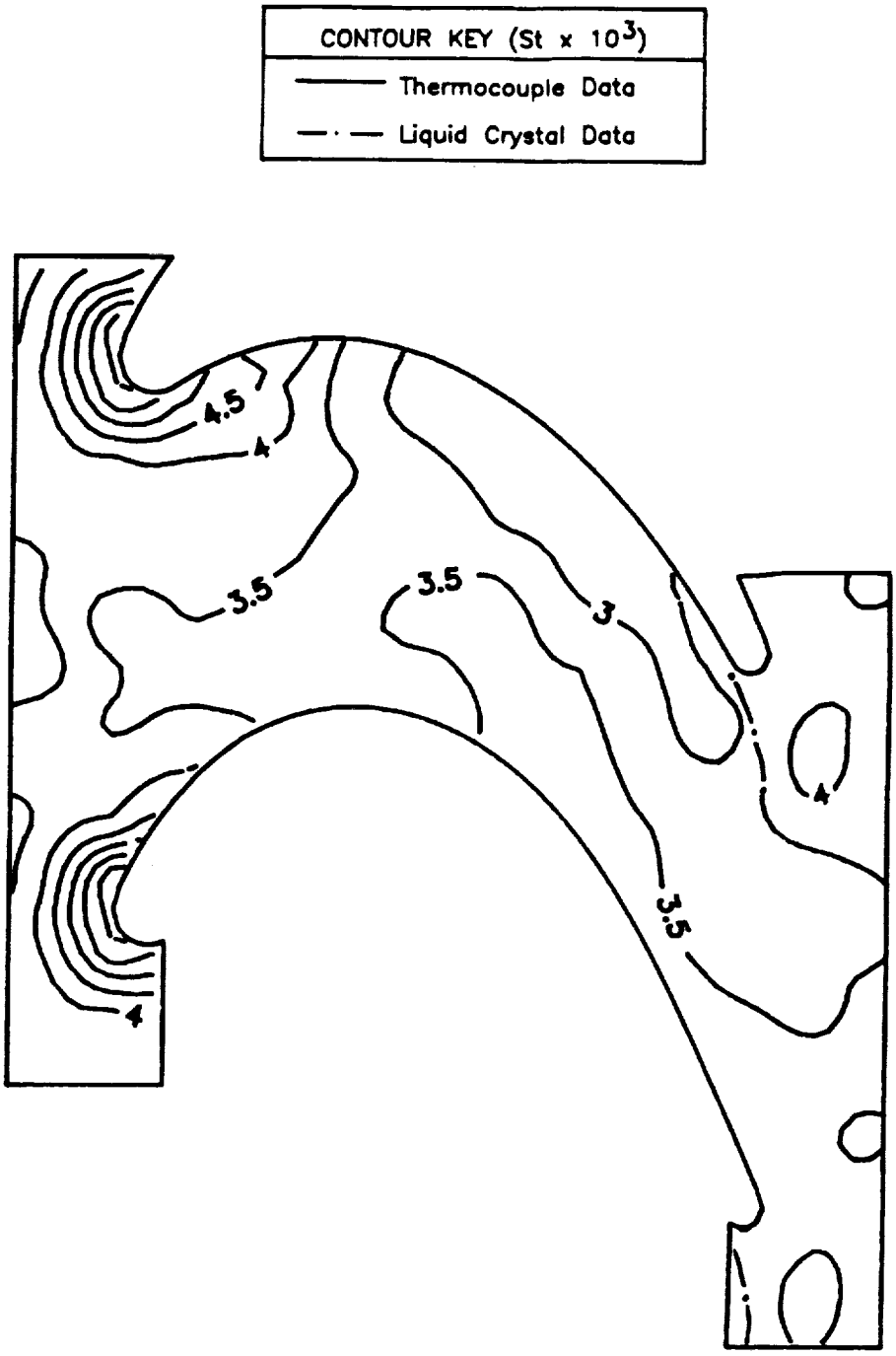

Figure 33c Details of the Stanton Number Contours on the Hub Endwall Surface

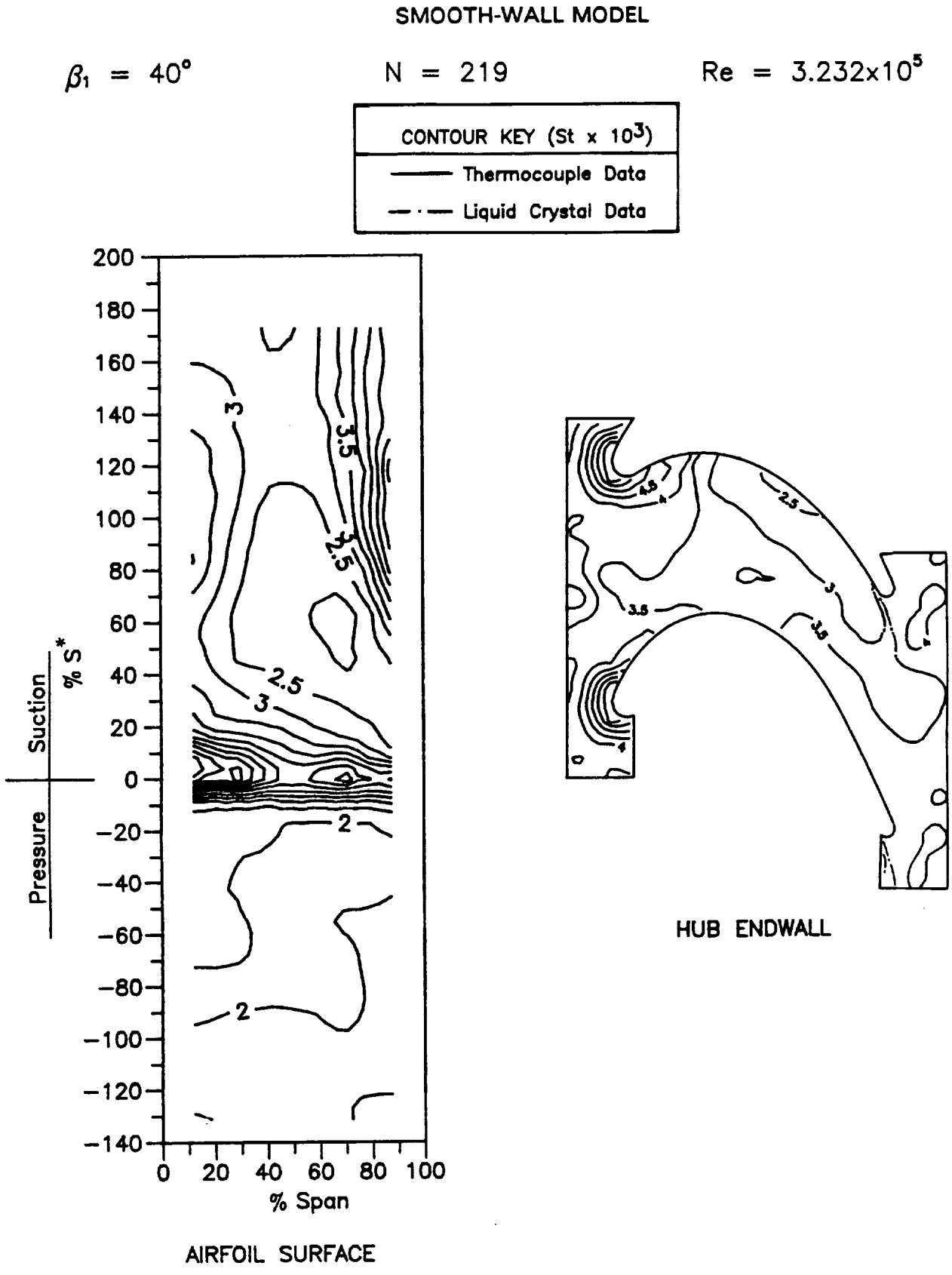

Figure 34a Stanton Number Contours on the Airfoil and Hub Endwall Surfaces

SMOOTH-WALL MODEL

β_1 = 40° N = 219 Re = 3.232x10^5

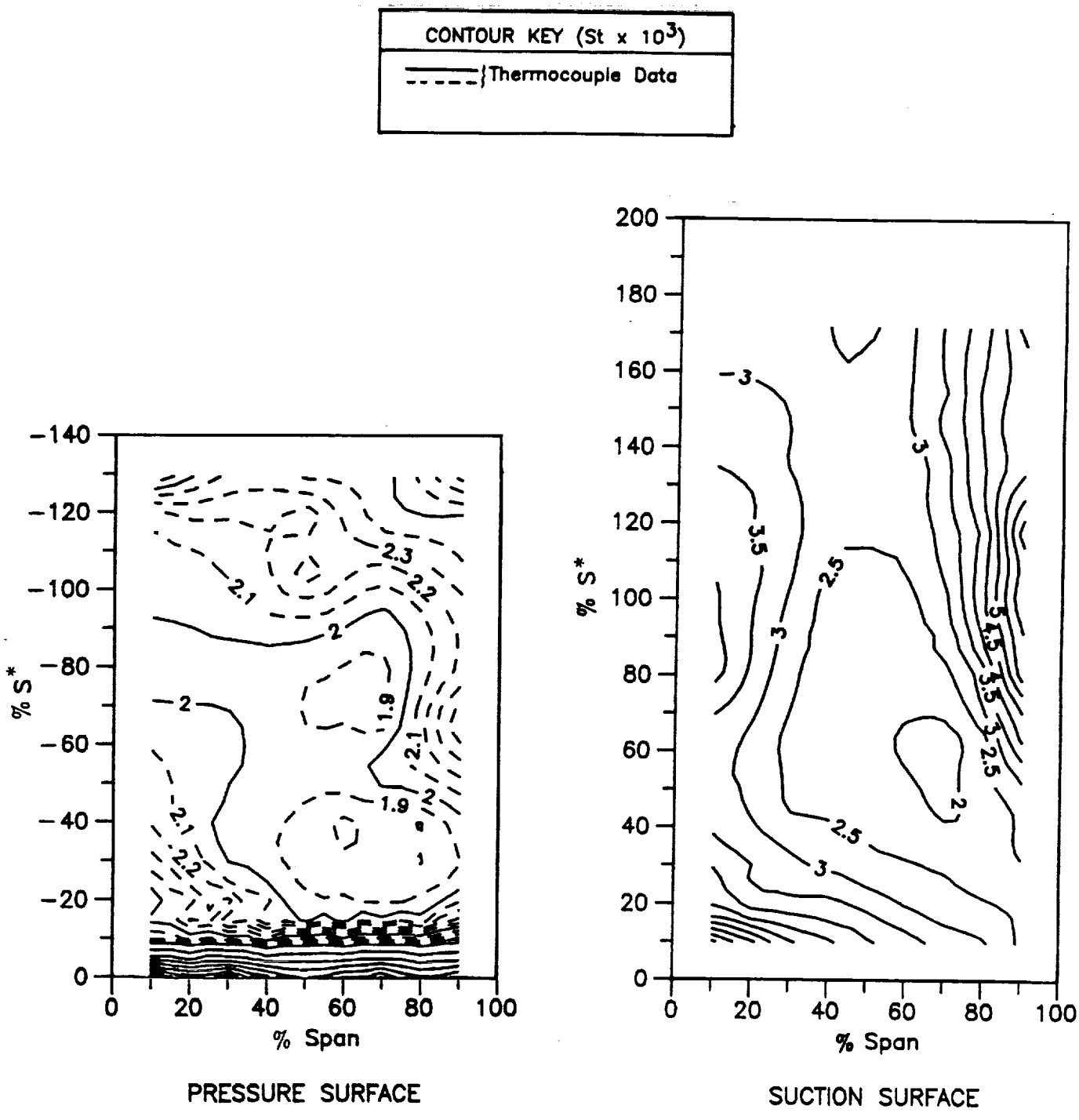

Figure 34b Details of the Stanton Number Contours on the Airfoil Suction and Pressure Surfaces

SMOOTH-WALL MODEL

β_1 = 40° N = 219 Re = 3.232×10^5

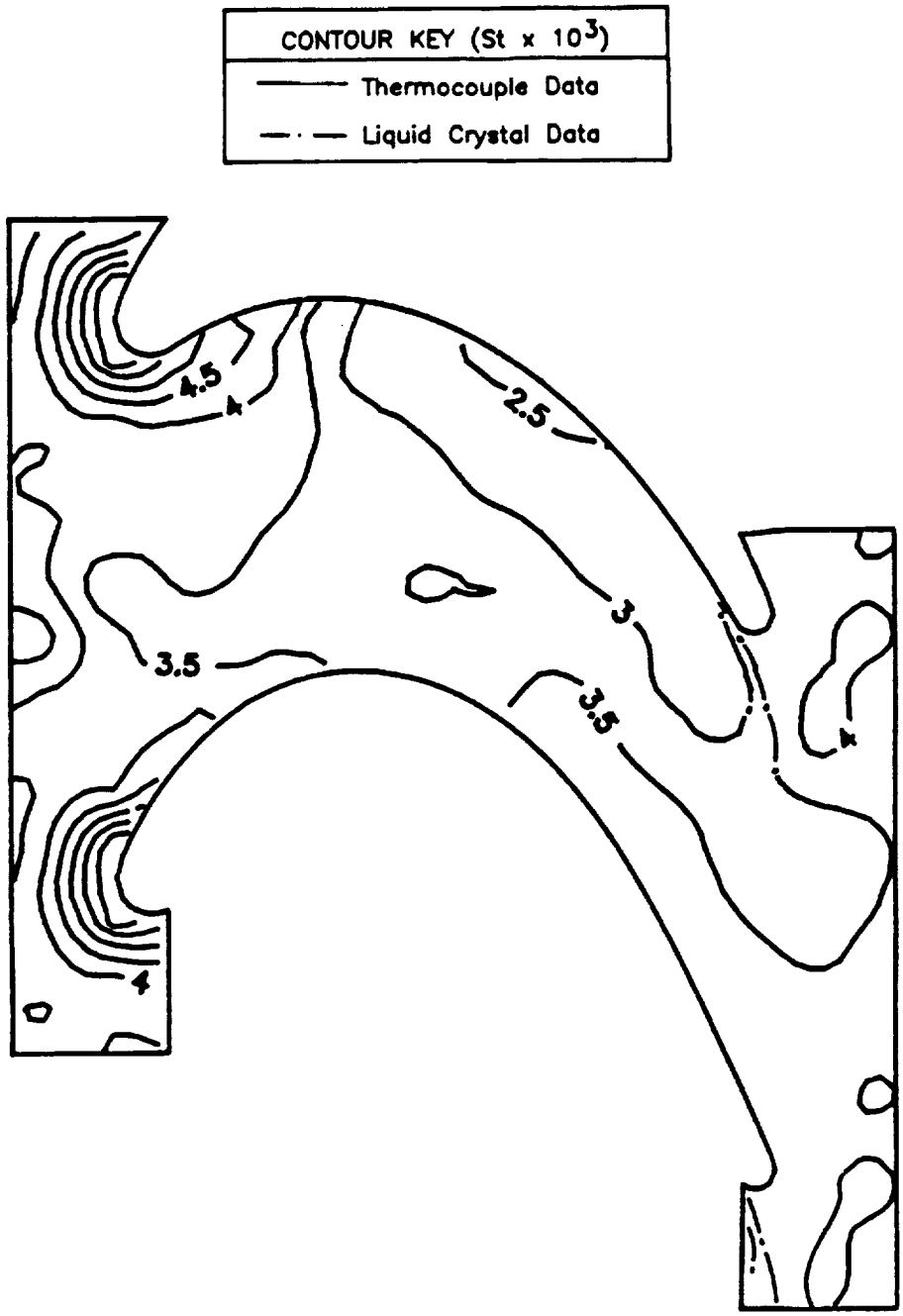

HUB ENDWALL

Figure 34c Details of the Stanton Number Contours on the Hub Endwall Surface

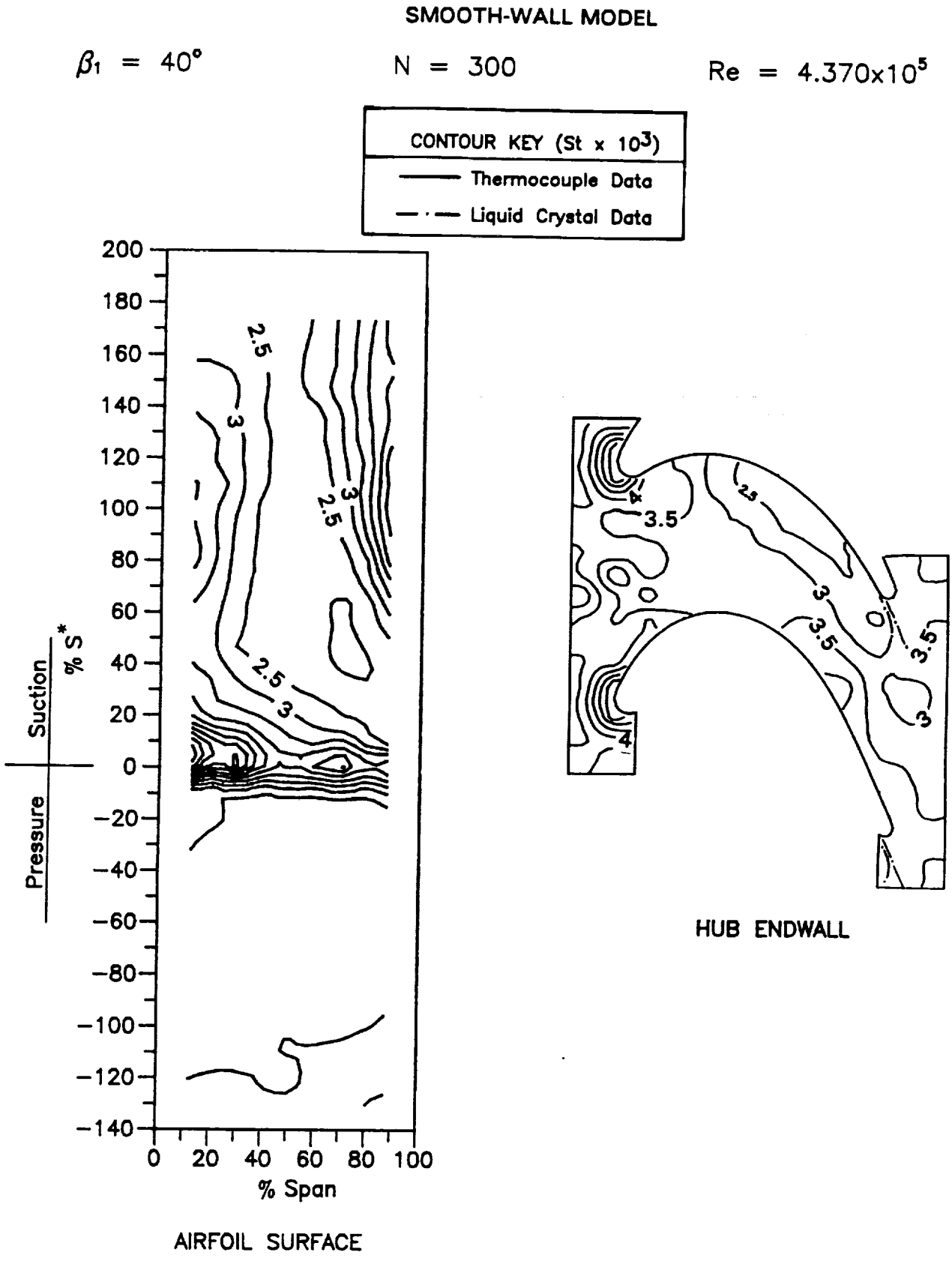

Figure 35a Stanton Number Contours on the Airfoil and Hub Endwall Surfaces

SMOOTH-WALL MODEL

β_1 = 40° N = 300 Re = 4.370×10^5

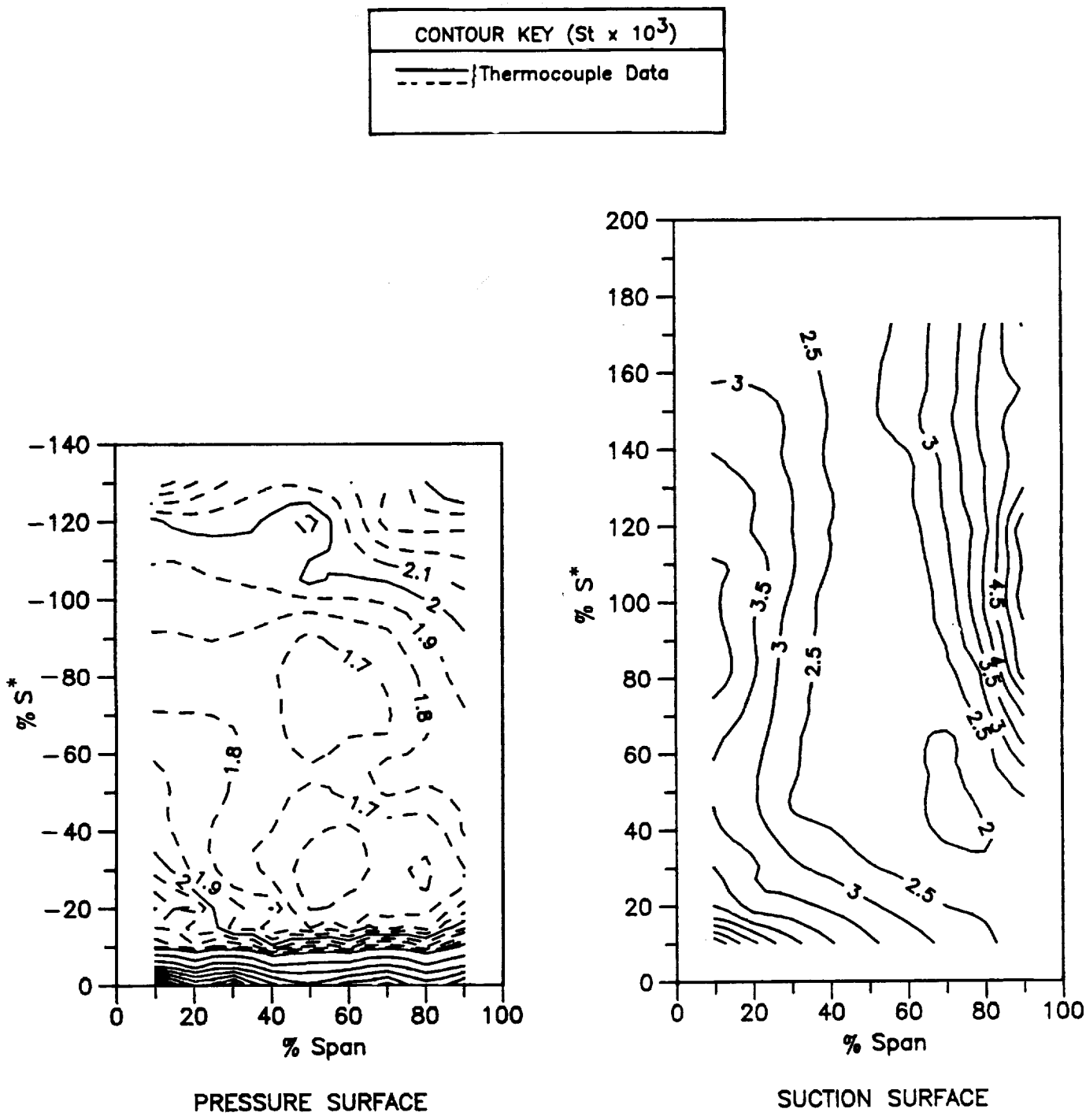

Figure 35b Details of the Stanton Number Contours on the Airfoil Suction and Pressure Surfaces

SMOOTH-WALL MODEL

$\beta_1 = 40°$ N = 300 Re = 4.370×10^5

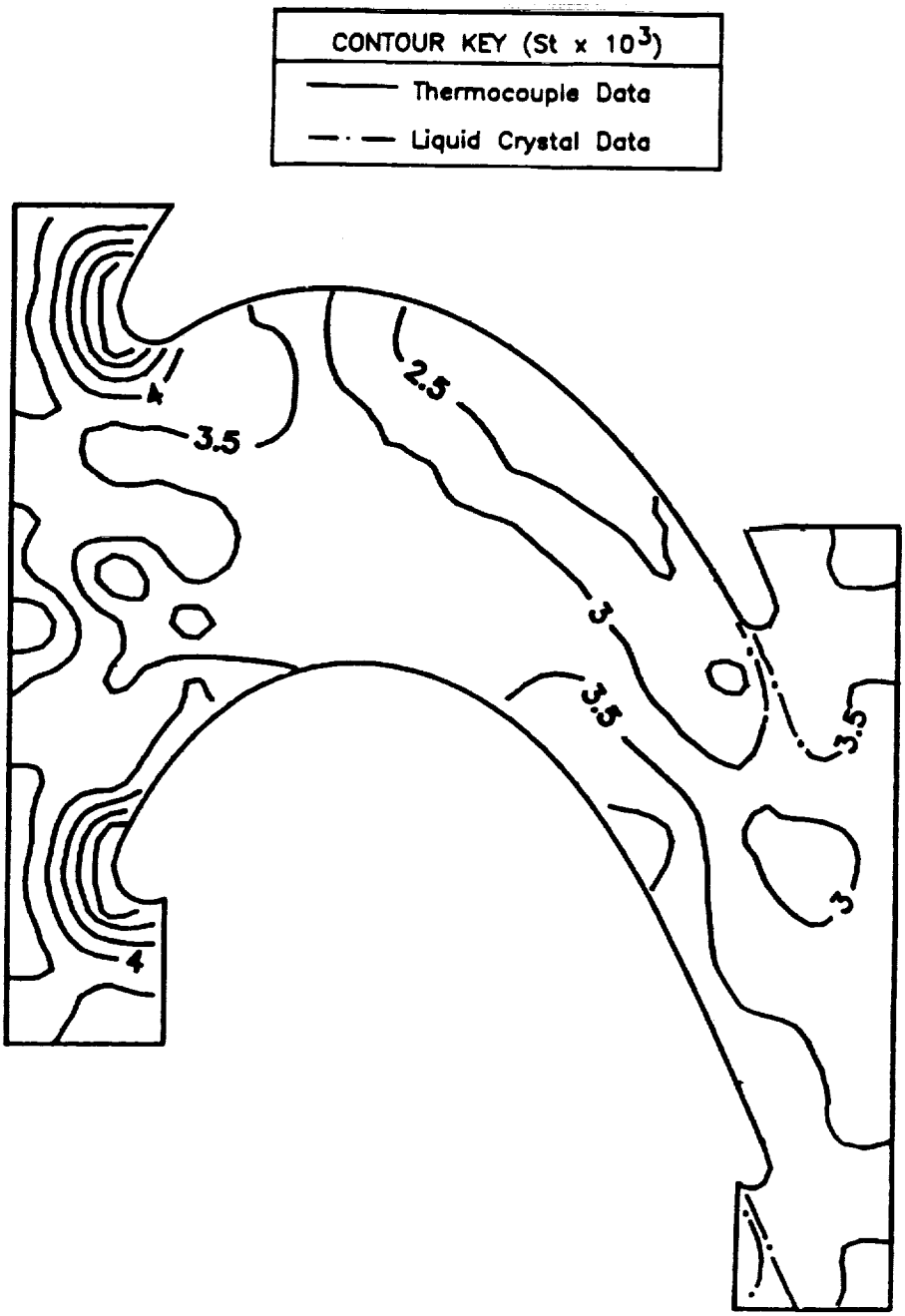

HUB ENDWALL

Figure 35c Details of the Stanton Number Contours on the Hub Endwall Surface

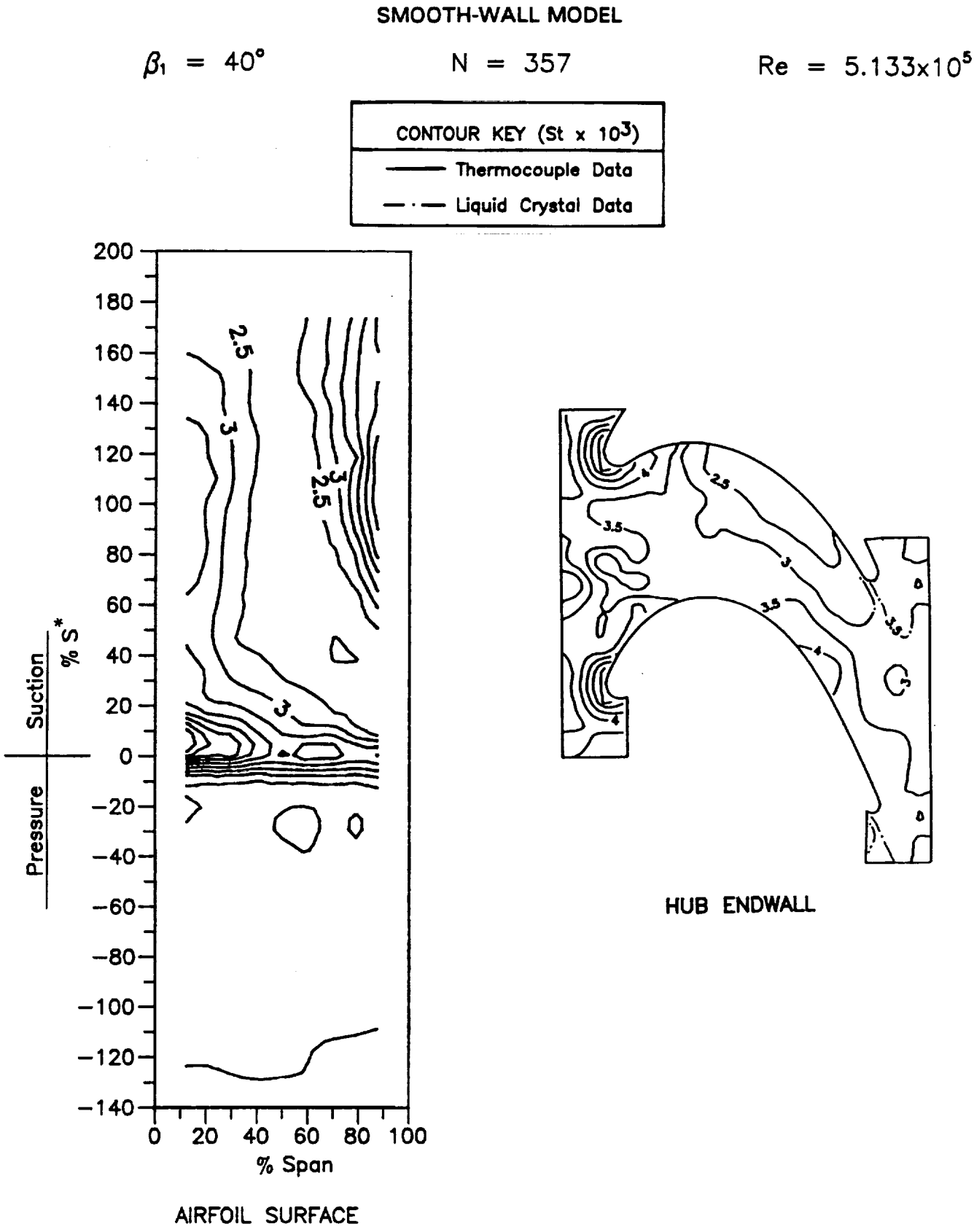

Figure 36a Stanton Number Contours on the Airfoil and Hub Endwall Surfaces

SMOOTH-WALL MODEL

$\beta_1 = 40°$ N = 357 Re = 5.133×10^5

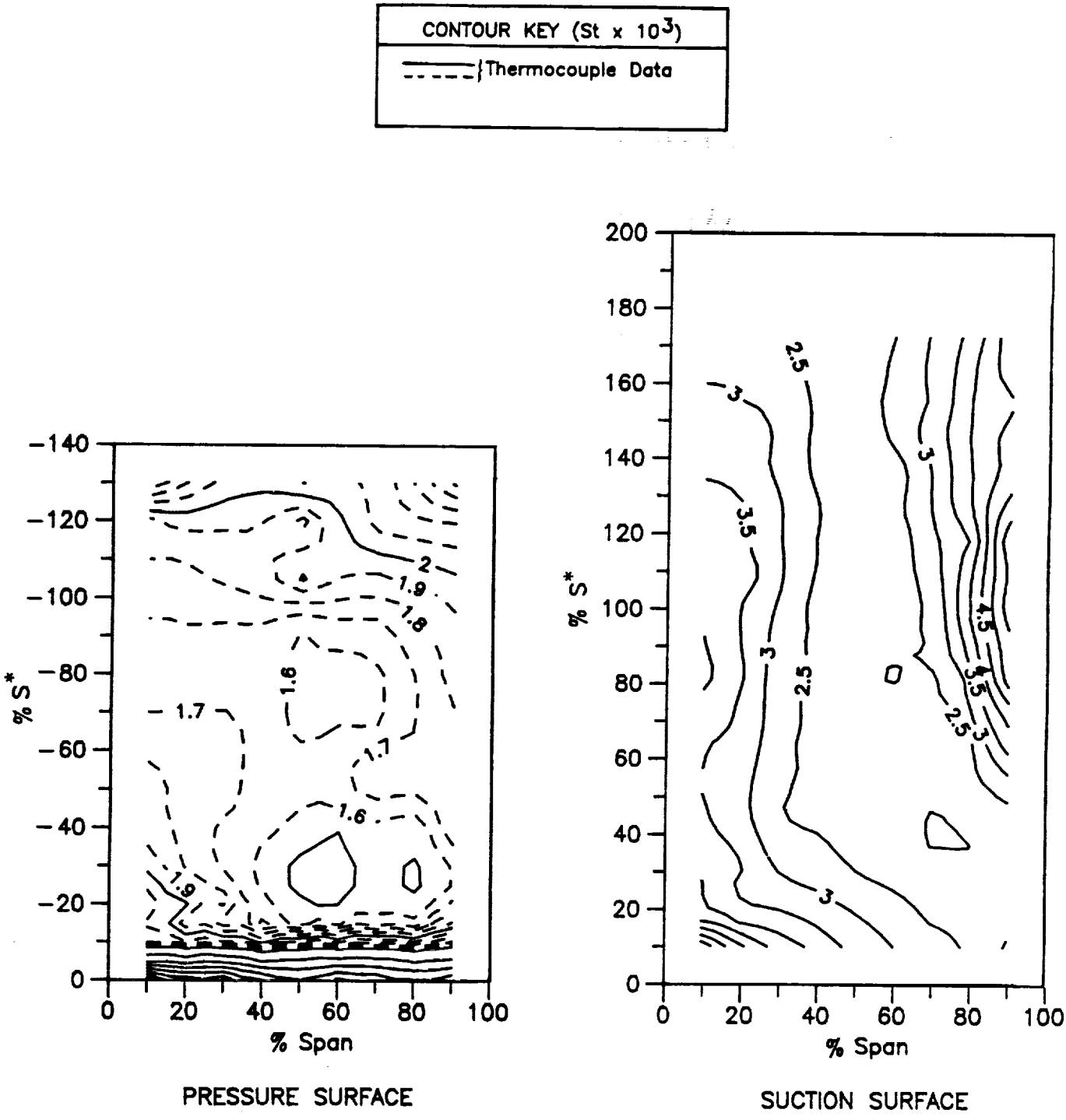

Figure 36b Details of the Stanton Number Contours on the Airfoil Suction and Pressure Surfaces

SMOOTH-WALL MODEL

β_1 = 40° N = 357 Re = 5.133×10^5

CONTOUR KEY (St x 10^3)
——— Thermocouple Data
—·— Liquid Crystal Data

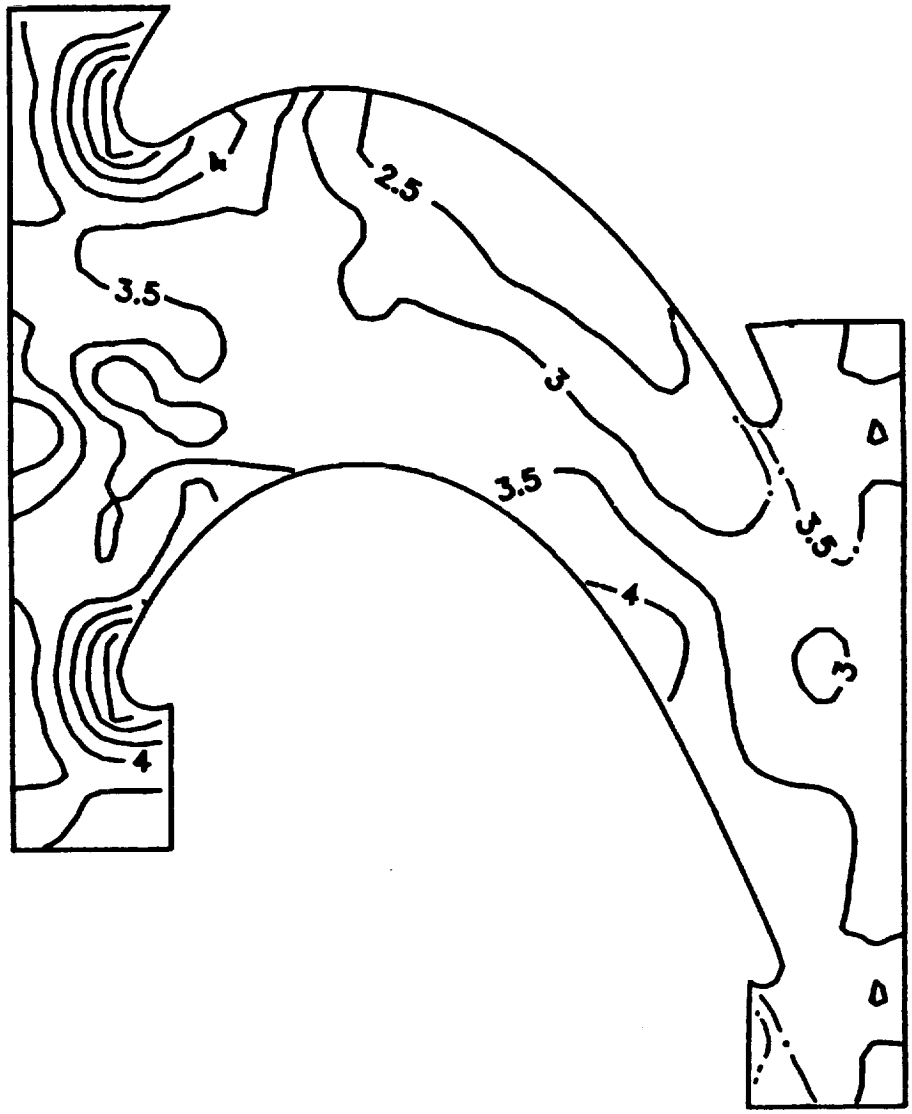

HUB ENDWALL

Figure 36c Details of the Stanton Number Contours on the Hub Endwall Surface

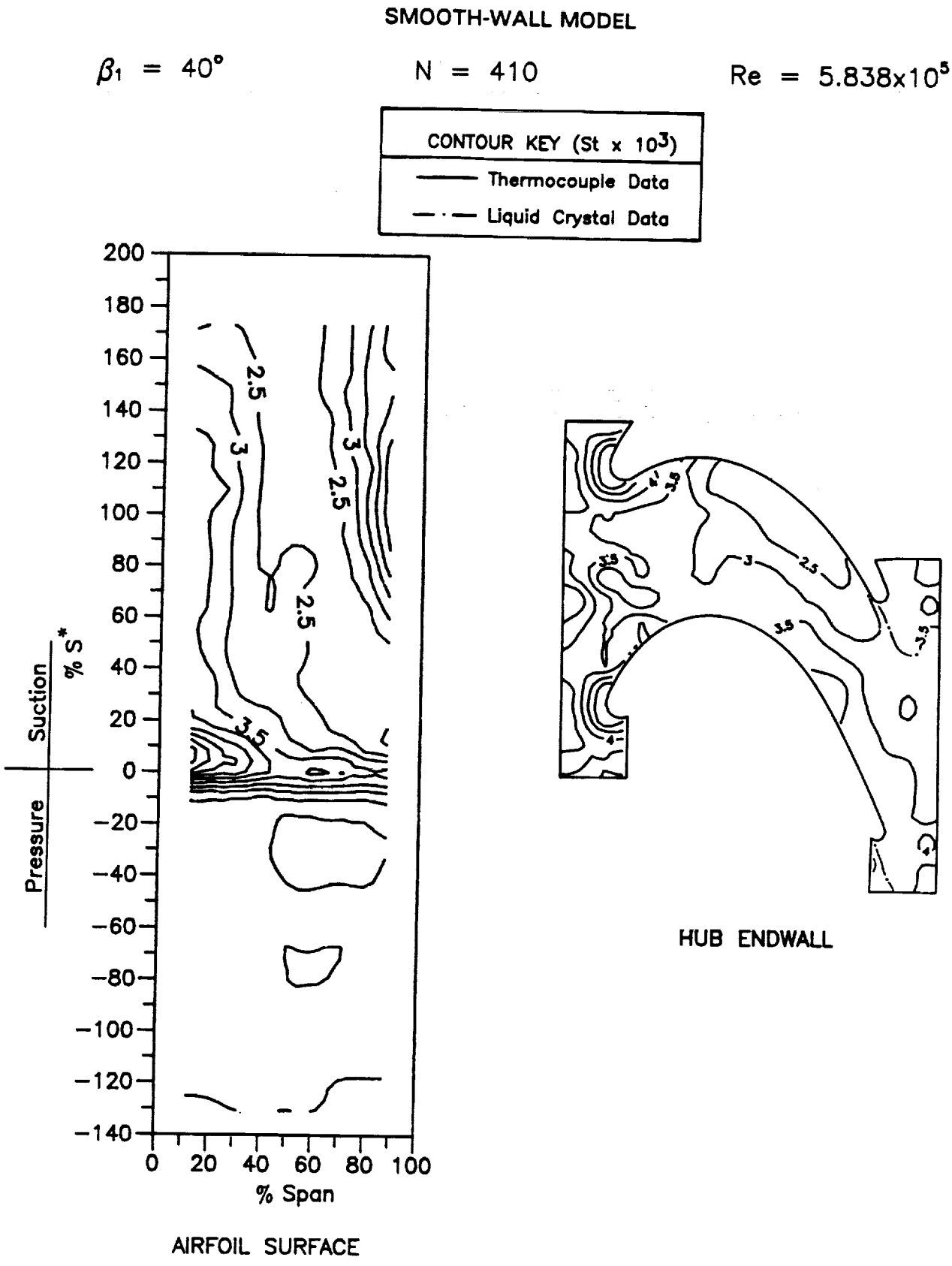

Figure 37a Stanton Number Contours on the Airfoil and Hub Endwall Surfaces

SMOOTH-WALL MODEL

β_1 = 40° N = 410 Re = 5.838×10^5

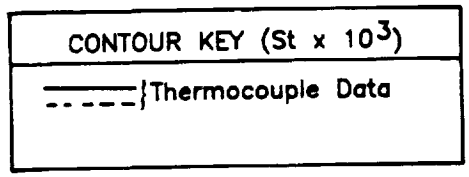

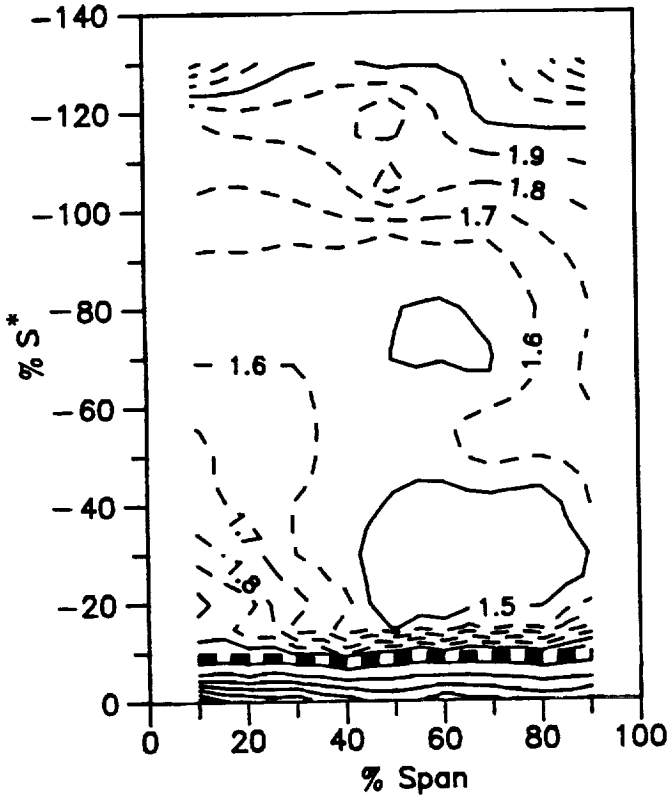

PRESSURE SURFACE

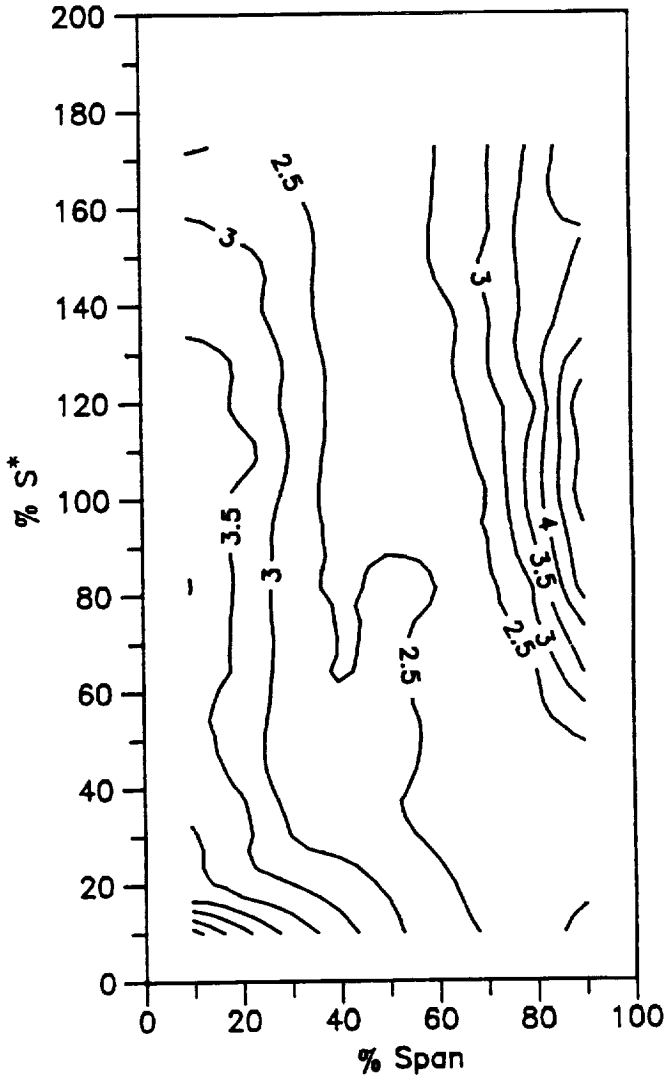

SUCTION SURFACE

Figure 37b Details of the Stanton Number Contours on the Airfoil Suction and Pressure Surfaces

SMOOTH-WALL MODEL

β_1 = 40° N = 410 Re = 5.838×10^5

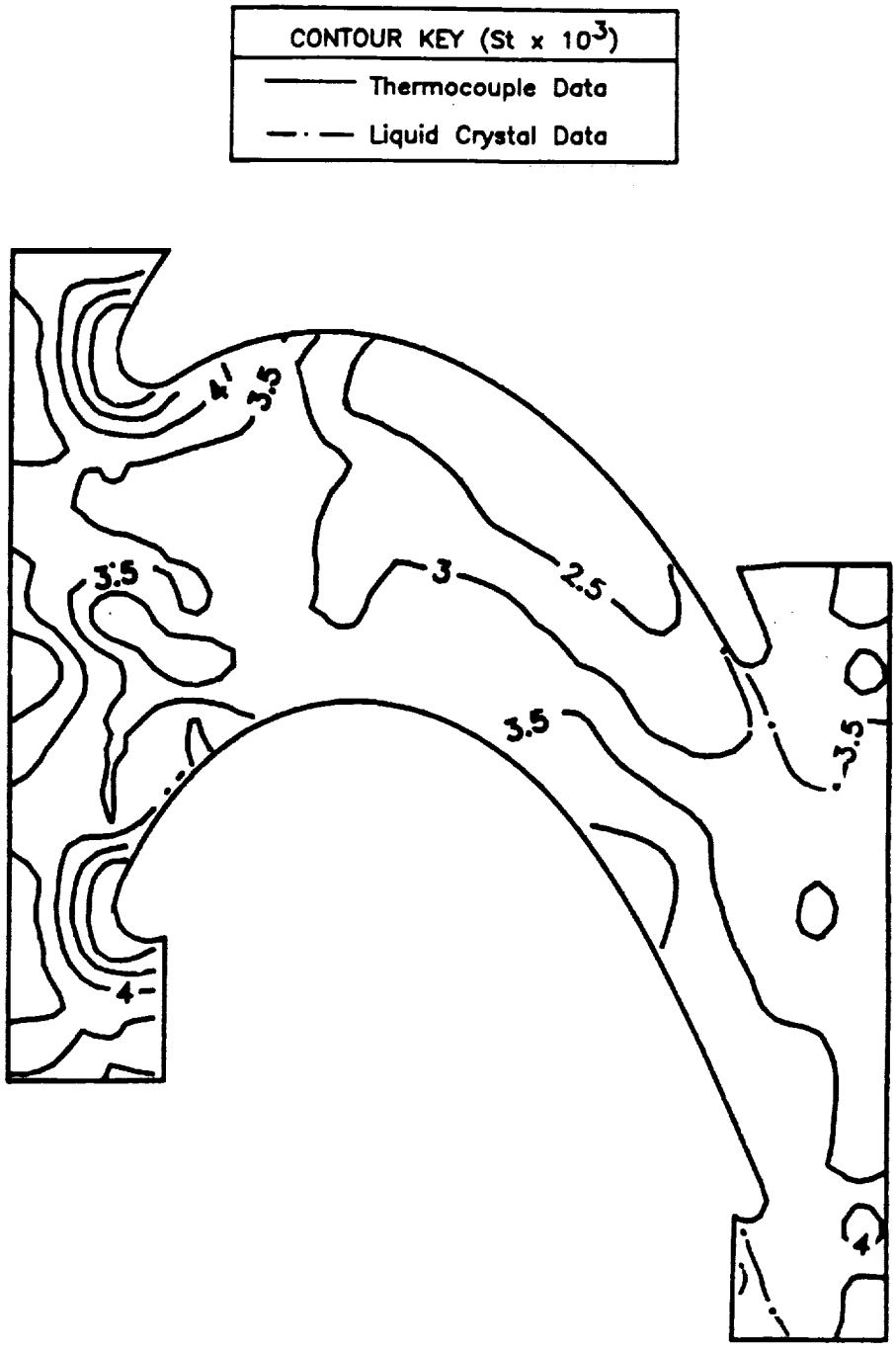

HUB ENDWALL

Figure 37c Details of the Stanton Number Contours on the Hub Endwall Surface

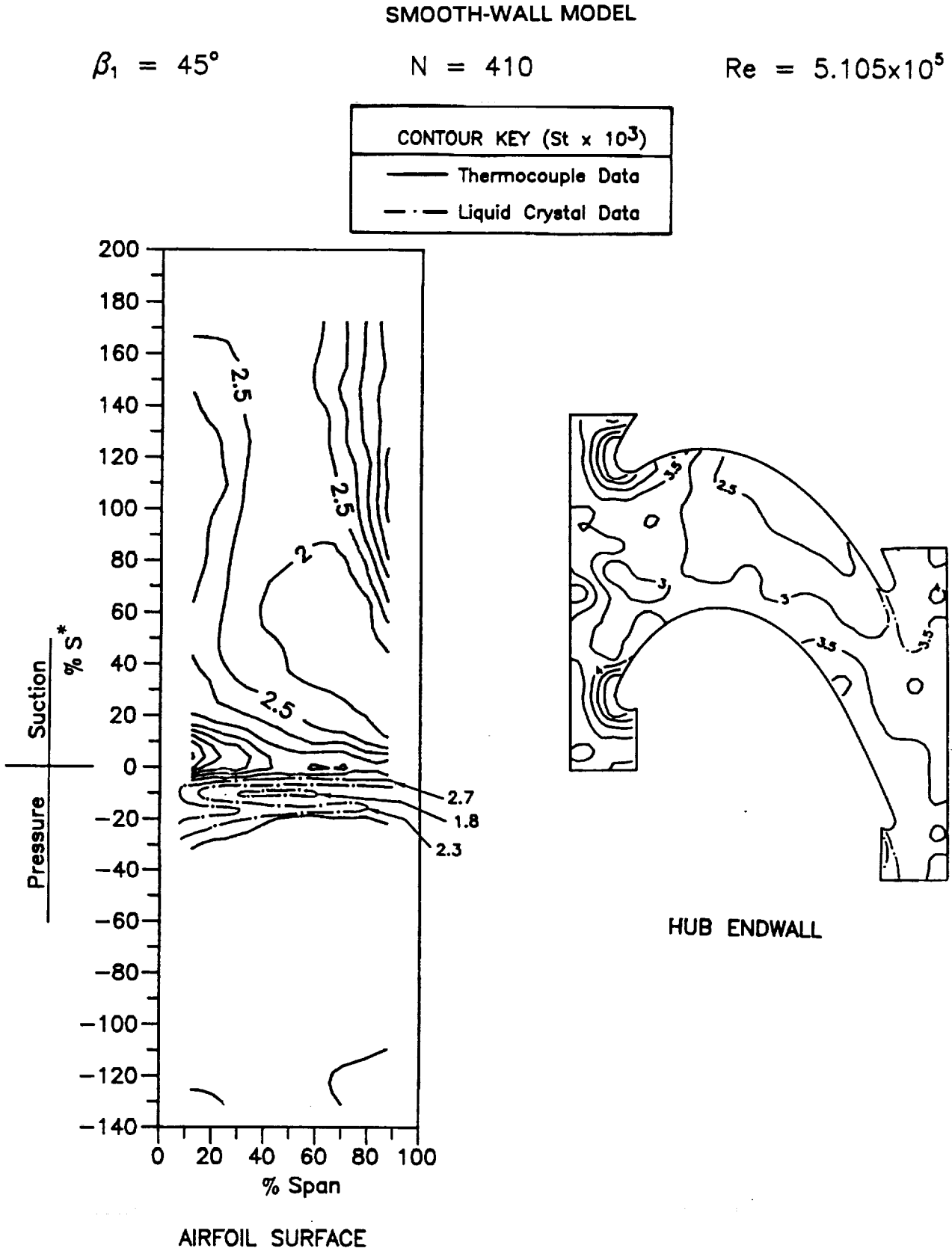

Figure 38a Stanton Number Contours on the Airfoil and Hub Endwall Surfaces

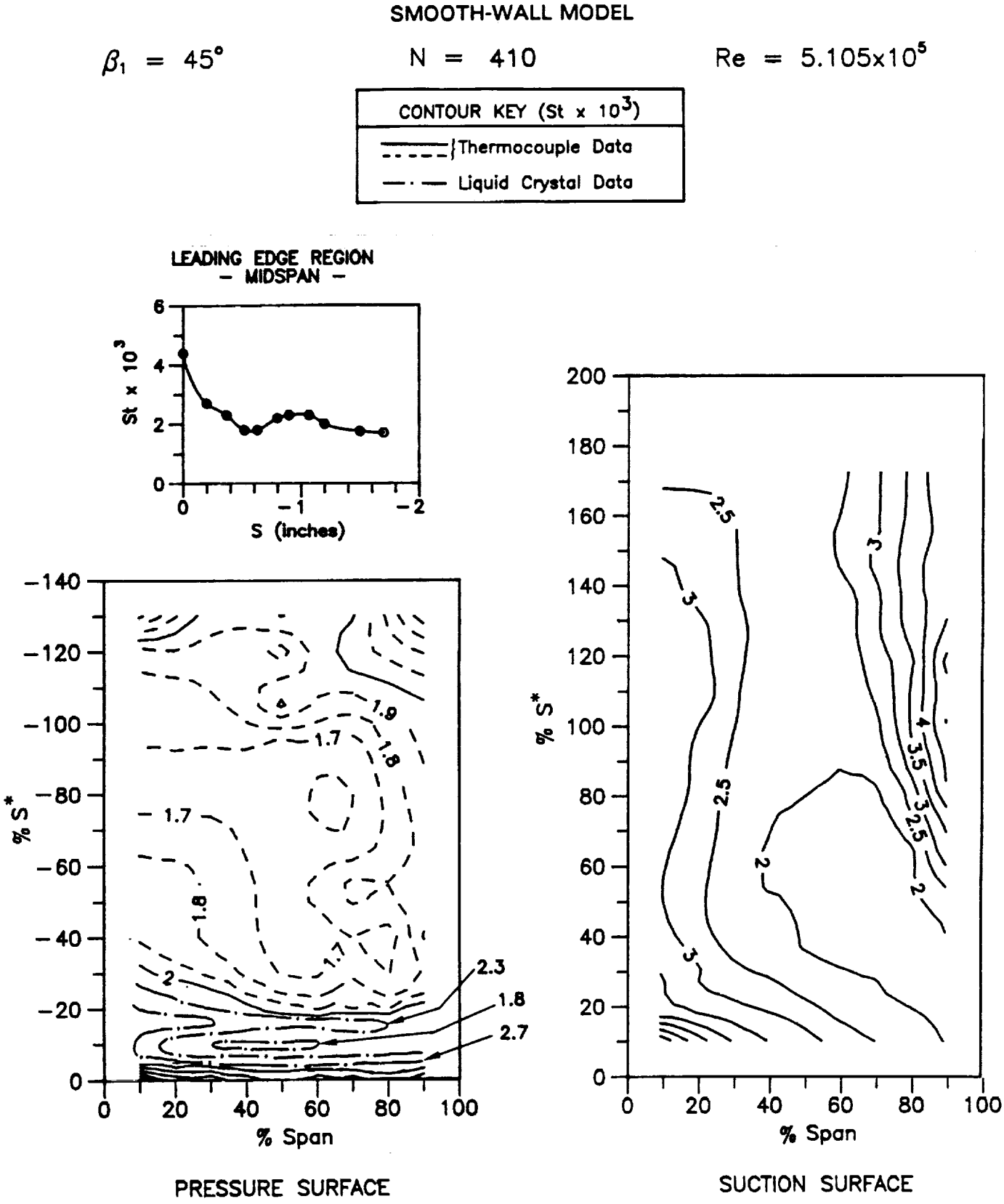

Figure 38b Details of the Stanton Number Contours on the Airfoil Suction and Pressure Surfaces

SMOOTH-WALL MODEL

β_1 = 45° N = 410 Re = 5.105x10^5

CONTOUR KEY (St x 10^3)
——— Thermocouple Data
—·— Liquid Crystal Data

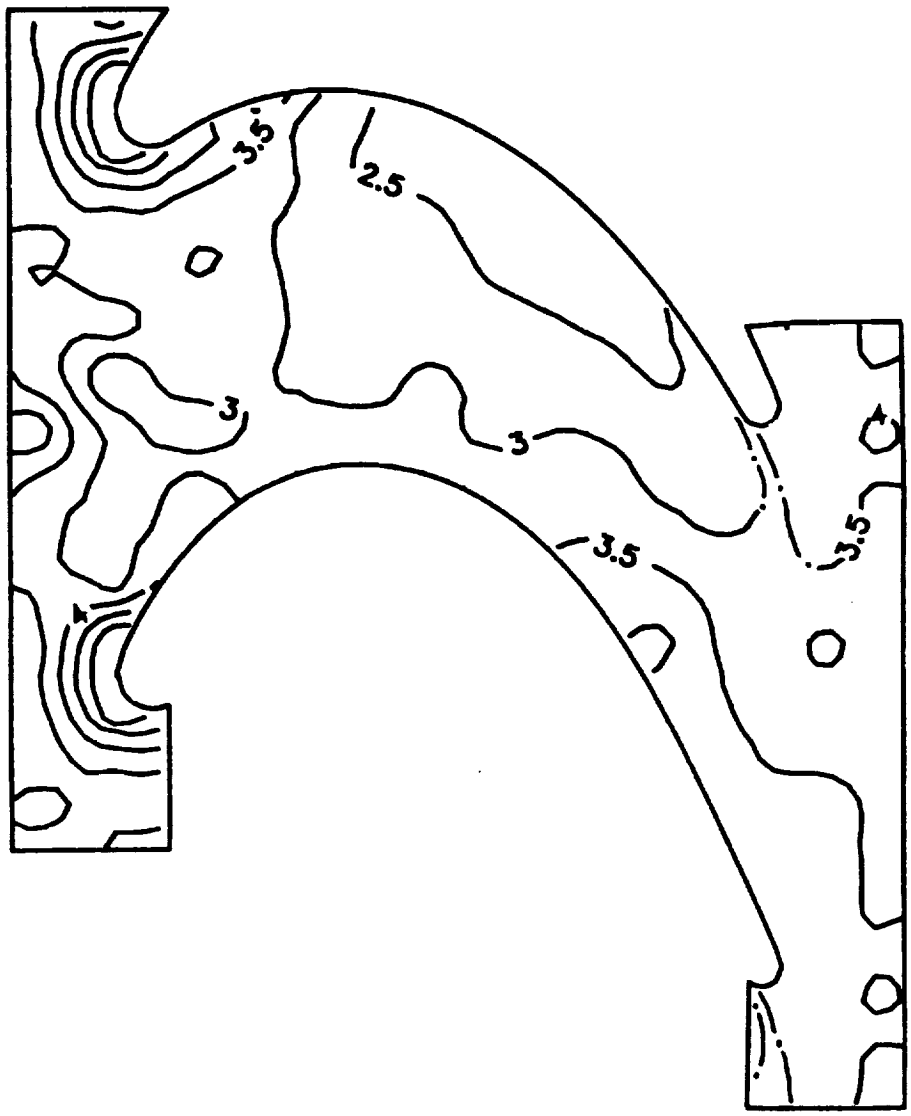

HUB ENDWALL

Figure 38c Details of the Stanton Number Contours on the Hub Endwall Surface

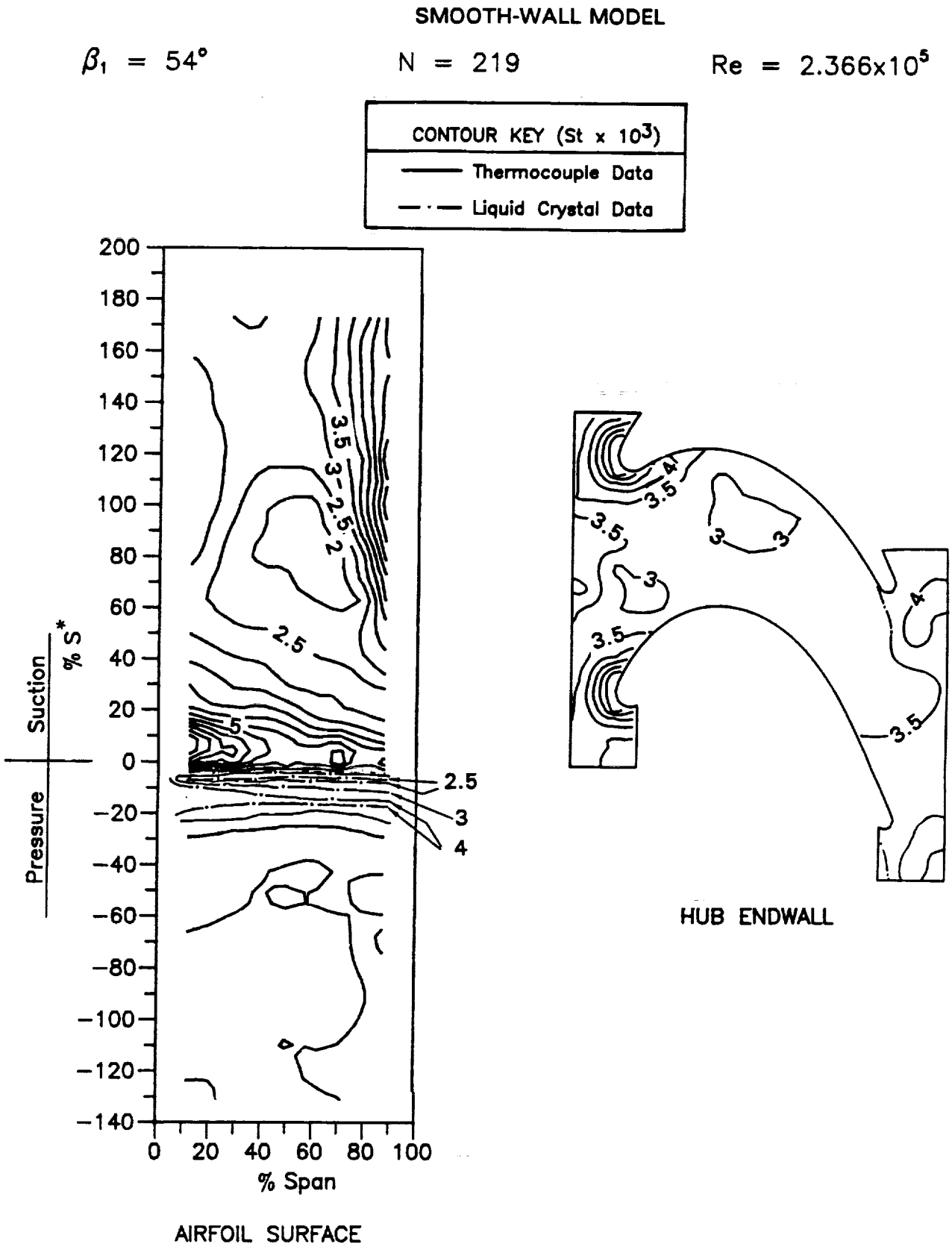

Figure 39a Stanton Number Contours on the Airfoil and Hub Endwall Surfaces

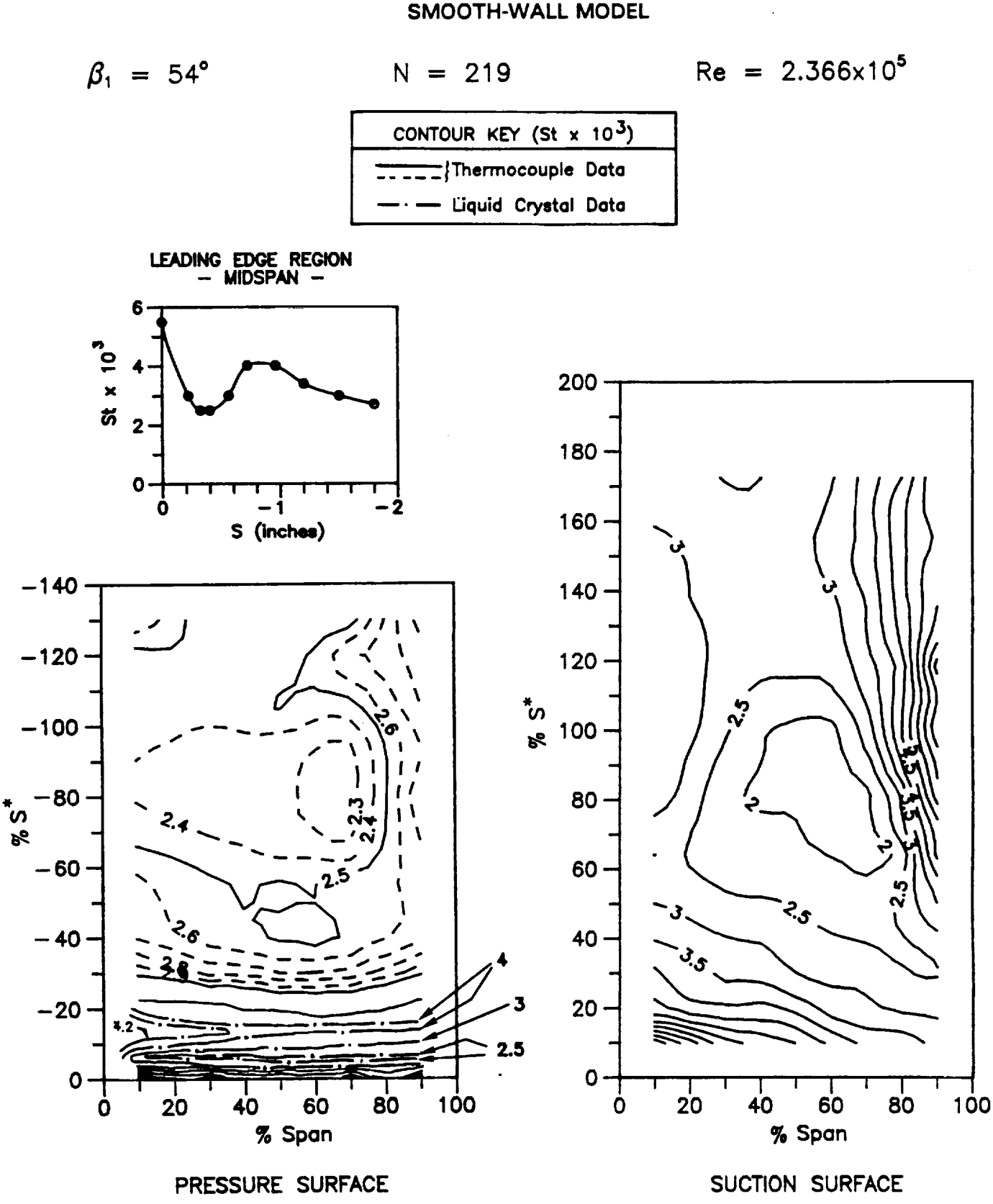

Figure 39b Details of the Stanton Number Contours on the Airfoil Suction and Pressure Surfaces

SMOOTH-WALL MODEL

$\beta_1 = 54°$ N = 219 Re = 2.366×10^5

CONTOUR KEY (St x 10^3)
——— Thermocouple Data
—·— Liquid Crystal Data

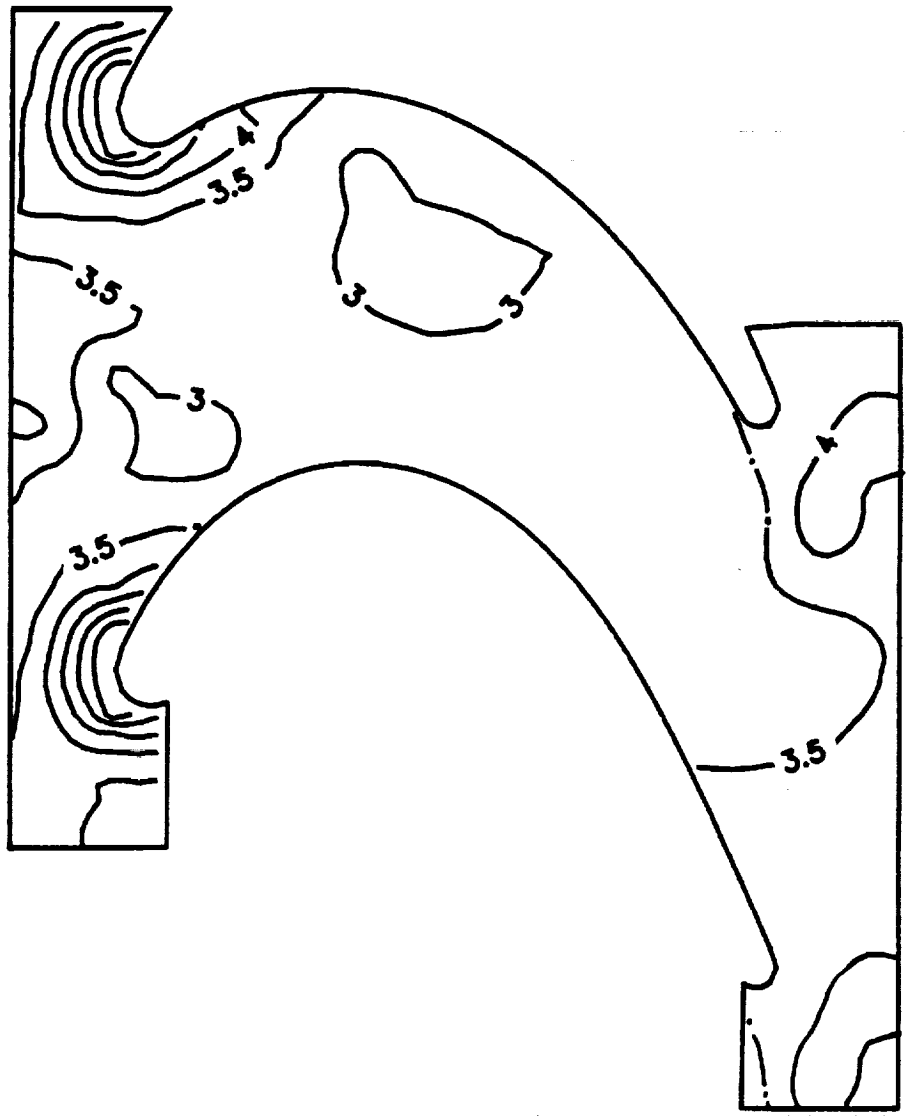

HUB ENDWALL

Figure 39c Details of the Stanton Number Contours on the Hub Endwall Surface

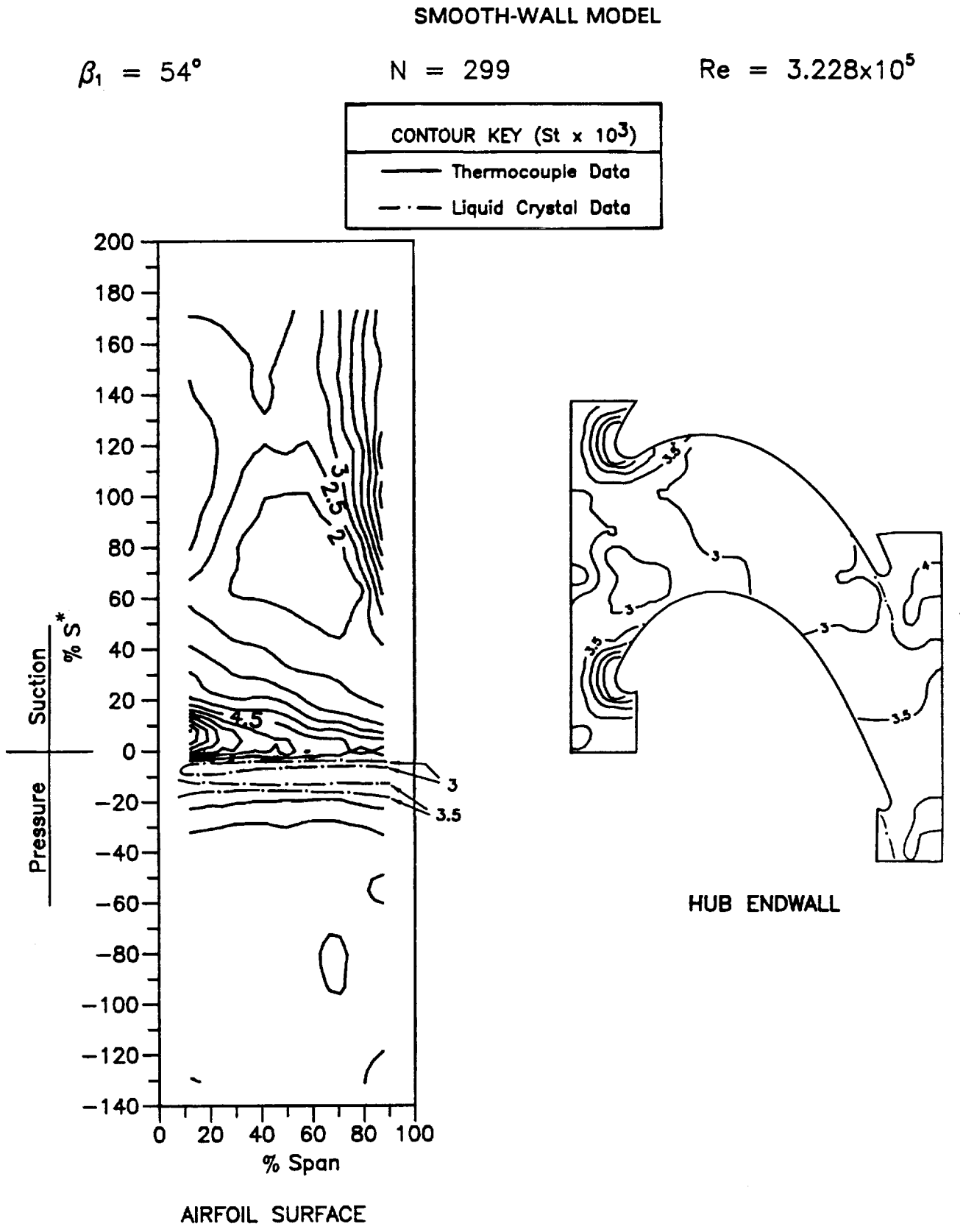

Figure 40a Stanton Number Contours on the Airfoil and Hub Endwall Surfaces

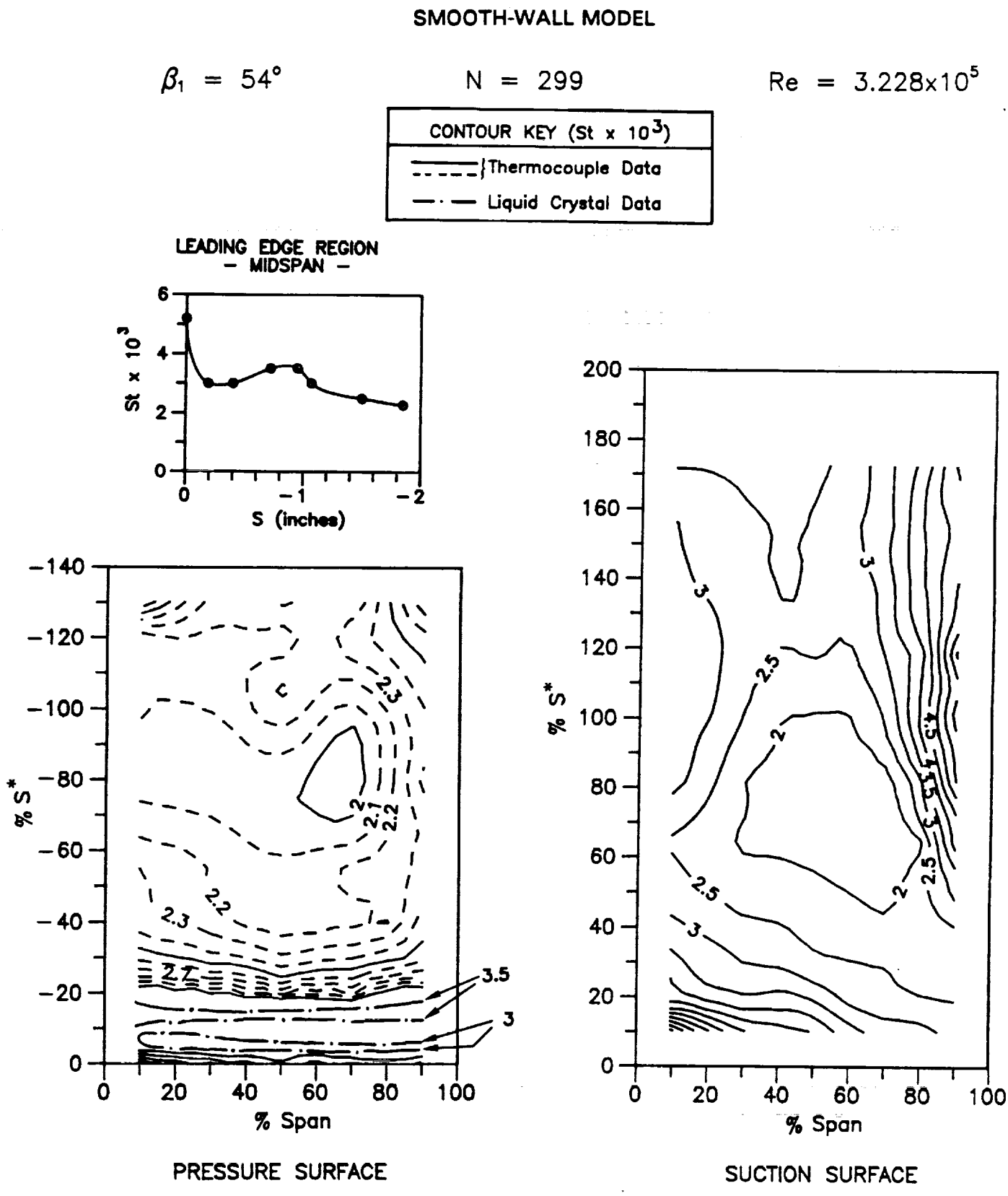

Figure 40b Details of the Stanton Number Contours on the Airfoil Suction and Pressure Surfaces

SMOOTH-WALL MODEL

$\beta_1 = 54°$ N = 299 Re = 3.228×10^5

CONTOUR KEY (St x 10^3)
——— Thermocouple Data
—·— Liquid Crystal Data

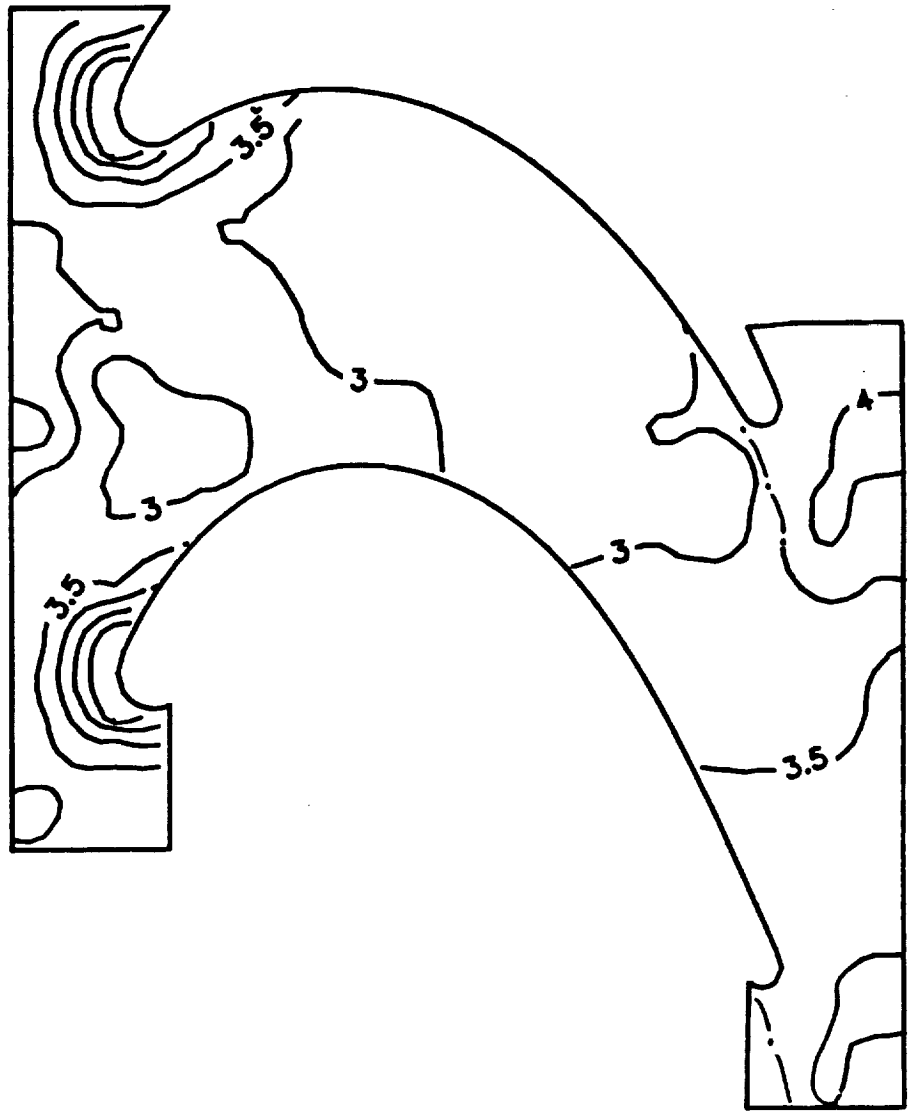

HUB ENDWALL

Figure 40c Details of the Stanton Number Contours on the Hub Endwall Surface

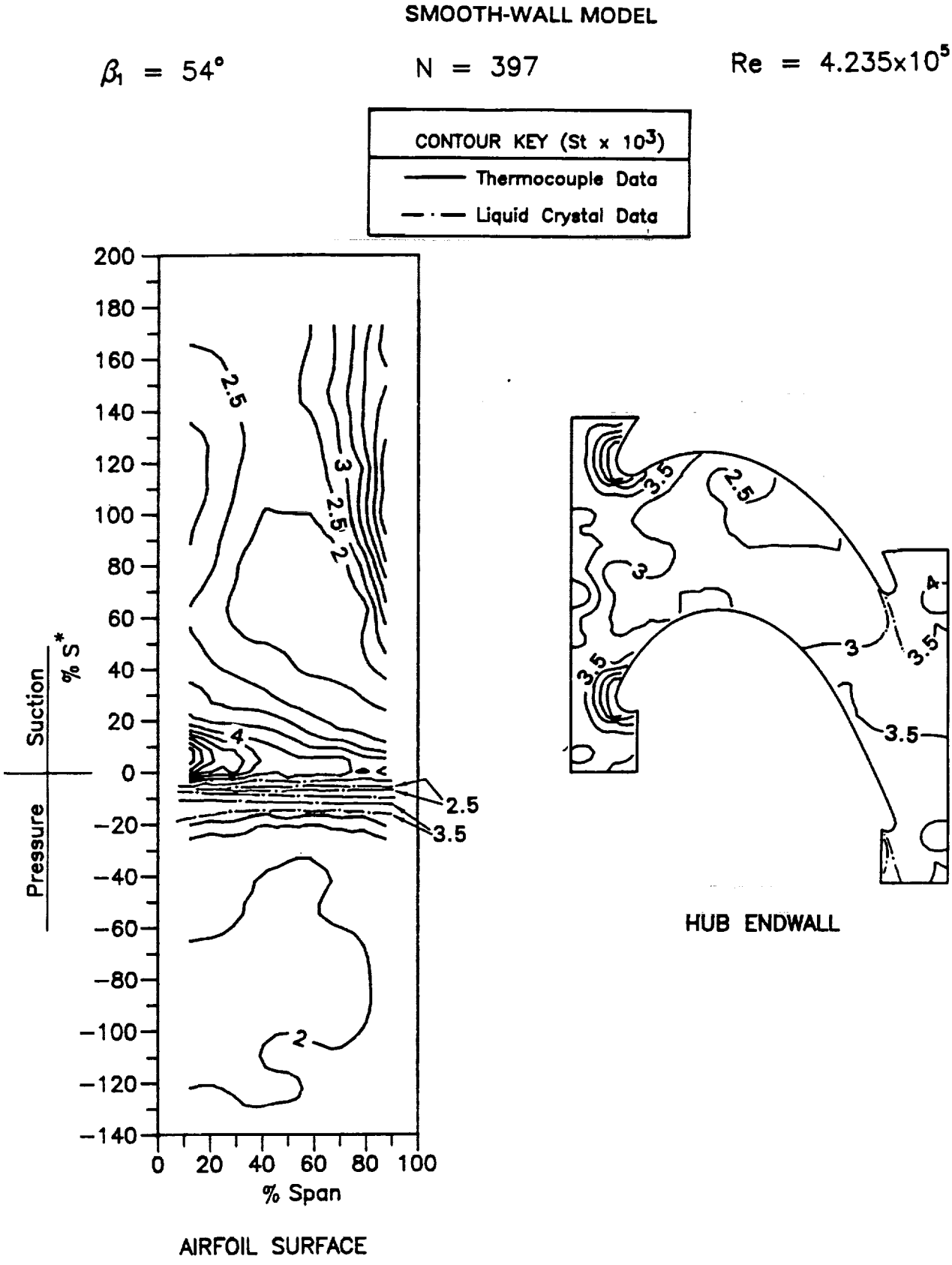

Figure 41a Stanton Number Contours on the Airfoil and Hub Endwall Surfaces

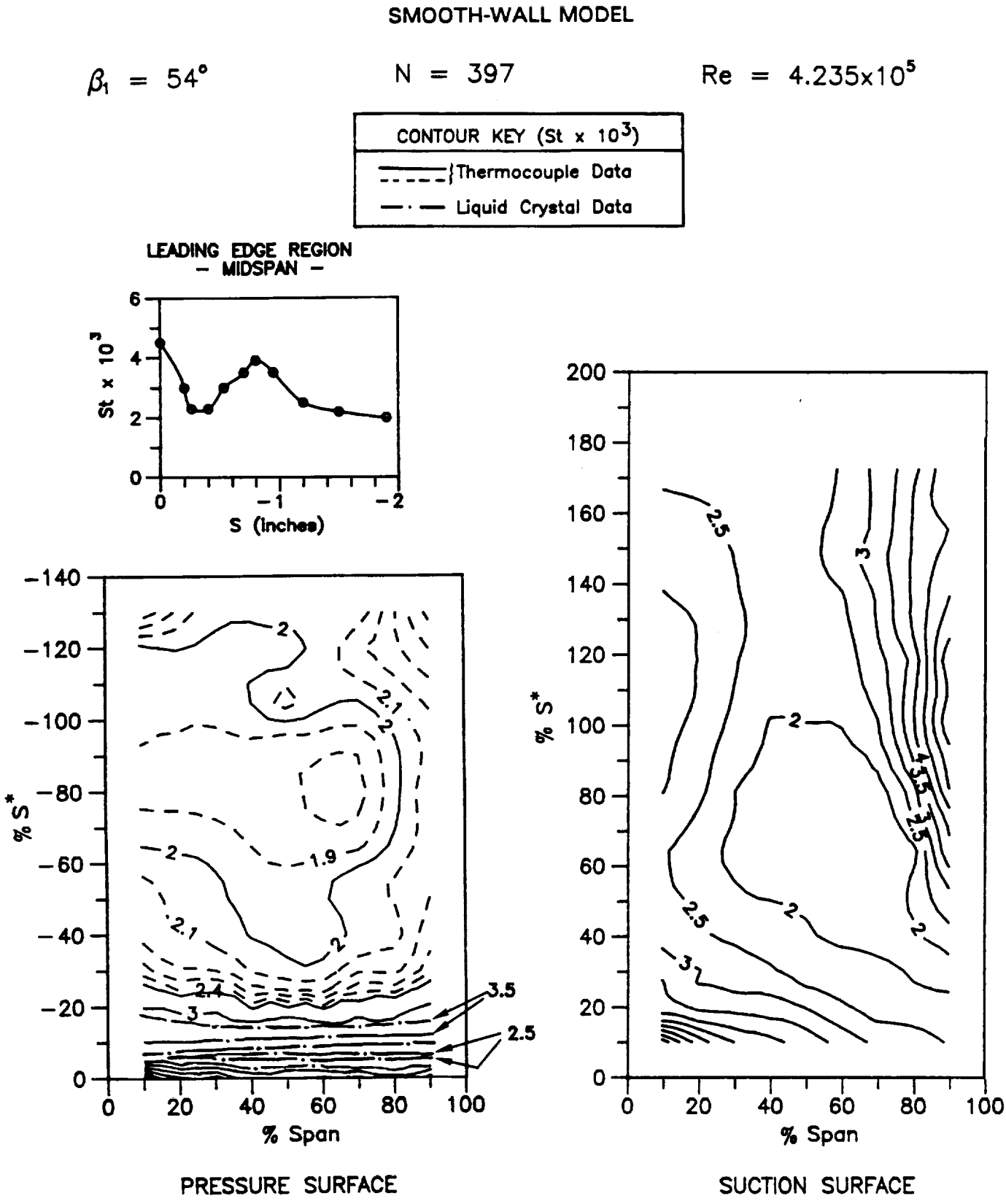

Figure 41b Details of the Stanton Number Contours on the Airfoil Suction and Pressure Surfaces

SMOOTH-WALL MODEL

β_1 = 54° N = 397 Re = 4.235×10^5

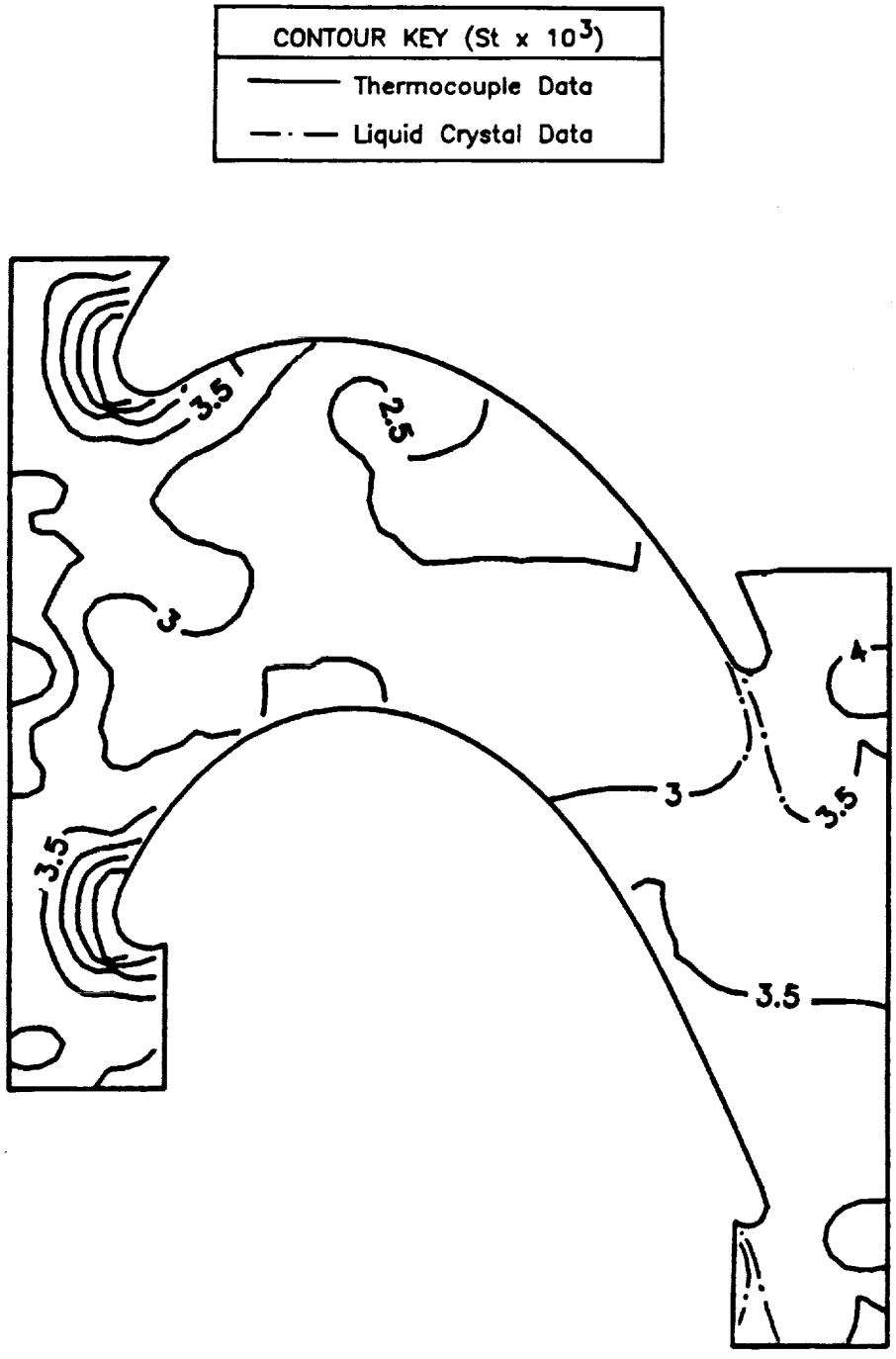

HUB ENDWALL

Figure 41c Details of the Stanton Number Contours on the Hub Endwall Surface

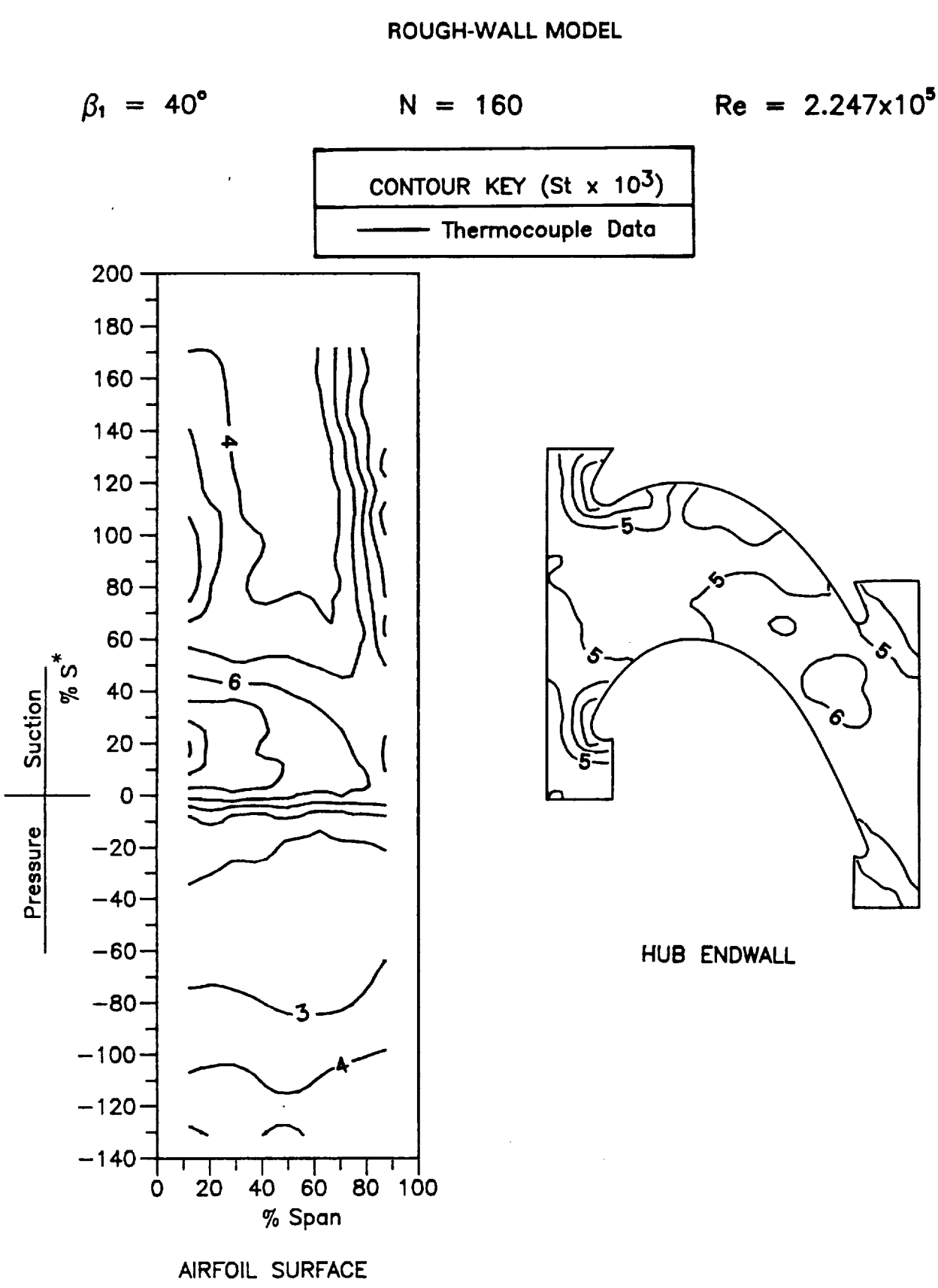

Figure 42a Stanton Number Contours on the Airfoil and Hub Endwall Surfaces

ROUGH-WALL MODEL

$\beta_1 = 40°$ N = 160 Re = 2.247×10^5

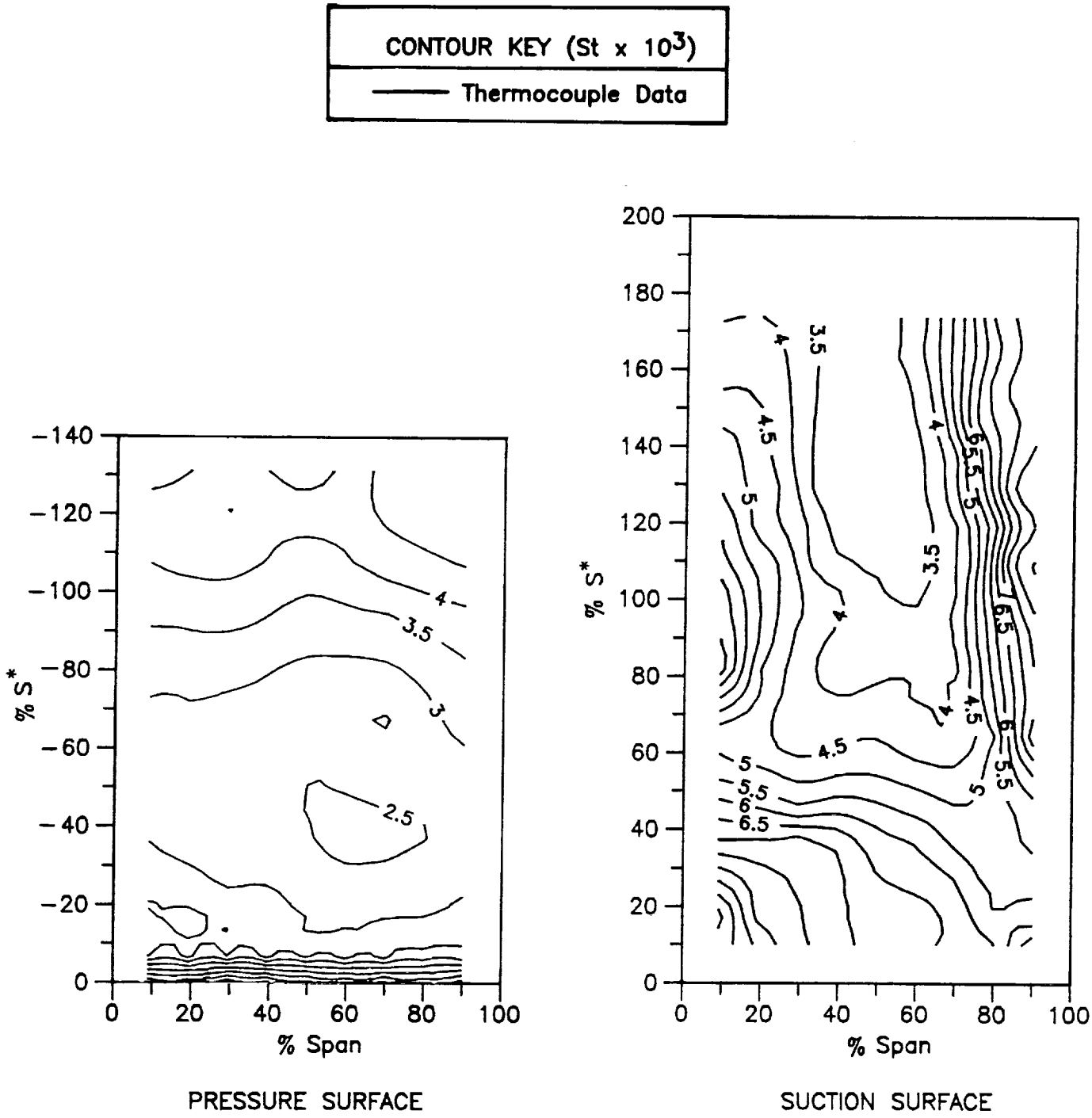

Figure 42b Details of the Stanton Number Contours on the Airfoil Suction and Pressure Surfaces

ROUGH-WALL MODEL

β_1 = 40° N = 160 Re = 2.247×10^5

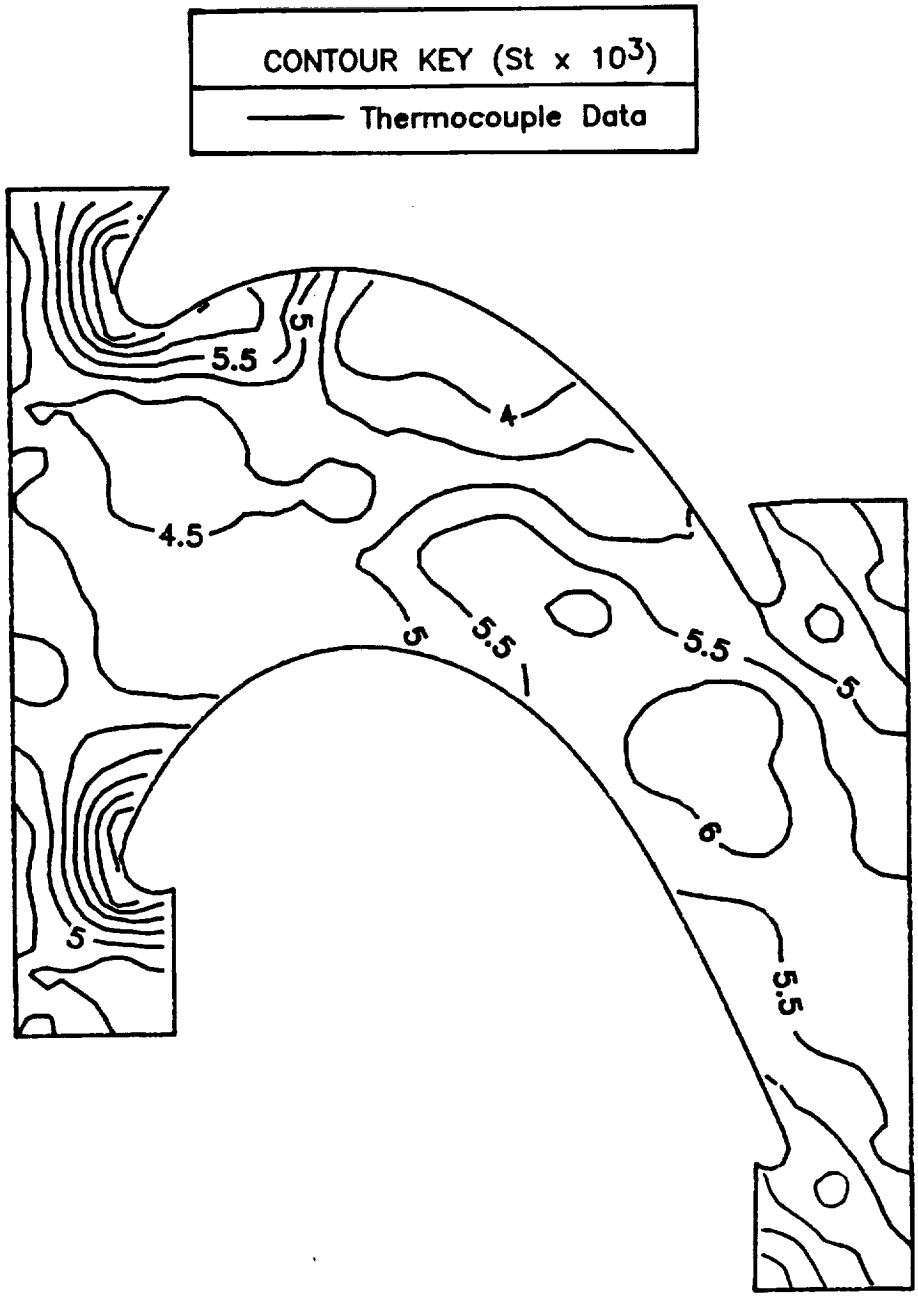

HUB ENDWALL

Figure 42c Details of the Stanton Number Contours on the Hub Endwall Surface

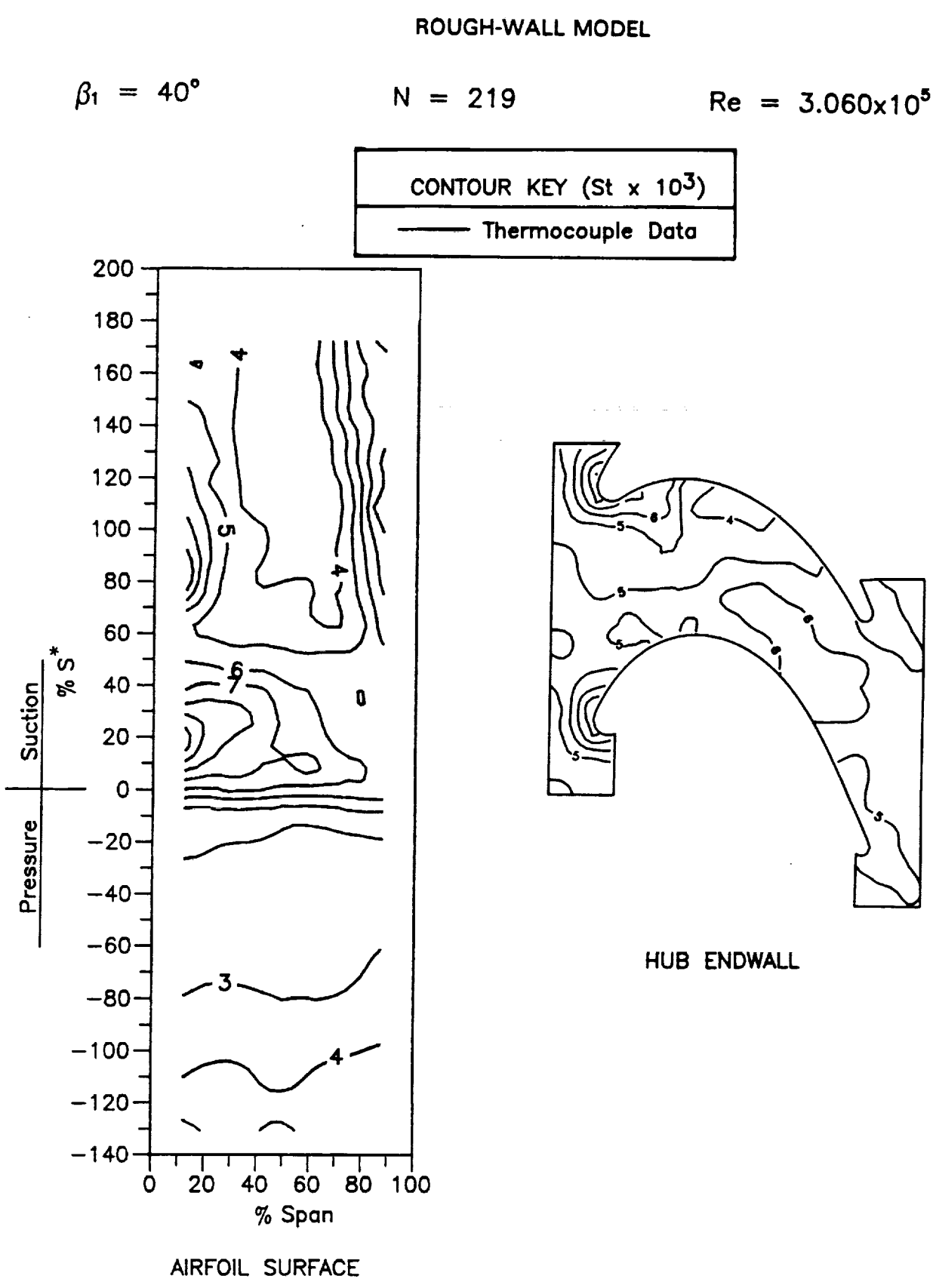

Figure 43a Stanton Number Contours on the Airfoil and Hub Endwall Surfaces

ROUGH-WALL MODEL

$\beta_1 = 40°$ N = 219 Re = 3.060×10^5

CONTOUR KEY (St x 10^3)

Thermocouple Data

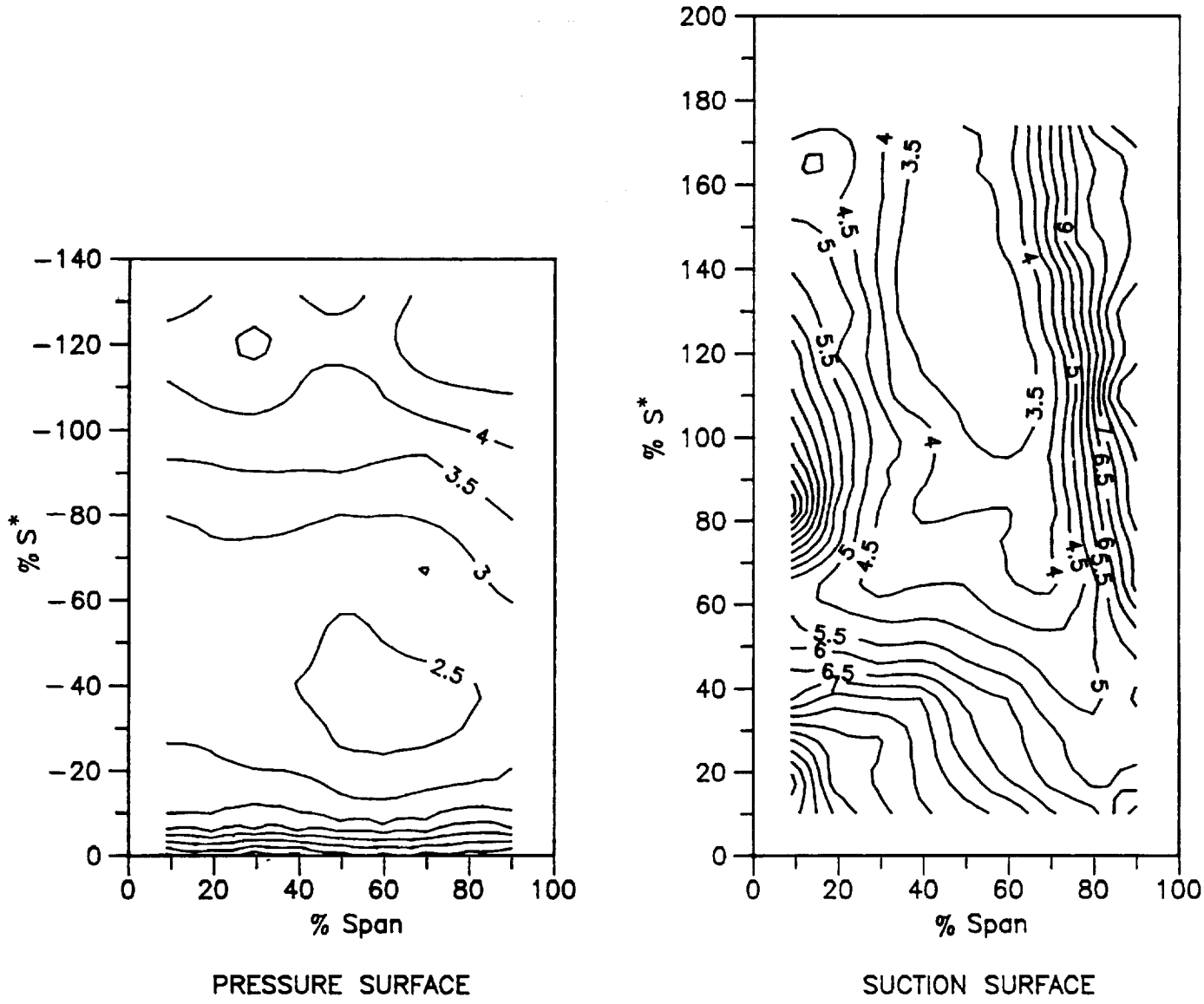

Figure 43b Details of the Stanton Number Contours on the Airfoil Suction and Pressure Surfaces

ROUGH-WALL MODEL

β_1 = 40° N = 219 Re = 3.060×10^5

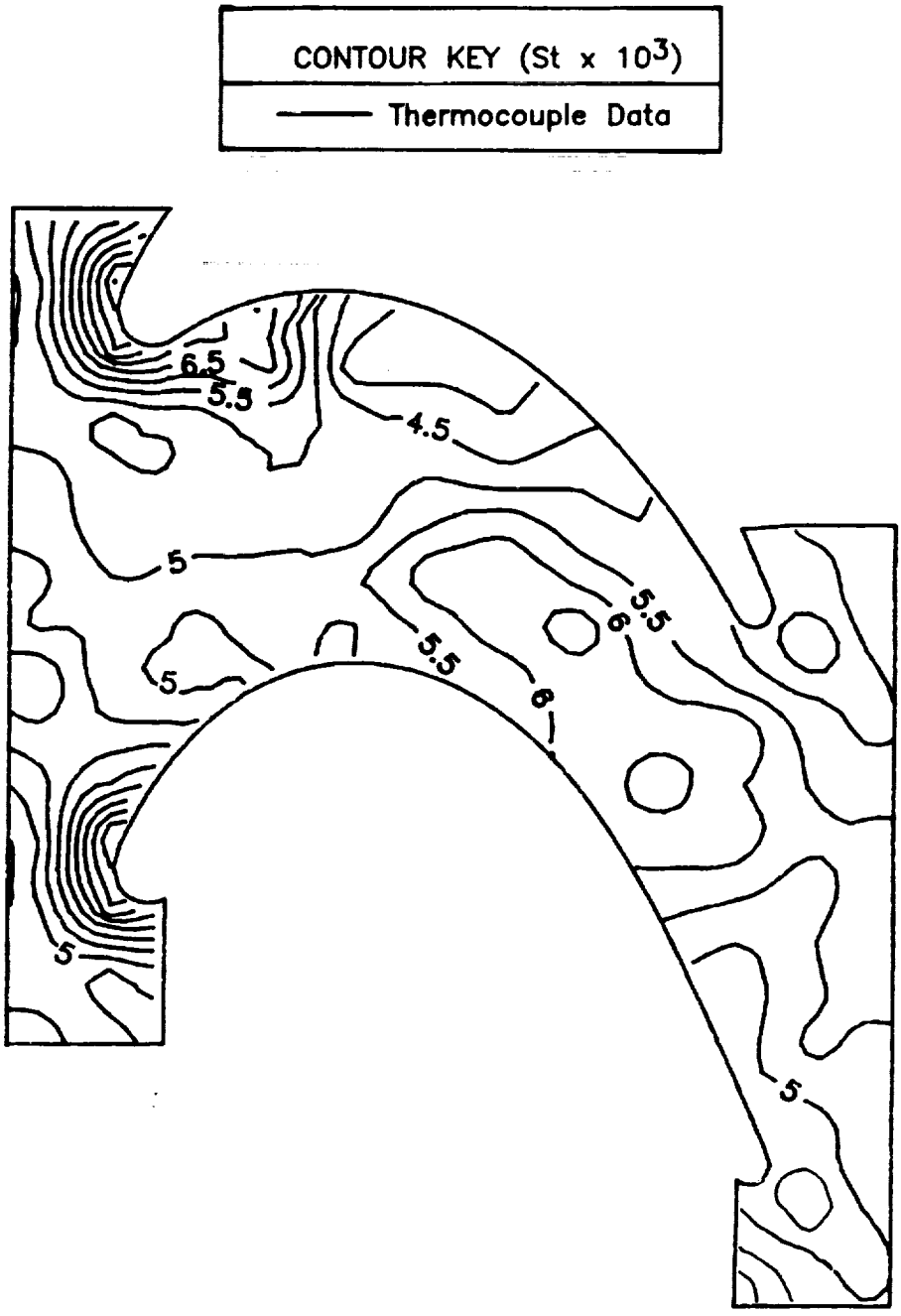

HUB ENDWALL

Figure 43c Details of the Stanton Number Contours on the Hub Endwall Surface

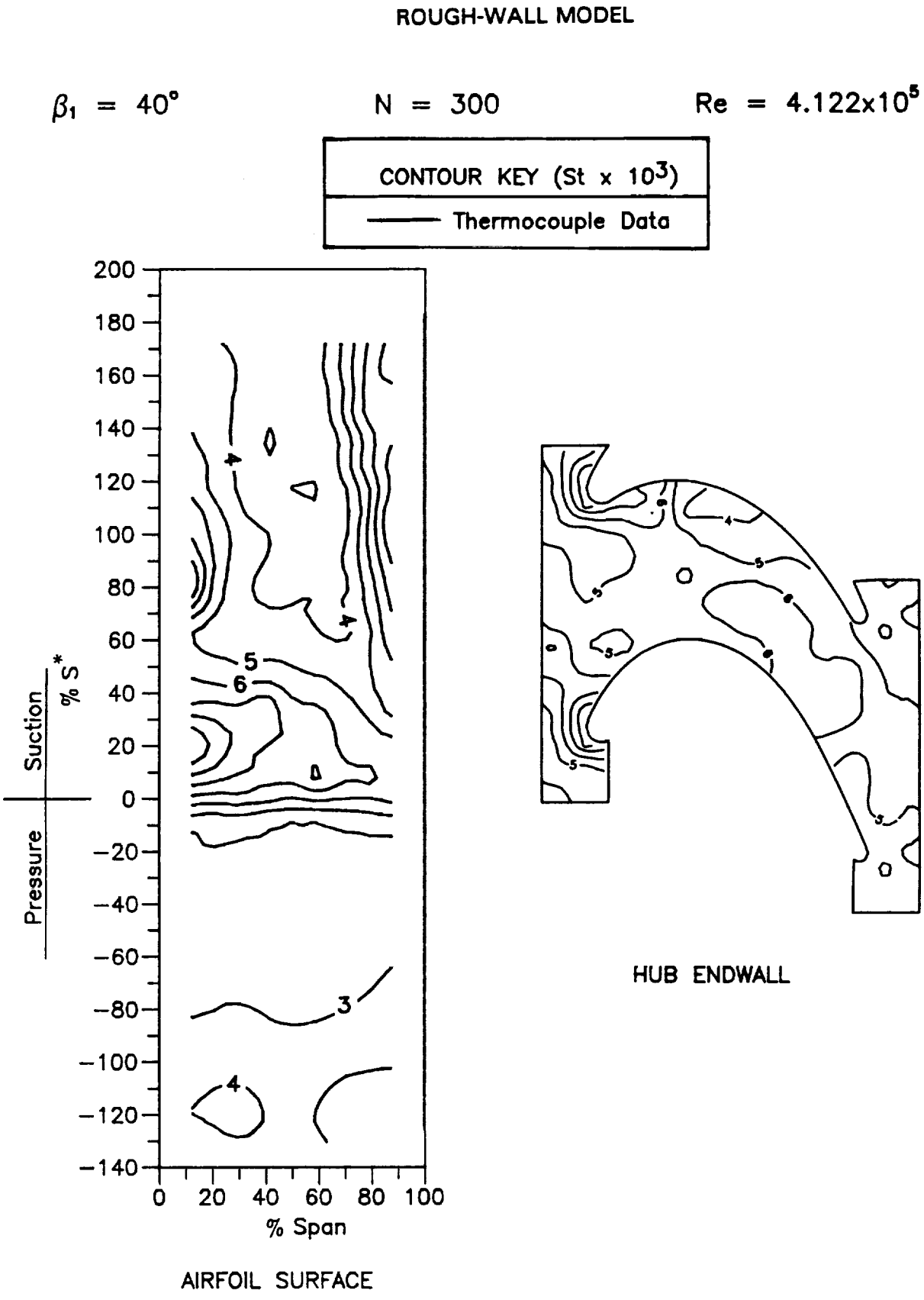

Figure 44a Stanton Number Contours on the Airfoil and Hub Endwall Surfaces

ROUGH-WALL MODEL

$\beta_1 = 40°$ N = 300 Re = 4.122×10^5

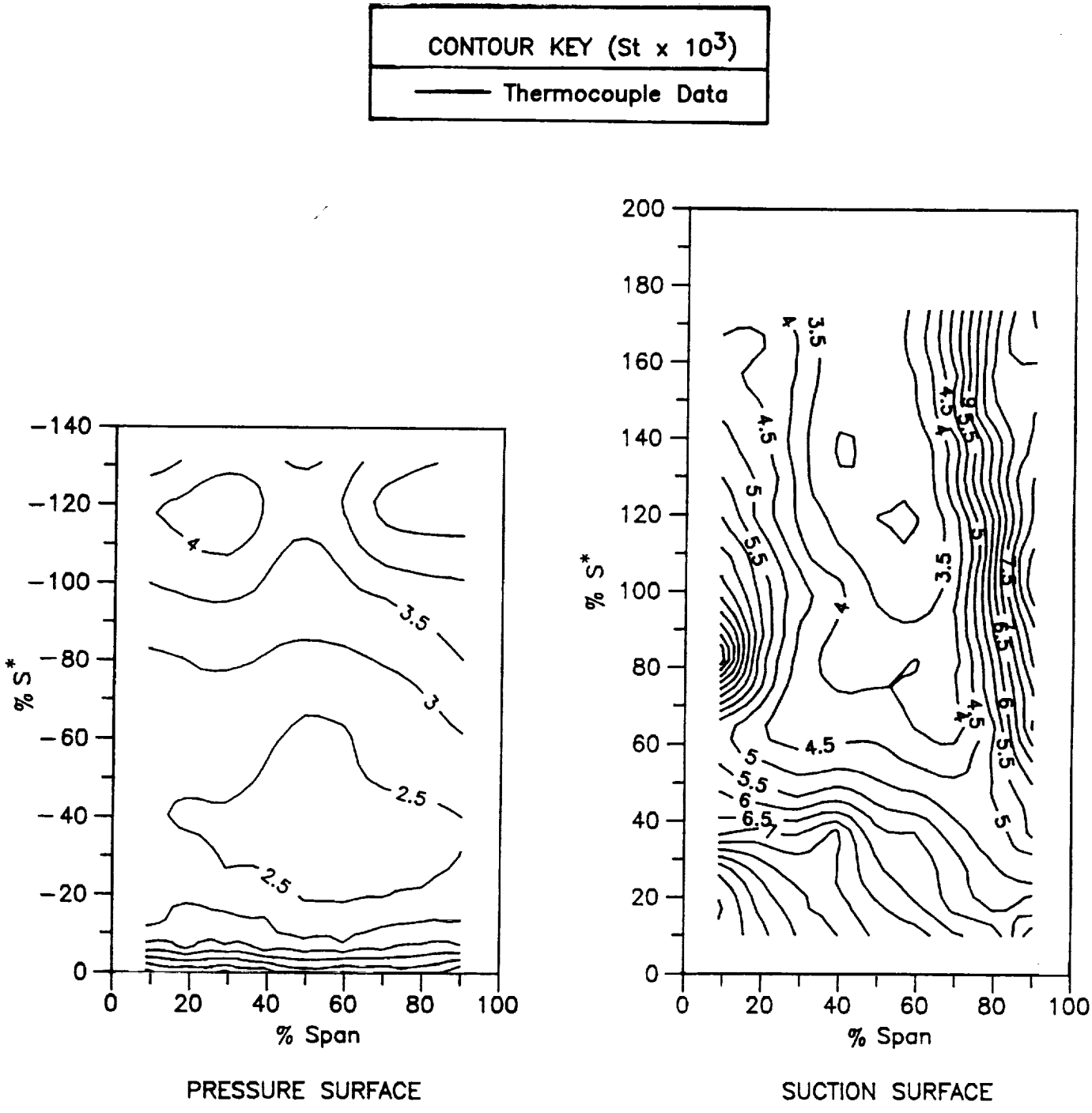

Figure 44b Details of the Stanton Number Contours on the Airfoil Suction and Pressure Surfaces

ROUGH-WALL MODEL

β_1 = 40° N = 300 Re = 4.122×10^5

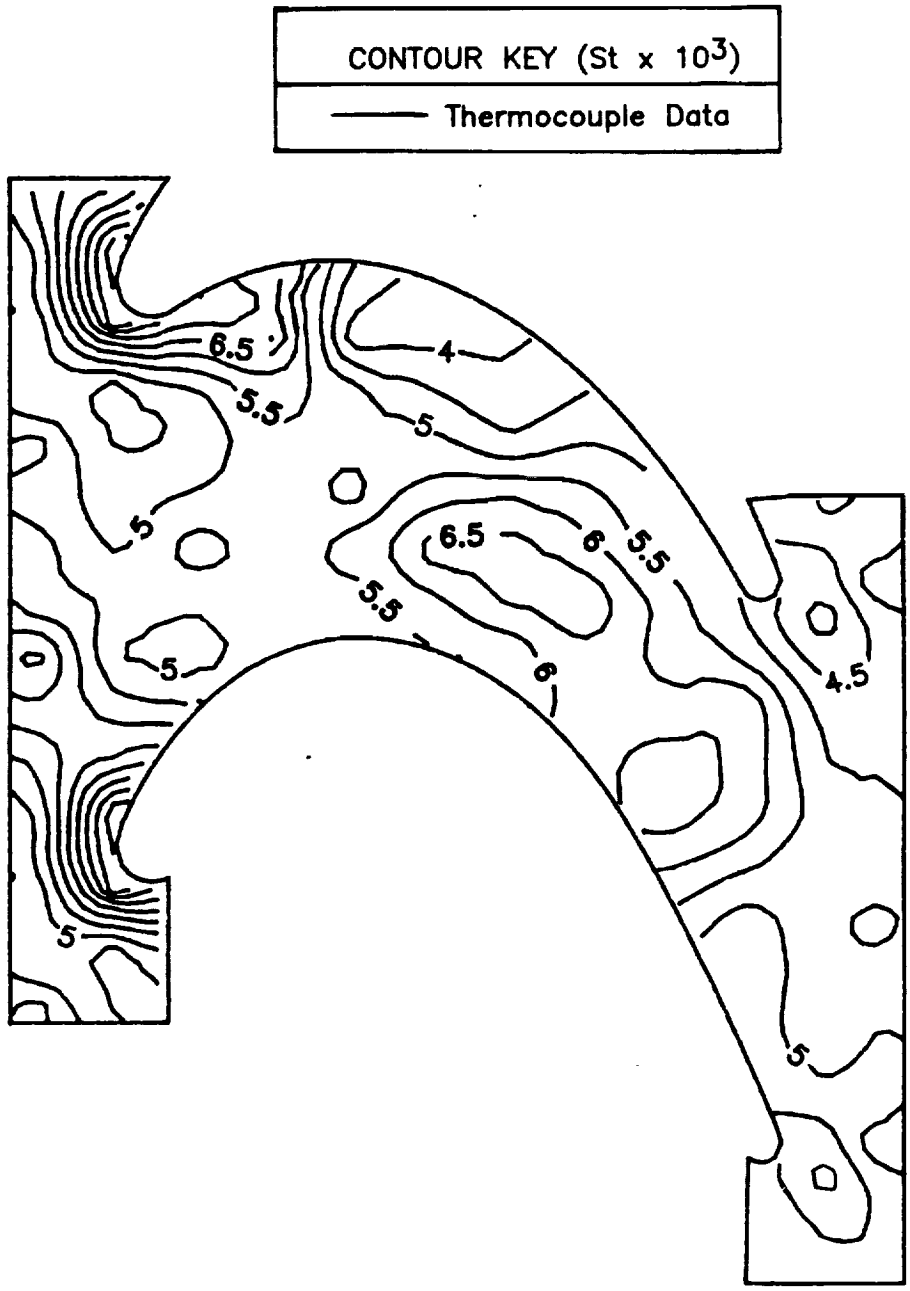

HUB ENDWALL

Figure 44c Details of the Stanton Number Contours on the Hub Endwall Surface

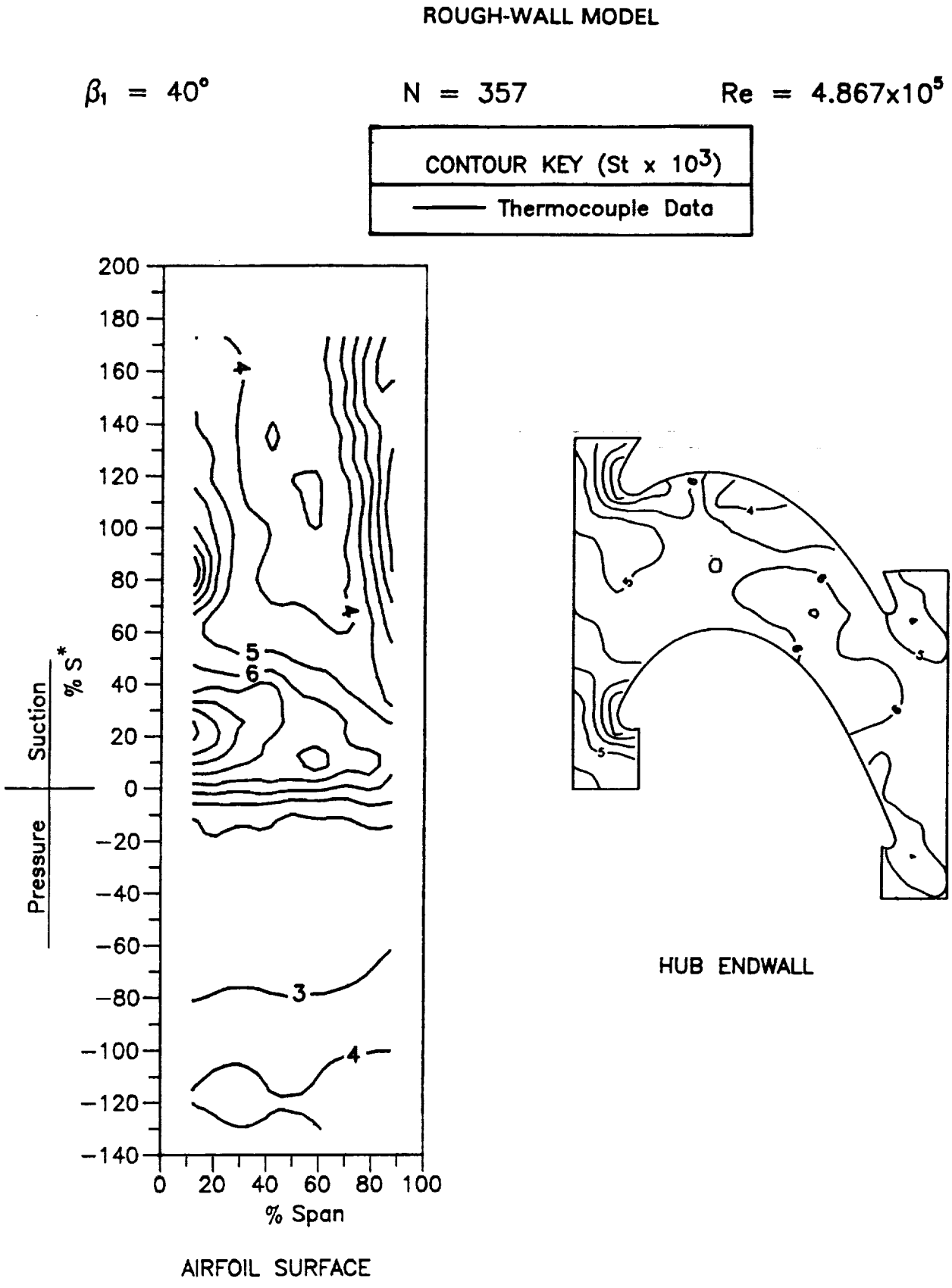

Figure 45a Stanton Number Contours on the Airfoil and Hub Endwall Surfaces

ROUGH-WALL MODEL

β_1 = 40° N = 357 Re = 4.867×10^5

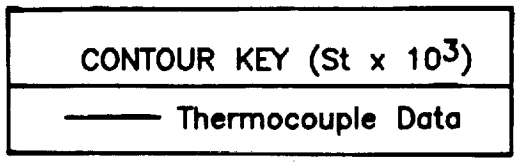

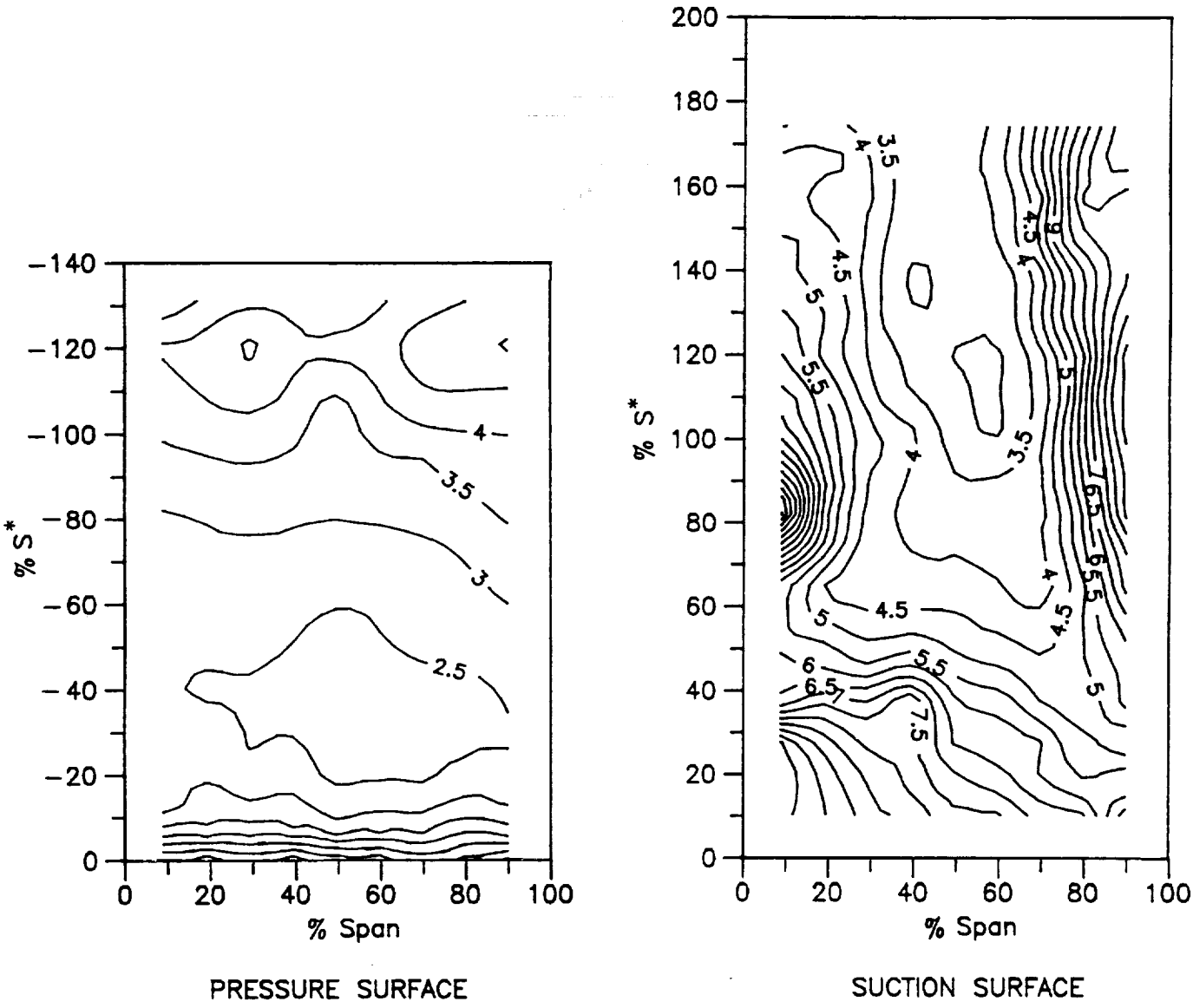

Figure 45b Details of the Stanton Number Contours on the Airfoil Suction and Pressure Surfaces

ROUGH-WALL MODEL

β_1 = 40° N = 357 Re = 4.867×10^5

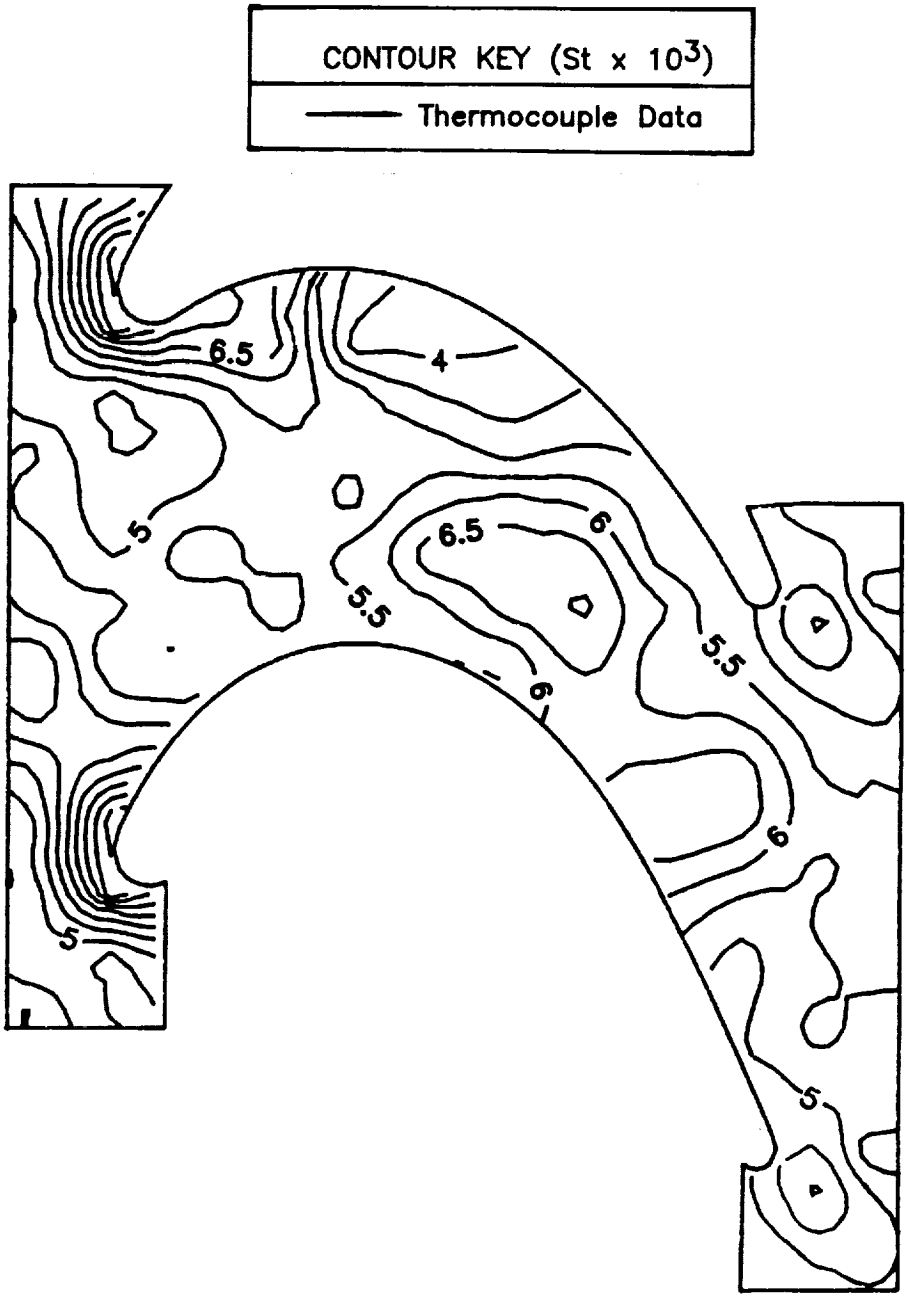

HUB ENDWALL

Figure 45c Details of the Stanton Number Contours on the Hub Endwall Surface

ROUGH-WALL MODEL

β_1 = 40° N = 410 Re = 5.533x10^5

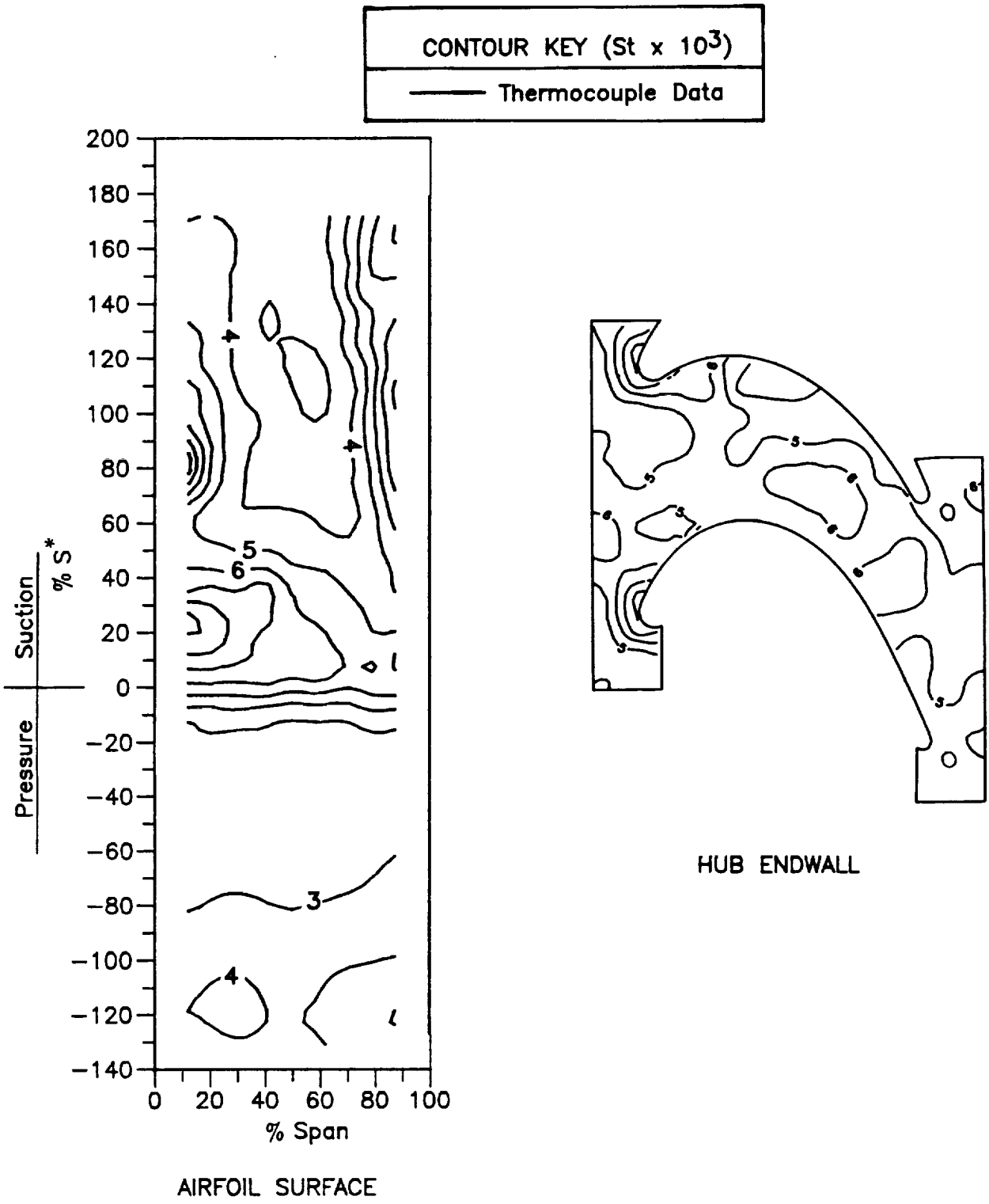

Figure 46a Stanton Number Contours on the Airfoil and Hub Endwall Surfaces

ROUGH-WALL MODEL

$\beta_1 = 40°$ N = 410 Re = 5.533×10^5

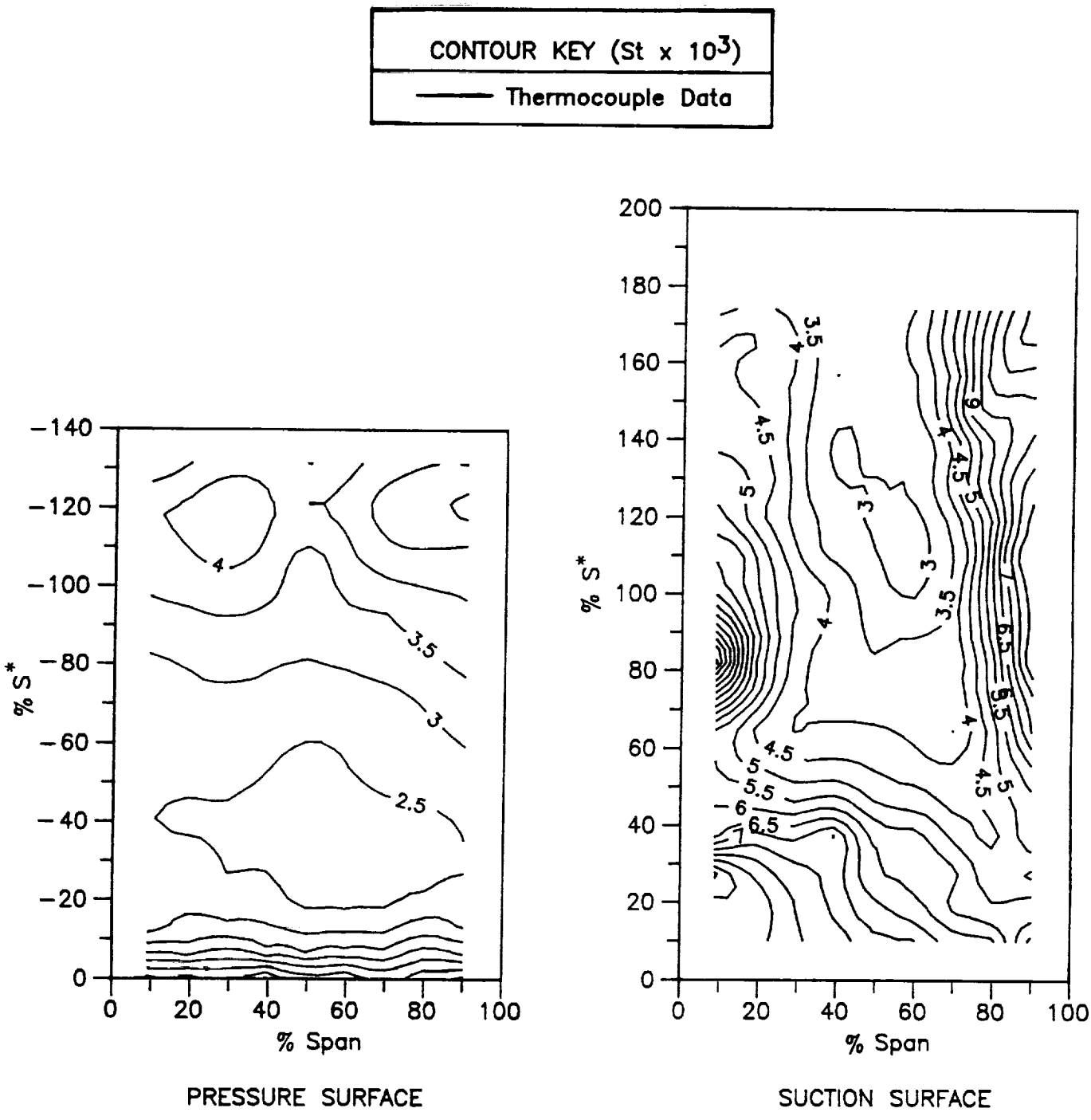

Figure 46b Details of the Stanton Number Contours on the Airfoil Suction and Pressure Surfaces

ROUGH-WALL MODEL

β_1 = 40° N = 410 Re = 5.533×10^5

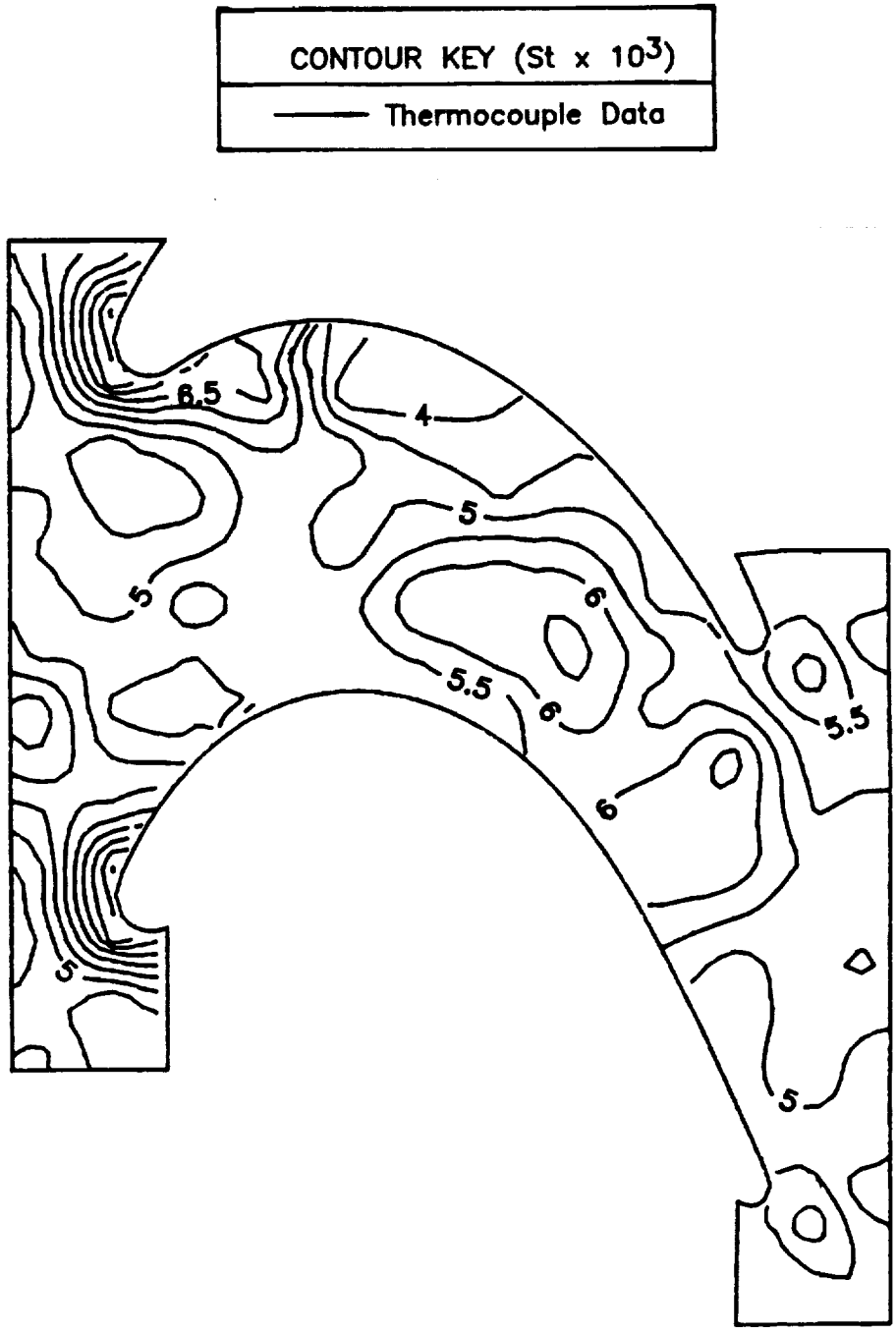

HUB ENDWALL

Figure 46c Details of the Stanton Number Contours on the Hub Endwall Surface

ROUGH-WALL MODEL

β_1 = 45° N = 409 Re = 4.889x10^5

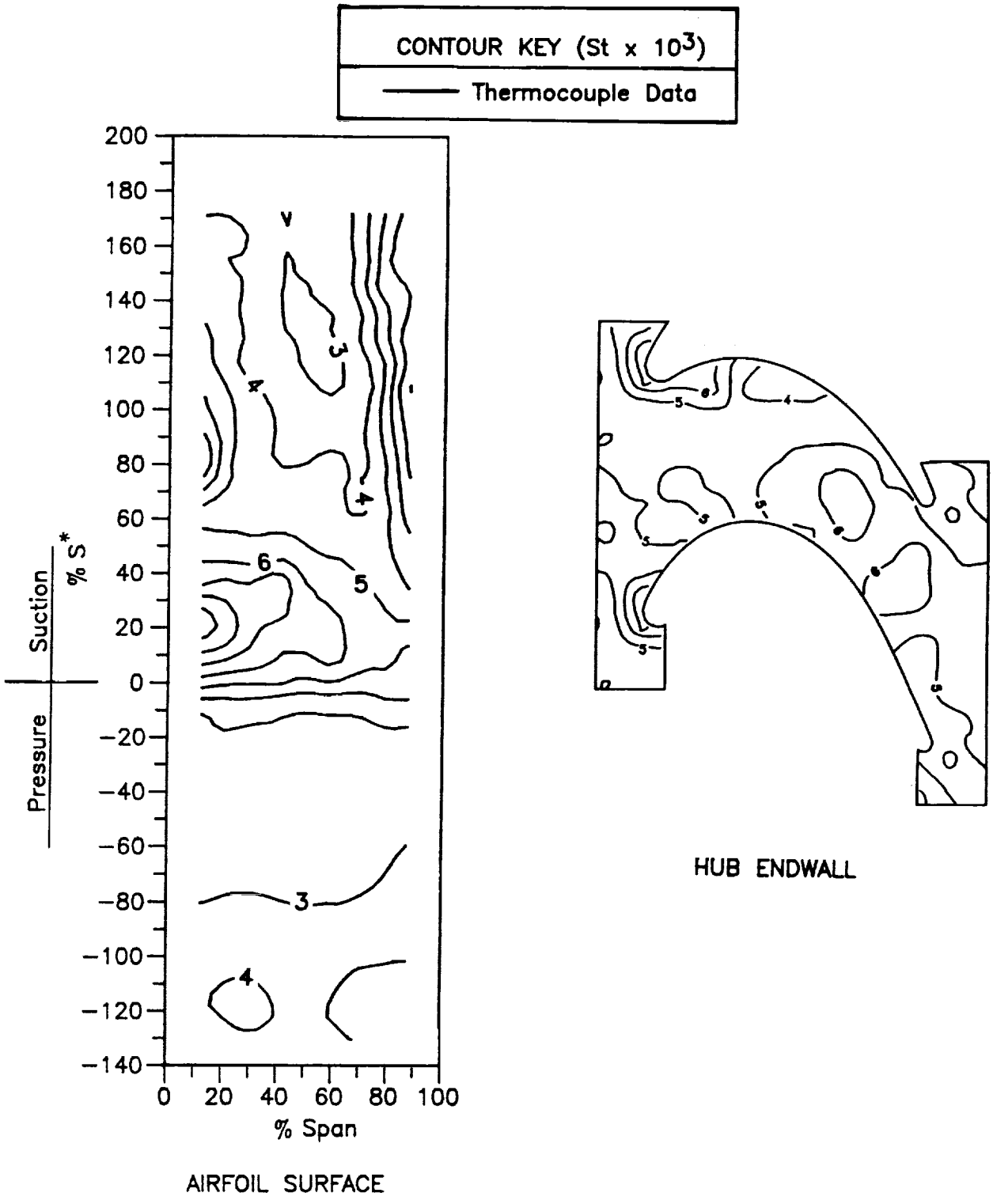

Figure 47a Stanton Number Contours on the Airfoil and Hub Endwall Surfaces

ROUGH-WALL MODEL

β_1 = 45° N = 409 Re = 4.889×10^5

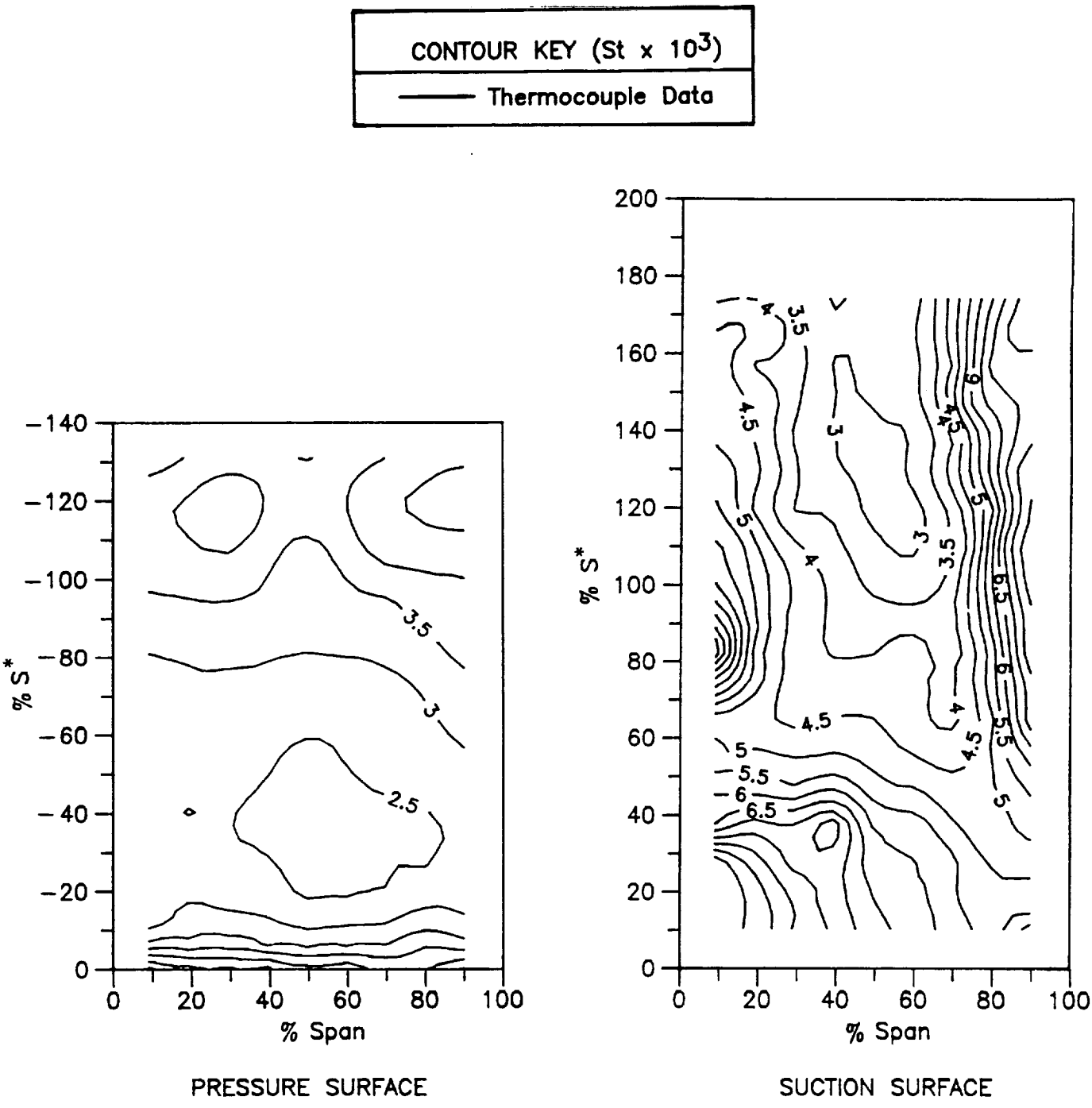

Figure 47b Details of the Stanton Number Contours on the Airfoil Suction and Pressure Surfaces

ROUGH-WALL MODEL

β_1 = 45° N = 409 Re = 4.889x10^5

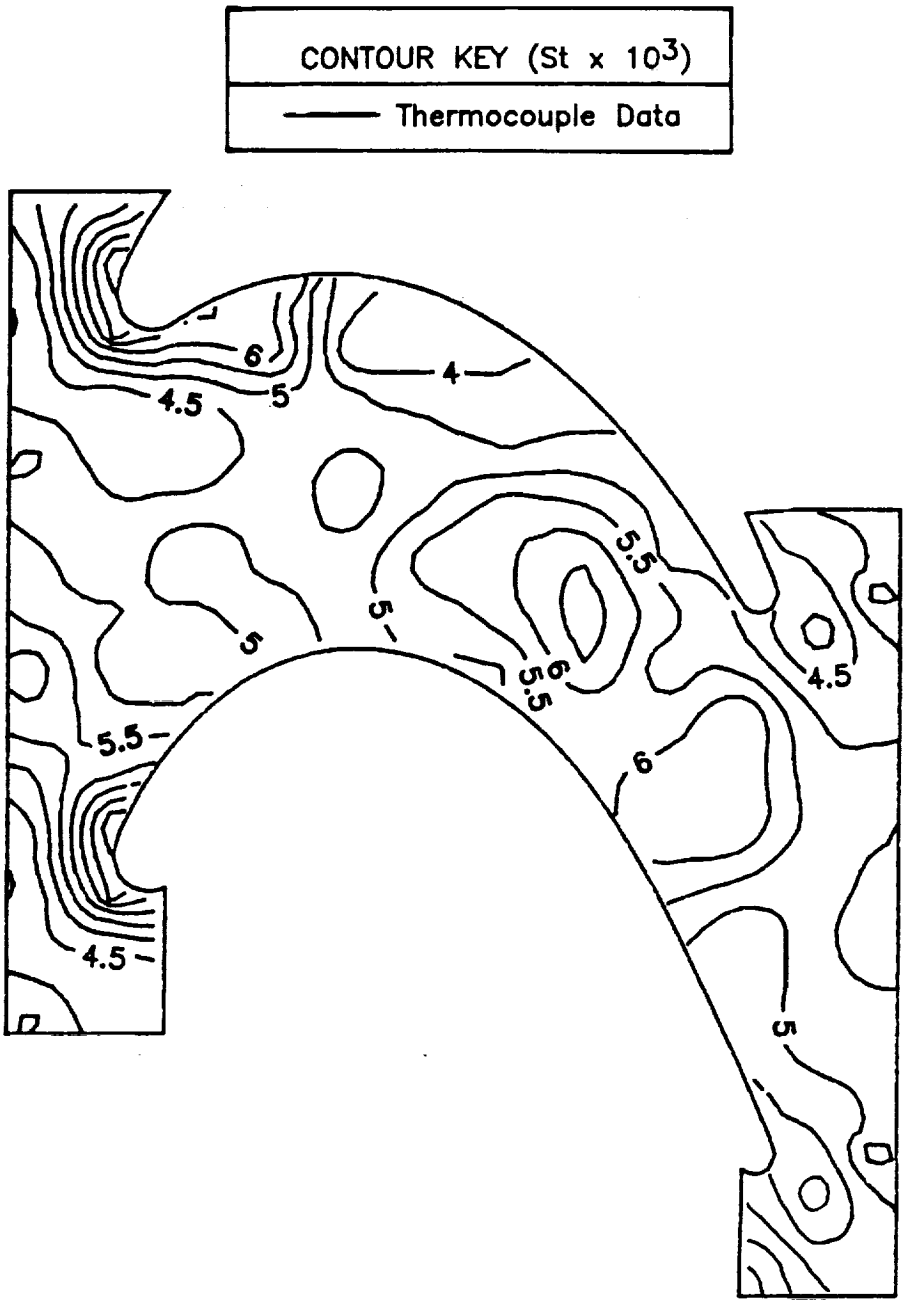

HUB ENDWALL

Figure 47c Details of the Stanton Number Contours on the Hub Endwall Surface

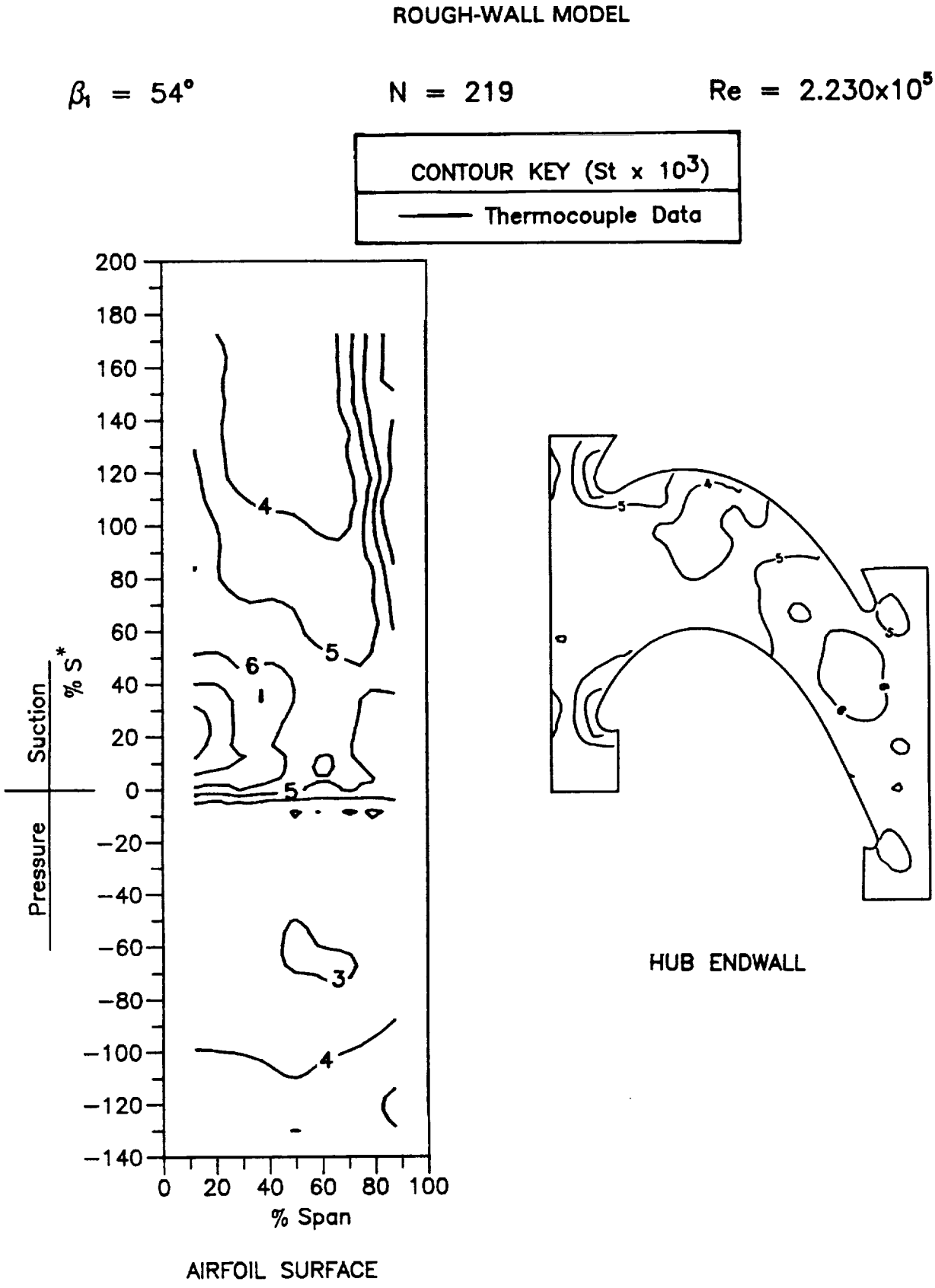

Figure 48a Stanton Number Contours on the Airfoil and Hub Endwall Surfaces

ROUGH-WALL MODEL

$\beta_1 = 54°$ N = 219 Re = 2.230×10^5

CONTOUR KEY (St x 10^3)
——— Thermocouple Data

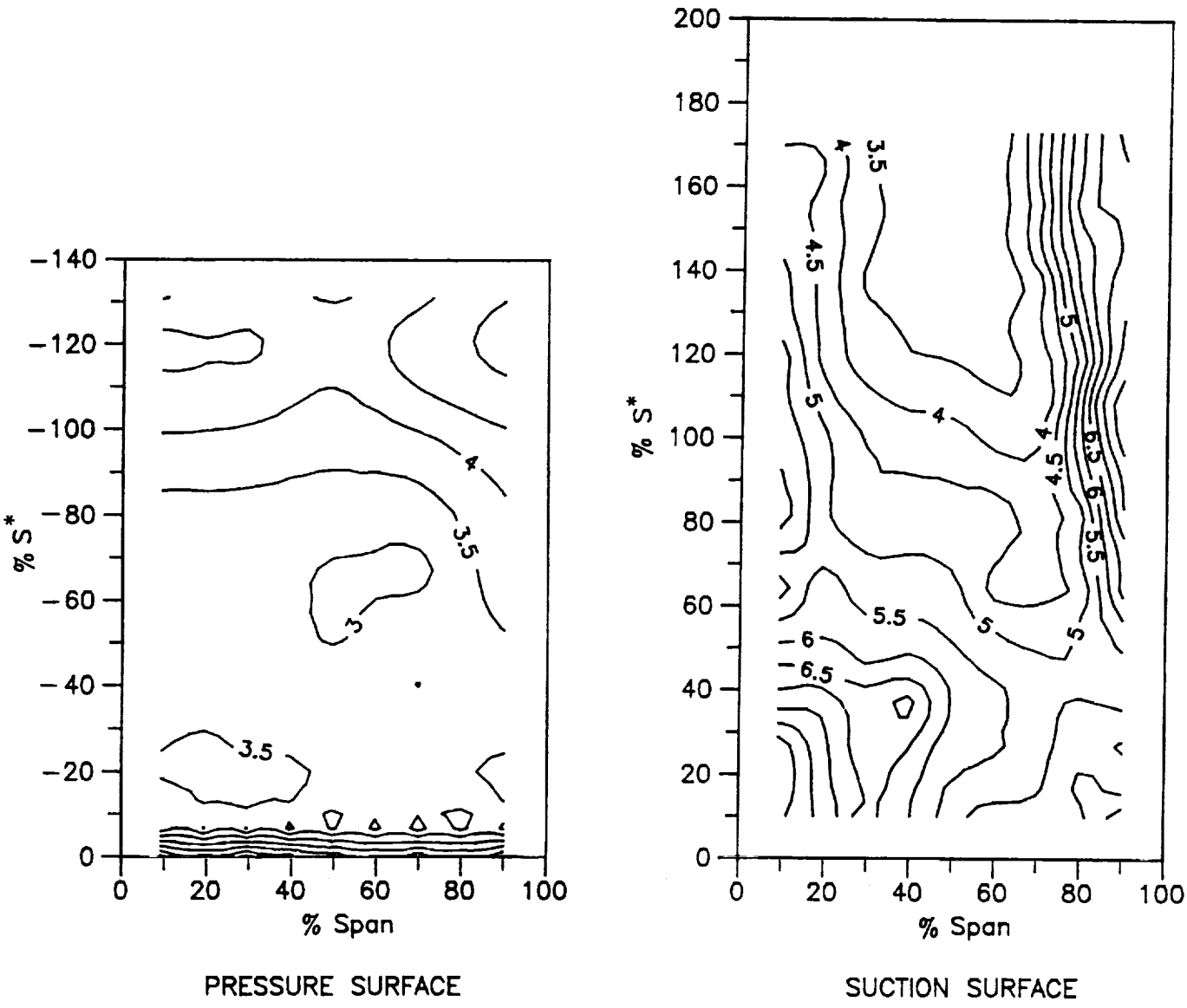

PRESSURE SURFACE SUCTION SURFACE

Figure 48b Details of the Stanton Number Contours on the Airfoil Suction and Pressure Surfaces

ROUGH-WALL MODEL

β_1 = 54° N = 219 Re = 2.230×10^5

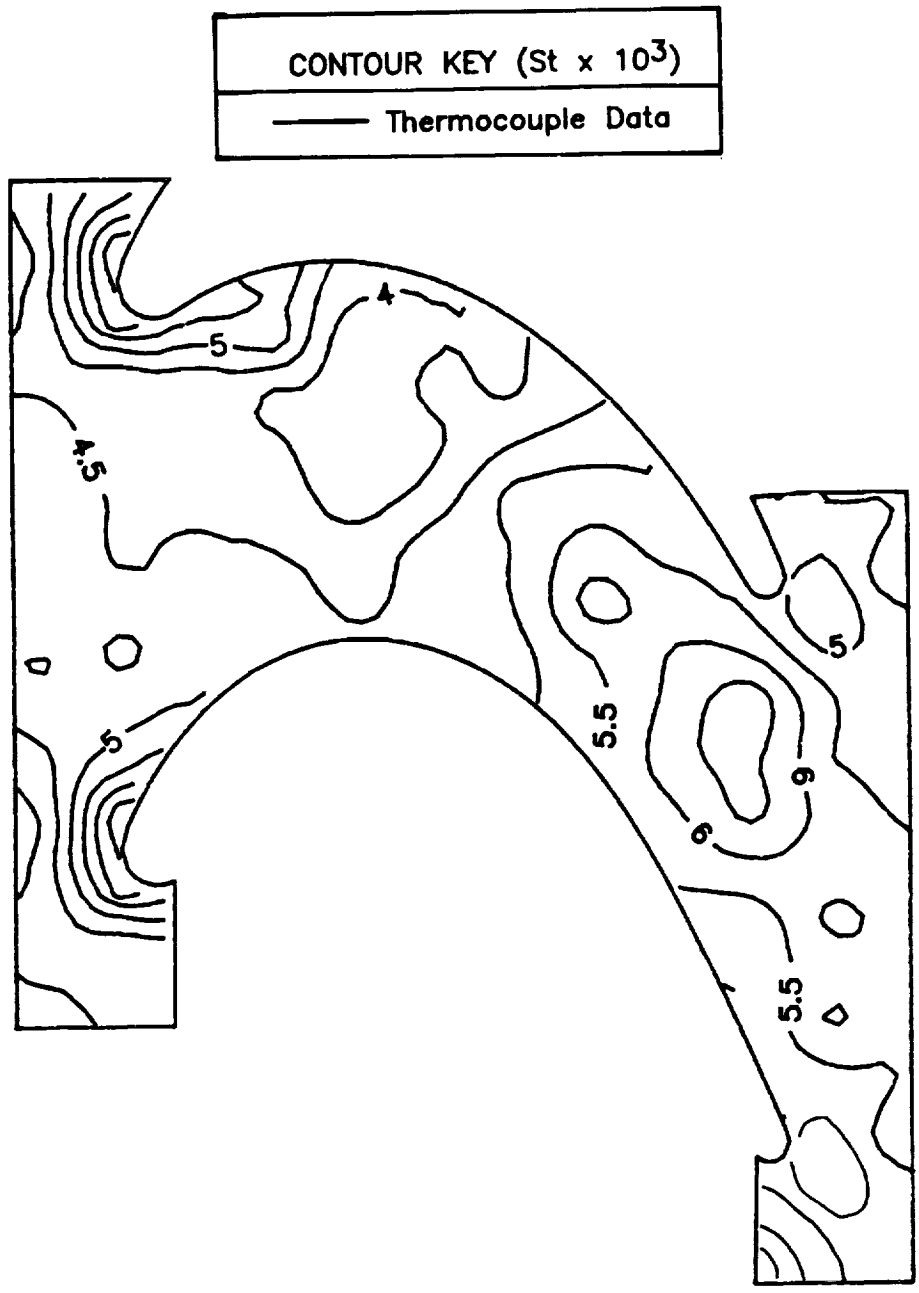

HUB ENDWALL

Figure 48c Details of the Stanton Number Contours on the Hub Endwall Surface

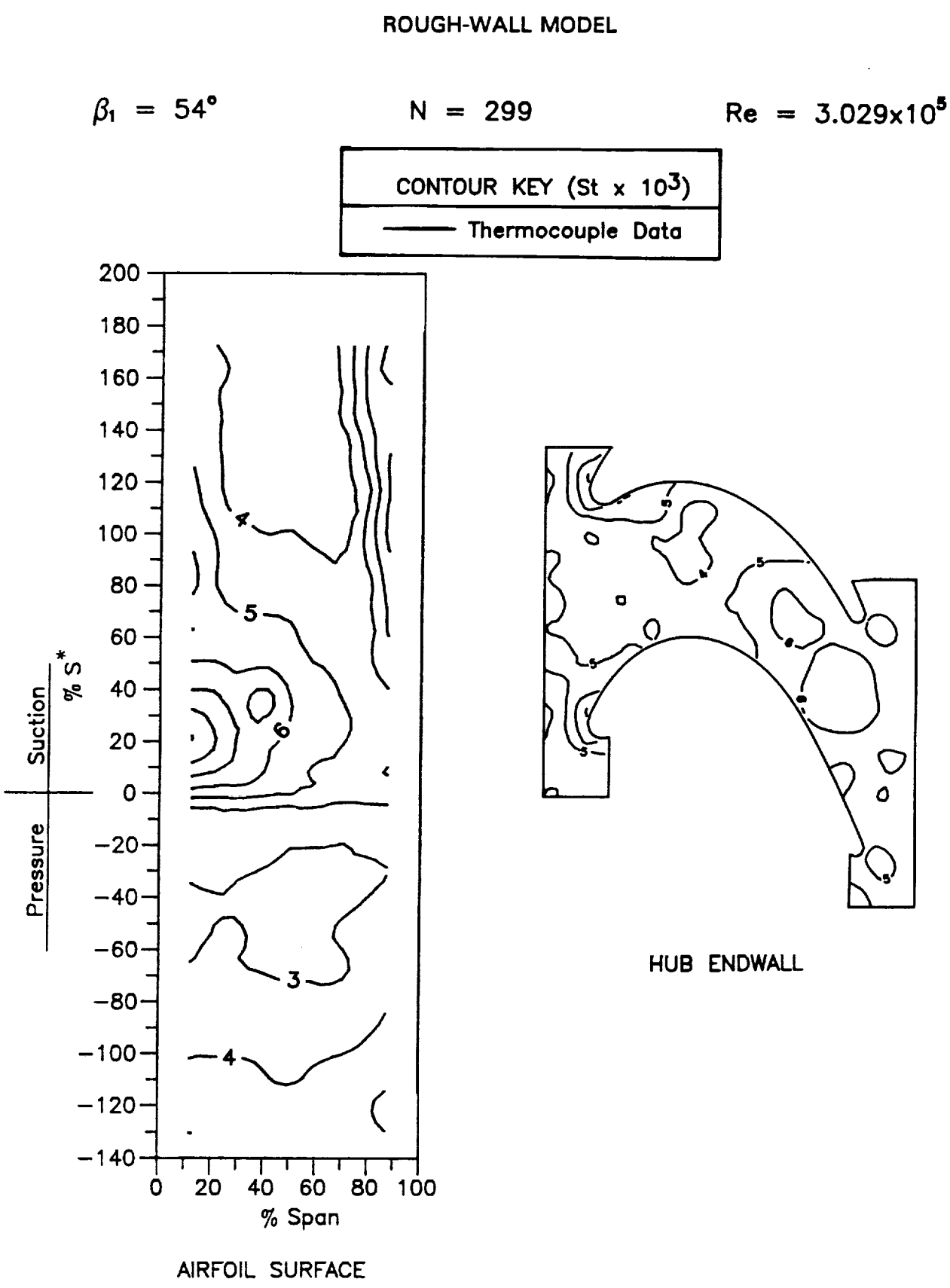

Figure 49a Stanton Number Contours on the Airfoil and Hub Endwall Surfaces

ROUGH-WALL MODEL

$\beta_1 = 54°$ N = 299 Re = 3.029×10^5

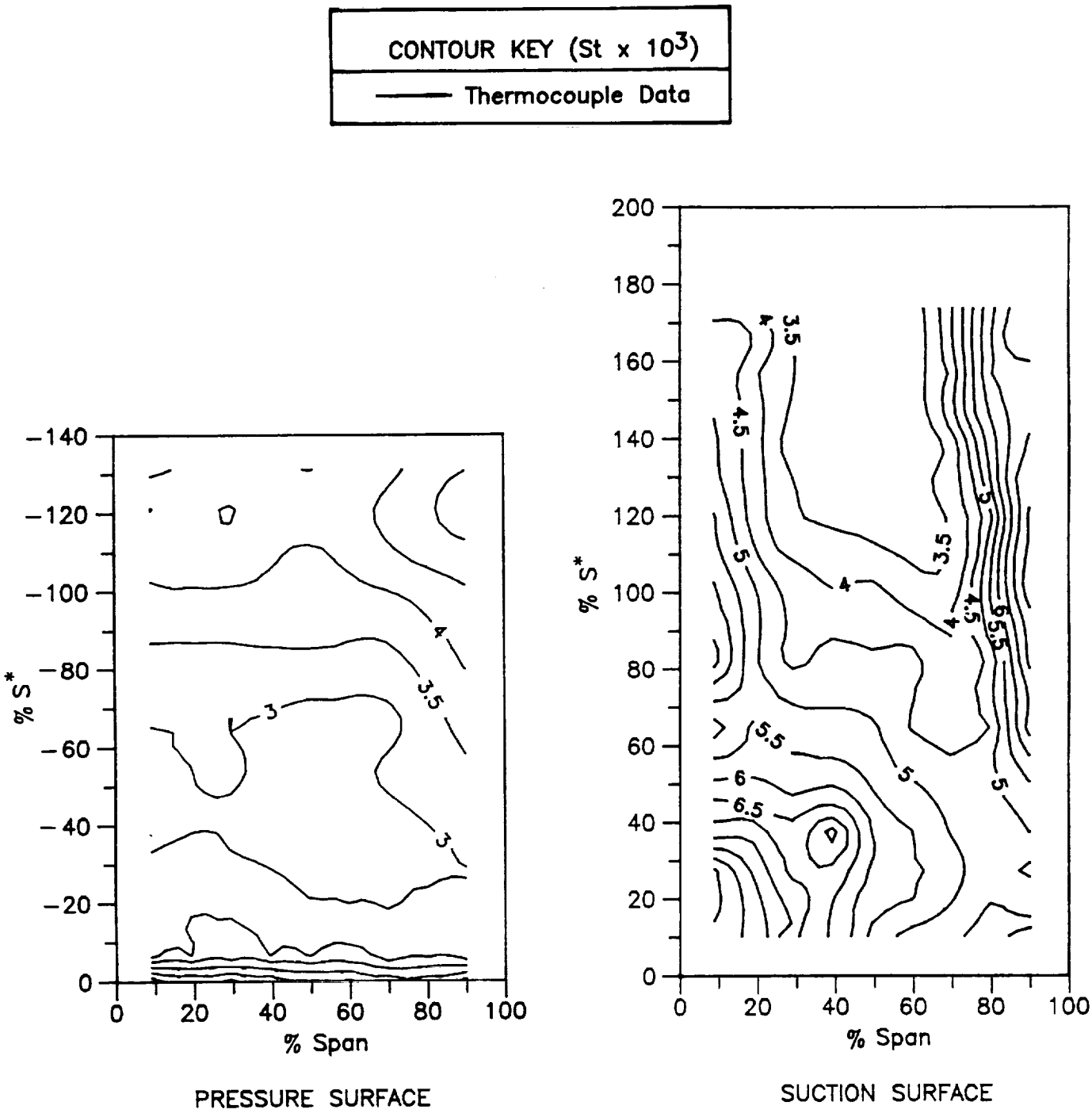

Figure 49b Details of the Stanton Number Contours on the Airfoil Suction and Pressure Surfaces

ROUGH-WALL MODEL

β_1 = 54° N = 299 Re = 3.029×10^5

HUB ENDWALL

Figure 49c Details of the Stanton Number Contours on the Hub Endwall Surface

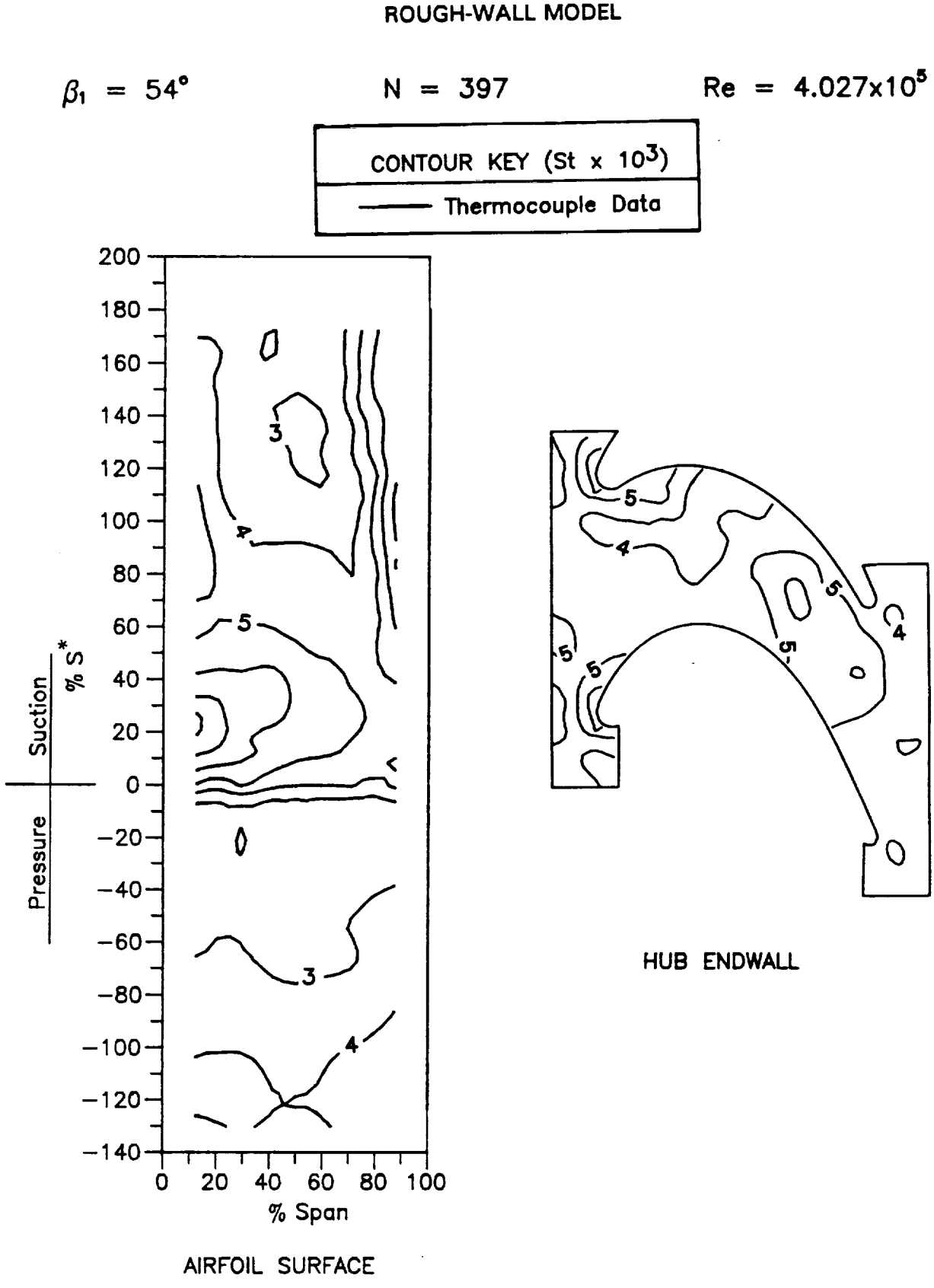

Figure 50a Stanton Number Contours on the Airfoil and Hub Endwall Surfaces

ROUGH-WALL MODEL

$\beta_1 = 54°$ N = 397 Re = 4.027×10^5

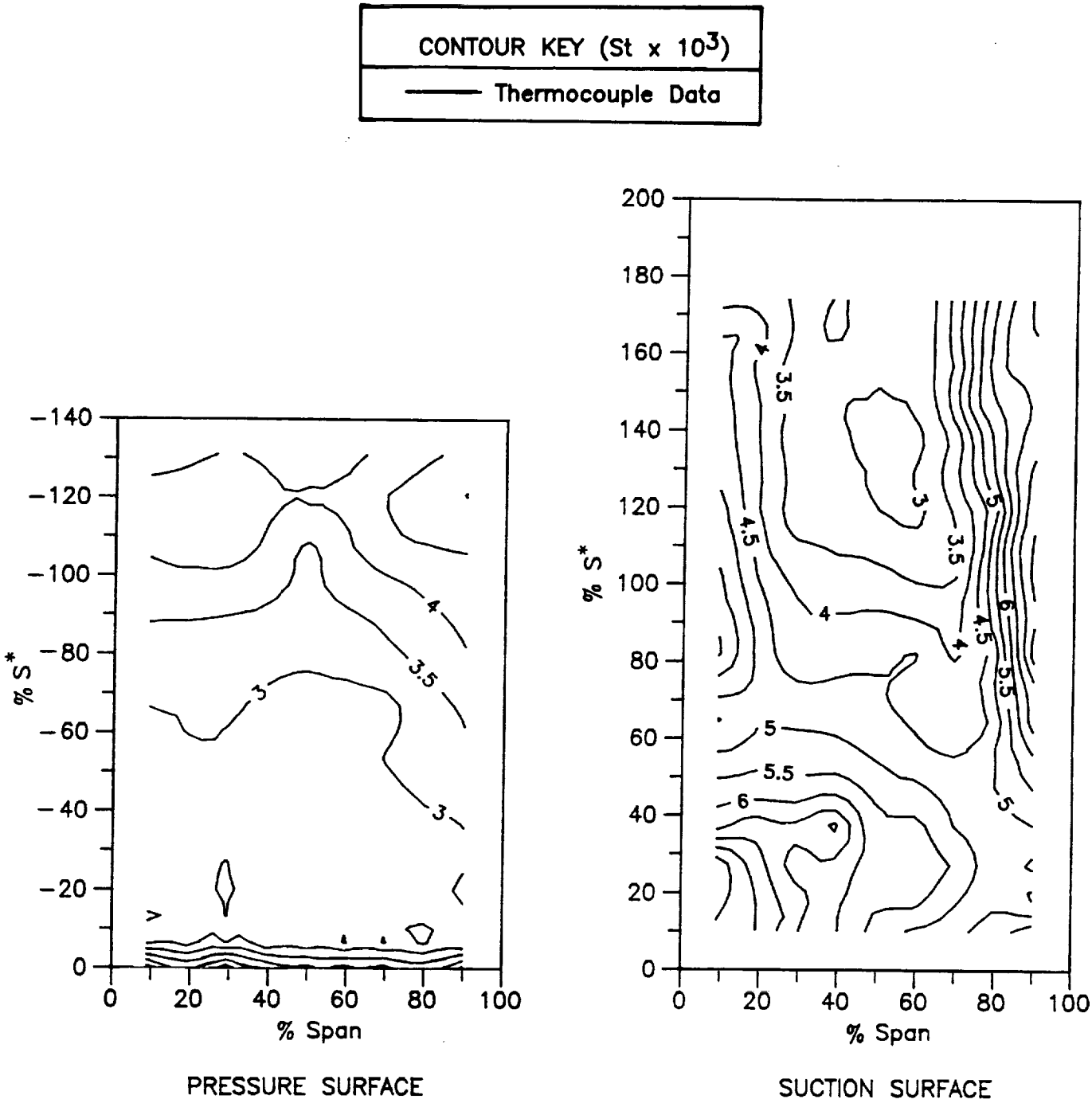

Figure 50b Details of the Stanton Number Contours on the Airfoil Suction and Pressure Surfaces

ROUGH-WALL MODEL

β_1 = 54° N = 397 Re = 4.027×10^5

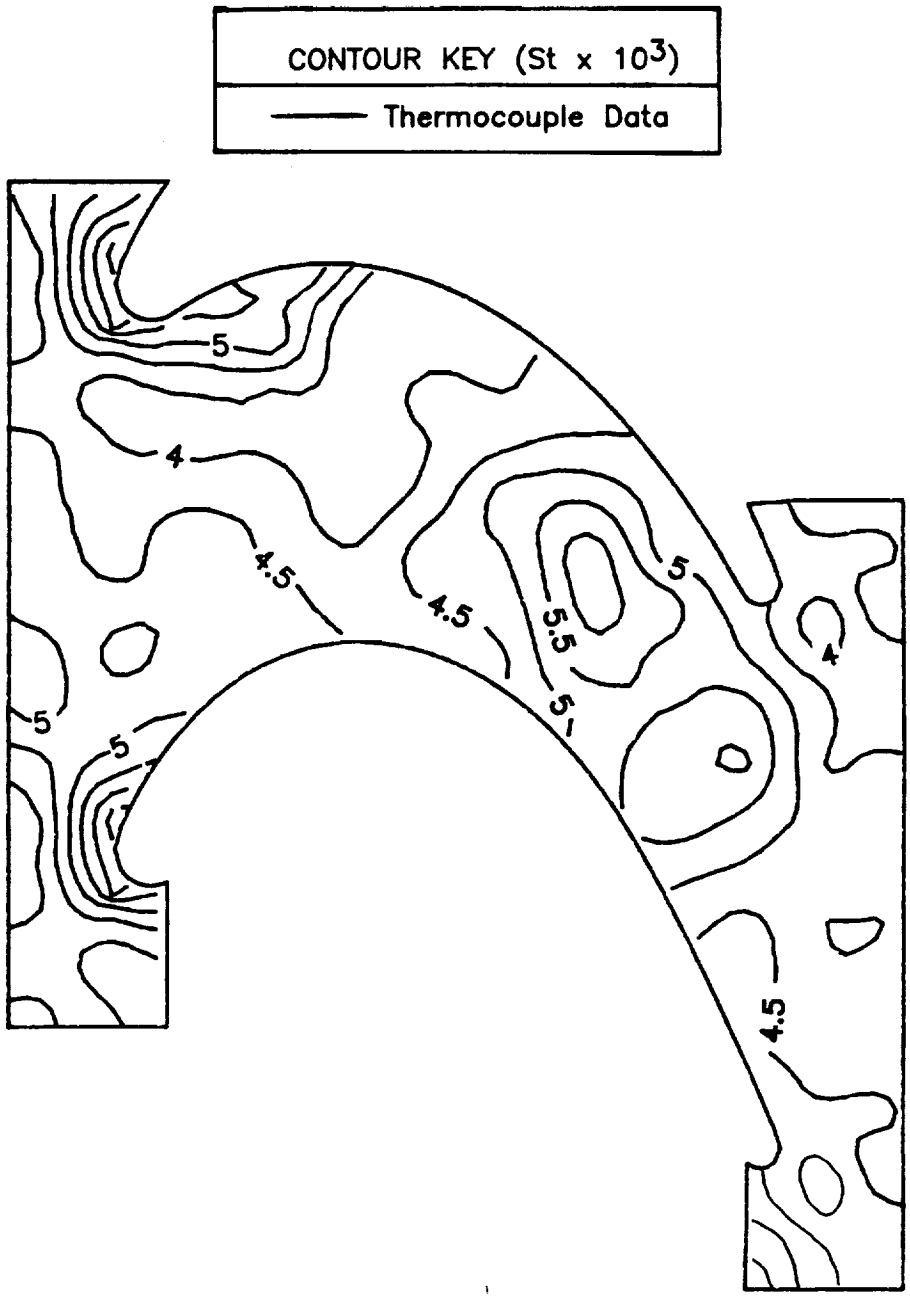

HUB ENDWALL

Figure 50c Details of the Stanton Number Contours on the Hub Endwall Surface

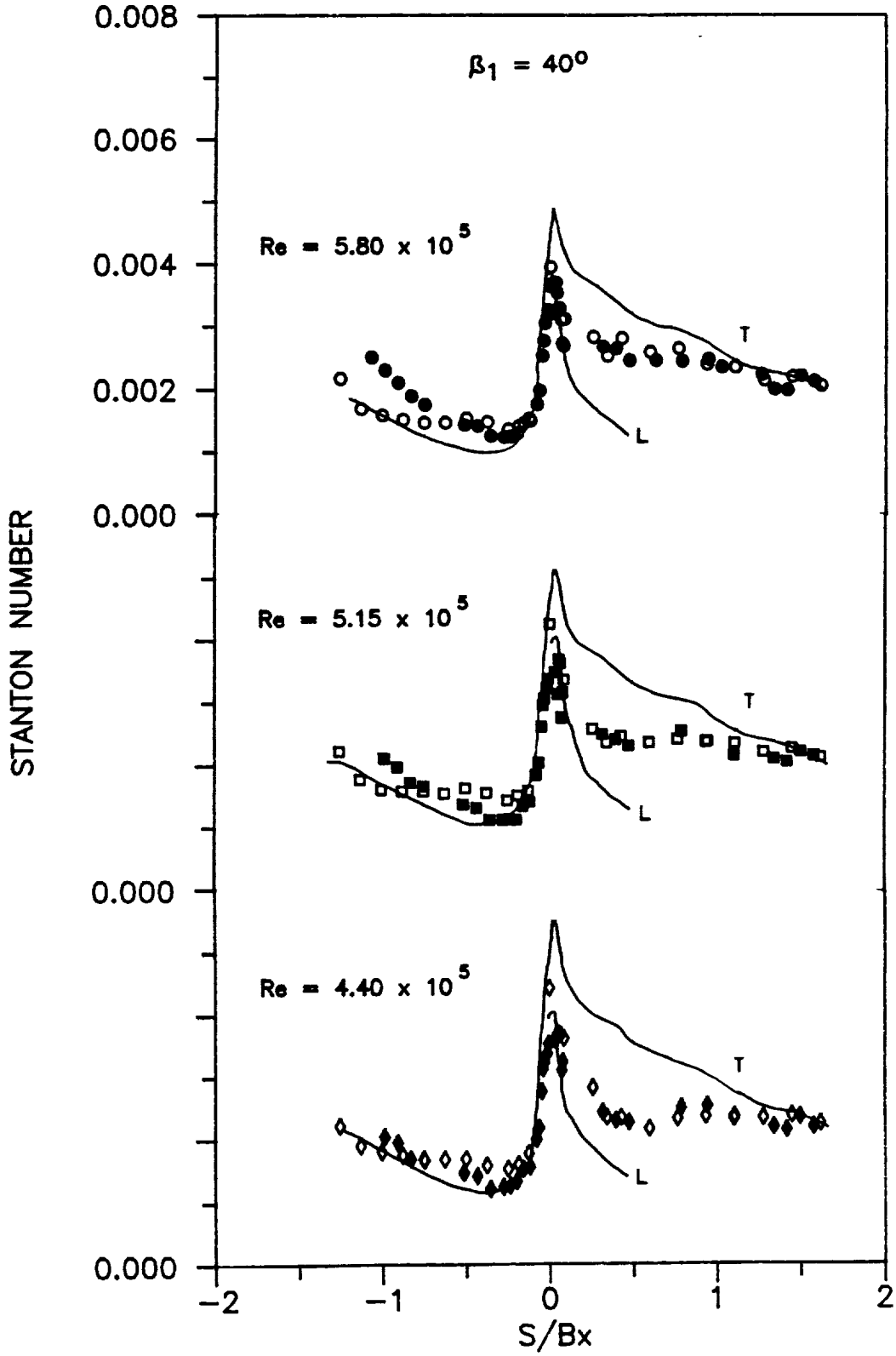

Figure 51a Comparisons of Midspan Rotor Airfoil Heat Transfer Distributions Obtained for Various Reynolds Numbers and $\beta_1 = 40^o$ (open symbols) With Those Recorded in the 1986 NASA-HOST Program (solid symbols)

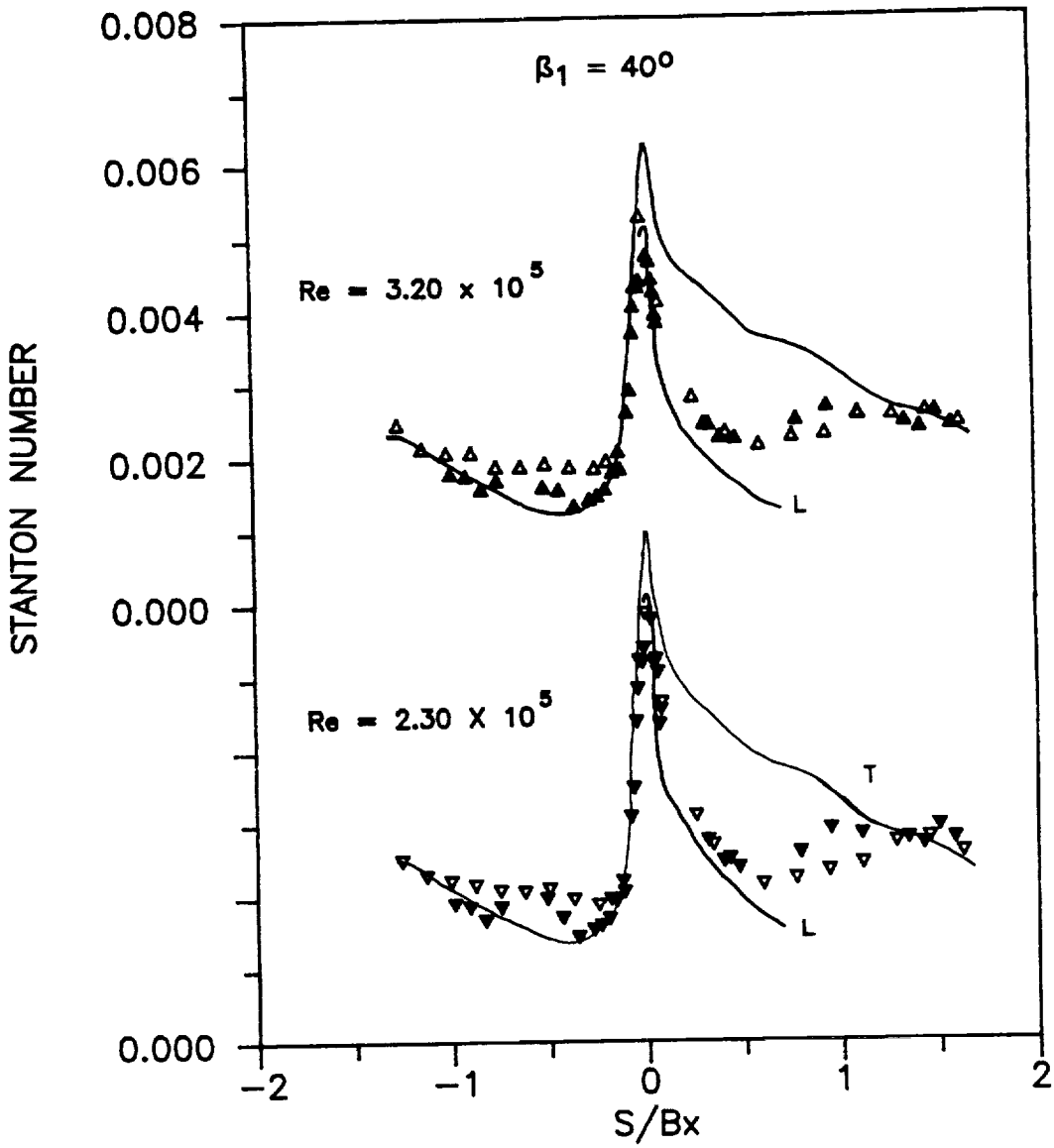

Figure 51b Comparisons of Midspan Rotor Airfoil Heat Transfer Distributions Obtained for Various Reynolds Numbers and $\beta_1 = 40^o$ (open symbols) With Those Recorded in the 1986 NASA-HOST Program (solid symbols)

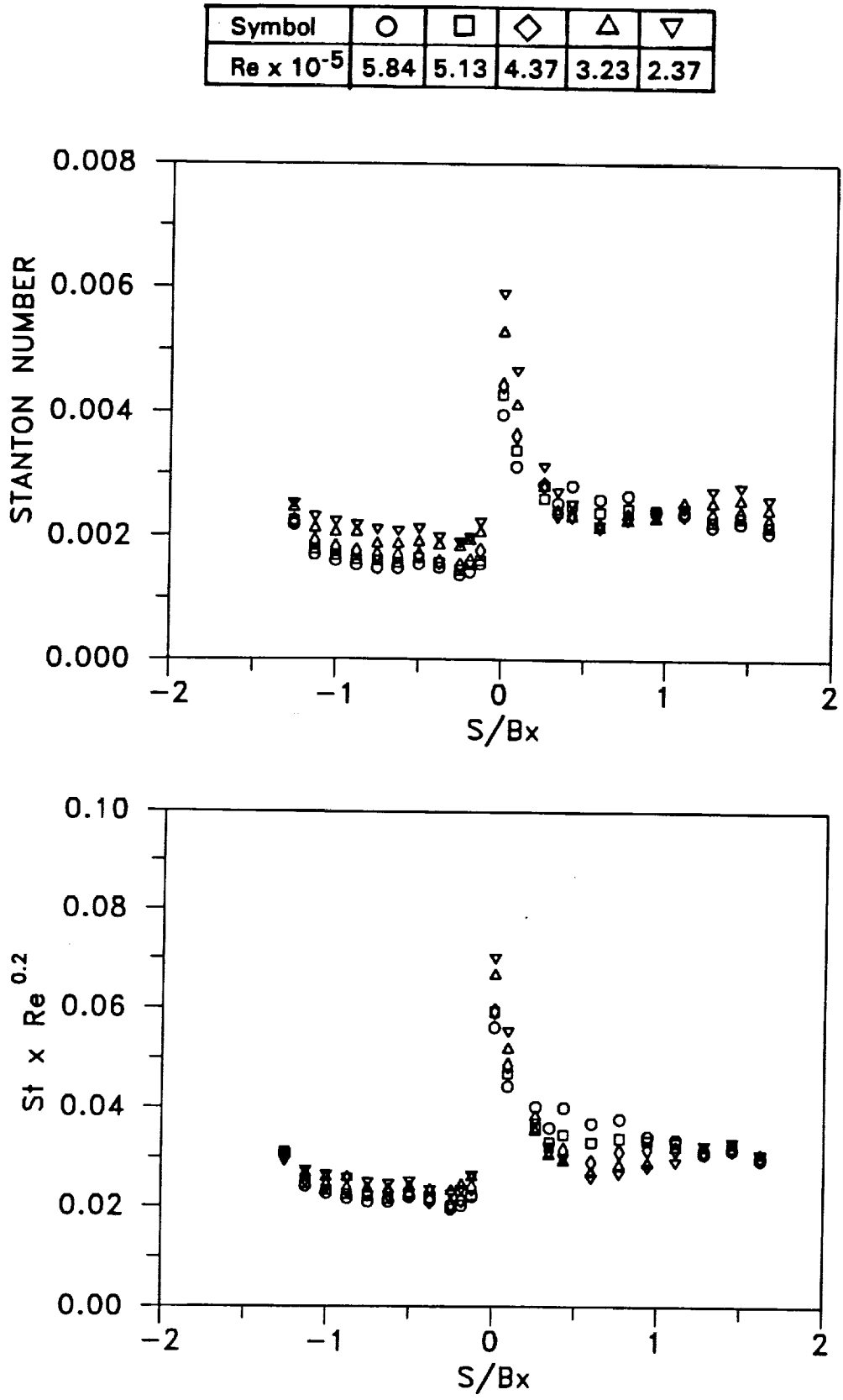

Figure 52 Comparisons of Midspan Rotor Airfoil Heat Transfer Distributions Obtained for Various Reynolds Numbers and $\beta_1 = 40^0$ for the Smooth Wall Model

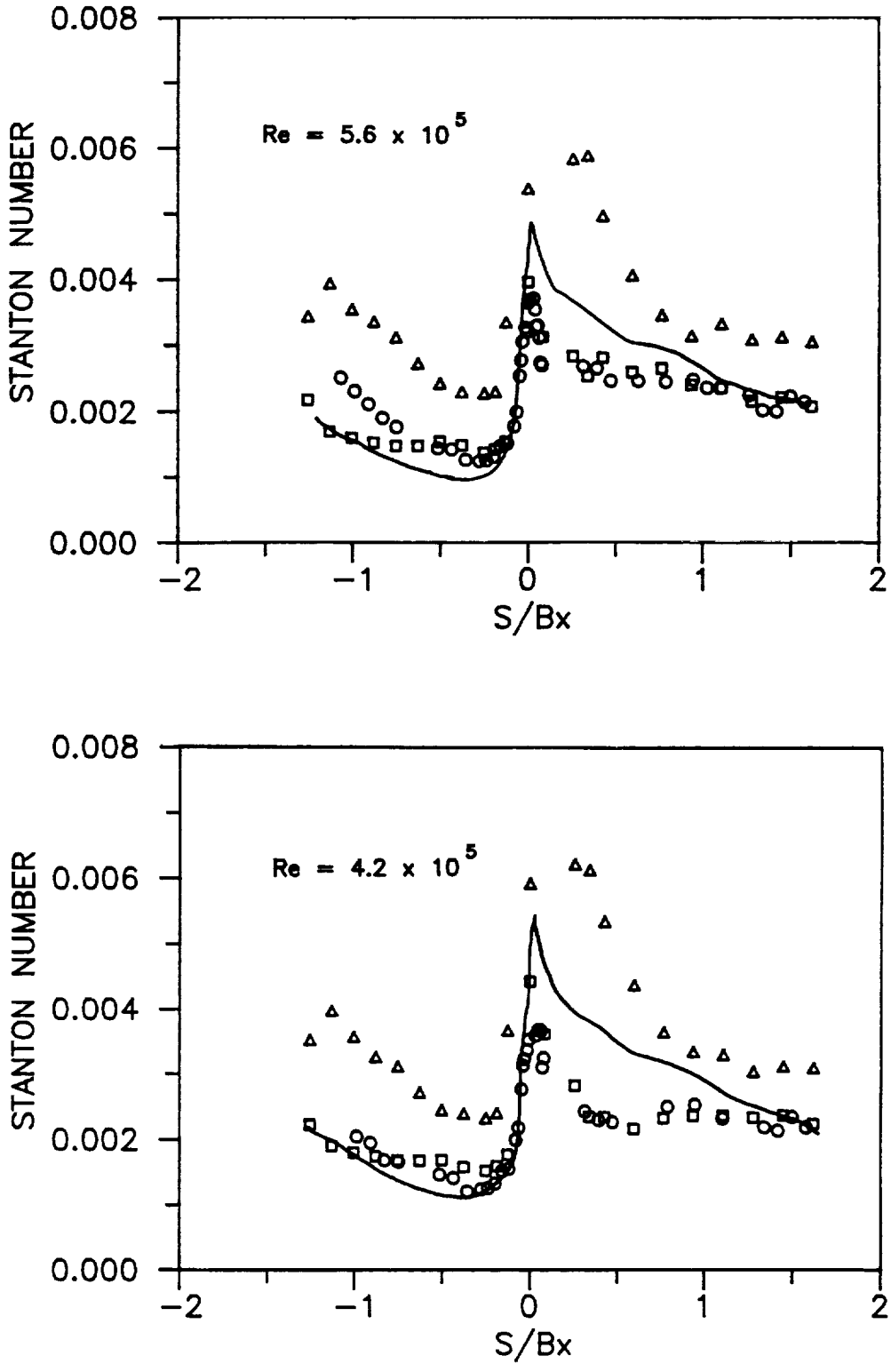

Figure 53 Comparison of Midspan Rotor Airfoil Heat Transfer Distributions Obtained for Two Reynolds Numbers at $\beta_1 = 40^0$; □ , smooth-wall data, △ , rough-wall data, ○ , 1986 NASA-HOST data

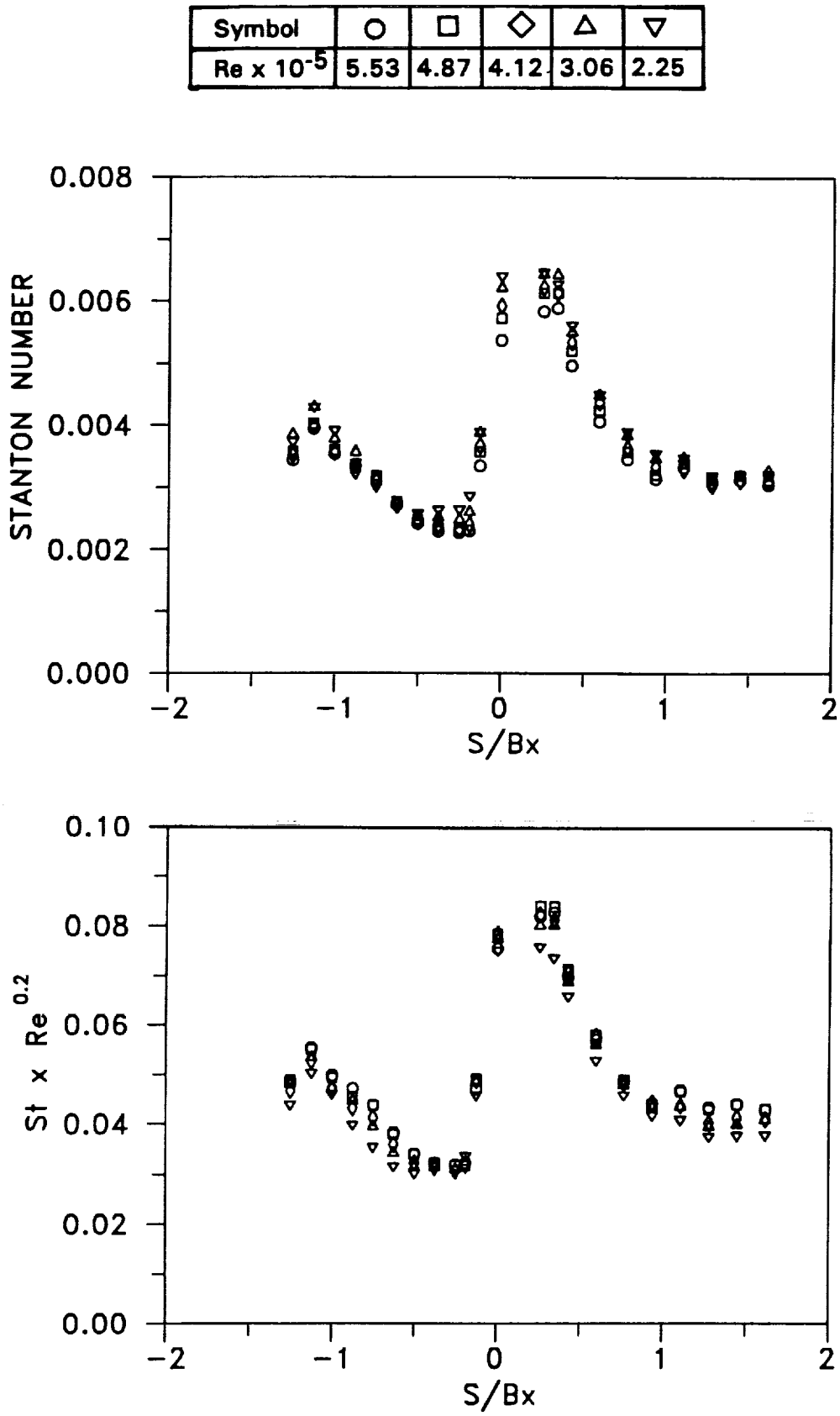

Figure 54 Comparisons of Midspan Rotor Airfoil Heat Transfer Distributions Obtained for Various Reynolds Numbers and $\beta_1 = 40^o$ for the Rough Wall Model

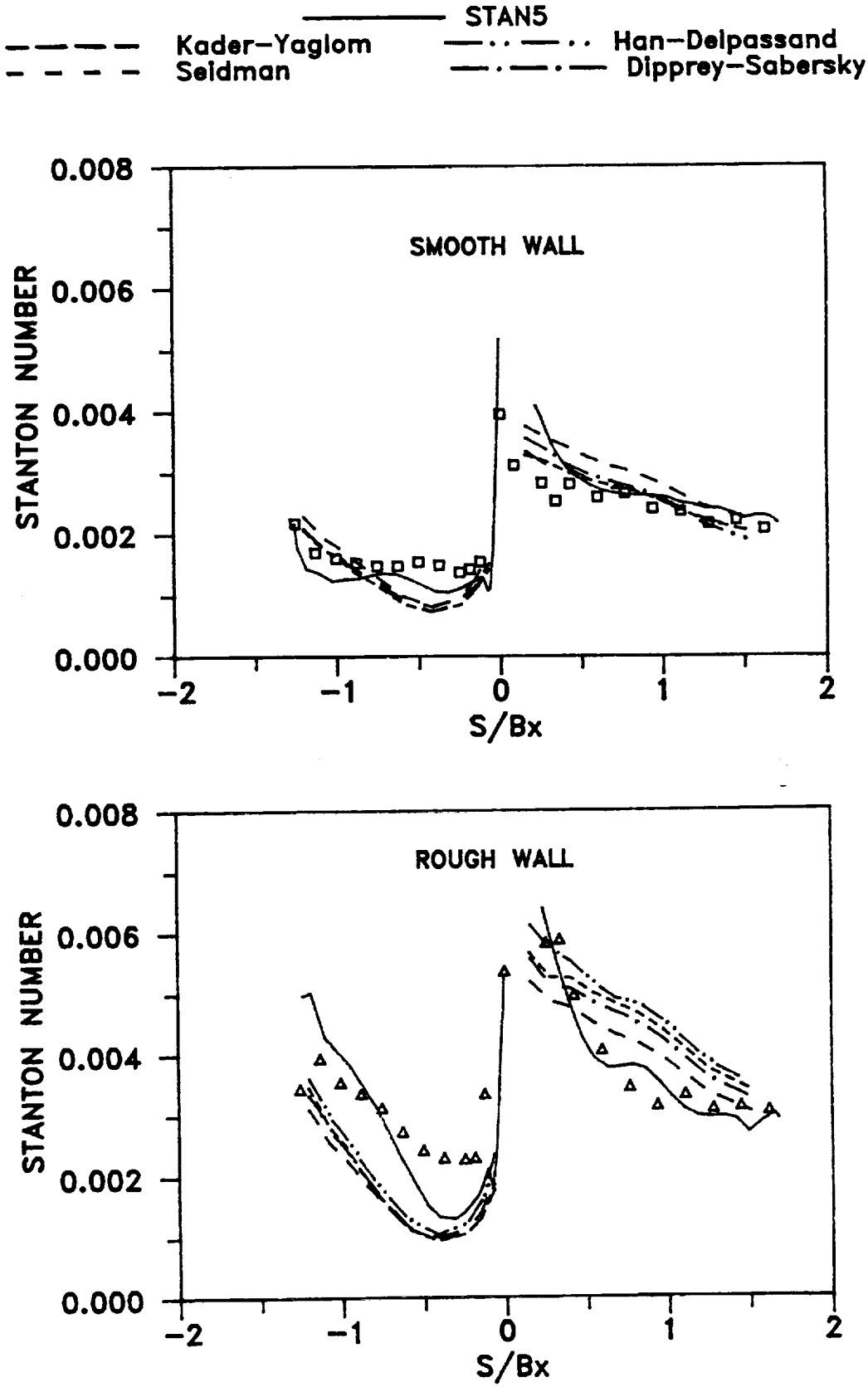

Figure 55 Comparison of Midspan Rotor Airfoil Heat Transfer Distributions Obtained at Re = 5.8×10^5 and $\beta_1 = 40^0$ With Various Analytical Predictions

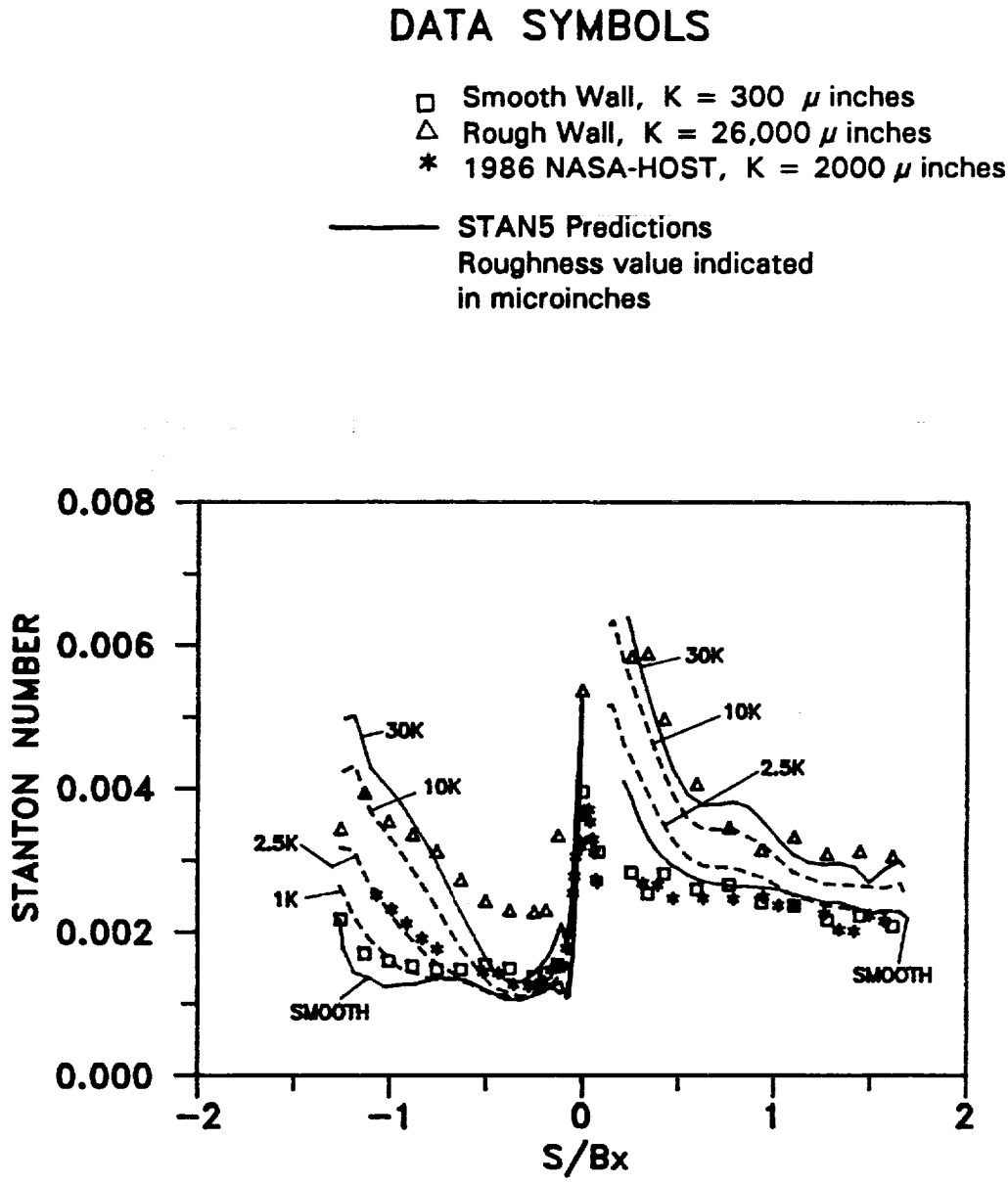

Figure 56 Comparison of Midspan Rotor Airfoil Heat Transfer Distributions Obtained at Re = 5.8 x 10^5 and β_1 = 40° With STAN5 Predictions for Various Wall Roughness Values

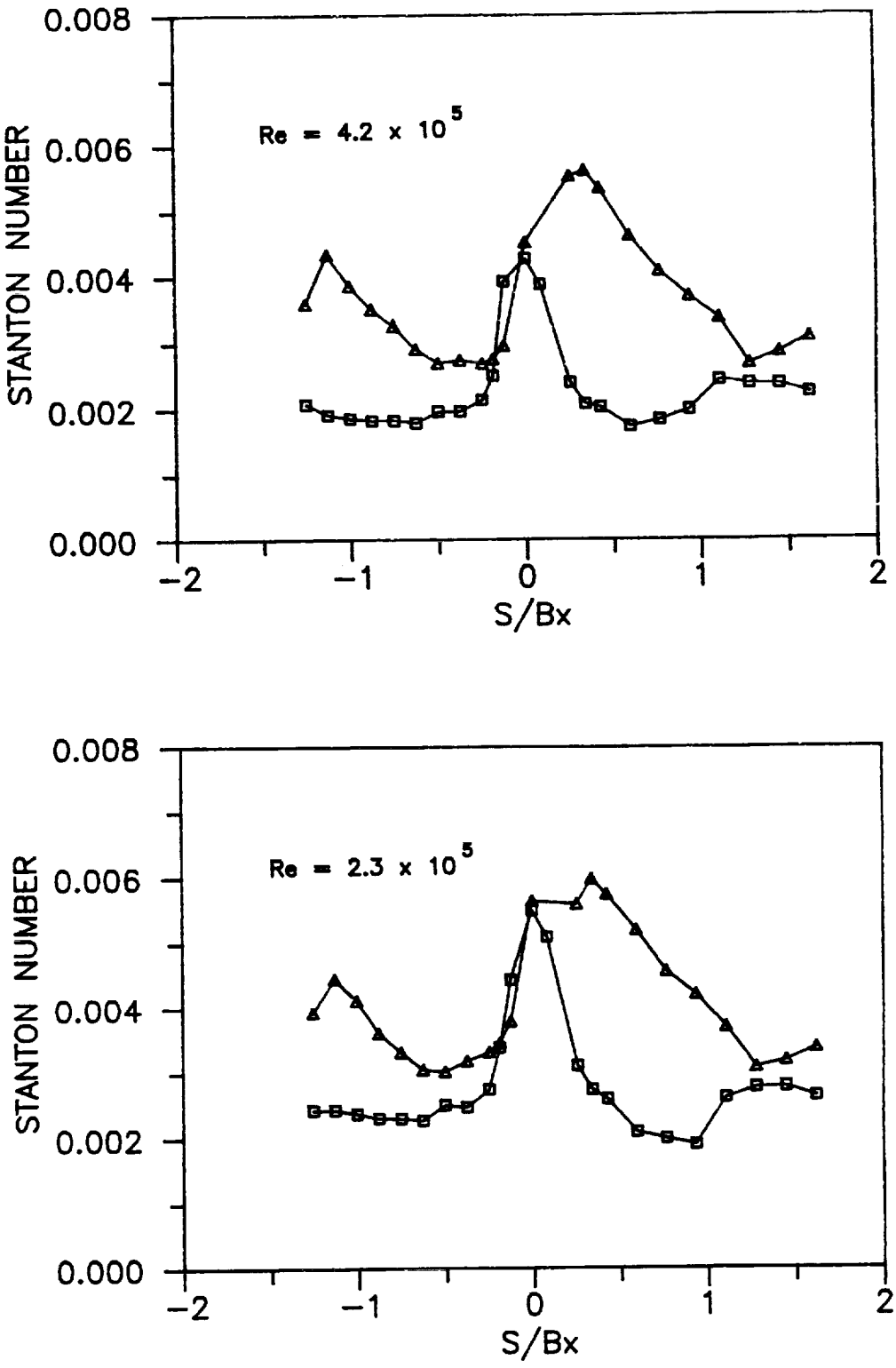

Figure 57 Comparison of Midspan Rotor Airfoil Heat Transfer Distributions Obtained for Two Reynolds Numbers at $\beta_1 = 54^0$; □, smooth-wall data, △, rough-wall data

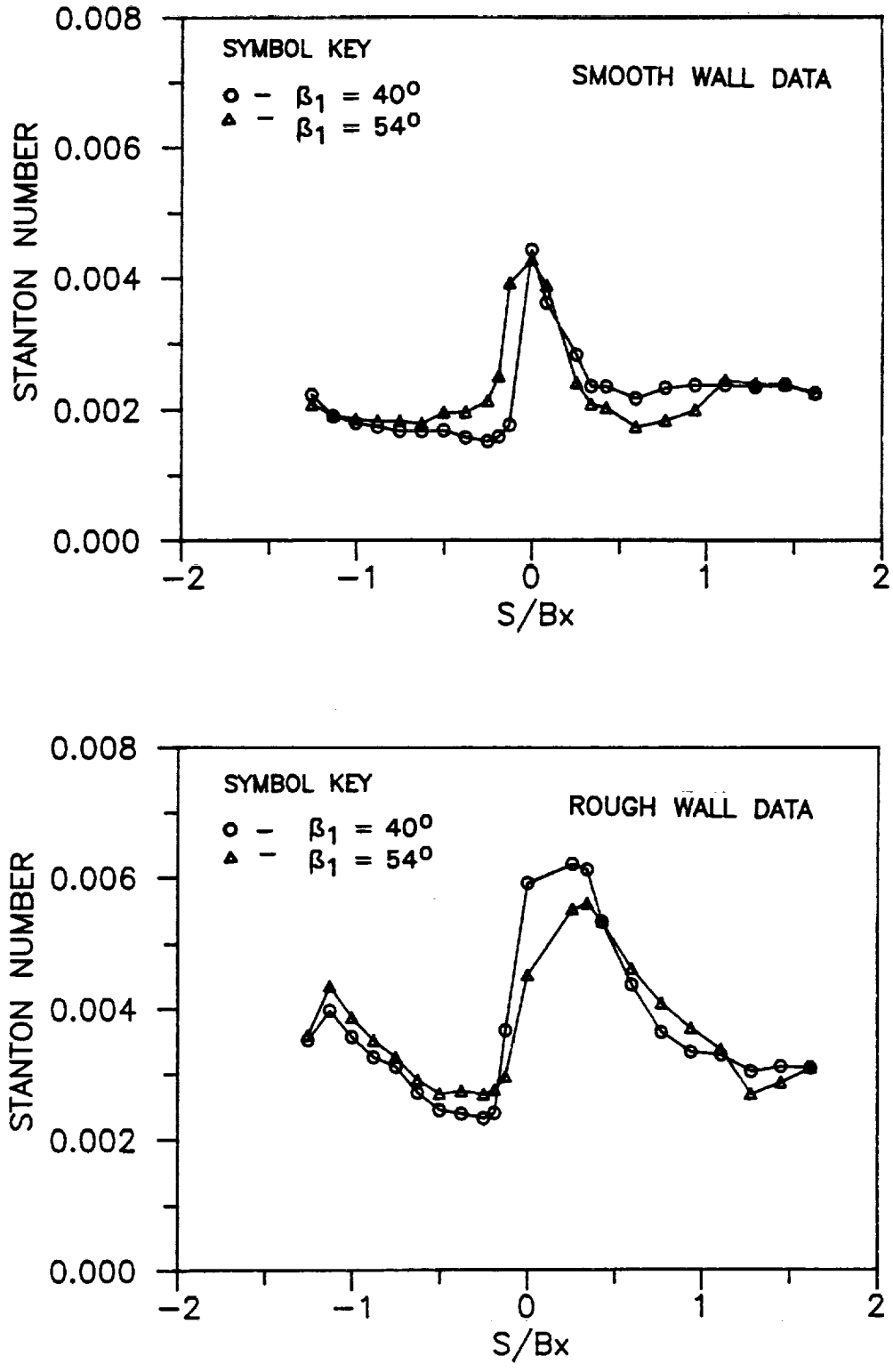

Figure 58 Comparison of Midspan Rotor Airfoil Heat Transfer Distributions Obtained for Two Flow Coefficients at Re = 4.2 x 10^5

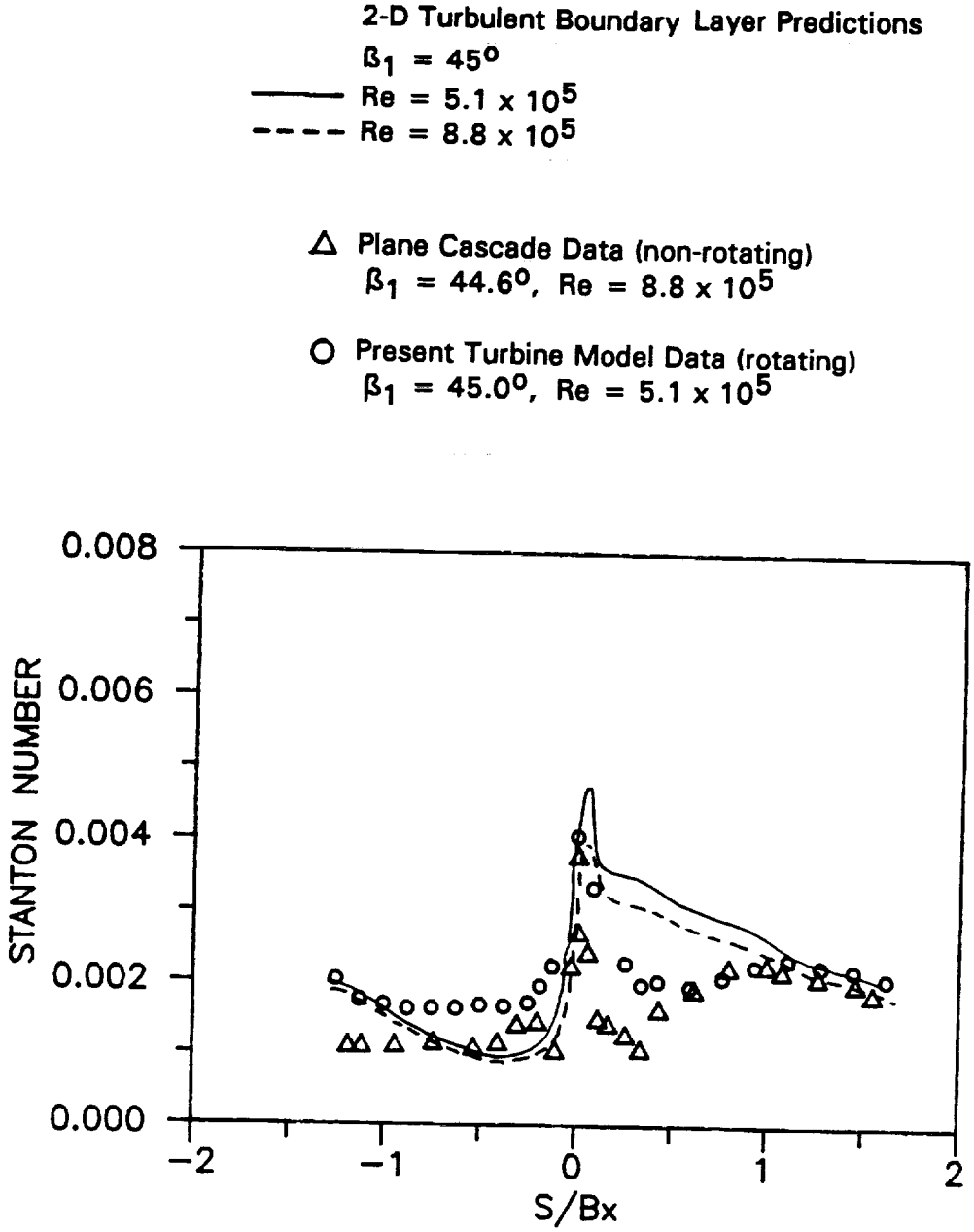

Figure 59 Comparison of Present Rotor Midspan Data With Previous Results Obtained in a 2-D Plane Cascade

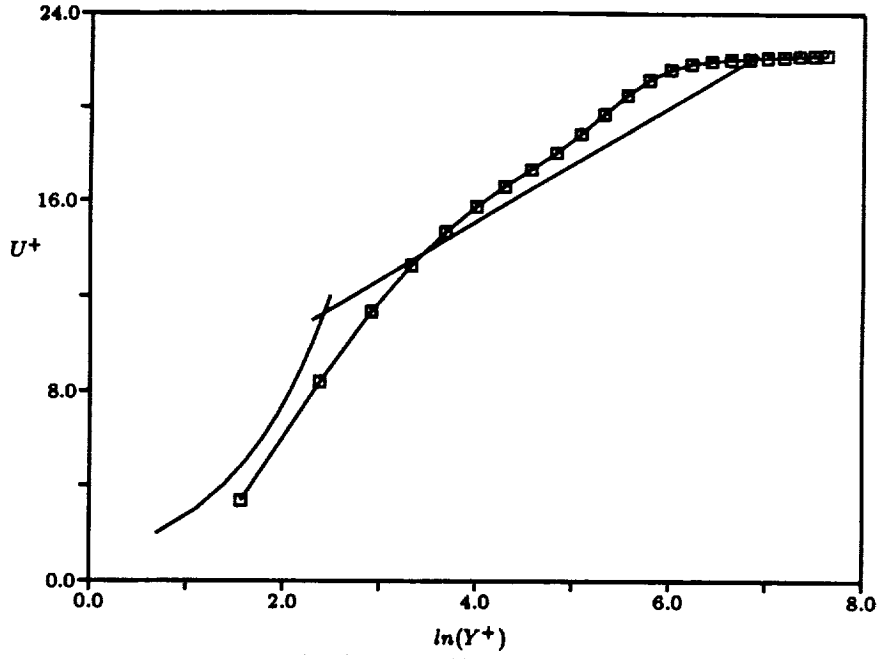

Figure 62 Calculated Universal Profile at θ=90 degs in the Square Curved Duct

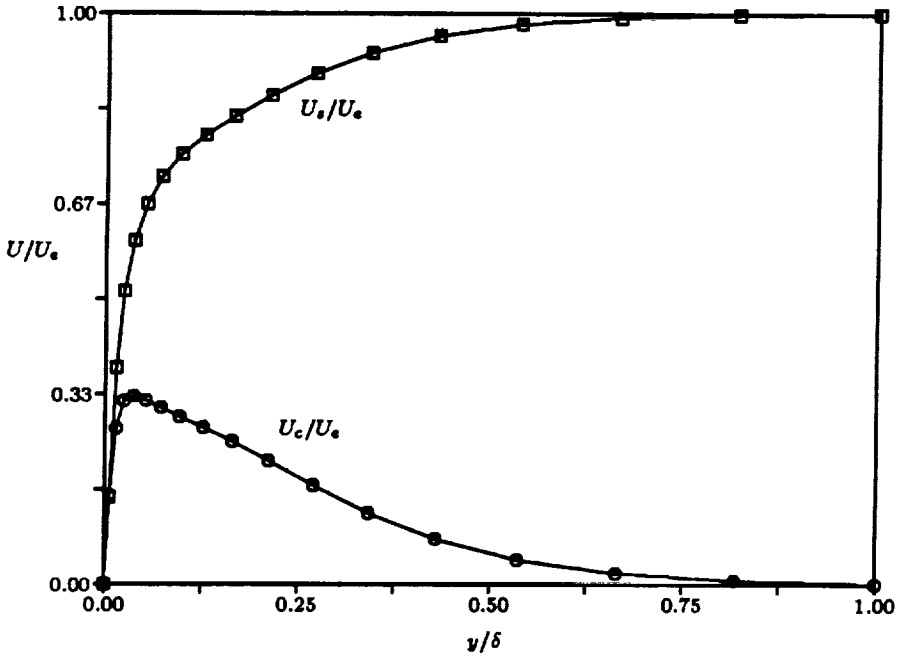

Figure 63 Streamwise and Crossflow Velocity at θ=90 degs in the Square Curved Duct

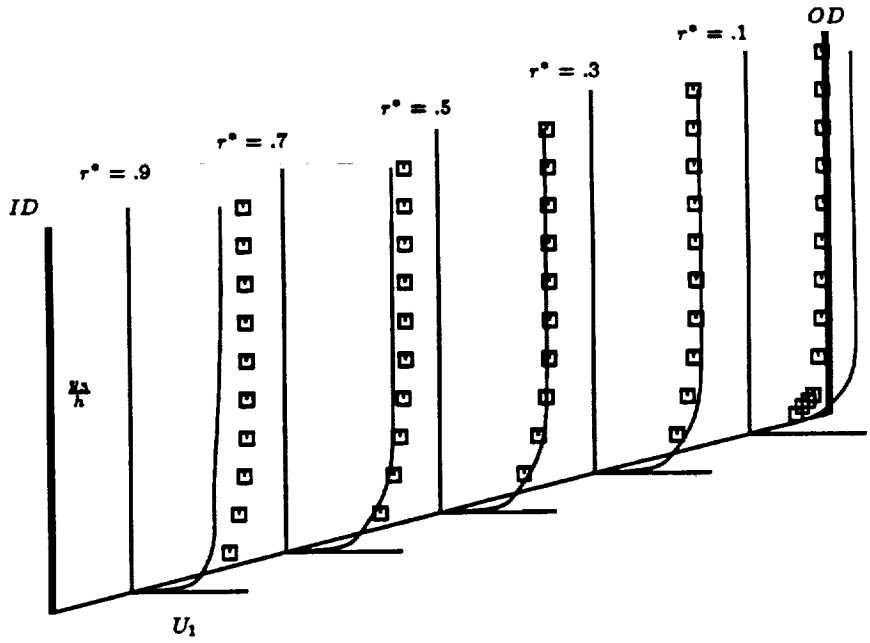

Figure 64 Streamwise Velocity Distribution θ=30 degs in the Square Curved Duct

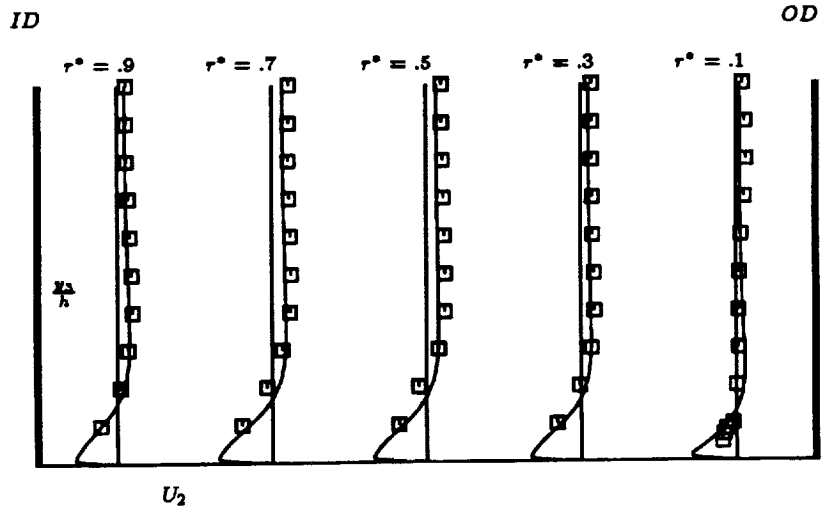

Figure 65 Crosswise Velocity Distribution θ=30 degs in the Square Curved Duct

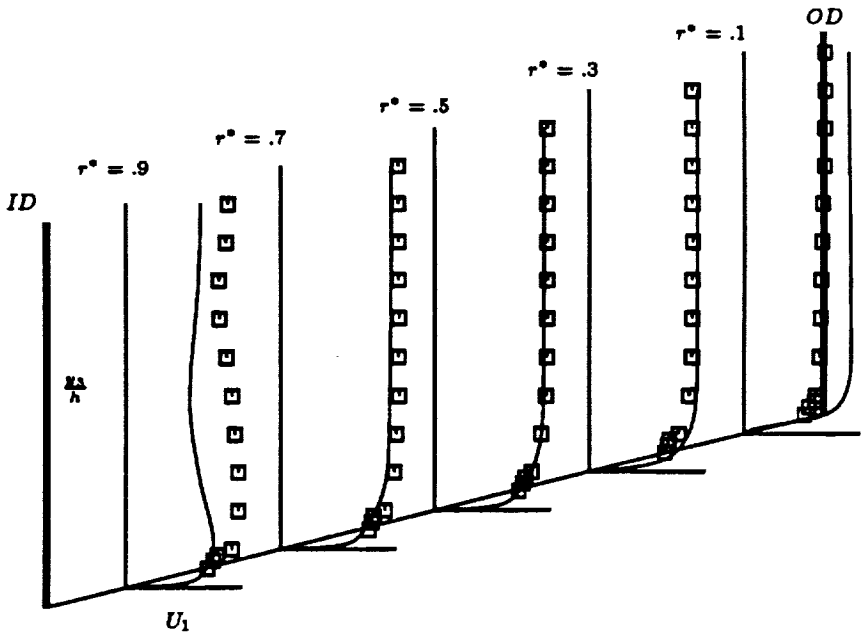

Figure 66 Streamwise Velocity Distribution θ=60 degs in the Square Curved Duct

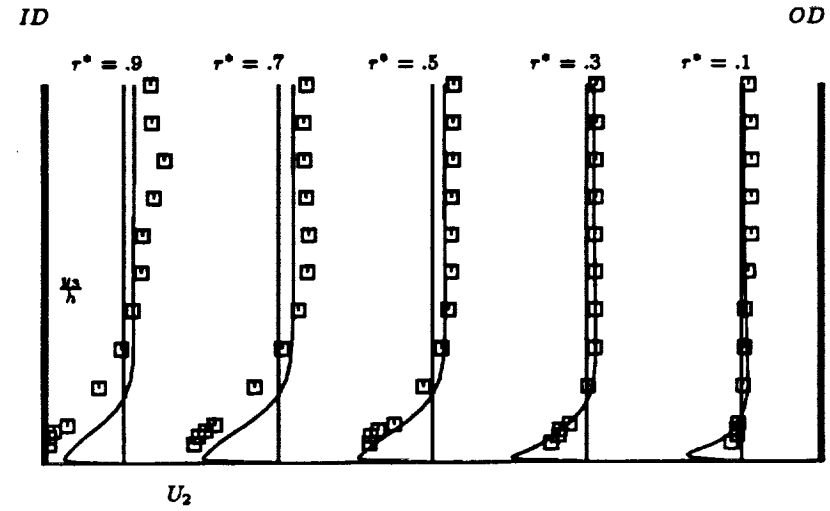

Figure 67 Crosswise Velocity Distribution θ=60 degs in the Square Curved Duct

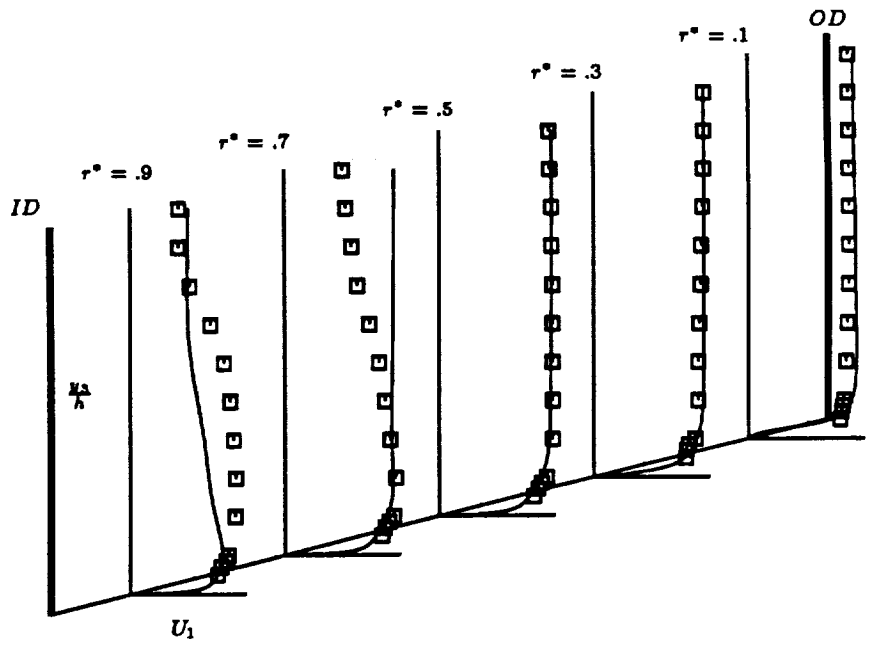

Figure 68 Streamwise Velocity Distribution θ=90 degs in the Square Curved Duct

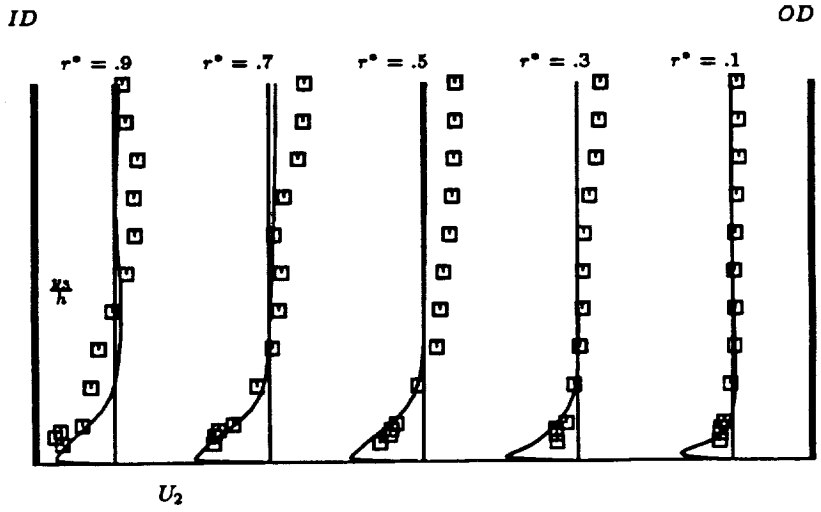

Figure 69 Crosswise Velocity Distribution θ=90 degs in the Square Curved Duct

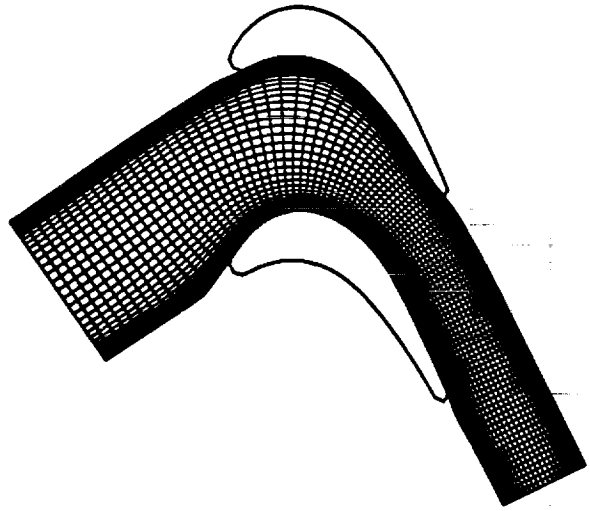

Figure 70 Coordinate Grid for LSRR Gas Turbine Cascade at Mid Span

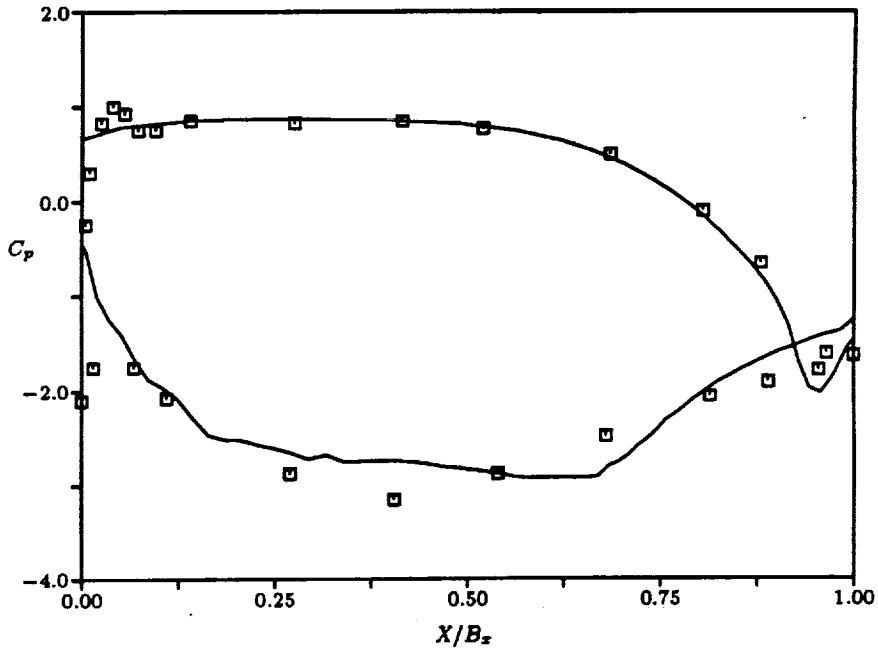

Figure 71 Calculated Mid Span Inviscid Static Pressure Distribution Compared to Experimental Data for LSRR Gas Turbine Cascade

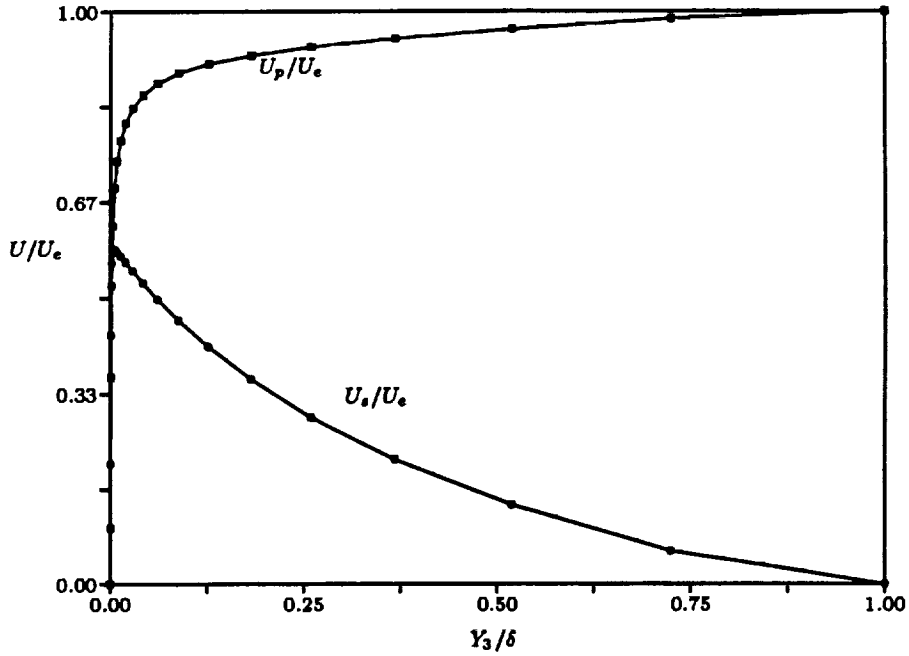

Figure 72 Detail of End Wall Boundary Layer at i-40 in LSRR Gas Turbine Cascade

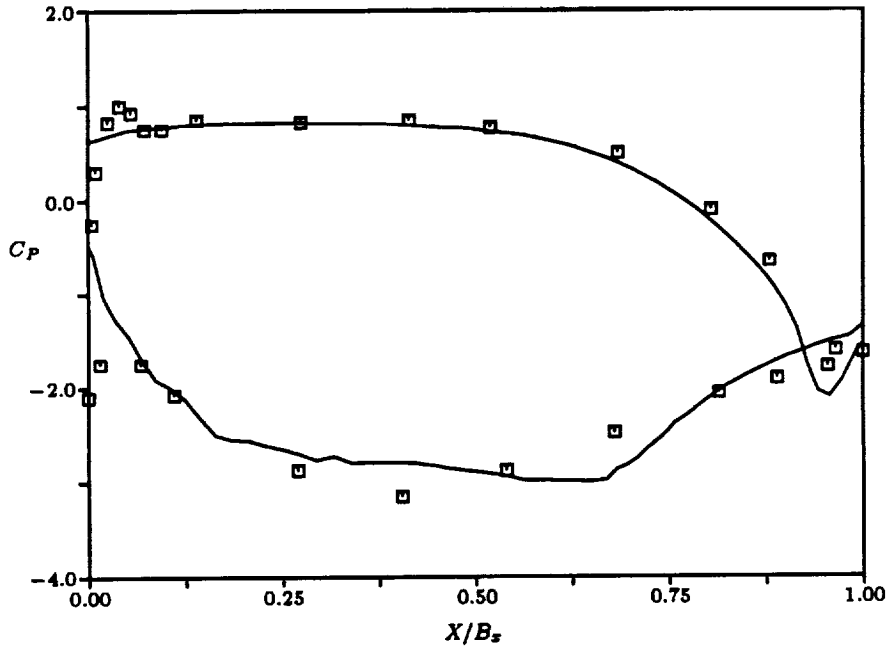

Figure 73 Comparison of Calculated and Measured Static Pressure Distribution at Mid Span for LSRR Gas Turbine Cascade

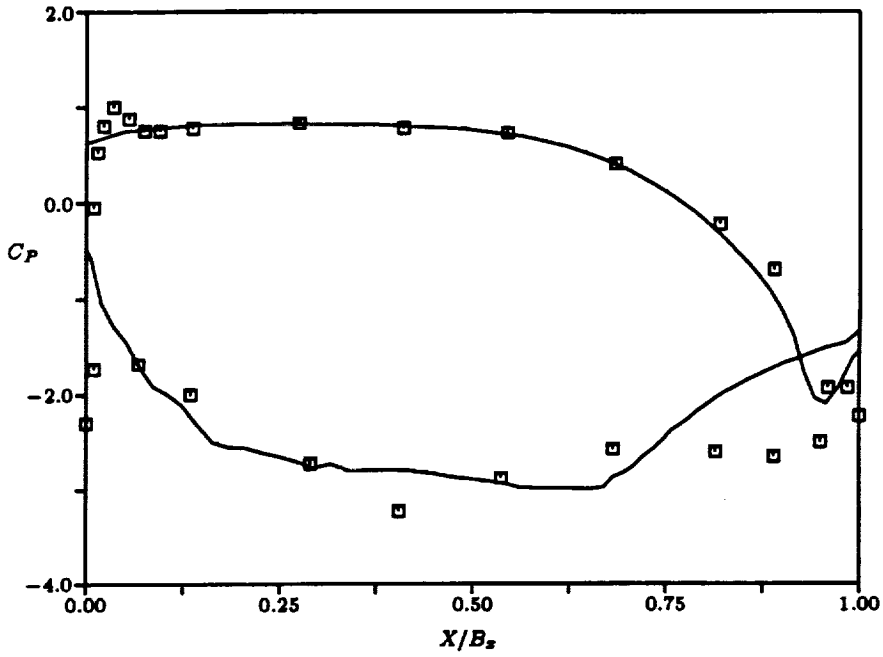

Figure 74 Comparison of Calculated and Measured Static Pressure Distribution at Quarter Span for LSRR Gas Turbine Cascade

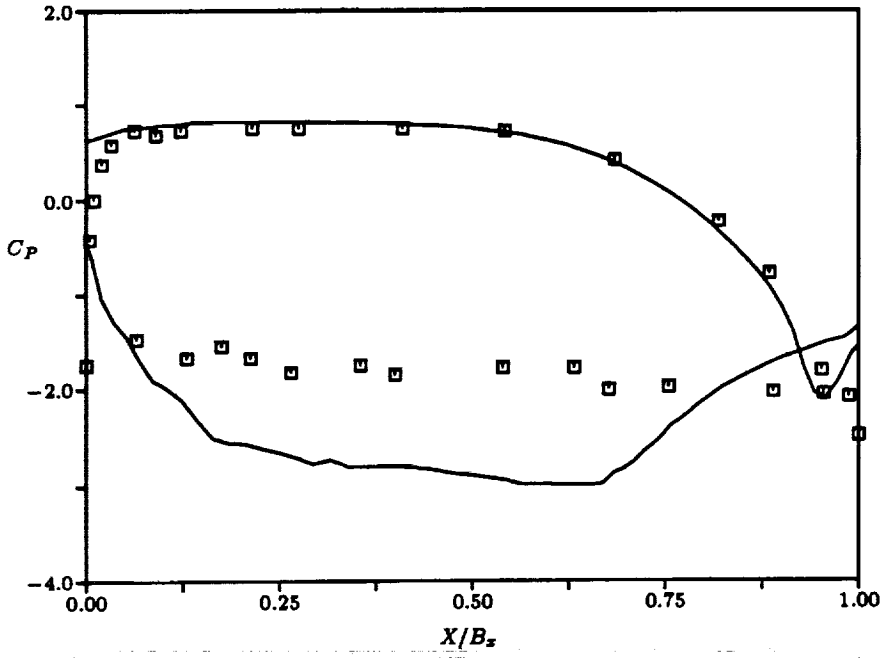

Figure 75 Comparison of Calculated and Measured Static Pressure Distribution at Hub Span for LSRR Gas Turbine Cascade

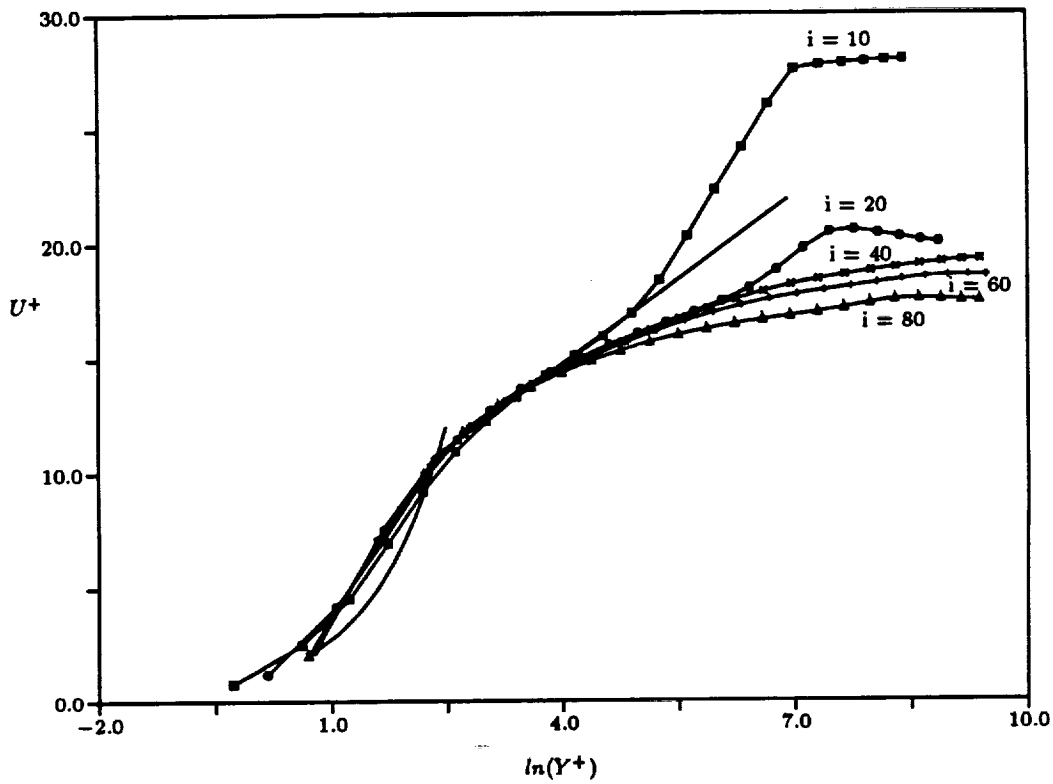

Figure 76 Development of End Wall Boundary Layer in Universal Coordinates at Mid Gap in LSRR Gas Turbine Cascade

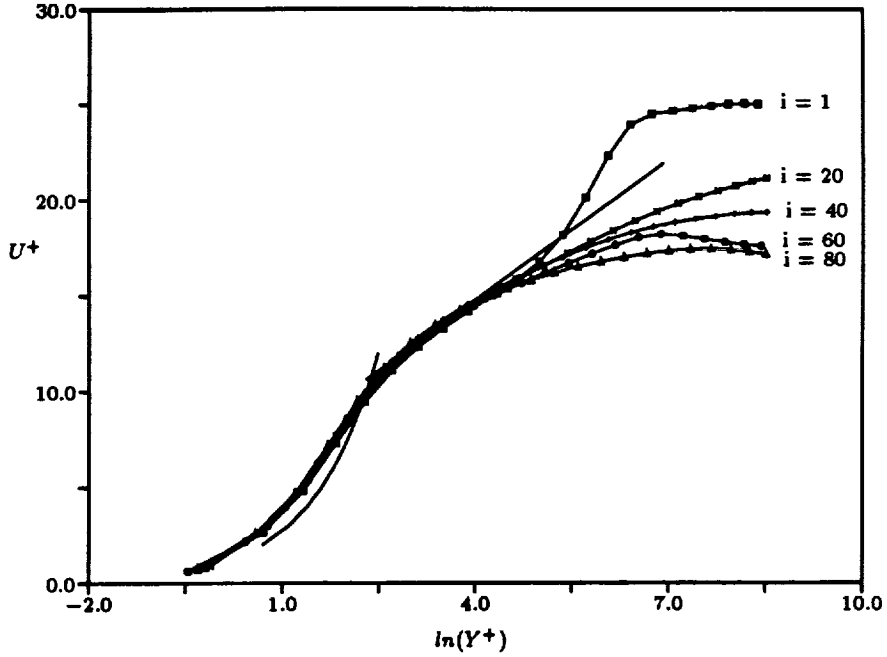

Figure 77 Development of Suction Surface Boundary Layer in Universal Coordinates at Mid Span in LSRR Gas Turbine Cascade

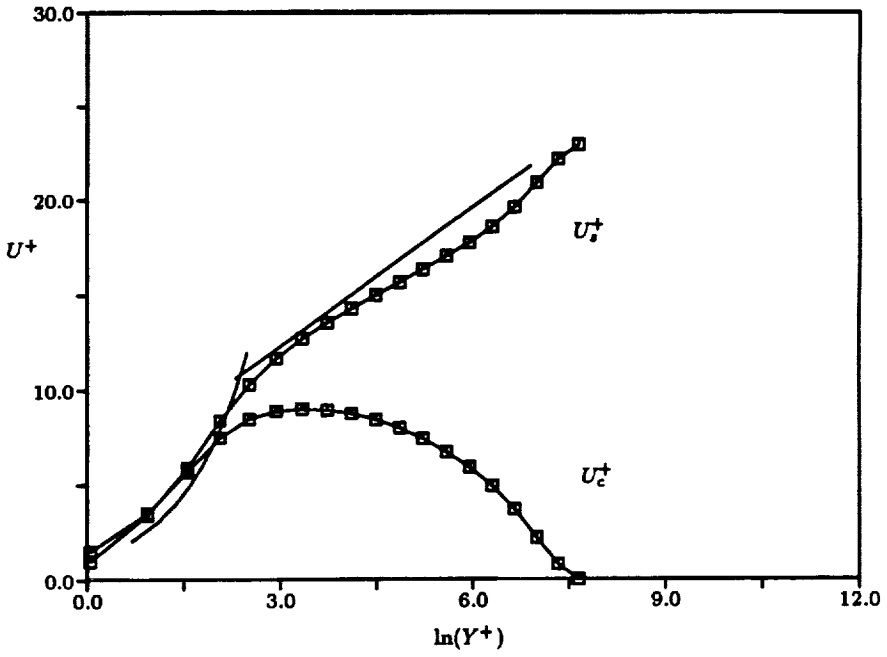

Figure 78 Calculated Streamwise and Crossflow Boundary Layer Velocity Distributions on End Wall in Universal Coordinates in the LSRR Gas Turbine Cascade

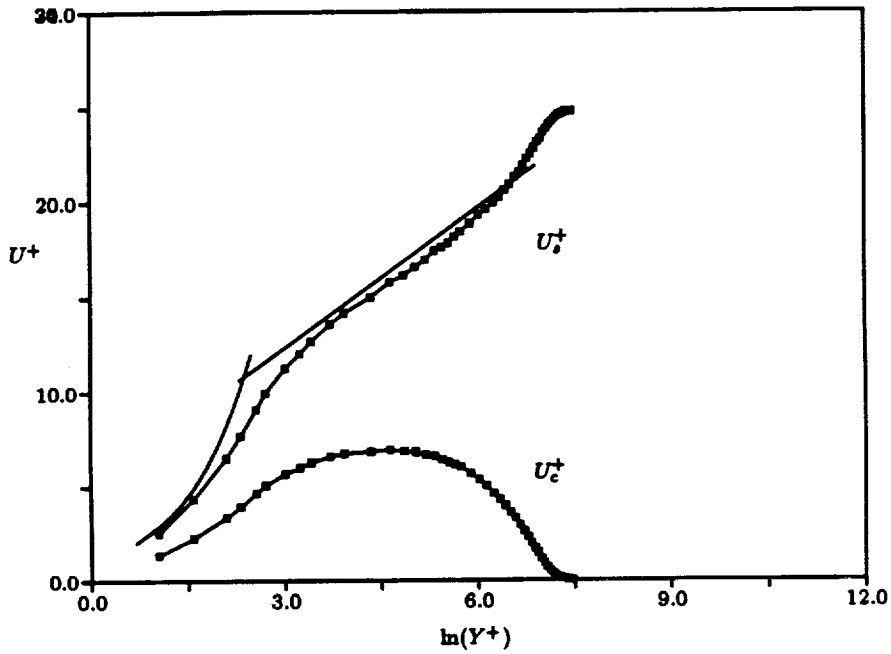

Figure 79 Measured Streamwise and Crossflow Boundary Layer Velocity Distributions on End Wall in Universal Coordinates in the Vermeulen Duct

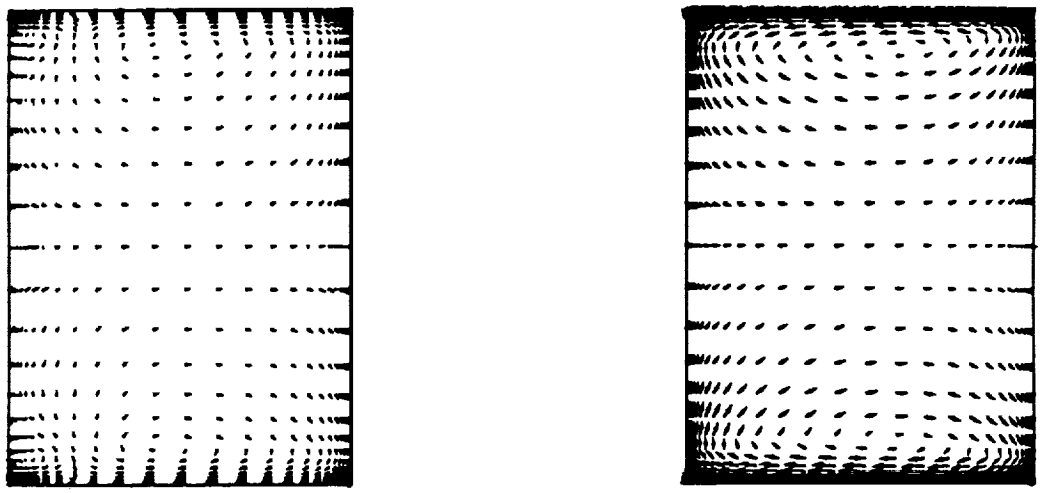

at i = 20

at i = 30

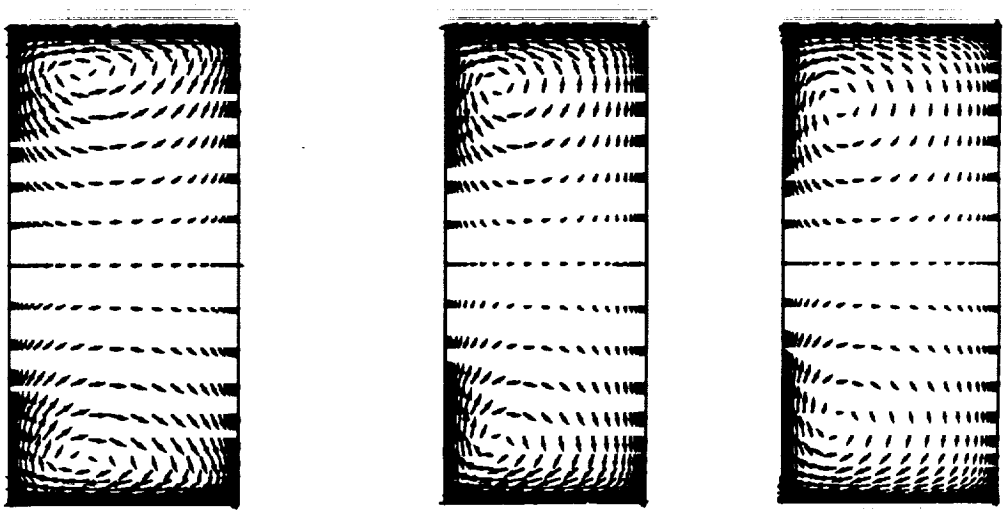

at i = 40

at i = 60

at i = 90

Figure 80 Development of Secondary Flow in LSRR Gas Turbine Cascade

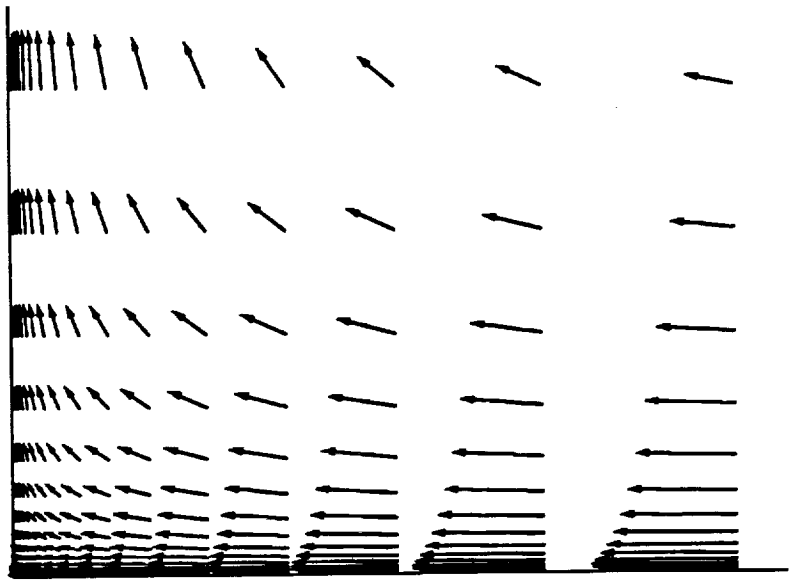

Figure 81 Detail of Corner Flow at i=60 in LSRR Gas Turbine Cascade

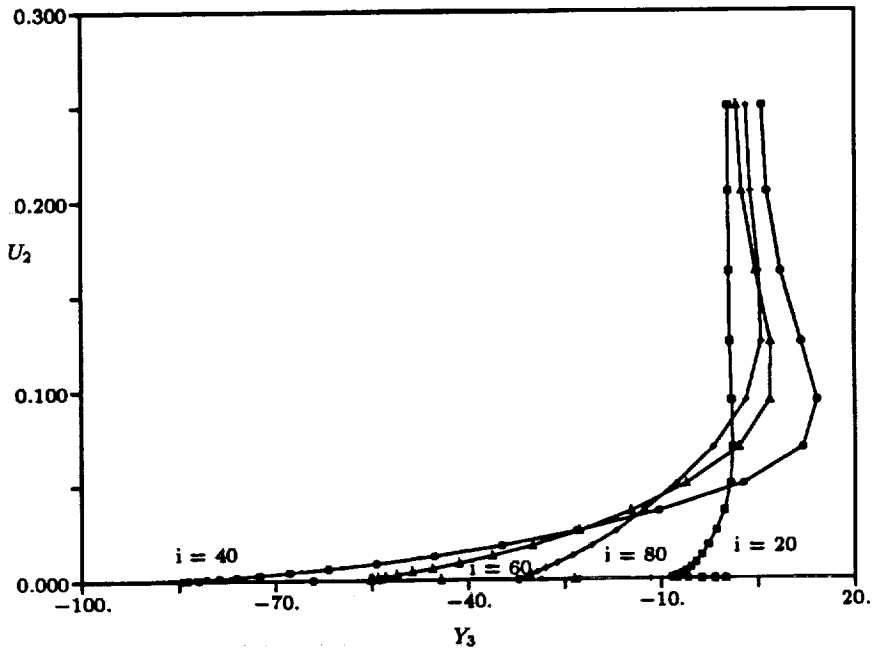

Figure 82 Development of Cross Flow Velocity on End Wall in LSRR Gas Turbine Cascade

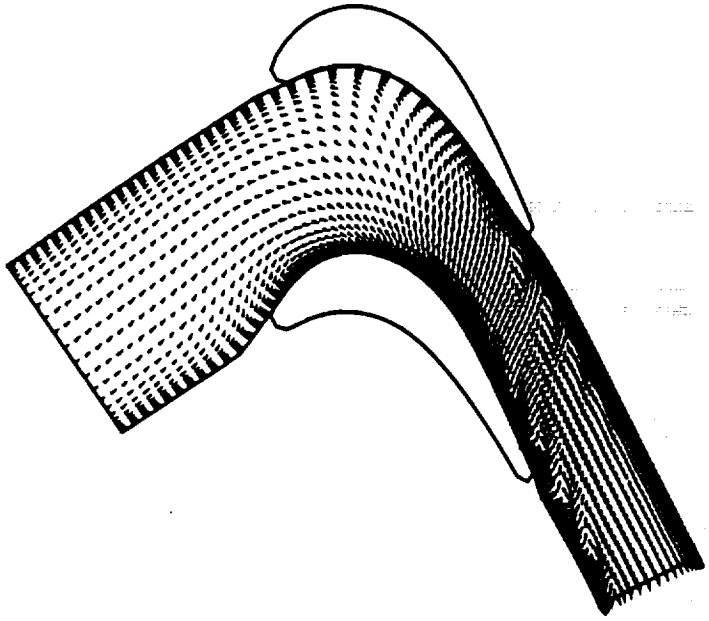

Figure 83 Calculated End Wall Limiting Vectors in LSRR Gas Turbine Cascade

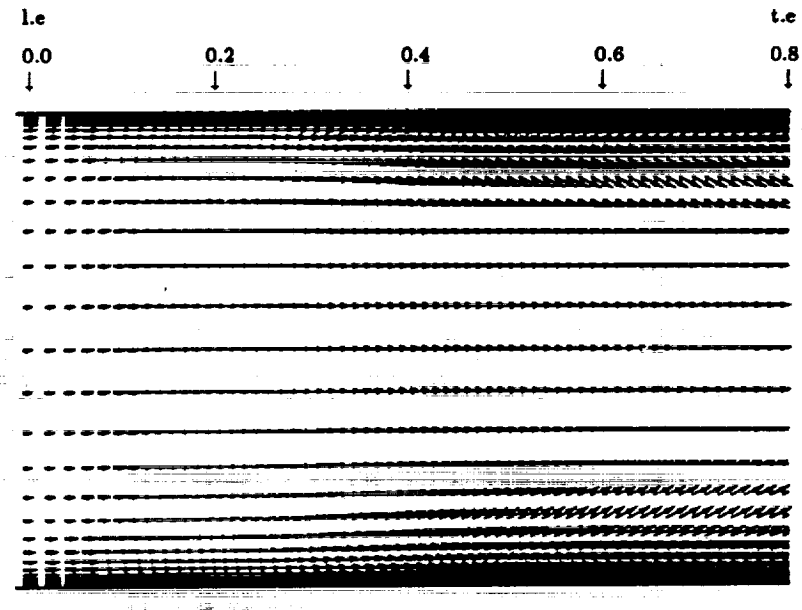

Figure 84 Calculated Suction Surface Limiting Vectors in LSRR Gas Turbine Cascade

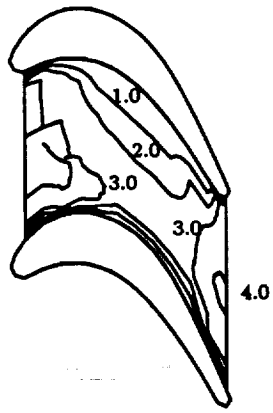

Figure 85 Experimental End Wall St Distribution in Graziani (1980) Cascade - Stx10^3

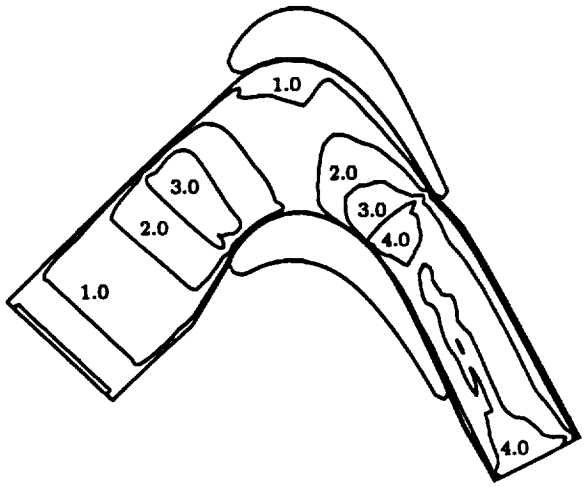

Figure 86 Calculated End Wall St Distribution in LSRR Gas Turbine Cascade - Stx10^3

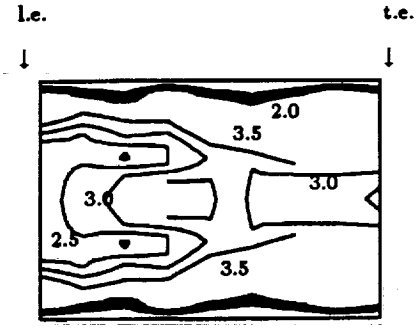

Figure 87 Experimental Suction Surface St Distribution in Graziani (1980) Cascade - Stx10³

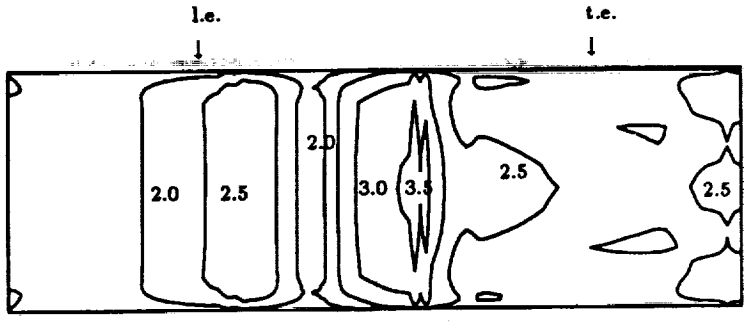

Figure 88 Calculated Suction Surface St Distribution in LSRR Gas Turbine Cascade - Stx10³

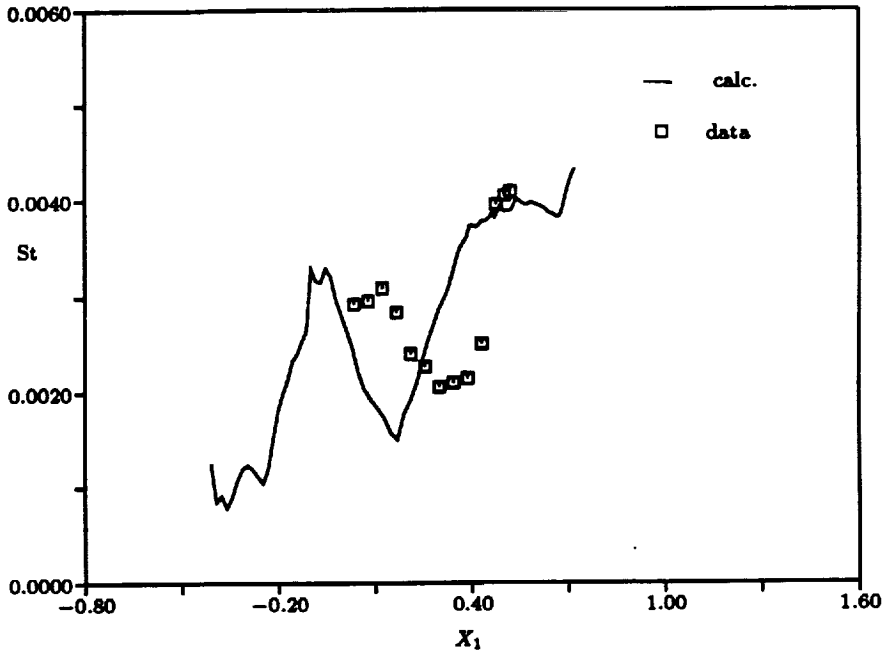

Figure 89 Comparison of Calculated and Measured St Distribution in Graziani (1980) Cascade End Wall at Mid Gap

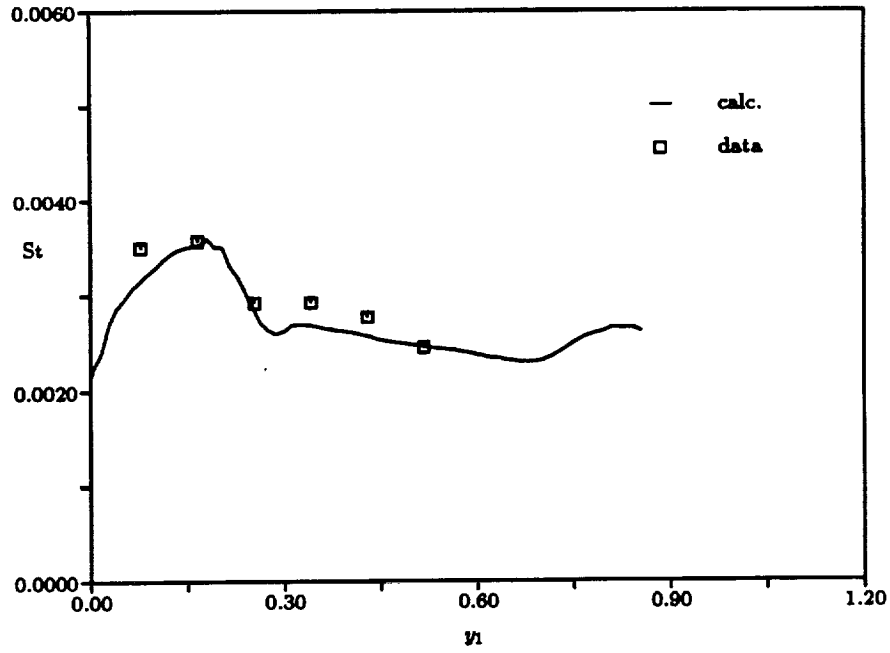

Figure 90 Comparison of Calculated and Measured St Distribution in Graziani (1980) Cascade Suction Surface at Mid Span

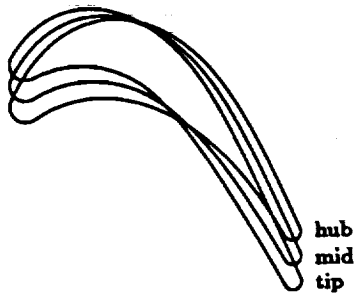

Figure 91 LSRR Gas Turbine Rotor Blade Sections

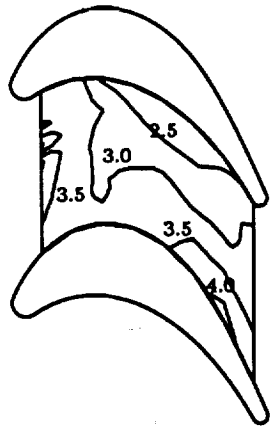

Figure 92 Experimental LSRR Gas Turbine Rotor End Wall St Distribution - Stx10^3 (See Fig. 34c)

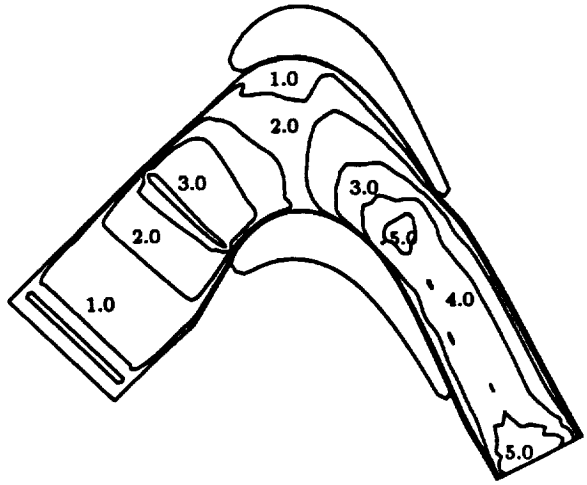

Figure 93 Calculated LSRR Gas Turbine Rotor End Wall St Distribution - Stx10^3

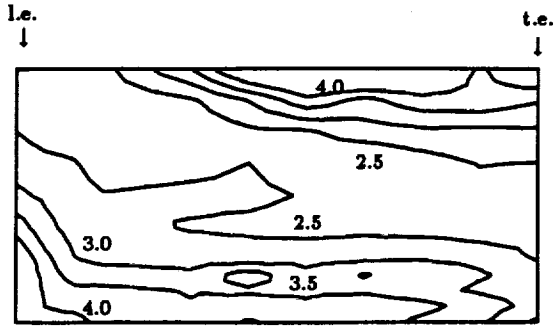

Figure 94 Experimental LSRR Gas Turbine Rotor Suction Surface St Distribution - Stx10³ (See Fig. 34b)

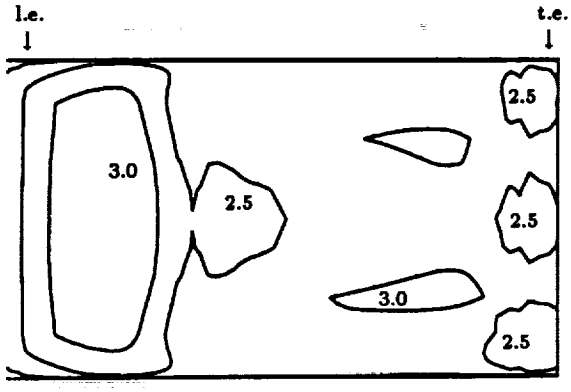

Figure 95 Calculated LSRR Gas Turbine Rotor Suction Surface St Distribution - Stx10³

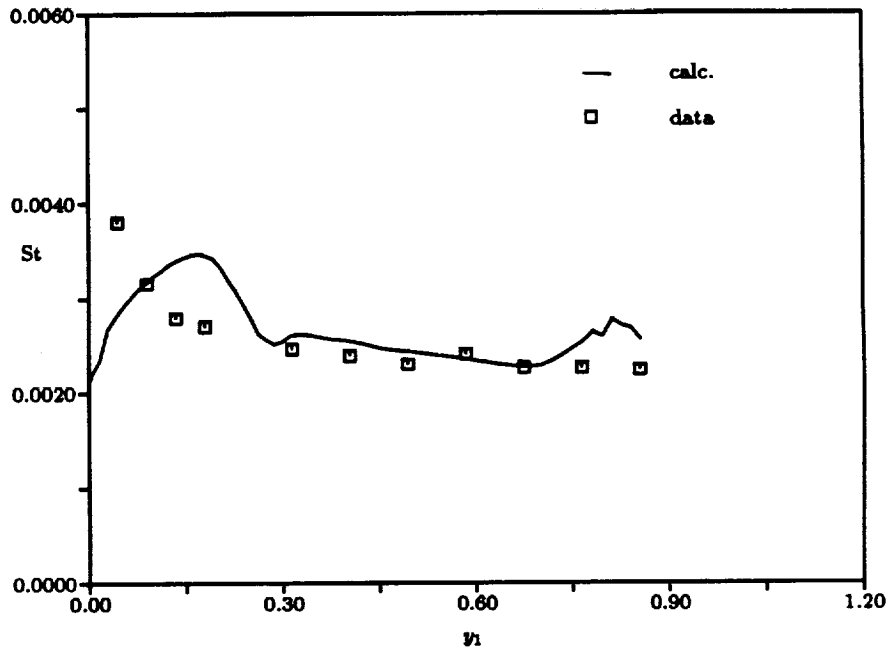

Figure 96 Comparison of Calculated and Measured St Distribution on LSRR Gas Turbine Rotor Suction Surface at Mid Span

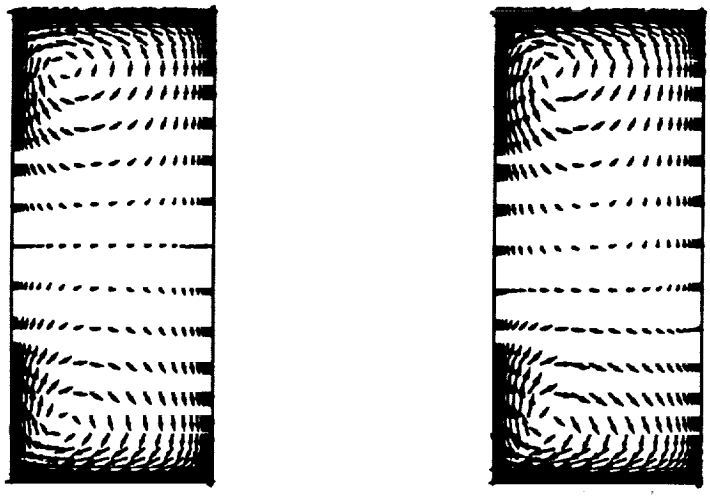

Stator Rotor

Figure 97 Comparison of Stator/Rotor Secondary Flow Near the Trailing Edge

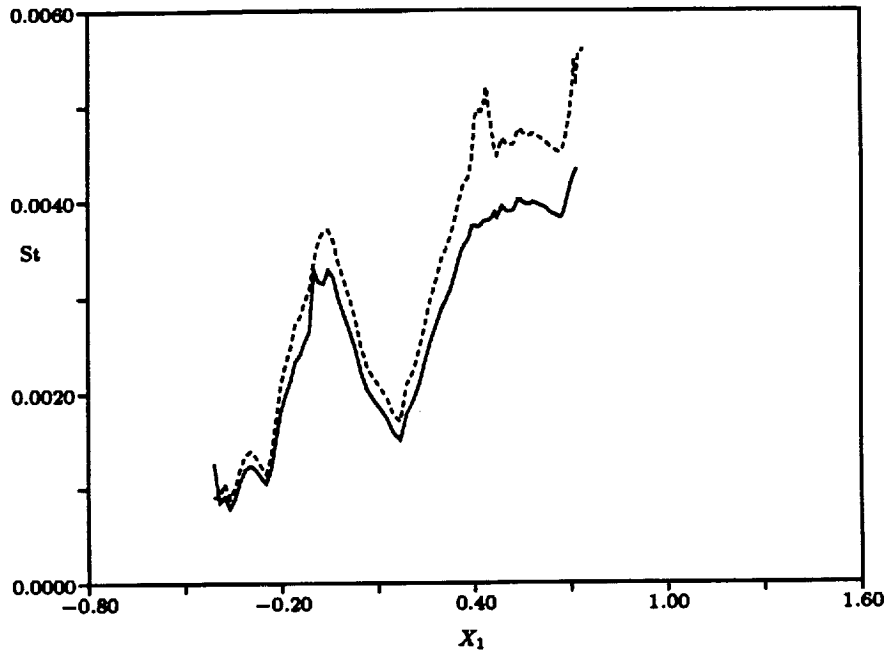

Figure 98 Calculated Stator/Rotor End Wall St Distribution at the Mid Gap Stx10³ (Solid-Stator, Dotted-Rotor)

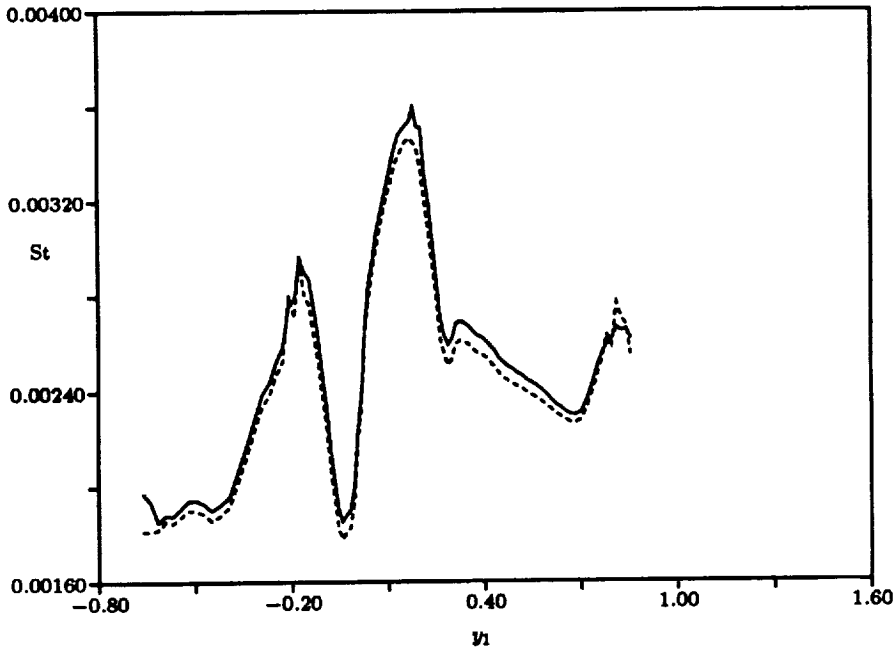

Figure 99 Experimental Stator/Rotor Suction Surface St Distribution at the Mid Span Stx10³ (Solid-Stator, Dotted-Rotor)

A P P E N D I X

Tabulated Stanton Number Distributions

for the Airfoil and Endwall Surfaces

Airfoil Surface Data for Smooth Wall Model

$\beta_1 = 40^0$ N = 160 Re = 2.371×10^5

(Data applies to Figure 33a and Figure 33b)

SPAN %	$\frac{s}{s_{tot(r)}}$ %	Stanton Number $x10^3$
10	-100	2.69
30	-100	2.47
50	-100	2.44
50	-100	2.55
70	-100	2.56
90	-100	2.97
10	-90	2.31
30	-90	2.38
50	-90	2.27
50	-90	2.30
70	-90	2.57
90	-90	2.61
10	-80	2.30
30	-80	2.30
50	-80	2.23
50	-80	2.37
70	-80	2.80
90	-80	2.64
10	-70	2.23
30	-70	2.26
50	-70	2.17
50	-70	2.14
70	-70	2.15
90	-70	2.47
10	-60	2.16
30	-60	2.16
50	-60	2.08
50	-60	2.07
70	-60	2.06
90	-60	2.43
10	-50	2.25
30	-50	2.19
50	-50	2.09
50	-50	2.04
70	-50	2.01
90	-50	2.50
10	-40	2.26
50	-40	2.13
50	-40	2.11
70	-40	2.24
10	-30	2.34
20	-30	2.13
40	-30	2.02
50	-30	1.99
60	-30	1.83
70	-30	1.91
80	-30	1.97
90	-30	1.93
10	-20	2.57
20	-20	2.33
30	-20	2.14
40	-20	2.08
50	-20	1.90
50	-20	1.88
60	-20	1.89
70	-20	1.97
80	-20	1.93
90	-20	2.09
10	-15	2.75
20	-15	2.56
30	-15	2.39
40	-15	2.13
50	-15	1.98
60	-15	1.96
70	-15	2.04
80	-15	2.05
90	-15	2.27
10	-10	2.54
20	-10	2.23
30	-10	2.22
40	-10	2.14
50	-10	2.18
60	-10	2.17

SPAN %	$\frac{s}{s_{tot(r)}}$ %	Stanton Number $x10^3$
70	-10	2.29
80	-10	2.25
90	-10	2.61
10	-5	3.22
20	-5	3.34
30	-5	3.56
40	-5	3.34
60	-5	3.47
70	-5	3.61
80	-5	3.60
90	-5	3.65
10	0	7.42
20	0	6.31
30	0	7.08
40	0	6.08
50	0	5.84
60	0	5.76
70	0	6.29
80	0	5.49
90	0	5.84
10	5	8.10
20	5	7.03
40	5	5.42
50	5	4.69
50	5	4.65
60	5	4.30
80	5	3.54
90	5	2.81
10	10	4.89
20	10	4.33
30	10	4.33
60	10	3.35
70	10	3.12
80	10	2.83
10	15	4.43
30	15	3.61
50	15	3.20
50	15	3.04
70	15	2.81
90	15	2.48
10	20	3.76
20	20	3.37
30	20	3.20
40	20	2.97
50	20	2.83
50	20	2.59
60	20	2.54
70	20	2.39
80	20	2.20
90	20	2.92
30	25	2.64
50	25	2.54
50	25	2.47
70	25	2.10
90	25	2.88
10	35	3.30
20	35	2.93
30	35	2.35
40	35	2.19
50	35	2.05
50	35	2.24
60	35	1.93
70	35	1.81
80	35	2.36
90	35	4.46
10	45	4.32
20	45	3.49
30	45	2.85
40	45	2.28
50	45	2.29
50	45	2.13
60	45	2.19
70	45	2.32

SPAN %	$\frac{s}{s_{tot(r)}}$ %	Stanton Number $x10^3$
80	45	3.37
90	45	5.68
10	55	4.40
20	55	3.63
40	55	2.46
50	55	2.40
50	55	2.23
60	55	2.44
70	55	3.01
90	55	6.53
15	60	4.00
25	60	3.53
35	60	2.90
65	60	3.03
75	60	3.67
85	60	5.50
10	65	4.08
20	65	3.65
30	65	3.27
40	65	2.73
50	65	2.59
50	65	2.82
60	65	2.79
70	65	3.33
80	65	4.26
90	65	6.56
15	70	3.80
25	70	3.39
35	70	2.99
65	70	3.12
75	70	3.98
85	70	5.35
10	75	3.71
20	75	3.38
40	75	2.73
50	75	2.60
50	75	2.77
60	75	2.80
70	75	3.50
90	75	5.45
15	80	3.50
25	80	3.28
35	80	2.97
65	80	3.42
75	80	4.23
85	80	5.20
10	85	3.27
20	85	3.25
30	85	3.08
40	85	2.77
50	85	2.67
50	85	2.87
60	85	3.16
70	85	3.73
80	85	4.56
90	85	5.33
15	90	2.95
25	90	2.94
35	90	2.78
65	90	3.43
75	90	4.13
85	90	4.96
10	95	2.76
30	95	2.75
40	95	2.59
50	95	2.49
50	95	2.72
60	95	3.03
70	95	3.61
80	95	4.55
90	95	5.56

Table A-1a Tabulated Data for Smooth-Wall Model

Endwall Data for Smooth Wall Model

$\beta_1 = 40^o$ N = 160 Re = 2.371×10^5

(Data applies to Figure 33c)

See Figure 20 for X-Y Origin

X in.	Y in.	Stanton Number $x10^3$
-0.75	2.15	3.89
-0.75	2.50	3.93
-0.75	2.65	3.61
-0.75	3.15	3.78
-0.75	3.25	3.88
-0.75	3.90	3.76
-0.75	4.50	3.49
-0.75	5.00	3.60
-0.75	5.50	3.72
-0.75	6.00	4.40
-0.75	6.50	4.04
-0.75	7.00	4.05
-0.75	7.50	3.89
-0.75	7.85	3.93
-0.75	8.00	3.61
-0.75	8.50	3.78
-0.75	8.60	3.88
-0.75	9.25	3.76
-0.75	9.85	3.49
0.00	2.15	3.56
0.00	2.50	3.76
0.00	2.65	3.80
0.00	3.15	5.39
0.00	3.25	6.01
0.00	4.00	6.49
0.00	4.50	4.10
0.00	5.50	3.40
0.00	6.00	3.58
0.00	6.50	3.05
0.00	7.00	3.84
0.00	7.50	3.56
0.00	7.85	3.76
0.00	8.00	3.80
0.00	8.50	5.39
0.00	8.60	6.01
0.00	9.35	6.49
0.00	9.85	4.10
0.75	2.15	3.68
0.75	2.65	3.92
0.75	5.50	3.69
0.75	6.00	3.06
0.75	6.50	3.55
0.75	7.00	3.58

X in.	Y in.	Stanton Number $x10^3$
0.75	7.50	3.68
0.75	8.00	3.92
1.50	6.00	3.40
1.50	6.50	3.43
1.50	7.00	3.52
1.50	7.50	3.77
1.50	8.00	3.84
1.50	8.50	4.28
2.25	6.00	3.46
2.25	6.50	3.44
2.25	7.00	3.33
2.25	7.50	3.39
2.25	8.00	3.56
2.25	8.50	3.14
3.00	6.00	3.32
3.00	6.50	3.69
3.00	7.00	3.45
3.00	7.50	3.49
3.00	8.00	3.14
3.00	8.50	2.80
3.75	5.50	3.53
3.75	6.00	3.60
3.75	6.50	3.75
3.75	7.00	3.45
3.75	7.50	2.90
3.75	8.00	2.75
4.50	5.00	3.70
4.50	5.50	3.64
4.50	6.00	3.52
4.50	6.50	3.12
4.50	7.00	2.83
4.50	7.50	2.81
5.25	4.00	3.52
5.25	4.50	3.50
5.25	5.50	3.07
5.25	6.00	3.01
5.25	6.50	2.92
6.00	2.50	3.75
6.00	3.00	3.44
6.00	4.00	3.36
6.00	5.00	3.09
6.00	5.50	2.83
6.75	-0.85	3.66

X in.	Y in.	Stanton Number $x10^3$
6.75	-0.35	4.23
6.75	0.00	4.35
6.75	0.15	4.16
6.75	1.00	3.71
6.75	1.50	3.67
6.75	2.00	3.68
6.75	2.50	3.50
6.75	3.00	3.25
6.75	3.50	3.12
6.75	4.00	3.19
6.75	4.50	3.66
6.75	5.00	4.23
6.75	5.35	4.35
6.75	5.50	4.16
6.75	6.35	3.71
6.75	6.85	3.67
6.75	7.35	3.68
7.25	-0.85	3.73
7.25	-0.35	3.79
7.25	0.00	3.88
7.25	0.50	3.92
7.25	0.90	3.94
7.25	1.00	3.69
7.25	1.50	3.39
7.25	2.00	3.58
7.25	3.00	3.57
7.25	3.50	3.33
7.25	4.50	3.73
7.25	5.00	3.79
7.25	5.35	3.88
7.25	5.85	3.92
7.25	6.25	3.94
7.25	6.35	3.69
7.25	6.85	3.39
7.25	7.35	3.58

Table A-1b Tabulated Data for Smooth-Wall Model

Airfoil Surface Data for Smooth Wall Model

$\beta_1 = 40^0$ N = 219 Re = 3.232×10^5

(Data applies to Figure 34a and Figure 34b)

SPAN %	$\frac{S}{S_{tot(r)}}$ %	Stanton Number $x10^3$
10	-100	2.82
30	-100	2.40
50	-100	2.45
50	-100	2.52
70	-100	2.45
90	-100	2.91
10	-90	2.11
30	-90	2.20
50	-90	2.10
50	-90	2.13
70	-90	2.49
90	-90	2.47
10	-80	2.08
30	-80	2.11
50	-80	2.07
50	-80	2.69
70	-80	2.15
90	-80	2.39
10	-70	2.00
30	-70	2.04
50	-70	2.09
50	-70	2.07
70	-70	1.95
90	-70	2.22
10	-60	1.94
30	-60	1.95
50	-60	1.89
50	-60	1.92
70	-60	1.87
90	-60	2.23
10	-50	2.04
30	-50	2.02
50	-50	1.92
50	-50	1.86
70	-50	1.86
90	-50	2.53
10	-40	2.14
50	-40	1.94
50	-40	1.97
70	-40	2.07
10	-30	2.19
20	-30	2.06
40	-30	1.92
50	-30	1.87
60	-30	1.77
70	-30	1.82
80	-30	1.79
90	-30	1.95
10	-20	2.42
20	-20	2.19
30	-20	2.02
40	-20	1.96
50	-20	1.83
50	-20	1.86
60	-20	1.83
70	-20	1.84
80	-20	1.80
90	-20	1.89
10	-15	2.58
20	-15	2.44
30	-15	2.34
40	-15	2.13
50	-15	1.95
60	-15	1.93
70	-15	1.89
80	-15	1.94
90	-15	2.10
10	-10	2.46
20	-10	2.26
30	-10	2.10
40	-10	2.03
50	-10	2.03
60	-10	2.03
70	-10	2.11
80	-10	2.08
90	-10	2.45
10	-5	3.03
20	-5	3.04
30	-5	3.24
40	-5	2.95
60	-5	3.19
70	-5	3.32
80	-5	3.23
90	-5	3.33
10	0	7.49
20	0	6.25
30	0	6.90
40	0	5.70
50	0	4.96
60	0	5.55
70	0	6.06
80	0	5.13
90	0	5.57
10	5	7.42
20	5	6.36
40	5	4.71
50	5	4.05
50	5	4.21
60	5	3.87
80	5	3.16
90	5	2.43
10	10	4.57
20	10	3.96
30	10	3.90
60	10	3.08
70	10	2.78
80	10	2.61
10	15	4.17
30	15	3.16
50	15	2.88
50	15	2.75
70	15	2.54
90	15	2.40
10	20	3.56
20	20	3.21
30	20	2.92
40	20	2.70
50	20	2.36
50	20	2.51
60	20	2.32
70	20	2.14
80	20	2.00
90	20	2.65
30	25	2.41
50	25	2.33
50	25	2.34
70	25	1.93
90	25	2.59
10	35	3.19
20	35	2.90
30	35	2.32
40	35	2.13
50	35	2.04
50	35	2.22
60	35	1.93
70	35	1.81
80	35	2.31
90	35	4.11
10	45	4.23
20	45	3.35
30	45	2.61
40	45	2.17
50	45	2.26
50	45	2.27
60	45	2.25
70	45	2.40
80	45	3.30
90	45	5.90
10	55	4.04
20	55	3.50
40	55	2.28
50	55	2.34
50	55	2.27
60	55	2.37
70	55	2.92
90	55	6.54
15	60	3.82
25	60	3.36
35	60	2.69
65	60	2.78
75	60	3.68
85	60	5.24
10	65	3.85
20	65	3.46
30	65	3.13
40	65	2.56
50	65	2.67
50	65	2.45
60	65	2.62
70	65	3.27
80	65	4.17
90	65	6.88
15	70	3.69
25	70	3.28
35	70	2.85
65	70	3.03
75	70	3.93
85	70	5.37
10	75	3.46
20	75	3.19
40	75	2.51
50	75	2.58
50	75	2.42
60	75	2.65
70	75	3.40
90	75	5.30
15	80	3.39
25	80	3.16
35	80	2.75
65	80	3.36
75	80	4.11
85	80	5.13
10	85	3.12
20	85	3.05
30	85	2.90
40	85	2.55
50	85	2.46
50	85	2.68
60	85	3.00
70	85	3.51
80	85	4.72
90	85	5.23
15	90	2.91
25	90	2.83
35	90	2.59
65	90	3.27
75	90	4.12
85	90	4.93
10	95	2.57
30	95	2.65
40	95	2.48
50	95	2.37
50	95	2.47
60	95	2.93
70	95	3.61
80	95	4.36
90	95	5.81

Table A-2a Tabulated Data for Smooth-Wall Model

Endwall Data for Smooth Wall Model

$\beta_1 = 40^0$ N = 219 Re = 3.232×10^5

(Data applies to Figure 34c)

See Figure 20 for X-Y Origin

X in.	Y in.	Stanton Number $x10^3$
-0.75	2.15	3.91
-0.75	2.50	4.16
-0.75	2.65	3.57
-0.75	3.15	3.76
-0.75	3.25	3.83
-0.75	3.90	3.71
-0.75	4.50	3.48
-0.75	5.00	3.72
-0.75	5.50	4.03
-0.75	6.00	4.88
-0.75	6.50	4.09
-0.75	7.00	4.15
-0.75	7.50	3.91
-0.75	7.85	4.16
-0.75	8.00	3.57
-0.75	8.50	3.76
-0.75	8.60	3.83
-0.75	9.25	3.71
-0.75	9.85	3.48
0.00	2.15	3.46
0.00	2.50	3.79
0.00	2.65	3.68
0.00	3.15	5.43
0.00	3.25	6.37
0.00	4.00	6.64
0.00	4.50	4.02
0.00	5.50	3.51
0.00	6.00	3.72
0.00	6.50	2.81
0.00	7.00	3.99
0.00	7.50	3.46
0.00	7.85	3.79
0.00	8.00	3.68
0.00	8.50	5.43
0.00	8.60	6.37
0.00	9.35	6.64
0.00	9.85	4.02
0.75	2.15	3.60
0.75	2.65	3.91
0.75	5.50	3.89
0.75	6.00	2.93
0.75	6.50	3.67
0.75	7.00	3.77

X in.	Y in.	Stanton Number $x10^3$
0.75	7.50	3.60
0.75	8.00	3.91
1.50	6.00	3.47
1.50	6.50	3.30
1.50	7.00	3.48
1.50	7.50	3.70
1.50	8.00	3.80
1.50	8.50	4.10
2.25	6.00	3.44
2.25	6.50	3.38
2.25	7.00	3.19
2.25	7.50	3.22
2.25	8.00	3.36
2.25	8.50	2.89
3.00	6.00	3.26
3.00	6.50	3.61
3.00	7.00	3.28
3.00	7.50	3.25
3.00	8.00	2.93
3.00	8.50	2.58
3.75	5.50	3.46
3.75	6.00	3.46
3.75	6.50	3.50
3.75	7.00	3.22
3.75	7.50	2.69
3.75	8.00	2.57
4.50	5.00	3.66
4.50	5.50	3.52
4.50	6.00	3.33
4.50	6.50	3.02
4.50	7.00	2.75
4.50	7.50	2.58
5.25	4.00	3.82
5.25	4.50	3.52
5.25	5.50	2.94
5.25	6.00	2.94
5.25	6.50	2.73
6.00	2.50	3.85
6.00	3.00	3.66
6.00	4.00	3.26
6.00	5.00	3.01
6.00	5.50	2.65
6.75	-0.85	3.63

X in.	Y in.	Stanton Number $x10^3$
6.75	-0.35	4.23
6.75	0.00	4.23
6.75	0.15	4.08
6.75	1.00	3.79
6.75	1.50	3.81
6.75	2.00	3.75
6.75	2.50	3.64
6.75	3.00	3.32
6.75	3.50	3.06
6.75	4.00	3.15
6.75	4.50	3.63
6.75	5.00	4.23
6.75	5.35	4.23
6.75	5.50	4.08
6.75	6.35	3.79
6.75	6.85	3.81
6.75	7.35	3.75
7.25	-0.85	3.65
7.25	-0.35	3.81
7.25	0.00	3.81
7.25	0.50	4.06
7.25	0.90	4.19
7.25	1.00	3.77
7.25	1.50	3.40
7.25	2.00	3.60
7.25	3.00	3.63
7.25	3.50	3.45
7.25	4.50	3.65
7.25	5.00	3.81
7.25	5.35	3.81
7.25	5.85	4.06
7.25	6.25	4.19
7.25	6.35	3.77
7.25	6.85	3.40
7.25	7.35	3.60

Table A-2b Tabulated Data for Smooth-Wall Model

Airfoil Surface Data for Smooth Wall Model

$\beta_1 = 40^0$ N = 300 Re = 4.370×10^5

(Data applies to Figure 35a and Figure 35b)

SPAN %	$\frac{S}{S_{tot(r)}}$ %	Stanton Number $x10^3$
10	-100	2.64
30	-100	2.22
50	-100	2.04
50	-100	2.36
70	-100	2.28
90	-100	2.77
10	-90	1.93
30	-90	2.04
50	-90	1.76
50	-90	1.90
70	-90	2.35
90	-90	2.31
10	-80	1.89
30	-80	1.91
50	-80	1.80
50	-80	2.32
70	-80	2.02
90	-80	2.14
10	-70	1.81
30	-70	1.82
50	-70	1.63
50	-70	1.74
70	-70	1.79
90	-70	2.00
10	-60	1.72
30	-60	1.75
50	-60	1.68
50	-60	1.65
70	-60	1.71
90	-60	1.95
10	-50	1.84
30	-50	1.81
50	-50	1.63
50	-50	1.67
70	-50	1.68
90	-50	1.87
10	-40	1.93
50	-40	1.68
50	-40	1.74
70	-40	1.89
10	-30	1.93
20	-30	1.85
40	-30	1.70
50	-30	1.62
60	-30	1.57
70	-30	1.65
80	-30	1.60
90	-30	1.82
10	-20	2.14
20	-20	1.90
30	-20	1.75
40	-20	1.68
50	-20	1.49
50	-20	1.54
60	-20	1.56
70	-20	1.64
80	-20	1.57
90	-20	1.68
10	-15	2.31
20	-15	2.24
30	-15	1.97
40	-15	1.91
50	-15	1.59
60	-15	1.67
70	-15	1.65
80	-15	1.68
90	-15	1.85
10	-10	2.18
20	-10	1.99
30	-10	1.84
40	-10	1.67
50	-10	1.77
60	-10	1.74
70	-10	1.84
80	-10	1.80
90	-10	2.18
10	-5	2.69
20	-5	2.57
30	-5	2.96
40	-5	2.47
60	-5	2.67
70	-5	3.06
80	-5	2.61
90	-5	3.02
10	0	7.85
20	0	5.46
30	0	6.35
40	0	4.67
50	0	4.09
60	0	4.80
70	0	5.22
80	0	4.28
90	0	5.05
10	5	7.22
20	5	5.82
40	5	4.11
50	5	3.64
50	5	3.59
60	5	3.32
80	5	2.71
90	5	2.04
10	10	4.60
20	10	3.87
30	10	3.83
60	10	2.85
70	10	2.52
80	10	2.43
10	15	4.19
30	15	3.19
50	15	2.77
50	15	2.49
70	15	2.33
90	15	2.28
10	20	3.62
20	20	3.40
30	20	2.84
40	20	2.60
50	20	2.22
50	20	2.47
60	20	2.15
70	20	1.99
80	20	1.90
90	20	2.47
30	25	2.43
50	25	2.35
50	25	2.33
70	25	1.88
90	25	2.34
10	35	3.56
20	35	3.25
30	35	2.58
40	35	2.31
50	35	2.10
50	35	2.32
60	35	2.11
70	35	1.92
80	35	2.31
90	35	3.64
10	45	4.38
20	45	3.61
30	45	2.69
40	45	2.36
50	45	2.40
50	45	2.28
60	45	2.40
70	45	2.37
80	45	3.11
90	45	5.37
10	55	4.08
20	55	3.55
40	55	2.28
50	55	2.53
50	55	2.21
60	55	2.27
70	55	2.65
90	55	5.78
15	60	4.02
25	60	3.51
35	60	2.73
65	60	2.45
75	60	3.37
85	60	4.74
10	65	3.80
20	65	3.48
30	65	3.03
40	65	2.49
50	65	2.53
50	65	2.20
60	65	2.29
70	65	2.98
80	65	3.76
90	65	5.96
15	70	3.78
25	70	3.35
35	70	2.75
65	70	2.68
75	70	3.60
85	70	4.47
10	75	3.54
20	75	3.23
40	75	2.41
50	75	2.44
50	75	2.15
60	75	2.35
70	75	3.11
90	75	4.74
15	80	3.37
25	80	3.19
35	80	2.66
65	80	3.13
75	80	3.73
85	80	4.54
10	85	3.05
20	85	3.03
30	85	2.88
40	85	2.44
50	85	2.20
50	85	2.59
60	85	2.78
70	85	3.18
80	85	4.18
90	85	4.50
15	90	2.86
25	90	2.76
35	90	2.51
65	90	2.97
75	90	3.63
85	90	4.54
10	95	2.46
30	95	2.59
40	95	2.36
50	95	2.12
50	95	2.30
60	95	2.68
70	95	3.22
80	95	3.91
90	95	5.06

Table A-3a Tabulated Data for Smooth-Wall Model

Endwall Data for Smooth Wall Model

$\beta_1 = 40^0$ N = 300 Re = 4.370×10^5

(Data applies to Figure 35c)

See Figure 20 for X-Y Origin

X in.	Y in.	Stanton Number $x10^3$
-0.75	2.15	3.67
-0.75	2.50	4.00
-0.75	2.65	3.27
-0.75	3.15	3.45
-0.75	3.25	3.53
-0.75	3.90	3.48
-0.75	4.50	3.43
-0.75	5.00	3.74
-0.75	5.50	3.96
-0.75	6.00	5.02
-0.75	6.50	3.83
-0.75	7.00	4.04
-0.75	7.50	3.67
-0.75	7.85	4.00
-0.75	8.00	3.27
-0.75	8.50	3.45
-0.75	9.25	3.48
0.00	2.15	3.18
0.00	2.50	3.50
0.00	2.65	3.50
0.00	3.15	5.07
0.00	3.25	5.97
0.00	4.00	6.00
0.00	4.50	3.68
0.00	5.50	3.39
0.00	6.00	3.63
0.00	6.50	2.42
0.00	7.00	4.06
0.00	7.50	3.18
0.00	7.85	3.50
0.00	8.00	3.50
0.00	8.50	5.07
0.00	8.60	5.97
0.00	9.35	6.00
0.00	9.85	3.68
0.75	2.15	3.29
0.75	2.65	3.68
0.75	5.50	4.09
0.75	6.00	2.63
0.75	6.50	3.75
0.75	7.00	3.74
0.75	7.50	3.29
0.75	8.00	3.68

X in.	Y in.	Stanton Number $x10^3$
0.75	8.60	3.53
0.75	9.85	3.43
1.50	6.00	3.34
1.50	6.50	3.20
1.50	7.00	3.33
1.50	7.50	3.41
1.50	8.00	3.60
1.50	8.50	3.77
2.25	6.00	3.29
2.25	6.50	3.14
2.25	7.00	3.05
2.25	7.50	3.04
2.25	8.00	3.21
2.25	8.50	2.65
3.00	6.00	3.22
3.00	6.50	3.30
3.00	7.00	3.10
3.00	7.50	3.05
3.00	8.00	2.71
3.00	8.50	2.36
3.75	5.50	3.44
3.75	6.00	3.41
3.75	6.50	3.33
3.75	7.00	3.03
3.75	7.50	2.49
3.75	8.00	2.38
4.50	5.00	3.73
4.50	5.50	3.53
4.50	6.00	3.15
4.50	6.50	2.94
4.50	7.00	2.57
4.50	7.50	2.30
5.25	4.00	4.21
5.25	4.50	3.61
5.25	5.50	2.76
5.25	6.00	2.74
5.25	6.50	2.46
6.00	2.50	3.47
6.00	3.00	3.34
6.00	4.00	2.99
6.00	5.00	2.77
6.00	5.50	2.38
6.75	-0.85	3.27

X in.	Y in.	Stanton Number $x10^3$
6.75	-0.35	3.76
6.75	0.00	3.77
6.75	0.15	3.45
6.75	1.00	3.42
6.75	1.50	3.62
6.75	2.00	3.49
6.75	2.50	3.45
6.75	3.00	3.05
6.75	3.50	2.86
6.75	4.00	2.86
6.75	4.50	3.27
6.75	5.00	3.76
6.75	5.35	3.77
6.75	5.50	3.45
6.75	6.35	3.42
6.75	6.85	3.62
6.75	7.35	3.49
7.25	-0.85	3.22
7.25	-0.35	3.38
7.25	0.00	3.27
7.25	0.50	3.96
7.25	0.90	3.97
7.25	1.00	3.49
7.25	1.50	3.19
7.25	2.00	3.33
7.25	3.00	3.24
7.25	3.50	3.08
7.25	4.50	3.22
7.25	5.00	3.38
7.25	5.35	3.27
7.25	5.85	3.96
7.25	6.25	3.97
7.25	6.35	3.49
7.25	6.85	3.19
7.25	7.35	3.33

Table A-3b Tabulated Data for Smooth-Wall Model

Airfoil Surface Data for Smooth Wall Model

$\beta_1 = 40^o$ N = 357 Re = 5.133×10^5

(Data applies to Figure 36a and Figure 36b)

SPAN %	$\frac{S}{S_{tot(r)}}$ %	Stanton Number x10^3
10	-100	2.50
30	-100	2.09
50	-100	2.13
50	-100	2.23
70	-100	2.12
90	-100	2.59
10	-90	1.84
30	-90	1.92
50	-90	1.72
50	-90	1.78
70	-90	2.15
90	-90	2.19
10	-80	1.78
30	-80	1.83
50	-80	1.68
50	-80	2.41
70	-80	1.88
90	-80	1.99
10	-70	1.69
30	-70	1.69
50	-70	1.58
50	-70	1.62
70	-70	1.67
90	-70	1.87
10	-60	1.62
30	-60	1.64
50	-60	1.60
50	-60	1.59
70	-60	1.58
90	-60	1.84
10	-50	1.73
30	-50	1.74
50	-50	1.59
50	-50	1.56
70	-50	1.58
90	-50	1.78
10	-40	1.83
50	-40	1.62
50	-40	1.65
70	-40	1.82
10	-30	1.85
20	-30	1.77
40	-30	1.64
50	-30	1.57
60	-30	1.50
70	-30	1.57
80	-30	1.51
90	-30	1.79
10	-20	2.03
20	-20	1.80
30	-20	1.70
40	-20	1.55
50	-20	1.45
50	-20	1.44
60	-20	1.44
70	-20	1.55
80	-20	1.46
90	-20	1.58
10	-15	2.19
20	-15	2.02
30	-15	1.91
40	-15	1.67
50	-15	1.54
60	-15	1.50
70	-15	1.55
80	-15	1.54
90	-15	1.73
10	-10	2.07
20	-10	1.80
30	-10	1.73
40	-10	1.58
50	-10	1.61
60	-10	1.64
70	-10	1.73
80	-10	1.67
90	-10	2.01
10	-5	2.38
20	-5	2.56
30	-5	2.64
40	-5	2.46
60	-5	2.66
70	-5	2.72
80	-5	2.60
90	-5	2.70
10	0	6.41
20	0	5.32
30	0	5.49
40	0	4.56
50	0	4.05
60	0	4.69
70	0	4.46
80	0	4.06
90	0	4.41
10	5	6.65
20	5	5.27
40	5	3.94
50	5	3.44
50	5	3.35
60	5	3.05
80	5	2.48
90	5	1.93
10	10	4.14
20	10	3.68
30	10	3.63
60	10	2.77
70	10	2.44
80	10	2.37
10	15	4.02
30	15	3.08
50	15	2.67
50	15	2.50
70	15	2.30
90	15	2.19
10	20	3.67
20	20	3.46
30	20	2.74
40	20	2.56
50	20	2.33
50	20	2.44
60	20	2.16
70	20	2.00
80	20	1.98
90	20	2.48
30	25	2.49
50	25	2.39
50	25	2.57
70	25	1.98
90	25	2.29
10	35	3.51
20	35	3.37
30	35	2.63
40	35	2.36
50	35	2.31
50	35	2.42
60	35	2.28
70	35	2.05
80	35	2.39
90	35	3.72
10	45	4.14
20	45	3.55
30	45	2.66
40	45	2.38
50	45	2.44
50	45	2.45
60	45	2.53
70	45	2.43
80	45	3.17
90	45	5.35
10	55	3.99
20	55	3.46
40	55	2.32
50	55	2.46
50	55	2.34
60	55	2.30
70	55	2.62
90	55	5.82
15	60	3.88
25	60	3.48
35	60	2.64
65	60	2.46
75	60	3.29
85	60	4.81
10	65	3.85
20	65	3.52
30	65	3.00
40	65	2.46
50	65	2.52
50	65	2.26
60	65	2.25
70	65	2.94
80	65	3.53
90	65	6.00
15	70	3.71
25	70	3.30
35	70	2.71
65	70	2.68
75	70	3.57
85	70	4.67
10	75	3.41
20	75	3.20
40	75	2.33
50	75	2.34
50	75	2.10
60	75	2.27
70	75	3.06
90	75	4.69
15	80	3.34
25	80	3.09
35	80	2.56
65	80	3.00
75	80	3.68
85	80	4.45
10	85	3.15
20	85	2.98
30	85	2.86
40	85	2.36
50	85	2.14
50	85	2.48
60	85	2.66
70	85	3.10
80	85	4.05
90	85	4.46
15	90	2.86
25	90	2.81
35	90	2.45
65	90	2.90
75	90	3.48
85	90	4.46
10	95	2.49
30	95	2.51
40	95	2.31
50	95	2.06
50	95	2.27
60	95	2.52
70	95	3.11
80	95	3.69
90	95	4.86

Table A-4a Tabulated Data for Smooth-Wall Model

Endwall Data for Smooth Wall Model

$\beta_1 = 40^o$ N = 357 Re = 5.133×10^5

(Data applies to Figure 36c)

See Figure 20 for X-Y Origin

X in.	Y in.	Stanton Number $x10^3$
-0.75	2.15	3.60
-0.75	2.50	4.07
-0.75	2.65	3.13
-0.75	3.15	3.44
-0.75	3.25	3.41
-0.75	3.90	3.43
-0.75	4.50	3.62
-0.75	5.00	3.84
-0.75	5.50	4.18
-0.75	6.00	5.21
-0.75	6.50	3.82
-0.75	7.00	4.01
-0.75	7.50	3.60
-0.75	7.85	4.07
-0.75	8.00	3.13
-0.75	8.50	3.44
-0.75	8.60	3.41
-0.75	9.25	3.43
-0.75	9.85	3.62
0.00	2.15	3.09
0.00	2.50	3.51
0.00	2.65	3.52
0.00	3.15	4.90
0.00	3.25	5.78
0.00	4.00	5.84
0.00	4.50	3.53
0.00	5.50	3.35
0.00	6.00	3.62
0.00	6.50	2.26
0.00	7.00	4.14
0.00	7.50	3.09
0.00	7.85	3.51
0.00	8.00	3.52
0.00	8.50	4.90
0.00	8.60	5.78
0.00	9.35	5.84
0.00	9.85	3.53
0.75	2.15	3.18
0.75	2.65	3.47
0.75	5.50	4.17
0.75	6.00	2.45
0.75	6.50	3.68
0.75	7.00	3.63

X in.	Y in.	Stanton Number $x10^3$
0.75	7.50	3.18
0.75	8.00	3.47
1.50	6.00	3.27
1.50	6.50	3.07
1.50	7.00	3.24
1.50	7.50	3.31
1.50	8.00	3.49
1.50	8.50	3.51
2.25	6.00	3.26
2.25	6.50	3.01
2.25	7.00	3.01
2.25	7.50	2.93
2.25	8.00	3.12
2.25	8.50	2.52
3.00	6.00	3.26
3.00	6.50	3.34
3.00	7.00	3.04
3.00	7.50	2.92
3.00	8.00	2.63
3.00	8.50	2.25
3.75	5.50	3.48
3.75	6.00	3.36
3.75	6.50	3.27
3.75	7.00	2.90
3.75	7.50	2.39
3.75	8.00	2.24
4.50	5.00	3.81
4.50	5.50	3.57
4.50	6.00	3.05
4.50	6.50	2.83
4.50	7.00	2.45
4.50	7.50	2.15
5.25	4.00	4.31
5.25	4.50	3.72
5.25	5.50	2.76
5.25	6.00	2.72
5.25	6.50	2.37
6.00	2.50	3.57
6.00	3.00	3.46
6.00	4.00	3.17
6.00	5.00	3.00
6.00	5.50	2.48
6.75	-0.85	3.37

X in.	Y in.	Stanton Number $x10^3$
6.75	-0.35	3.83
6.75	0.00	3.88
6.75	0.15	3.48
6.75	1.00	3.48
6.75	1.50	3.68
6.75	2.00	3.67
6.75	2.50	3.54
6.75	3.00	3.15
6.75	3.50	2.93
6.75	4.00	2.93
6.75	4.50	3.37
6.75	5.00	3.83
6.75	5.35	3.88
6.75	5.50	3.48
6.75	6.35	3.48
6.75	6.85	3.68
6.75	7.35	3.67
7.25	-0.85	3.24
7.25	-0.35	3.37
7.25	0.00	3.33
7.25	0.50	4.07
7.25	0.90	3.97
7.25	1.00	3.50
7.25	1.50	3.27
7.25	2.00	3.38
7.25	3.00	3.30
7.25	3.50	3.20
7.25	4.50	3.24
7.25	5.00	3.37
7.25	5.35	3.33
7.25	5.85	4.07
7.25	6.25	3.97
7.25	6.35	3.50
7.25	6.86	3.27
7.25	7.35	3.38

Table A-4b Tabulated Data for Smooth-Wall Model

Airfoil Surface Data for Smooth Wall Model

$\beta_1 = 40^0$ N = 410 Re = 5.838×10^5

(Data applies to Figure 37a and Figure 37b)

SPAN %	$\frac{S}{S_{tot(r)}}$ %	Stanton Number $x10^3$
10	-100	2.46
30	-100	2.05
50	-100	2.06
50	-100	2.17
70	-100	2.03
90	-100	2.52
10	-90	1.78
30	-90	1.86
50	-90	1.66
50	-90	1.69
70	-90	2.04
90	-90	2.04
10	-80	1.72
30	-80	1.74
50	-80	1.59
50	-80	2.39
70	-80	1.81
90	-80	1.86
10	-70	1.61
30	-70	1.59
50	-70	1.52
50	-70	1.52
70	-70	1.58
90	-70	1.75
10	-60	1.51
30	-60	1.55
50	-60	1.48
50	-60	1.53
70	-60	1.52
90	-60	1.70
10	-50	1.62
30	-50	1.62
50	-50	1.52
50	-50	1.47
70	-50	1.48
90	-50	1.73
10	-40	1.72
50	-40	1.55
50	-40	1.54
70	-40	1.71
10	-30	1.73
20	-30	1.68
40	-30	1.55
50	-30	1.49
60	-30	1.43
70	-30	1.47
80	-30	1.43
90	-30	1.60
10	-20	1.92
20	-20	1.76
30	-20	1.60
40	-20	1.55
50	-20	1.37
50	-20	1.42
60	-20	1.41
70	-20	1.47
80	-20	1.44
90	-20	1.49
10	-15	2.05
20	-15	1.96
30	-15	1.78
40	-15	1.64
50	-15	1.42
60	-15	1.46
70	-15	1.46
80	-15	1.49
90	-15	1.61
10	-10	1.93
20	-10	1.80
30	-10	1.62
40	-10	1.53
50	-10	1.54
60	-10	1.58

SPAN %	$\frac{S}{S_{tot(r)}}$ %	Stanton Number $x10^3$
70	-10	1.61
80	-10	1.60
90	-10	1.88
10	-5	2.28
20	-5	2.44
30	-5	2.48
40	-5	2.27
60	-5	2.55
70	-5	2.57
80	-5	2.43
90	-5	2.53
10	0	5.95
20	0	5.04
30	0	5.00
40	0	4.32
50	0	3.86
60	0	4.43
70	0	4.13
80	0	3.81
90	0	4.11
10	5	6.51
20	5	5.33
40	5	3.79
50	5	3.19
50	5	3.05
60	5	2.78
80	5	2.24
90	5	1.78
10	10	4.14
20	10	3.85
30	10	3.65
60	10	2.66
70	10	2.28
80	10	2.34
10	15	4.17
30	15	3.02
50	15	2.79
50	15	2.55
70	15	2.27
90	15	2.21
10	20	3.85
20	20	3.62
30	20	2.87
40	20	2.70
50	20	2.47
50	20	2.59
60	20	2.29
70	20	2.05
80	20	2.12
90	20	2.38
30	25	2.63
50	25	2.62
50	25	2.89
70	25	2.08
90	25	2.29
10	35	3.59
20	35	3.47
30	35	2.77
40	35	2.46
50	35	2.50
50	35	2.72
60	35	2.36
70	35	2.12
80	35	2.43
90	35	3.52
10	45	4.05
20	45	3.43
30	45	2.76
40	45	2.38
50	45	2.66
50	45	2.58
60	45	2.50
70	45	2.38

SPAN %	$\frac{S}{S_{tot(r)}}$ %	Stanton Number $x10^3$
80	45	3.03
90	45	4.85
10	55	3.79
20	55	3.41
40	55	2.29
50	55	2.55
50	55	2.38
60	55	2.22
70	55	2.42
90	55	5.27
15	60	3.83
25	60	3.53
35	60	2.59
65	60	2.33
75	60	3.07
85	60	4.40
10	65	3.81
20	65	3.41
30	65	2.91
40	65	2.40
50	65	2.54
50	65	2.18
60	65	2.16
70	65	2.78
80	65	3.35
90	65	5.42
15	70	3.66
25	70	3.31
35	70	2.62
65	70	2.57
75	70	3.34
85	70	4.35
10	75	3.39
20	75	3.17
40	75	2.26
50	75	2.26
50	75	1.98
60	75	2.15
70	75	2.86
90	75	4.27
15	80	3.28
25	80	3.06
35	80	2.51
65	80	2.83
75	80	3.38
85	80	3.90
10	85	3.09
20	85	2.92
30	85	2.88
40	85	2.25
50	85	2.02
50	85	2.43
60	85	2.53
70	85	2.84
80	85	3.84
90	85	3.97
15	90	2.81
25	90	2.77
35	90	2.37
65	90	2.71
75	90	3.22
85	90	4.13
10	95	2.40
30	95	2.46
40	95	2.23
50	95	1.94
50	95	2.19
60	95	2.47
70	95	2.91
80	95	3.55
90	95	4.44

Table A-5a Tabulated Data for Smooth-Wall Model

Endwall Data for Smooth Wall Model

$\beta_1 = 40^0$ N = 410 Re = 5.838×10^5

(Data applies to Figure 37c)

See Figure 20 for X-Y Origin

X in.	Y in.	Stanton Number $x10^3$
-0.75	2.15	3.55
-0.75	2.50	4.11
-0.75	2.65	3.08
-0.75	3.15	3.40
-0.75	3.25	3.29
-0.75	3.90	3.36
-0.75	4.50	3.88
-0.75	5.00	4.00
-0.75	5.50	4.31
-0.75	6.00	5.22
-0.75	6.50	3.88
-0.75	7.00	4.02
-0.75	7.50	3.55
-0.75	7.85	4.11
-0.75	8.00	3.08
-0.75	8.50	3.40
-0.75	8.60	3.29
-0.75	9.25	3.36
-0.75	9.85	3.88
0.00	2.15	2.96
0.00	2.50	3.68
0.00	2.65	3.40
0.00	3.15	4.82
0.00	3.25	5.78
0.00	4.00	5.56
0.00	4.50	3.45
0.00	5.50	3.35
0.00	6.00	3.73
0.00	6.50	2.15
0.00	7.00	4.10
0.00	7.50	2.96
0.00	7.85	3.68
0.00	8.00	3.40
0.00	8.50	4.82
0.00	8.60	5.78
0.00	9.35	5.56
0.00	9.85	3.45
0.75	2.15	3.07
0.75	2.65	3.35
0.75	5.50	4.09
0.75	6.00	2.30
0.75	6.50	3.64
0.75	7.00	3.48

X in.	Y in.	Stanton Number $x10^3$
0.75	7.50	3.07
0.75	8.00	3.35
1.50	6.00	3.15
1.50	6.50	3.15
1.50	7.00	3.10
1.50	7.50	3.24
1.50	8.00	3.37
1.50	8.50	3.44
2.25	6.00	3.17
2.25	6.50	2.92
2.25	7.00	2.96
2.25	7.50	2.84
2.25	8.00	3.04
2.25	8.50	2.43
3.00	6.00	3.23
3.00	6.50	3.34
3.00	7.00	2.97
3.00	7.50	2.93
3.00	8.00	2.56
3.00	8.50	2.23
3.75	5.50	3.45
3.75	6.00	3.22
3.75	6.50	3.15
3.75	7.00	2.81
3.75	7.50	2.30
3.75	8.00	2.20
4.50	5.00	3.78
4.50	5.50	3.57
4.50	6.00	3.00
4.50	6.50	2.83
4.50	7.00	2.35
4.50	7.50	2.11
5.25	4.00	4.30
5.25	4.50	3.78
5.25	5.50	2.79
5.25	6.00	2.72
5.25	6.50	2.35
6.00	2.50	3.55
6.00	3.00	3.64
6.00	4.00	3.24
6.00	5.00	3.17
6.00	5.50	2.60
6.75	-0.85	3.38

X in.	Y in.	Stanton Number $x10^3$
6.75	-0.35	3.83
6.75	0.00	4.05
6.75	0.15	3.45
6.75	1.00	3.51
6.75	1.50	3.71
6.75	2.00	3.62
6.75	2.50	3.52
6.75	3.00	3.13
6.75	3.50	2.94
6.75	4.00	3.01
6.75	4.50	3.38
6.75	5.00	3.83
6.75	5.35	4.05
6.75	5.50	3.45
6.75	6.35	3.51
6.75	6.85	3.71
6.75	7.35	3.62
7.25	-0.85	3.17
7.25	-0.35	3.33
7.25	0.00	3.25
7.25	0.50	4.23
7.25	0.90	3.99
7.25	1.00	3.44
7.25	1.50	3.29
7.25	2.00	3.39
7.25	3.00	3.29
7.25	3.50	3.10
7.25	4.50	3.17
7.25	5.00	3.33
7.25	5.35	3.25
7.25	5.85	4.23
7.25	6.25	3.99
7.25	6.35	3.44
7.25	6.85	3.29
7.25	7.35	3.39

Table A-5b Tabulated Data for Smooth-Wall Model

Airfoil Surface Data for Smooth Wall Model

$\beta_1 = 45^o$ N = 408 Re = 5.105×10^5

(Data applies to Figure 38a and Figure 38b)

SPAN %	$\frac{S}{S_{tot(r)}}$ %	Stanton Number $x10^3$
10	-100	2.45
30	-100	1.96
50	-100	2.02
50	-100	2.11
70	-100	1.95
90	-100	2.53
10	-90	1.82
30	-90	1.86
50	-90	1.72
50	-90	1.75
70	-90	2.08
90	-90	2.19
10	-80	1.77
30	-80	1.78
50	-80	1.69
50	-80	2.42
70	-80	1.85
90	-80	1.99
10	-70	1.70
30	-70	1.70
50	-70	1.60
50	-70	1.64
70	-70	1.64
90	-70	1.92
10	-60	1.67
30	-60	1.66
50	-60	1.64
50	-60	1.62
70	-60	1.60
90	-60	1.88
10	-50	1.76
30	-50	1.77
50	-50	1.63
50	-50	1.59
70	-50	1.60
90	-50	1.82
10	-40	1.91
50	-40	1.67
50	-40	1.69
70	-40	1.86
10	-30	1.88
20	-30	1.84
40	-30	1.73
50	-30	1.66
60	-30	1.62
70	-30	1.70
80	-30	1.63
90	-30	1.91
10	-20	2.12
20	-20	2.00
30	-20	1.95
40	-20	1.82
50	-20	1.72
50	-20	1.72
60	-20	1.71
70	-20	1.85
80	-20	1.71
90	-20	1.81
10	-15	2.37
20	-15	2.34
30	-15	2.29
40	-15	2.05
50	-15	1.96
60	-15	1.89
70	-15	1.89
80	-15	1.88
90	-15	2.06
10	-10	2.71
20	-10	2.69
30	-10	2.46
40	-10	2.17
50	-10	2.17
60	-10	2.25
70	-10	2.34
80	-10	2.29
90	-10	2.70
10	-5	2.23
20	-5	2.33
30	-5	2.38
40	-5	2.13
60	-5	2.30
70	-5	2.35
80	-5	2.13
90	-5	2.42
10	0	6.28
20	0	4.92
30	0	5.03
40	0	4.40
50	0	3.89
60	0	4.39
70	0	4.25
80	0	3.90
90	0	4.48
10	5	6.13
20	5	4.95
40	5	3.55
50	5	3.32
50	5	3.22
60	5	2.90
80	5	2.41
90	5	1.98
10	10	3.64
20	10	3.40
30	10	3.25
60	10	2.37
70	10	2.12
80	10	2.05
10	15	3.59
30	15	2.70
50	15	2.39
50	15	2.08
70	15	2.03
90	15	1.67
10	20	3.22
20	20	2.89
30	20	2.38
40	20	2.25
50	20	1.87
50	20	2.09
60	20	1.86
70	20	1.71
80	20	1.62
90	20	1.97
30	25	2.06
50	25	2.01
50	25	1.95
70	25	1.59
90	25	2.06
10	35	3.06
20	35	2.76
30	35	2.18
40	35	1.96
50	35	1.79
50	35	1.95
60	35	1.72
70	35	1.58
80	35	1.78
90	35	3.33
10	45	3.35
20	45	2.88
30	45	2.31
40	45	2.08
50	45	2.06
50	45	2.00
60	45	1.95
70	45	1.93
80	45	2.66
90	45	4.52
10	55	3.30
20	55	3.02
40	55	2.11
50	55	2.21
50	55	2.10
60	55	2.11
70	55	2.33
90	55	5.05
15	60	3.45
25	60	3.03
35	60	2.27
65	60	2.30
75	60	2.96
85	60	4.17
10	65	3.21
20	65	3.16
30	65	2.66
40	65	2.23
50	65	2.42
50	65	2.26
60	65	2.16
70	65	2.76
80	65	3.35
90	65	5.19
15	70	3.33
25	70	2.91
35	70	2.45
65	70	2.52
75	70	3.36
85	70	4.08
10	75	3.14
20	75	2.86
40	75	2.21
50	75	2.28
50	75	2.09
60	75	2.20
70	75	2.86
90	75	4.39
15	80	2.98
25	80	2.72
35	80	2.34
65	80	2.86
75	80	3.43
85	80	4.11
10	85	2.88
20	85	2.71
30	85	2.54
40	85	2.16
50	85	2.05
50	85	2.30
60	85	2.58
70	85	2.92
80	85	3.71
90	85	4.15
15	90	2.58
25	90	2.53
35	90	2.18
65	90	2.68
75	90	3.23
85	90	4.03
10	95	2.32
30	95	2.29
40	95	2.06
50	95	1.95
50	95	2.09
60	95	2.39
70	95	2.93
80	95	3.61
90	95	4.51

Table A-6a Tabulated Data for Smooth-Wall Model

Endwall Data for Smooth Wall Model

$\beta_1 = 45^o$ N = 408 Re = 5.105×10^5

(Data applies to Figure 38c)

See Figure 20 for X-Y Origin

X in.	Y in.	Stanton Number $x10^3$
-0.75	2.15	3.40
-0.75	2.50	3.99
-0.75	2.65	3.11
-0.75	3.15	3.24
-0.75	3.25	3.26
-0.75	3.90	3.30
-0.75	4.50	3.54
-0.75	5.00	3.69
-0.75	5.50	3.85
-0.75	6.00	4.96
-0.75	6.50	3.65
-0.75	7.00	3.90
-0.75	7.50	3.40
-0.75	7.85	3.99
-0.75	8.00	3.11
-0.75	8.50	3.24
-0.75	8.60	3.26
-0.75	9.25	3.30
-0.75	9.85	3.54
0.00	2.15	2.96
0.00	2.50	3.62
0.00	2.65	3.28
0.00	3.15	4.53
0.00	3.25	5.62
0.00	4.00	5.69
0.00	4.50	3.33
0.00	5.50	3.20
0.00	6.00	3.42
0.00	6.50	2.23
0.00	7.00	3.92
0.00	7.50	2.96
0.00	7.85	3.62
0.00	8.00	3.28
0.00	8.50	4.53
0.00	8.60	5.62
0.00	9.35	5.69
0.00	9.85	3.33
0.75	2.15	2.95
0.75	2.65	3.07
0.75	5.50	3.75
0.75	6.00	2.38
0.75	6.50	3.57
0.75	7.00	3.41

X in.	Y in.	Stanton Number $x10^3$
0.75	7.50	2.95
0.75	8.00	3.07
1.50	6.00	3.12
1.50	6.50	2.98
1.50	7.00	3.08
1.50	7.50	3.04
1.50	8.00	3.01
1.50	8.50	3.26
2.25	6.00	3.12
2.25	6.50	2.81
2.25	7.00	2.78
2.25	7.50	2.63
2.25	8.00	2.80
2.25	8.50	2.47
3.00	6.00	2.99
3.00	6.50	3.09
3.00	7.00	2.72
3.00	7.50	2.66
3.00	8.00	2.58
3.00	8.50	2.32
3.75	5.50	3.08
3.75	6.00	2.94
3.75	6.50	2.92
3.75	7.00	2.69
3.75	7.50	2.37
3.75	8.00	2.30
4.50	5.00	3.48
4.50	5.50	3.28
4.50	6.00	2.97
4.50	6.50	2.80
4.50	7.00	2.43
4.50	7.50	2.18
5.25	4.00	4.10
5.25	4.50	3.60
5.25	5.50	2.80
5.25	6.00	2.79
5.25	6.50	2.38
6.00	2.50	3.52
6.00	3.00	3.52
6.00	4.00	3.13
6.00	5.00	3.01
6.00	5.50	2.54
6.75	-0.85	3.37

X in.	Y in.	Stanton Number $x10^3$
6.75	-0.35	3.94
6.75	0.00	3.92
6.75	0.15	3.51
6.75	1.00	3.39
6.75	1.50	3.82
6.75	2.00	3.61
6.75	2.50	3.68
6.75	3.00	3.17
6.75	3.50	3.03
6.75	4.00	2.95
6.75	4.50	3.37
6.75	5.00	3.94
6.75	5.35	3.92
6.75	5.50	3.51
6.75	6.35	3.39
6.75	6.85	3.82
6.75	7.35	3.61
7.25	-0.85	3.14
7.25	-0.35	3.30
7.25	0.00	3.32
7.25	0.50	4.21
7.25	0.90	3.93
7.25	1.00	3.58
7.25	1.50	3.39
7.25	2.00	3.42
7.25	3.00	3.26
7.25	3.50	3.17
7.25	4.50	3.14
7.25	5.00	3.30
7.25	5.35	3.32
7.25	5.85	4.21
7.25	6.25	3.93
7.25	6.35	3.58
7.25	6.85	3.39
7.25	7.35	3.42

Table A-6b Tabulated Data for Smooth-Wall Model

Airfoil Surface Data for Smooth Wall Model

$\beta_1 = 54^0$ N = 219 Re = 2.366×10^5

(Data applies to Figure 39a and Figure 39b)

SPAN %	$\frac{S}{S_{tot(r)}}$ %	Stanton Number $x10^3$
10	-100	2.75
30	-100	2.42
50	-100	2.38
50	-100	2.49
70	-100	2.36
90	-100	2.96
10	-90	2.44
30	-90	2.50
50	-90	2.44
50	-90	2.39
70	-90	2.71
90	-90	2.84
10	-80	2.48
30	-80	2.42
50	-80	2.66
50	-80	2.38
70	-80	2.44
90	-80	2.80
10	-70	2.41
30	-70	2.36
50	-70	2.31
50	-70	2.34
70	-70	2.25
90	-70	2.68
10	-60	2.39
30	-60	2.30
50	-60	2.36
50	-60	2.31
70	-60	2.22
90	-60	2.80
10	-50	2.49
30	-50	2.43
50	-50	2.28
50	-50	2.40
70	-50	2.28
90	-50	3.38
10	-40	2.67
50	-40	2.57
50	-40	2.52
70	-40	2.61
90	-40	1.94
10	-30	2.70
20	-30	2.65
40	-30	2.52
50	-30	2.48
60	-30	2.44
70	-30	2.51
80	-30	2.59
90	-30	2.67
10	-20	3.11
20	-20	3.08
30	-20	2.91
40	-20	2.94
50	-20	2.75
50	-20	2.92
60	-20	2.84
70	-20	2.86
80	-20	2.97
90	-20	3.10
10	-15	3.82
20	-15	3.71
30	-15	3.73
40	-15	3.50
50	-15	3.39
60	-15	3.34
70	-15	3.36
80	-15	3.44
90	-15	3.72
10	-10	4.38
20	-10	4.27
30	-10	4.52
40	-10	4.04
50	-10	4.61

SPAN %	$\frac{S}{S_{tot(r)}}$ %	Stanton Number $x10^3$
60	-10	3.87
70	-10	4.25
80	-10	3.44
90	-10	4.60
10	-5	2.72
20	-5	2.67
30	-5	2.73
40	-5	2.59
60	-5	2.75
70	-5	2.69
80	-5	2.64
90	-5	2.92
10	0	7.46
20	0	6.24
30	0	6.54
40	0	5.60
50	0	5.23
60	0	5.54
70	0	6.12
80	0	4.98
90	0	5.93
10	5	8.31
20	5	7.04
40	5	5.49
50	5	4.88
50	5	5.30
60	5	4.52
80	5	3.97
90	5	3.35
10	10	4.76
20	10	4.40
30	10	4.28
60	10	3.39
70	10	3.10
80	10	2.99
10	15	4.35
30	15	3.50
50	15	3.00
50	15	3.22
70	15	2.98
90	15	2.50
10	20	3.66
20	20	3.43
30	20	3.19
40	20	3.10
50	20	2.82
50	20	2.68
60	20	2.60
70	20	2.57
80	20	2.35
90	20	2.55
30	25	2.75
50	25	2.63
50	25	2.58
70	25	2.31
90	25	3.31
10	35	2.48
20	35	2.49
30	35	2.13
40	35	2.19
50	35	2.17
50	35	1.96
60	35	1.99
70	35	1.89
80	35	2.06
90	35	4.64
10	45	3.34
20	45	2.79
30	45	2.08
40	45	1.93
50	45	2.01
50	45	1.93
60	45	1.85

SPAN %	$\frac{S}{S_{tot(r)}}$ %	Stanton Number $x10^3$
70	45	1.88
80	45	3.11
90	45	5.96
10	55	3.46
20	55	3.15
40	55	2.03
50	55	1.95
50	55	1.86
60	55	1.84
70	55	2.72
90	55	6.99
15	60	3.35
25	60	2.96
35	60	2.49
65	60	2.66
75	60	3.63
85	60	5.23
10	65	3.37
20	65	3.14
30	65	2.86
40	65	2.60
50	65	2.67
50	65	2.58
60	65	2.64
70	65	3.32
80	65	4.19
90	65	7.29
15	70	3.34
25	70	2.97
35	70	2.77
65	70	3.09
75	70	4.04
85	70	5.41
10	75	3.27
20	75	3.00
40	75	2.69
50	75	2.75
50	75	2.81
60	75	2.88
70	75	3.50
90	75	5.99
15	80	3.11
25	80	2.88
35	80	2.78
65	80	3.44
75	80	4.22
85	80	5.45
10	85	3.08
20	85	2.92
30	85	2.77
40	85	2.68
50	85	2.88
50	85	2.68
60	85	3.23
70	85	3.66
80	85	4.91
90	85	5.55
15	90	2.83
25	90	2.71
35	90	2.53
65	90	3.32
75	90	4.35
85	90	5.43
10	95	2.60
30	95	2.46
40	95	2.49
50	95	2.61
50	95	2.67
60	95	2.92
70	95	3.69
80	95	4.43
90	95	6.00

Table A-7a Tabulated Data for Smooth-Wall Model

Endwall Data for Smooth Wall Model

$\beta_1 = 54^0$ N = 219 Re = 2.366×10^5

(Data applies to Figure 39c)

See Figure 20 for X-Y Origin

X in.	Y in.	Stanton Number $x10^3$
-0.75	2.15	3.75
-0.75	2.50	3.90
-0.75	2.65	3.60
-0.75	3.15	3.60
-0.75	3.25	3.66
-0.75	3.90	3.59
-0.75	4.50	3.26
-0.75	5.00	3.51
-0.75	5.50	3.39
-0.75	6.00	4.16
-0.75	6.50	3.74
-0.75	7.00	3.98
-0.75	7.50	3.75
-0.75	7.85	3.00
-0.75	8.00	3.60
-0.75	8.50	3.60
-0.75	8.60	3.66
-0.75	9.25	3.59
-0.75	9.85	3.26
0.00	2.15	3.34
0.00	2.50	3.49
0.00	2.65	3.42
0.00	3.15	4.68
0.00	3.25	5.93
0.00	4.00	6.18
0.00	4.50	3.92
0.00	5.50	3.00
0.00	6.00	3.20
0.00	6.50	2.85
0.00	7.00	3.66
0.00	7.50	3.34
0.00	7.85	3.49
0.00	8.00	3.42
0.00	8.50	4.68
0.00	8.60	5.93
0.00	9.35	6.18
0.00	9.85	3.92
0.75	2.15	3.30
0.75	2.65	3.30
0.75	5.50	3.01
0.75	6.00	2.60
0.75	6.50	3.30
0.75	7.00	3.52
0.75	7.50	3.30
0.75	8.00	3.30
1.50	6.00	3.23
1.50	6.50	3.20
1.50	7.00	3.32
1.50	7.50	3.25
1.50	8.00	3.19
1.50	8.50	3.47
2.25	6.00	3.50
2.25	6.50	3.22
2.25	7.00	3.08
2.25	7.50	2.92
2.25	8.00	2.99
2.25	8.50	2.93
3.00	6.00	3.26
3.00	6.50	3.24
3.00	7.00	2.93
3.00	7.50	2.85
3.00	8.00	2.97
3.00	8.50	3.08
3.75	5.50	3.00
3.75	6.00	3.04
3.75	6.50	3.04
3.75	7.00	3.01
3.75	7.50	2.96
3.75	8.00	3.03
4.50	5.00	3.11
4.50	5.50	3.12
4.50	6.00	3.14
4.50	6.50	3.12
4.50	7.00	3.18
4.50	7.50	3.00
5.25	4.00	3.41
5.25	4.50	3.29
5.25	5.50	3.11
5.25	6.00	3.34
5.25	6.50	3.15
6.00	2.50	3.61
6.00	3.00	3.37
6.00	4.00	3.33
6.00	5.00	3.19
6.00	5.50	3.02
6.75	-0.85	3.70
6.75	-0.35	4.29
6.75	0.00	4.38
6.75	0.15	4.17
6.75	1.00	3.74
6.75	1.50	3.83
6.75	2.00	3.75
6.75	2.50	3.70
6.75	3.00	3.44
6.75	3.50	3.26
6.75	4.00	3.28
6.75	4.50	3.70
6.75	5.00	4.29
6.75	5.35	4.38
6.75	5.50	4.17
6.75	6.35	3.74
6.75	6.85	3.83
6.75	7.35	3.75
7.25	-0.85	3.67
7.25	-0.35	3.88
7.25	0.00	3.89
7.25	0.50	4.26
7.25	0.90	4.16
7.25	1.00	3.91
7.25	1.50	3.58
7.25	2.00	3.74
7.25	3.00	3.64
7.25	3.50	3.48
7.25	4.50	3.67
7.25	5.00	3.88
7.25	5.35	3.89
7.25	5.85	4.26
7.25	6.25	4.16
7.25	6.35	3.91
7.25	6.85	3.58
7.25	7.35	3.74

Table A-7b Tabulated Data for Smooth-Wall Model

Airfoil Surface Data for Smooth Wall Model

$\beta_1 = 54^o$ N = 299 Re = 3.228×10^5

(Data applies to Figure 40a and Figure 40b)

SPAN %	$\frac{S}{S_{tot(r)}}$ %	Stanton Number x10^3
10	-100	2.83
30	-100	2.28
50	-100	2.38
50	-100	2.38
70	-100	2.17
90	-100	2.83
10	-90	2.10
30	-90	2.17
50	-90	2.14
50	-90	2.39
70	-90	2.39
90	-90	2.55
10	-80	2.13
30	-80	2.14
50	-80	2.66
50	-80	2.12
70	-80	2.15
90	-80	2.45
10	-70	2.09
30	-70	2.05
50	-70	2.34
50	-70	2.16
70	-70	1.95
90	-70	2.36
10	-60	2.05
30	-60	2.01
50	-60	2.36
50	-60	2.01
70	-60	1.93
90	-60	2.44
10	-50	2.17
30	-50	2.13
50	-50	1.98
50	-50	2.40
70	-50	2.01
90	-50	2.31
10	-40	2.32
30	-40	2.27
50	-40	2.57
50	-40	2.14
70	-40	2.26
90	-40	1.73
10	-30	2.34
20	-30	2.30
40	-30	2.17
50	-30	2.14
60	-30	2.14
70	-30	2.18
80	-30	2.20
90	-30	2.46
10	-20	2.67
20	-20	2.64
30	-20	2.55
40	-20	2.54
50	-20	2.92
50	-20	2.37
60	-20	2.50
70	-20	2.51
80	-20	2.60
90	-20	2.65
10	-15	3.14
20	-15	3.07
30	-15	3.00
40	-15	2.88
50	-15	2.76
60	-15	2.85
70	-15	2.78
80	-15	3.08
90	-15	3.15
10	-10	3.84
20	-10	3.94
30	-10	3.71
40	-10	3.58
50	-10	3.80
60	-10	3.56
70	-10	3.52
80	-10	3.66
90	-10	4.17
10	-5	2.68
20	-5	2.84
30	-5	2.73
40	-5	2.98
60	-5	3.52
70	-5	3.04
80	-5	3.40
90	-5	3.21
10	0	6.69
20	0	5.91
30	0	5.59
40	0	5.24
50	0	5.23
60	0	5.19
70	0	5.06
80	0	4.75
90	0	5.19
10	5	8.04
20	5	6.34
40	5	4.84
50	5	4.67
50	5	4.51
60	5	3.86
80	5	3.31
90	5	2.88
10	10	4.24
20	10	3.97
30	10	3.70
60	10	2.94
70	10	2.68
80	10	2.60
10	15	3.96
30	15	3.07
50	15	2.60
50	15	2.90
70	15	2.55
90	15	2.14
10	20	3.27
20	20	3.01
30	20	2.79
40	20	2.69
50	20	2.48
50	20	2.30
60	20	2.26
70	20	2.20
80	20	2.03
90	20	2.23
30	25	2.39
50	25	2.19
50	25	2.28
70	25	1.96
90	25	2.90
10	35	2.43
20	35	2.26
30	35	1.92
40	35	1.94
50	35	1.94
50	35	1.74
60	35	1.75
70	35	1.63
80	35	1.82
90	35	4.19
10	45	3.22
20	45	2.65
30	45	2.00
40	45	1.85
50	45	1.91
50	45	1.85
60	45	1.78
70	45	1.79
80	45	2.88
90	45	5.63
10	55	3.33
20	55	3.03
40	55	2.00
50	55	1.95
50	55	1.99
60	55	1.97
70	55	2.54
90	55	6.26
15	60	3.28
25	60	2.89
35	60	2.39
65	60	2.48
75	60	3.32
85	60	4.80
10	65	3.23
20	65	3.14
30	65	2.73
40	65	2.48
50	65	2.63
50	65	2.48
60	65	2.44
70	65	3.06
80	65	3.80
90	65	6.64
15	70	3.30
25	70	2.87
35	70	2.59
65	70	2.80
75	70	3.82
85	70	4.93
10	75	3.12
20	75	2.87
40	75	2.47
50	75	2.50
50	75	2.58
60	75	2.57
70	75	3.25
90	75	5.57
15	80	2.95
25	80	2.78
35	80	2.49
65	80	3.10
75	80	3.95
85	80	4.93
10	85	3.02
20	85	2.76
30	85	2.67
40	85	2.44
50	85	2.70
50	85	2.40
60	85	2.93
70	85	3.33
80	85	4.50
90	85	5.13
15	90	2.71
25	90	2.58
35	90	2.30
65	90	3.03
75	90	3.85
85	90	5.10
10	95	2.42
30	95	2.31
40	95	2.32
50	95	2.35
50	95	2.47
60	95	2.72
70	95	3.41
80	95	4.14
90	95	5.65

Table A-8a Tabulated Data for Smooth-Wall Model

Endwall Data for Smooth Wall Model

$\beta_1 = 54^0$ N = 299 Re = 3.228×10^5

(Data applies to Figure 40c)

See Figure 20 for X-Y Origin

X in.	Y in.	Stanton Number $x10^3$
-0.75	2.15	3.53
-0.75	2.50	3.73
-0.75	2.65	3.36
-0.75	3.15	3.36
-0.75	3.25	3.35
-0.75	3.90	3.36
-0.75	4.50	3.18
-0.75	5.00	3.34
-0.75	5.50	3.32
-0.75	6.00	4.37
-0.75	6.50	3.60
-0.75	7.00	3.81
-0.75	7.50	3.53
-0.75	7.85	3.73
-0.75	8.00	3.36
-0.75	8.50	3.36
-0.75	8.60	3.35
-0.75	9.25	3.36
-0.75	9.85	3.18
0.00	2.15	3.11
0.00	2.50	3.30
0.00	2.65	3.26
0.00	3.15	4.26
0.00	3.25	5.62
0.00	4.00	5.77
0.00	4.50	3.51
0.00	5.50	2.85
0.00	6.00	3.09
0.00	6.50	2.55
0.00	7.00	3.60
0.00	7.50	3.11
0.00	7.85	3.30
0.00	8.00	3.26
0.00	8.50	4.26
0.00	8.60	5.62
0.00	9.35	5.77
0.00	9.85	3.51
0.75	2.15	3.05
0.75	2.65	3.03
0.75	5.50	2.95
0.75	6.00	2.46
0.75	6.50	3.33
0.75	7.00	3.39

X in.	Y in.	Stanton Number $x10^3$
0.75	7.50	3.05
0.75	8.00	3.03
1.50	6.00	3.16
1.50	6.50	3.03
1.50	7.00	3.13
1.50	7.50	3.01
1.50	8.00	2.92
1.50	8.50	3.11
2.25	6.00	3.29
2.25	6.50	2.96
2.25	7.00	2.88
2.25	7.50	2.69
2.25	8.00	2.71
2.25	8.50	2.61
3.00	6.00	3.03
3.00	6.50	2.98
3.00	7.00	2.67
3.00	7.50	2.56
3.00	8.00	2.65
3.00	8.50	2.74
3.75	5.50	2.79
3.75	6.00	2.75
3.75	6.50	2.75
3.75	7.00	2.70
3.75	7.50	2.61
3.75	8.00	2.71
4.50	5.00	2.92
4.50	5.50	2.94
4.50	6.00	2.81
4.50	6.50	2.85
4.50	7.00	2.82
4.50	7.50	2.63
5.25	4.00	3.40
5.25	4.50	3.15
5.25	5.50	2.84
5.25	6.00	3.08
5.25	6.50	2.80
6.00	2.50	3.57
6.00	3.00	3.40
6.00	4.00	3.07
6.00	5.00	2.95
6.00	5.50	2.81
6.75	-0.85	3.65

X in.	Y in.	Stanton Number $x10^3$
6.75	-0.35	4.16
6.75	0.00	4.18
6.75	0.15	3.98
6.75	1.00	3.72
6.75	1.50	3.89
6.75	2.00	3.75
6.75	2.50	3.72
6.75	3.00	3.34
6.75	3.50	3.20
6.75	4.00	3.24
6.75	4.50	3.65
6.75	5.00	4.16
6.75	5.35	4.18
6.75	5.50	3.98
6.75	6.35	3.72
6.75	6.85	3.89
6.75	7.35	3.75
7.25	-0.85	3.46
7.25	-0.35	3.69
7.25	0.00	3.74
7.25	0.50	4.46
7.25	0.90	4.22
7.25	1.00	3.80
7.25	1.50	3.64
7.25	2.00	3.73
7.25	3.00	3.60
7.25	3.50	3.58
7.25	4.50	3.46
7.25	5.00	3.69
7.25	5.35	3.74
7.25	5.85	4.46
7.25	6.25	4.22
7.25	6.35	3.80
7.25	6.85	3.64
7.25	7.35	3.73

Table A-8b Tabulated Data for Smooth-Wall Model

Airfoil Surface Data for Smooth Wall Model

$\beta_1 = 54^0$ N = 397 Re = 4.235×10^5

(Data applies to Figure 41a and Figure 41b)

SPAN %	$\frac{S}{S_{tot(r)}}$ %	Stanton Number x10^3
10	-100	2.49
30	-100	2.03
50	-100	2.04
50	-100	2.16
70	-100	1.96
90	-100	2.56
10	-90	1.94
30	-90	1.98
50	-90	1.88
50	-90	1.91
70	-90	2.20
90	-90	2.39
10	-80	1.95
30	-80	1.93
50	-80	1.86
50	-80	2.50
70	-80	2.00
90	-80	2.23
10	-70	1.90
30	-70	1.87
50	-70	1.79
50	-70	1.83
70	-70	1.81
90	-70	2.12
10	-60	1.87
30	-60	1.85
50	-60	1.83
50	-60	1.81
70	-60	1.75
90	-60	2.19
10	-50	1.98
30	-50	1.96
50	-50	1.84
50	-50	1.79
70	-50	1.84
90	-50	2.14
10	-40	2.14
50	-40	1.95
50	-40	1.96
70	-40	2.12
10	-30	2.17
20	-30	2.12
40	-30	1.99
50	-30	1.96
60	-30	1.92
70	-30	2.02
80	-30	2.05
90	-30	2.27
10	-20	2.46
20	-20	2.30
30	-20	2.34
40	-20	2.18
50	-20	2.13
50	-20	2.09
60	-20	2.09
70	-20	2.32
80	-20	2.24
90	-20	2.45
10	-15	3.00
20	-15	2.73
30	-15	2.81
40	-15	2.45
50	-15	2.50
60	-15	2.43
70	-15	2.57
80	-15	2.67
90	-15	3.12
10	-10	3.95
20	-10	3.82
30	-10	3.65
40	-10	3.30
50	-10	3.93
60	-10	3.30
70	-10	3.64
80	-10	3.35
90	-10	4.12
10	-5	2.37
20	-5	2.35
30	-5	2.43
40	-5	2.22
60	-5	2.65
70	-5	2.50
80	-5	2.43
90	-5	2.68
10	0	6.62
20	0	5.14
30	0	5.31
40	0	4.44
50	0	4.20
60	0	4.58
70	0	4.61
80	0	4.19
90	0	4.71
10	5	7.17
20	5	5.51
40	5	4.26
50	5	3.87
50	5	3.89
60	5	3.44
80	5	2.87
90	5	2.49
10	10	3.76
20	10	3.52
30	10	3.49
60	10	2.66
70	10	2.34
80	10	2.28
10	15	3.53
30	15	2.81
50	15	2.55
50	15	2.24
70	15	2.25
90	15	1.90
10	20	2.99
20	20	2.73
30	20	2.55
40	20	2.38
50	20	2.01
50	20	2.13
60	20	2.01
70	20	1.93
80	20	1.82
90	20	2.02
30	25	2.15
50	25	2.03
50	25	1.96
70	25	1.74
90	25	2.62
10	35	2.52
20	35	2.29
30	35	1.83
40	35	1.77
50	35	1.62
50	35	1.77
60	35	1.61
70	35	1.51
80	35	1.72
90	35	3.95
10	45	3.04
20	45	2.66
30	45	2.00
40	45	1.82
50	45	1.85
50	45	1.75
60	45	1.71
70	45	1.80
80	45	2.80
90	45	5.09
10	55	3.17
20	55	2.85
40	55	1.95
50	55	2.06
50	55	1.93
60	55	2.00
70	55	2.44
90	55	5.95
15	60	3.17
25	60	2.73
35	60	2.24
65	60	2.41
75	60	3.17
85	60	4.69
10	65	3.05
20	65	2.99
30	65	2.53
40	65	2.32
50	65	2.49
50	65	2.38
60	65	2.28
70	65	2.85
80	65	3.61
90	65	5.99
15	70	3.16
25	70	2.78
35	70	2.46
65	70	2.60
75	70	3.56
85	70	4.74
10	75	3.01
20	75	2.80
40	75	2.32
50	75	2.46
50	75	2.31
60	75	2.45
70	75	3.06
90	75	5.00
15	80	2.89
25	80	2.65
35	80	2.35
65	80	3.01
75	80	3.70
85	80	4.45
10	85	2.85
20	85	2.64
30	85	2.44
40	85	2.26
50	85	2.23
50	85	2.50
60	85	2.66
70	85	3.12
80	85	4.06
90	85	4.50
15	90	2.52
25	90	2.46
35	90	2.19
65	90	2.81
75	90	3.51
85	90	4.58
10	95	2.30
30	95	2.19
40	95	2.13
50	95	2.13
50	95	2.25
60	95	2.55
70	95	3.15
80	95	3.80
90	95	4.89

Table A-9a Tabulated Data for Smooth-Wall Model

Endwall Data for Smooth Wall Model

$\beta_1 = 54^o$ N = 397 Re = 4.235×10^5

(Data applies to Figure 41c)

See Figure 20 for X-Y Origin

X in.	Y in.	Stanton Number $x10^3$
-0.75	2.15	3.40
-0.75	2.50	3.98
-0.75	2.65	3.16
-0.75	3.15	3.17
-0.75	3.25	3.15
-0.75	3.90	3.23
-0.75	4.50	3.38
-0.75	5.00	3.59
-0.75	5.50	3.42
-0.75	6.00	4.54
-0.75	6.50	3.52
-0.75	7.00	3.80
-0.75	7.50	3.40
-0.75	7.85	3.98
-0.75	8.00	3.16
-0.75	8.50	3.17
-0.75	8.60	3.15
-0.75	9.25	3.23
-0.75	9.85	3.38
0.00	2.15	2.90
0.00	2.50	3.65
0.00	2.65	3.12
0.00	3.15	3.95
0.00	3.25	5.46
0.00	4.00	5.49
0.00	4.50	3.29
0.00	5.50	2.84
0.00	6.00	2.99
0.00	6.50	2.32
0.00	7.00	3.61
0.00	7.50	2.90
0.00	7.85	3.65
0.00	8.00	3.12
0.00	8.50	3.95
0.00	8.60	5.46
0.00	9.35	5.49
0.00	9.85	3.29
0.75	2.15	2.83
0.75	2.65	2.88
0.75	5.50	2.97
0.75	6.00	2.35
0.75	6.50	3.24
0.75	7.00	3.21

X in.	Y in.	Stanton Number $x10^3$
0.75	7.50	2.83
0.75	8.00	2.88
1.50	6.00	3.03
1.50	6.50	2.83
1.50	7.00	2.97
1.50	7.50	2.87
1.50	8.00	2.73
1.50	8.50	2.85
2.25	6.00	3.09
2.25	6.50	2.75
2.25	7.00	2.72
2.25	7.50	2.54
2.25	8.00	2.55
2.25	8.50	2.40
3.00	6.00	2.88
3.00	6.50	2.94
3.00	7.00	2.51
3.00	7.50	2.39
3.00	8.00	2.49
3.00	8.50	2.57
3.75	5.50	2.72
3.75	6.00	2.65
3.75	6.50	2.63
3.75	7.00	2.53
3.75	7.50	2.41
3.75	8.00	2.46
4.50	5.00	2.95
4.50	5.50	2.83
4.50	6.00	2.68
4.50	6.50	2.70
4.50	7.00	2.54
4.50	7.50	2.35
5.25	4.00	3.53
5.25	4.50	3.23
5.25	5.50	2.67
5.25	6.00	2.95
5.25	6.50	2.56
6.00	2.50	3.68
6.00	3.00	3.46
6.00	4.00	3.17
6.00	5.00	3.02
6.00	5.50	2.62
6.75	-0.85	3.46

X in.	Y in.	Stanton Number $x10^3$
6.75	-0.35	3.89
6.75	0.00	3.94
6.75	0.15	3.66
6.75	1.00	3.60
6.75	1.50	3.93
6.75	2.00	3.70
6.75	2.50	3.83
6.75	3.00	3.31
6.75	3.50	3.18
6.75	4.00	3.14
6.75	4.50	3.46
6.75	5.00	3.89
6.75	5.35	3.94
6.75	5.50	3.66
6.75	6.35	3.60
6.75	6.85	3.93
6.75	7.35	3.70
7.25	-0.85	3.24
7.25	-0.35	3.45
7.25	0.00	3.47
7.25	0.50	4.64
7.25	0.90	4.06
7.25	1.00	3.67
7.25	1.50	3.67
7.25	2.00	3.62
7.25	3.00	3.43
7.25	3.50	3.33
7.25	4.50	3.24
7.25	5.00	3.45
7.25	5.35	3.47
7.25	5.85	4.64
7.25	6.25	4.06
7.25	6.35	3.67
7.25	6.85	3.67
7.25	7.35	3.62

Table A-9b Tabulated Data for Smooth-Wall Model

Airfoil Surface Data for Rough Wall Model

$\beta_1 = 40^o$ N = 160 Re = 2.247×10^5

(Data applies to Figure 42a and Figure 42b)

SPAN %	$\frac{s}{s_{tot(r)}}$ %	Stanton Number $x10^3$
10	-100	3.42
30	-100	4.15
50	-100	3.50
50	-100	3.68
70	-100	4.67
90	-100	4.77
10	-90	4.41
30	-90	4.53
50	-90	4.21
50	-90	4.27
70	-90	4.59
90	-90	4.91
10	-80	3.99
30	-80	4.16
50	-80	3.90
50	-80	3.27
70	-80	4.21
90	-80	4.52
10	-70	3.60
30	-70	3.66
50	-70	3.40
50	-70	3.38
70	-70	3.44
90	-70	3.85
10	-60	3.09
30	-60	3.15
50	-60	2.85
50	-60	2.86
70	-60	2.91
90	-60	3.41
10	-50	2.94
30	-50	2.86
50	-50	2.67
50	-50	2.61
70	-50	2.44
90	-50	3.16
10	-40	2.85
30	-40	3.00
50	-40	2.46
50	-40	2.54
70	-40	2.81
90	-40	2.81
10	-30	2.93
20	-30	2.60
40	-30	2.55
50	-30	2.52
60	-30	2.33
70	-30	2.36
80	-30	2.50
90	-30	2.56
10	-20	3.23
20	-20	3.17
30	-20	2.83
40	-20	2.88
50	-20	2.60
50	-20	2.67
60	-20	2.57
70	-20	2.60
80	-20	2.59
90	-20	2.79
10	-15	3.53
20	-15	3.47
30	-15	3.29
40	-15	3.31
50	-15	2.85
60	-15	2.77
70	-15	2.75
80	-15	2.79
90	-15	3.11
10	-10	3.42
20	-10	3.69
30	-10	3.51
40	-10	3.22
60	-10	3.02
70	-10	3.23
90	-10	3.27
10	-5	3.48
20	-5	3.28
30	-5	3.50
40	-5	3.29
60	-5	3.26
70	-5	3.28
80	-5	3.73
90	-5	3.69
10	0	6.38
20	0	6.34
30	0	6.89
40	0	6.64
50	0	6.17
60	0	5.92
70	0	6.09
80	0	5.83
90	0	6.25
10	5	12.59
20	5	11.21
40	5	8.28
60	5	6.57
80	5	6.13
90	5	4.49
10	10	9.76
20	10	7.75
30	10	9.29
60	10	6.70
70	10	6.41
80	10	5.44
10	15	8.37
30	15	7.46
50	15	7.02
50	15	6.05
70	15	6.01
90	15	4.99
10	20	7.02
20	20	7.08
30	20	7.27
40	20	6.94
50	20	6.50
50	20	6.02
60	20	6.00
70	20	5.43
80	20	5.03
90	20	5.71
30	25	5.45
50	25	5.91
50	25	5.27
70	25	5.02
90	25	5.80
10	35	4.65
20	35	4.68
30	35	4.08
40	35	4.42
50	35	4.52
50	35	4.45
60	35	4.16
70	35	4.03
80	35	4.92
90	35	7.83
10	45	7.44
20	45	5.00
30	45	4.31
40	45	3.62
50	45	3.86
50	45	3.95
60	45	3.95
70	45	3.79
80	45	5.77
90	45	7.51
10	55	6.77
20	55	5.46
40	55	4.08
50	55	3.50
50	55	3.58
60	55	3.40
70	55	3.94
90	55	8.31
15	60	5.62
25	60	4.98
35	60	3.63
65	60	3.59
75	60	4.67
85	60	8.23
10	65	5.97
20	65	4.68
30	65	4.19
40	65	3.32
50	65	3.21
50	65	3.29
60	65	3.27
70	65	3.95
80	65	5.83
90	65	7.97
15	70	5.07
25	70	4.52
35	70	3.24
65	70	3.71
75	70	5.50
85	70	8.19
10	75	5.22
20	75	4.68
40	75	2.97
50	75	3.31
50	75	3.19
60	75	3.38
70	75	4.43
90	75	7.38
15	80	4.88
25	80	4.23
35	80	3.36
65	80	4.01
75	80	6.62
85	80	7.38
10	85	4.40
20	85	4.36
30	85	3.80
40	85	3.09
50	85	3.15
50	85	3.39
60	85	3.59
70	85	5.32
80	85	7.32
90	85	7.91
15	90	4.49
25	90	4.03
35	90	3.46
65	90	4.49
75	90	6.08
85	90	7.39
10	95	3.87
30	95	3.74
40	95	3.06
50	95	3.36
50	95	3.29
60	95	3.74
70	95	5.24
80	95	7.21
90	95	7.79

Table A-10a Tabulated Data for Rough-Wall Model

Endwall Data for Rough Wall Model
$\beta_1 = 40^o$ N = 160 Re = 2.247×10^5
(Data applies to Figure 42c)

See Figure 20 for X-Y Origin

X in.	Y in.	Stanton Number $x10^3$
-0.75	2.15	5.16
-0.75	2.50	4.37
-0.75	2.65	4.55
-0.75	3.15	4.53
-0.75	3.25	4.60
-0.75	3.90	4.53
-0.75	4.50	4.96
-0.75	5.00	5.37
-0.75	5.50	5.98
-0.75	6.00	5.09
-0.75	6.50	5.32
-0.75	7.00	4.82
-0.75	7.50	5.16
-0.75	7.85	4.37
-0.75	8.00	4.55
-0.75	8.50	4.53
-0.75	8.60	4.60
-0.75	9.25	4.53
-0.75	9.85	4.96
0.00	2.15	4.43
0.00	2.50	4.40
0.00	2.65	4.17
0.00	3.15	6.21
0.00	3.25	7.45
0.00	4.00	8.02
0.00	4.50	6.15
0.00	5.50	4.69
0.00	6.00	4.92
0.00	6.50	4.70
0.00	7.00	4.45
0.00	7.50	4.43
0.00	7.85	4.40
0.00	8.00	4.17
0.00	8.50	6.21
0.00	8.60	7.45
0.00	9.45	8.02
0.00	9.85	6.15
0.75	2.15	4.35
0.75	2.65	4.38
0.75	5.50	4.62
0.75	6.00	4.55
0.75	6.50	4.65
0.75	7.00	4.28

X in.	Y in.	Stanton Number $x10^3$
0.75	7.50	4.35
0.75	8.00	4.38
1.50	6.00	4.70
1.50	6.50	4.85
1.50	7.00	4.44
1.50	7.50	4.64
1.50	8.00	4.63
1.50	8.50	6.03
2.25	6.00	4.50
2.25	6.50	5.05
2.25	7.00	4.24
2.25	7.50	4.58
2.25	8.00	4.43
2.25	8.50	3.49
3.00	6.00	5.18
3.00	6.50	5.76
3.00	7.00	5.08
3.00	7.50	4.60
3.00	8.00	4.19
3.00	8.50	3.76
3.75	5.50	5.43
3.75	6.00	5.90
3.75	6.50	6.04
3.75	7.00	5.35
3.75	7.50	4.33
3.75	8.00	3.76
4.50	5.00	5.76
4.50	5.50	5.72
4.50	6.00	6.34
4.50	6.50	5.19
4.50	7.00	4.63
4.50	7.50	4.59
5.25	4.00	5.71
5.25	4.50	6.41
5.25	5.50	5.79
5.25	6.00	5.23
5.25	6.50	5.10
6.00	2.50	5.16
6.00	3.00	5.30
6.00	4.00	6.52
6.00	4.50	6.35
6.00	4.50	5.71
6.00	5.00	6.57

X in.	Y in.	Stanton Number $x10^3$
6.00	5.50	5.46
6.75	-0.85	5.47
6.75	-0.35	5.38
6.75	0.00	4.94
6.75	0.15	4.74
6.75	0.50	4.15
6.75	1.00	5.01
6.75	1.50	5.24
6.75	2.00	5.88
6.75	2.50	5.83
6.75	3.00	6.07
6.75	3.50	5.54
6.75	4.00	5.67
6.75	4.50	5.47
6.75	5.00	5.38
6.75	5.35	4.94
6.75	5.50	4.74
6.75	5.85	4.15
6.75	6.35	5.01
6.75	6.85	5.24
6.75	7.35	5.88
7.25	-0.85	5.30
7.25	-0.35	4.74
7.25	0.00	4.95
7.25	0.50	5.21
7.25	0.90	5.89
7.25	1.00	5.47
7.25	1.50	5.59
7.25	2.00	5.57
7.25	3.00	5.78
7.25	3.50	5.45
7.25	4.50	5.30
7.25	5.00	4.74
7.25	5.35	4.95
7.25	5.85	5.21
7.25	6.25	5.89
7.25	6.35	5.47
7.25	6.85	5.59
7.25	7.35	5.57

Table A-10b Tabulated Data for Rough-Wall Model

Airfoil Surface Data for Rough Wall Model

$\beta_1 = 40^o$ N = 219 Re = 3.060×10^5

(Data applies to Figure 43a and Figure 43b)

SPAN %	$\frac{S}{S_{tot(r)}}$ %	Stanton Number $x10^3$
10	-100	3.45
30	-100	4.12
50	-100	3.52
50	-100	3.78
70	-100	4.57
90	-100	4.78
10	-90	4.28
30	-90	4.65
50	-90	4.13
50	-90	4.31
70	-90	4.86
90	-90	5.00
10	-80	3.84
30	-80	4.16
50	-80	3.80
50	-80	3.19
70	-80	4.25
90	-80	4.43
10	-70	3.53
30	-70	3.62
50	-70	3.77
50	-70	3.60
70	-70	3.47
90	-70	3.92
10	-60	3.00
30	-60	3.17
50	-60	2.91
50	-60	3.09
70	-60	3.08
90	-60	3.54
10	-50	2.85
30	-50	2.85
50	-50	2.69
50	-50	2.59
70	-50	2.46
90	-50	3.24
10	-40	2.76
30	-40	2.91
50	-40	2.42
50	-40	2.47
70	-40	2.78
90	-40	2.83
10	-30	2.72
20	-30	2.55
40	-30	2.49
50	-30	2.42
60	-30	2.32
70	-30	2.33
80	-30	2.48
90	-30	2.59
10	-20	2.98
20	-20	2.96
30	-20	2.66
40	-20	2.65
50	-20	2.44
50	-20	2.51
60	-20	2.46
70	-20	2.49
80	-20	2.54
90	-20	2.69
10	-15	3.26
20	-15	3.11
30	-15	3.02
40	-15	2.94
50	-15	2.63
60	-15	2.58
70	-15	2.61
80	-15	2.73
90	-15	3.02
10	-10	3.21
20	-10	3.43
30	-10	3.45
40	-10	3.45
60	-10	2.98
70	-10	3.18
90	-10	3.22
10	-5	3.80
20	-5	3.63
30	-5	3.81
40	-5	3.68
60	-5	3.56
70	-5	3.63
80	-5	4.15
90	-5	3.93
10	0	6.07
20	0	5.86
30	0	6.33
40	0	6.21
50	0	5.72
60	0	5.63
70	0	5.72
80	0	5.72
90	0	5.99
10	5	20.03
20	5	16.98
40	5	11.26
60	5	7.61
80	5	6.29
90	5	4.65
10	10	11.36
20	10	8.56
30	10	11.81
60	10	6.45
70	10	5.80
80	10	5.30
10	15	9.52
30	15	8.59
50	15	6.69
50	15	6.68
70	15	5.73
90	15	4.98
10	20	7.01
20	20	7.90
30	20	7.65
40	20	7.63
50	20	7.00
50	20	5.89
60	20	6.07
70	20	5.14
80	20	4.86
90	20	5.61
30	25	5.86
50	25	5.54
50	25	5.51
70	25	5.79
90	25	5.41
10	35	5.11
20	35	4.76
30	35	4.29
40	35	4.50
50	35	4.89
50	35	4.13
60	35	4.04
70	35	3.88
80	35	4.64
90	35	7.19
10	45	10.13
20	45	5.82
30	45	4.50
40	45	3.86
50	45	3.94
50	45	4.01
60	45	4.05
70	45	3.67
80	45	5.69
90	45	7.91
10	55	7.78
20	55	6.06
40	55	4.22
50	55	3.43
50	55	3.56
60	55	3.19
70	55	3.84
90	55	8.40
15	60	6.31
25	60	5.12
35	60	3.72
65	60	3.34
75	60	4.51
85	60	8.73
10	65	6.84
20	65	4.98
30	65	4.23
40	65	3.43
50	65	3.32
50	65	3.12
60	65	3.09
70	65	3.86
80	65	6.24
90	65	8.34
15	70	5.53
25	70	5.04
35	70	3.34
65	70	3.63
75	70	5.53
85	70	8.11
10	75	5.51
20	75	5.03
40	75	2.99
50	75	3.25
50	75	3.35
60	75	3.34
70	75	4.32
90	75	7.36
15	80	5.18
25	80	4.50
35	80	3.45
65	80	4.18
75	80	6.51
85	80	7.17
10	85	4.76
20	85	4.52
30	85	4.11
40	85	3.18
50	85	3.35
50	85	3.29
60	85	3.57
70	85	5.05
80	85	7.24
90	85	7.68
15	90	5.22
25	90	4.49
35	90	3.66
65	90	4.52
75	90	6.48
85	90	7.16
10	95	4.07
30	95	4.14
40	95	3.39
50	95	3.41
50	95	3.65
60	95	3.59
70	95	5.49
80	95	7.77
90	95	8.52

Table A-11a Tabulated Data for Rough-Wall Model

Endwall Data for Rough Wall Model

$\beta_1 = 40^o$ N = 219 Re = 3.060×10^5

(Data applies to Figure 43c)

See Figure 20 for X-Y Origin

X in.	Y in.	Stanton Number $x10^3$
-0.75	2.15	5.41
-0.75	2.50	4.60
-0.75	2.65	4.75
-0.75	3.15	4.73
-0.75	3.25	4.79
-0.75	3.90	4.77
-0.75	4.50	5.20
-0.75	5.00	5.92
-0.75	5.50	6.58
-0.75	6.00	5.37
-0.75	6.50	5.67
-0.75	7.00	5.17
-0.75	7.50	5.41
-0.75	7.85	4.60
-0.75	8.00	4.75
-0.75	8.50	4.73
-0.75	8.60	4.79
-0.75	9.25	4.77
-0.75	9.86	5.20
0.00	2.15	4.57
0.00	2.50	4.41
0.00	2.65	4.22
0.00	3.15	6.67
0.00	3.25	8.04
0.00	4.00	9.18
0.00	4.50	6.50
0.00	5.50	4.97
0.00	6.00	5.46
0.00	6.50	4.93
0.00	7.00	4.67
0.00	7.50	4.57
0.00	7.85	4.41
0.00	8.00	4.22
0.00	8.50	6.67
0.00	8.60	8.04
0.00	9.35	9.18
0.00	9.85	6.50
0.75	2.15	4.51
0.75	2.65	4.68
0.75	5.50	4.86
0.75	6.00	4.89
0.75	6.50	5.18
0.75	7.00	4.69

X in.	Y in.	Stanton Number $x10^3$
0.75	7.50	4.51
0.75	8.00	4.68
1.50	6.00	5.16
1.50	6.50	5.10
1.50	7.00	4.86
1.50	7.50	5.01
1.50	8.00	5.15
1.50	8.50	6.70
2.25	6.00	4.90
2.25	6.50	5.52
2.25	7.00	4.52
2.25	7.50	4.91
2.25	8.00	4.88
2.25	8.50	3.64
3.00	6.00	5.53
3.00	6.50	6.34
3.00	7.00	5.44
3.00	7.50	4.96
3.00	8.00	4.40
3.00	8.50	3.85
3.75	5.50	5.62
3.75	6.00	6.37
3.75	6.50	6.48
3.75	7.00	5.85
3.75	7.50	4.58
3.75	8.00	4.01
4.50	5.00	6.11
4.50	5.50	6.24
4.50	6.00	6.85
4.50	6.50	5.73
4.50	7.00	5.15
4.50	7.50	4.92
5.25	4.00	6.27
5.25	4.50	6.75
5.25	5.50	5.91
5.25	6.00	5.45
5.25	6.50	5.21
6.00	2.50	4.61
6.00	3.00	5.02
6.00	4.00	6.37
6.00	4.50	5.95
6.00	4.50	6.08
6.00	5.00	6.46

X in.	Y in.	Stanton Number $x10^3$
6.00	5.50	5.28
6.75	-0.85	5.41
6.75	-0.35	5.26
6.75	0.00	5.01
6.75	0.15	4.63
6.75	0.50	3.96
6.75	1.00	4.78
6.75	1.50	5.02
6.75	2.00	5.68
6.75	2.50	5.41
6.75	3.00	5.51
6.75	3.50	5.17
6.75	4.00	5.61
6.75	4.50	5.41
6.75	5.00	5.26
6.75	5.35	5.01
6.75	5.50	4.63
6.75	5.85	3.96
6.75	6.35	4.78
6.75	6.85	5.02
6.75	7.35	5.68
7.25	-0.85	5.30
7.25	-0.35	4.90
7.25	0.00	4.85
7.25	0.50	5.09
7.25	0.90	5.62
7.25	1.00	5.17
7.25	1.50	5.13
7.25	2.00	5.36
7.25	3.00	5.87
7.25	3.50	5.89
7.25	4.50	5.30
7.25	5.00	4.90
7.25	5.35	4.85
7.25	5.85	5.09
7.25	6.00	5.17
7.25	6.25	5.62
7.25	6.85	5.13
7.25	7.35	5.36

Table A-11b Tabulated Data for Rough-Wall Model

Airfoil Surface Data for Rough Wall Model

$\beta_1 = 40^o$ N = 300 Re = 4.122×10^5

(Data applies to Figure 44a and Figure 44b)

SPAN %	$\frac{S}{S_{tot(r)}}$ %	Stanton Number x10^3
10	-100	2.94
30	-100	3.69
50	-100	3.03
50	-100	3.40
70	-100	4.13
90	-100	4.42
10	-90	4.03
30	-90	4.45
50	-90	3.77
50	-90	3.97
70	-90	4.71
90	-90	4.90
10	-80	3.65
30	-80	4.00
50	-80	3.57
50	-80	2.79
70	-80	4.14
90	-80	4.18
10	-70	3.35
30	-70	3.45
50	-70	3.25
50	-70	3.26
70	-70	3.35
90	-70	3.78
10	-60	2.90
30	-60	3.08
50	-60	2.81
50	-60	2.81
70	-60	3.07
90	-60	3.49
10	-50	2.74
30	-50	2.80
50	-50	2.51
50	-50	2.50
70	-50	2.49
90	-50	3.14
10	-40	2.67
30	-40	2.72
50	-40	2.30
50	-40	2.28
70	-40	2.68
90	-40	2.81
10	-30	2.55
20	-30	2.42
40	-30	2.34
50	-30	2.23
60	-30	2.20
70	-30	2.32
80	-30	2.37
90	-30	2.50
10	-20	2.75
20	-20	2.78
30	-20	2.50
40	-20	2.49
50	-20	2.25
50	-20	2.25
60	-20	2.27
70	-20	2.38
80	-20	2.37
90	-20	2.53
10	-15	2.95
20	-15	2.90
30	-15	2.75
40	-15	2.73
50	-15	2.40
60	-15	2.36
70	-15	2.46
80	-15	2.57
90	-15	2.90
10	-10	2.82
20	-10	3.21
30	-10	3.12
40	-10	3.04
60	-10	2.84
70	-10	2.93
90	-10	3.00
10	-5	3.61
20	-5	3.28
30	-5	3.53
40	-5	3.11
60	-5	3.04
70	-5	3.30
80	-5	3.58
90	-5	3.55
10	0	5.71
20	0	5.46
30	0	5.63
40	0	5.39
50	0	4.79
60	0	5.11
70	0	4.93
80	0	4.83
90	0	5.51
10	5	21.46
20	5	14.94
40	5	9.85
60	5	7.42
80	5	6.54
90	5	4.48
10	10	10.14
20	10	8.85
30	10	10.21
60	10	6.53
70	10	5.78
80	10	5.29
10	15	9.36
30	15	7.72
50	15	6.84
50	15	6.32
70	15	5.84
90	15	4.50
10	20	6.79
20	20	7.21
30	20	6.96
40	20	7.75
50	20	6.61
50	20	5.65
60	20	6.07
70	20	5.27
80	20	4.66
90	20	5.64
30	25	5.45
50	25	5.50
50	25	5.18
70	25	4.68
90	25	5.70
10	35	5.08
20	35	4.56
30	35	4.10
40	35	4.26
50	35	4.70
50	35	4.04
60	35	3.98
70	35	3.75
80	35	4.87
90	35	7.56
10	45	10.23
20	45	5.70
30	45	4.35
40	45	3.73
50	45	3.80
50	45	3.70
60	45	4.05
70	45	3.75
80	45	5.67
90	45	8.17
10	55	7.15
20	55	5.84
40	55	4.16
50	55	3.34
50	55	3.34
60	55	3.02
70	55	3.80
90	55	9.49
15	60	6.23
25	60	4.80
35	60	3.66
65	60	3.28
75	60	4.51
85	60	8.30
10	65	5.98
20	65	4.70
30	65	3.88
40	65	3.41
50	65	2.98
50	65	2.98
60	65	2.98
70	65	3.85
80	65	6.14
90	65	8.59
15	70	5.26
25	70	4.49
35	70	3.15
65	70	3.56
75	70	5.83
85	70	8.06
10	75	5.14
20	75	4.59
40	75	2.92
50	75	3.19
50	75	3.19
60	75	3.17
70	75	4.25
90	75	7.28
15	80	4.85
25	80	4.24
35	80	3.25
65	80	4.04
75	80	6.74
85	80	7.87
10	85	4.58
20	85	4.19
30	85	3.94
40	85	3.00
50	85	3.19
50	85	3.20
60	85	3.52
70	85	4.99
80	85	7.83
90	85	7.63
15	90	4.80
25	90	4.40
35	90	3.42
65	90	4.48
75	90	6.54
85	90	8.30
10	95	3.94
30	95	3.67
40	95	3.10
50	95	3.32
50	95	3.31
60	95	3.60
70	95	5.25
80	95	7.31
90	95	8.59

Table A-12a Tabulated Data for Rough-Wall Model

Endwall Data for Rough Wall Model

$\beta_1 = 40^o$ N = 300 Re = 4.122×10^5

(Data applies to Figure 44c)

See Figure 20 for X-Y Origin

X in.	Y in.	Stanton Number $x10^3$
-0.75	2.15	5.75
-0.75	2.50	4.64
-0.75	2.65	4.85
-0.75	3.15	4.77
-0.75	3.25	4.69
-0.75	3.90	4.93
-0.75	4.50	5.58
-0.75	5.00	6.42
-0.75	5.50	7.23
-0.75	6.00	5.54
-0.75	6.50	5.78
-0.75	7.00	5.17
-0.75	7.50	5.75
-0.75	7.85	4.64
-0.75	8.00	4.85
-0.75	8.50	4.77
-0.75	8.60	4.69
-0.75	9.25	4.93
-0.75	9.85	5.58
0.00	2.15	4.46
0.00	2.50	4.46
0.00	2.65	4.09
0.00	3.15	6.83
0.00	3.25	8.45
0.00	4.00	9.01
0.00	4.50	6.54
0.00	5.50	4.95
0.00	6.00	5.49
0.00	6.50	4.92
0.00	7.00	4.73
0.00	7.50	4.46
0.00	7.85	4.46
0.00	8.00	4.09
0.00	8.50	6.83
0.00	8.60	8.45
0.00	9.35	9.01
0.00	9.85	6.54
0.75	2.15	4.55
0.75	2.65	4.92
0.75	5.50	4.77
0.75	6.00	5.04
0.75	6.50	5.75
0.75	7.00	5.06

X in.	Y in.	Stanton Number $x10^3$
0.75	7.50	4.55
0.75	8.00	4.92
1.50	6.00	5.52
1.50	6.50	5.34
1.50	7.00	5.27
1.50	7.50	5.46
1.50	8.00	5.63
1.50	8.50	7.05
2.25	6.00	5.09
2.25	6.50	5.84
2.25	7.00	4.80
2.25	7.50	5.17
2.25	8.00	5.23
2.25	8.50	3.66
3.00	6.00	5.80
3.00	6.50	6.72
3.00	7.00	5.74
3.00	7.50	5.14
3.00	8.00	4.51
3.00	8.50	3.89
3.75	5.50	5.59
3.75	6.00	6.58
3.75	6.50	6.73
3.75	7.00	5.99
3.75	7.50	4.57
3.75	8.00	4.13
4.50	5.00	6.12
4.50	5.50	6.37
4.50	6.00	6.89
4.50	6.50	6.14
4.50	7.00	5.64
4.50	7.50	5.00
5.25	4.00	6.78
5.25	4.50	6.67
5.25	5.50	5.78
5.25	6.00	5.86
5.25	6.50	5.09
6.00	2.50	4.51
6.00	3.00	4.82
6.00	4.00	6.30
6.00	4.50	6.32
6.00	4.50	6.28
6.00	5.00	6.42

X in.	Y in.	Stanton Number $x10^3$
6.00	5.50	5.29
6.75	-0.85	4.99
6.75	-0.35	4.79
6.75	0.00	4.40
6.75	0.15	4.22
6.75	0.50	3.71
6.75	1.00	4.43
6.75	1.50	5.04
6.75	2.00	5.43
6.75	2.50	5.30
6.75	3.00	5.43
6.75	3.50	5.04
6.75	4.00	5.31
6.75	4.50	4.99
6.75	5.00	4.79
6.75	5.35	4.40
6.75	5.50	4.22
6.75	5.85	3.71
6.75	6.35	4.43
6.75	6.85	5.04
6.75	7.35	5.43
7.25	-0.85	4.92
7.25	-0.35	4.51
7.25	0.00	4.56
7.25	0.50	4.70
7.25	0.90	5.57
7.25	1.00	4.90
7.25	1.50	4.83
7.25	2.00	5.01
7.25	3.00	5.63
7.25	3.50	5.08
7.25	4.50	4.92
7.25	5.00	4.51
7.25	5.35	4.56
7.25	5.85	4.70
7.25	6.25	5.57
7.25	6.35	4.90
7.25	6.85	4.83
7.25	7.35	5.01

Table A-12b Tabulated Data for Rough-Wall Model

Airfoil Surface Data for Rough Wall Model

$\beta_1 = 40^0$ N = 357 Re = 4.867×10^5

(Data applies to Figure 45a and Figure 45b)

SPAN %	$\frac{S}{S_{tot(r)}}$ %	Stanton Number $x10^3$
10	-100	2.86
30	-100	3.74
50	-100	3.38
50	-100	3.45
70	-100	4.14
90	-100	4.40
10	-90	4.06
30	-90	4.62
50	-90	4.24
50	-90	4.02
70	-90	4.77
90	-90	5.09
10	-80	3.66
30	-80	4.11
50	-80	3.60
50	-80	3.03
70	-80	4.33
90	-80	4.24
10	-70	3.40
30	-70	3.51
50	-70	3.54
50	-70	3.32
70	-70	3.45
90	-70	3.81
10	-60	2.93
30	-60	3.09
50	-60	2.85
50	-60	3.15
70	-60	3.19
90	-60	3.54
10	-50	2.74
30	-50	2.83
50	-50	2.75
50	-50	2.52
70	-50	2.54
90	-50	3.17
10	-40	2.68
30	-40	2.72
50	-40	2.31
50	-40	2.46
70	-40	2.72
90	-40	2.85
10	-30	2.54
20	-30	2.42
40	-30	2.34
50	-30	2.18
60	-30	2.20
70	-30	2.34
80	-30	2.36
90	-30	2.56
10	-20	2.65
20	-20	2.93
30	-20	2.48
40	-20	2.57
50	-20	2.19
50	-20	2.36
60	-20	2.33
70	-20	2.39
80	-20	2.45
90	-20	2.47
10	-15	2.90
20	-15	2.93
30	-15	2.68
40	-15	2.81
50	-15	2.32
60	-15	2.43
70	-15	2.40
80	-15	2.63
90	-15	2.82
10	-10	2.70
20	-10	3.25
30	-10	3.04
40	-10	3.13
60	-10	2.85
70	-10	2.80
90	-10	2.94
10	-5	3.69
20	-5	3.63
30	-5	3.79
40	-5	3.59
60	-5	3.45
70	-5	3.43
80	-5	3.98
90	-5	3.69
10	0	5.54
20	0	5.88
30	0	5.40
40	0	5.88
50	0	5.37
60	0	5.37
70	0	4.80
80	0	5.15
90	0	4.63
10	5	31.15
20	5	15.92
40	5	10.48
60	5	7.71
80	5	6.76
90	5	4.55
10	10	10.32
20	10	9.36
30	10	11.52
60	10	6.76
70	10	5.99
80	10	5.45
10	15	10.05
30	15	7.87
50	15	6.58
50	15	6.36
70	15	6.09
90	15	4.55
10	20	6.60
20	20	7.54
30	20	7.02
40	20	8.15
50	20	6.68
50	20	5.57
60	20	5.90
70	20	5.05
80	20	4.60
90	20	5.65
30	25	5.40
50	25	5.29
50	25	5.12
70	25	4.56
90	25	5.70
10	35	5.66
20	35	4.47
30	35	4.18
40	35	4.18
50	35	4.59
50	35	3.88
60	35	4.06
70	35	3.67
80	35	4.84
90	35	7.15
10	45	11.45
20	45	6.12
30	45	4.33
40	45	3.83
50	45	3.58
50	45	3.61
60	45	3.99
70	45	3.74
80	45	5.58
90	45	8.76
10	55	7.20
20	55	5.87
40	55	4.12
50	55	3.17
50	55	3.26
60	55	2.91
70	55	3.78
90	55	9.19
15	60	6.30
25	60	4.84
35	60	3.63
65	60	3.20
75	60	4.44
85	60	8.19
10	65	6.00
20	65	4.75
30	65	3.95
40	65	3.39
50	65	3.02
50	65	2.91
60	65	2.93
70	65	3.84
80	65	5.95
90	65	9.29
15	70	5.38
25	70	4.61
35	70	3.18
65	70	3.62
75	70	5.69
85	70	7.66
10	75	5.06
20	75	4.74
40	75	2.87
50	75	3.15
50	75	3.28
60	75	3.13
70	75	4.20
90	75	7.18
15	80	4.98
25	80	4.39
35	80	3.36
65	80	4.11
75	80	6.73
85	80	7.74
10	85	4.80
20	85	4.10
30	85	4.11
40	85	3.08
50	85	3.33
50	85	3.14
60	85	3.57
70	85	4.85
80	85	8.13
90	85	7.63
15	90	4.81
25	90	4.59
35	90	3.50
65	90	4.50
75	90	6.77
85	90	8.65
10	95	3.88
30	95	3.64
40	95	3.15
50	95	3.28
50	95	3.33
60	95	3.60
70	95	5.20
80	95	7.18
90	95	8.89

Table A-13a Tabulated Data for Rough-Wall Model

Endwall Data for Rough Wall Model

$\beta_1 = 40^o$ N = 357 Re = 4.867×10^5

(Data applies to Figure 45c)

See Figure 20 for X-Y Origin

X in.	Y in.	Stanton Number $x10^3$
-0.75	2.15	5.62
-0.75	2.50	4.80
-0.75	2.65	4.86
-0.75	3.15	4.78
-0.75	3.25	4.71
-0.75	3.90	4.83
-0.75	4.50	5.53
-0.75	5.00	6.74
-0.75	5.50	6.96
-0.75	6.00	5.71
-0.75	6.50	5.71
-0.75	7.00	5.29
-0.75	7.50	5.62
-0.75	7.85	4.80
-0.75	8.00	4.86
-0.75	8.50	4.78
-0.75	8.60	4.71
-0.75	9.25	4.83
-0.75	9.85	5.53
0.00	2.15	4.46
0.00	2.50	4.50
0.00	2.65	4.20
0.00	3.15	6.66
0.00	3.25	8.53
0.00	4.00	8.93
0.00	4.50	6.59
0.00	5.50	4.95
0.00	6.00	5.68
0.00	6.50	4.90
0.00	7.00	4.71
0.00	7.50	4.46
0.00	7.85	4.50
0.00	8.00	4.20
0.00	8.50	6.66
0.00	8.65	8.53
0.00	9.35	8.93
0.00	9.85	6.59
0.75	2.15	4.64
0.75	2.65	4.98
0.75	5.50	4.99
0.75	6.00	5.06
0.75	6.50	5.89
0.75	7.00	5.10

X in.	Y in.	Stanton Number $x10^3$
0.75	7.50	4.64
0.75	8.00	4.98
1.50	6.00	5.65
1.50	6.50	5.37
1.50	7.00	5.42
1.50	7.50	5.43
1.50	8.00	5.68
1.50	8.50	6.83
2.25	6.00	5.31
2.25	6.50	5.66
2.25	7.00	4.86
2.25	7.50	5.08
2.25	8.00	5.45
2.25	8.50	3.73
3.00	6.00	5.76
3.00	6.50	6.84
3.00	7.00	5.79
3.00	7.50	5.29
3.00	8.00	4.52
3.00	8.50	3.86
3.75	5.50	5.55
3.75	6.00	6.75
3.75	6.50	6.78
3.75	7.00	6.26
3.75	7.50	4.71
3.75	8.00	4.32
4.50	5.00	6.17
4.50	5.50	6.71
4.50	6.00	7.09
4.50	6.50	6.71
4.50	7.00	5.90
4.50	7.50	5.07
5.25	4.00	7.05
5.25	4.50	6.54
5.25	5.50	5.54
5.25	6.00	6.08
5.25	6.50	5.17
6.00	2.50	4.79
6.00	3.00	5.07
6.00	4.00	6.77
6.00	4.50	7.05
6.00	4.50	6.39
6.00	5.00	5.83

X in.	Y in.	Stanton Number $x10^3$
6.00	5.50	5.38
6.75	-0.85	5.37
6.75	-0.35	5.13
6.75	0.00	4.62
6.75	0.15	4.36
6.75	0.50	3.79
6.75	1.00	4.69
6.75	1.50	5.21
6.75	2.00	5.72
6.75	2.50	5.37
6.75	3.00	5.59
6.75	3.50	5.37
6.75	4.00	5.68
6.75	4.50	5.37
6.75	5.00	5.13
6.75	5.35	4.62
6.75	5.50	4.36
6.75	5.85	3.79
6.75	6.35	4.69
6.75	6.85	5.21
6.75	7.35	5.72
7.25	-0.85	5.43
7.25	-0.35	4.86
7.25	0.00	4.72
7.25	0.50	5.09
7.25	0.90	6.12
7.25	1.00	5.14
7.25	1.50	5.19
7.25	2.00	5.25
7.25	3.00	5.94
7.25	3.50	5.72
7.25	4.50	5.43
7.25	5.00	4.86
7.25	5.35	4.72
7.25	5.85	5.09
7.25	6.25	6.12
7.25	6.35	5.14
7.25	6.85	5.19
7.25	7.35	5.25

Table A-13b Tabulated Data for Rough-Wall Model

Airfoil Surface Data for Rough Wall Model

$\beta_1 = 40^0$ N = 410 Re = 5.533×10^5

(Data applies to Figure 46a and Figure 46b)

SPAN %	$\frac{S}{S_{tot(r)}}$ %	Stanton Number x10^3
10	-100	2.77
30	-100	3.63
50	-100	3.24
50	-100	3.40
70	-100	4.13
90	-100	4.31
10	-90	4.00
30	-90	4.50
50	-90	4.12
50	-90	3.94
70	-90	4.78
90	-90	5.22
10	-80	3.64
30	-80	4.15
50	-80	3.54
50	-80	2.99
70	-80	4.34
90	-80	4.25
10	-70	3.44
30	-70	3.56
50	-70	3.35
50	-70	3.54
70	-70	3.50
90	-70	3.94
10	-60	2.92
30	-60	3.11
50	-60	3.07
50	-60	2.87
70	-60	3.25
90	-60	3.62
10	-50	2.75
30	-50	2.89
50	-50	2.50
50	-50	2.70
70	-50	2.61
90	-50	3.19
10	-40	2.66
30	-40	2.70
50	-40	2.31
50	-40	2.40
70	-40	2.73
90	-40	2.88
10	-30	2.51
20	-30	2.41
40	-30	2.30
50	-30	2.16
60	-30	2.17
70	-30	2.34
80	-30	2.37
90	-30	2.54
10	-20	2.64
20	-20	2.82
30	-20	2.49
40	-20	2.51
50	-20	2.19
50	-20	2.31
60	-20	2.28
70	-20	2.39
80	-20	2.36
90	-20	2.49
10	-15	2.86
20	-15	2.81
30	-15	2.69
40	-15	2.71
50	-15	2.30
60	-15	2.34
70	-15	2.38
80	-15	2.59
90	-15	2.86
10	-10	2.64
20	-10	3.15
30	-10	3.06
40	-10	3.02

SPAN %	$\frac{S}{S_{tot(r)}}$ %	Stanton Number x10^3
60	-10	2.82
70	-10	2.79
90	-10	2.94
10	-5	3.90
20	-5	3.70
30	-5	4.11
40	-5	3.63
60	-5	3.63
70	-5	3.59
80	-5	4.21
90	-5	3.87
10	0	5.58
20	0	5.69
30	0	5.48
40	0	6.03
50	0	5.26
60	0	5.48
70	0	4.89
80	0	5.36
90	0	5.64
20	5	14.96
40	5	9.66
60	5	7.17
80	5	6.29
90	5	4.23
10	10	8.67
20	10	8.89
30	10	10.14
60	10	6.21
70	10	5.37
80	10	5.01
10	15	9.64
30	15	7.62
50	15	6.09
50	15	5.97
70	15	5.68
90	15	4.38
10	20	6.36
20	20	7.31
30	20	6.92
40	20	7.67
50	20	5.29
50	20	6.49
60	20	5.79
70	20	4.96
80	20	4.29
90	20	5.41
30	25	5.40
50	25	5.14
50	25	4.79
70	25	4.34
90	25	5.29
10	35	5.43
20	35	4.43
30	35	3.97
40	35	4.10
50	35	4.37
50	35	3.75
60	35	3.92
70	35	3.48
80	35	4.68
90	35	7.02
10	45	10.98
20	45	5.95
30	45	4.25
40	45	3.68
50	45	3.51
50	45	3.48
60	45	3.85
70	45	3.55
80	45	5.34
90	45	8.66
10	55	6.69

SPAN %	$\frac{S}{S_{tot(r)}}$ %	Stanton Number x10^3
20	55	5.56
40	55	3.93
50	55	3.07
50	55	3.21
60	55	2.86
70	55	3.61
90	55	8.38
15	60	6.27
25	60	4.72
35	60	3.52
65	60	3.03
75	60	4.19
85	60	7.90
10	65	5.63
20	65	4.61
30	65	3.80
40	65	3.33
50	65	2.91
50	65	2.80
60	65	2.85
70	65	3.73
80	65	5.58
90	65	8.25
15	70	5.20
25	70	4.49
35	70	3.14
65	70	3.57
75	70	5.47
85	70	7.24
10	75	4.92
20	75	4.70
40	75	2.86
50	75	3.05
50	75	3.29
60	75	3.05
70	75	4.03
90	75	6.80
15	80	4.87
25	80	4.27
35	80	3.32
65	80	3.93
75	80	6.43
85	80	6.50
10	85	4.65
20	85	4.03
30	85	3.96
40	85	2.98
50	85	3.26
50	85	3.12
60	85	3.48
70	85	4.72
80	85	7.47
90	85	7.18
15	90	4.63
25	90	4.57
35	90	3.42
65	90	4.34
75	90	6.21
85	90	8.04
10	95	3.79
30	95	3.62
40	95	3.08
50	95	3.18
50	95	3.27
60	95	3.49
70	95	4.87
80	95	6.76
90	95	8.20

Table A-14a Tabulated Data for Rough-Wall Model

Endwall Data for Rough Wall Model

$\beta_1 = 40^o$ N = 410 Re = 5.533×10^5

(Data applies to Figure 46c)

See Figure 20 for X-Y Origin

X in.	Y in.	Stanton Number $x10^3$
-0.75	2.15	5.20
-0.75	2.50	4.53
-0.75	2.65	4.63
-0.75	3.15	4.55
-0.75	3.25	4.42
-0.75	3.90	4.68
-0.75	4.50	5.38
-0.75	5.00	6.47
-0.75	5.50	6.87
-0.75	6.00	5.38
-0.75	6.50	5.33
-0.75	7.00	4.98
-0.75	7.50	5.20
-0.75	7.85	4.53
-0.75	8.00	4.63
-0.75	8.50	4.55
-0.75	8.60	4.42
-0.75	9.25	4.68
-0.75	9.85	5.38
0.00	2.15	4.22
0.00	2.50	4.34
0.00	2.65	3.96
0.00	3.15	6.47
0.00	3.25	7.97
0.00	4.00	8.70
0.00	4.50	6.14
0.00	5.50	4.79
0.00	6.00	5.50
0.00	6.50	4.71
0.00	7.00	4.60
0.00	7.50	4.22
0.00	7.85	4.34
0.00	8.00	3.96
0.00	8.50	6.47
0.00	8.60	7.97
0.00	9.35	8.70
0.00	9.85	6.14
0.75	2.15	4.29
0.75	2.65	4.79
0.75	5.50	4.76
0.75	6.00	4.96
0.75	6.50	5.90
0.75	7.00	4.90

X in.	Y in.	Stanton Number $x10^3$
0.75	7.50	4.29
0.75	8.00	4.79
1.50	6.00	5.38
1.50	6.50	5.23
1.50	7.00	5.31
1.50	7.50	5.27
1.50	8.00	5.52
1.50	8.50	6.66
2.25	6.00	5.07
2.25	6.50	5.42
2.25	7.00	4.75
2.25	7.50	4.86
2.25	8.00	5.29
2.25	8.50	3.59
3.00	6.00	5.55
3.00	6.50	6.66
3.00	7.00	5.56
3.00	7.50	4.99
3.00	8.00	4.38
3.00	8.50	3.71
3.75	5.50	5.21
3.75	6.00	6.29
3.75	6.50	6.38
3.75	7.00	5.90
3.75	7.50	4.44
3.75	8.00	4.22
4.50	5.00	5.72
4.50	5.50	6.45
4.50	6.00	6.63
4.50	6.50	6.42
4.50	7.00	5.59
4.50	7.50	4.87
5.25	4.00	6.53
5.25	4.50	6.26
5.25	5.50	5.20
5.25	6.00	5.84
5.25	6.50	4.83
6.00	2.50	4.59
6.00	3.00	4.80
6.00	4.00	6.38
6.00	4.50	6.58
6.00	4.50	6.08
6.00	5.00	6.72

Y in.	Y in.	Stanton Number $x10^3$
6.00	5.50	5.39
6.75	-0.85	4.94
6.75	-0.35	4.75
6.75	0.00	4.54
6.75	0.15	4.14
6.75	0.50	3.65
6.75	1.00	4.53
6.75	1.50	4.90
6.75	2.00	5.52
6.75	2.50	5.20
6.75	3.00	5.49
6.75	3.50	5.02
6.75	4.00	5.41
6.75	4.50	4.94
6.75	5.00	4.75
6.75	5.35	4.54
6.75	5.50	4.14
6.75	5.85	3.65
6.75	6.35	4.53
6.75	6.85	4.90
6.75	7.35	5.52
7.25	-0.85	5.23
7.25	-0.35	4.56
7.25	0.00	4.54
7.25	0.50	4.87
7.25	0.90	5.53
7.25	1.00	4.84
7.25	1.50	4.80
7.25	2.00	4.67
7.25	3.00	5.56
7.25	3.50	5.37
7.25	4.50	5.23
7.25	5.00	4.56
7.25	5.35	4.54
7.25	5.85	4.87
7.25	6.25	5.53
7.25	6.35	4.84
7.25	6.85	4.80
7.25	7.35	4.67

Table A-14b Tabulated Data for Rough-Wall Model

Airfoil Surface Data for Rough Wall Model

$\beta_1 = 45^0$ N = 409 Re = 4.889×10^5

(Data applies to Figure 47a and Figure 47b)

SPAN %	$\frac{S}{S_{tot(r)}}$ %	Stanton Number $x10^3$
10	-100	2.93
30	-100	3.66
50	-100	3.21
50	-100	3.41
70	-100	3.88
90	-100	4.24
10	-90	3.96
30	-90	4.37
50	-90	3.98
50	-90	3.98
70	-90	4.46
90	-90	4.97
10	-80	3.67
30	-80	4.02
50	-80	3.58
50	-80	2.80
70	-80	4.19
90	-80	4.13
10	-70	3.44
30	-70	3.47
50	-70	3.41
50	-70	3.33
70	-70	3.38
90	-70	3.88
10	-60	2.97
30	-60	3.07
50	-60	2.89
50	-60	3.03
70	-60	3.10
90	-60	3.59
10	-50	2.80
30	-50	2.86
50	-50	2.70
50	-50	2.56
70	-50	2.56
90	-50	3.23
10	-40	2.73
30	-40	2.75
50	-40	2.37
50	-40	2.38
70	-40	2.78
90	-40	2.93
10	-30	2.56
20	-30	2.48
40	-30	2.39
50	-30	2.26
60	-30	2.24
70	-30	2.42
80	-30	2.48
90	-30	2.61
10	-20	2.72
20	-20	2.91
30	-20	2.58
40	-20	2.56
50	-20	2.26
50	-20	2.36
60	-20	2.38
70	-20	2.49
80	-20	2.49
90	-20	2.57
10	-15	2.86
20	-15	2.90
30	-15	2.75
40	-15	2.75
50	-15	2.37
60	-15	2.41
70	-15	2.51
80	-15	2.70
90	-15	2.93
10	-10	2.60
20	-10	3.18
30	-10	3.10
40	-10	3.00
60	-10	2.86
70	-10	2.86
90	-10	3.01
10	-5	3.58
20	-5	3.60
30	-5	3.70
40	-5	3.35
60	-5	3.33
70	-5	3.44
80	-5	3.91
90	-5	3.60
10	0	5.62
20	0	5.21
30	0	5.11
40	0	5.20
50	0	4.67
60	0	4.94
70	0	4.40
80	0	4.47
90	0	5.05
10	5	22.87
20	5	13.11
40	5	8.80
60	5	6.40
80	5	5.34
90	5	4.12
10	10	9.40
20	10	8.84
30	10	9.66
60	10	6.23
70	10	5.59
80	10	5.01
10	15	9.43
30	15	7.31
50	15	6.24
50	15	6.19
70	15	5.66
90	15	4.47
10	20	6.54
20	20	7.34
30	20	7.05
40	20	7.98
50	20	6.58
50	20	5.35
60	20	5.89
70	20	5.13
80	20	4.61
90	20	5.31
30	25	5.57
50	25	5.35
50	25	5.13
70	25	4.61
90	25	5.52
10	35	4.73
20	35	4.64
30	35	4.38
40	35	4.56
50	35	4.87
50	35	4.19
60	35	4.17
70	35	3.85
80	35	4.81
90	35	7.31
10	45	9.07
20	45	5.22
30	45	4.27
40	45	3.93
50	45	3.96
50	45	3.93
60	45	4.34
70	45	3.63
80	45	5.19
90	45	8.03
10	55	6.35
20	55	5.37
40	55	3.84
50	55	3.27
50	55	3.37
60	55	3.10
70	55	3.63
90	55	8.37
15	60	5.78
25	60	4.39
35	60	3.81
65	60	3.10
75	60	4.17
85	60	7.69
10	65	5.57
20	65	4.35
30	65	3.44
40	65	3.48
50	65	2.83
50	65	2.69
60	65	2.81
70	65	3.67
80	65	5.40
90	65	8.09
15	70	5.03
25	70	4.21
35	70	3.11
65	70	3.58
75	70	5.18
85	70	7.39
10	75	4.91
20	75	4.45
40	75	3.01
50	75	2.82
50	75	2.93
60	75	3.03
70	75	3.93
90	75	6.66
15	80	4.69
25	80	4.11
35	80	3.13
65	80	3.84
75	80	6.22
85	80	6.92
10	85	4.70
20	85	3.93
30	85	3.76
40	85	2.95
50	85	3.16
50	85	3.08
60	85	3.33
70	85	4.51
80	85	7.22
90	85	7.12
15	90	4.66
25	90	4.29
35	90	3.18
65	90	3.94
75	90	5.84
85	90	7.76
10	95	3.82
30	95	3.39
40	95	2.93
50	95	3.25
50	95	3.28
60	95	3.24
70	95	4.73
80	95	6.42
90	95	7.85

Table A-15a Tabulated Data for Rough-Wall Model

Endwall Data for Rough Wall Model
$\beta_1 = 45^o$ N = 409 Re = 4.889×10^5
(Data applies to Figure 47c)

See Figure 20 for X-Y Origin

X in.	Y in.	Stanton Number $x10^3$
-0.75	2.15	5.11
-0.75	2.50	4.46
-0.75	2.65	4.45
-0.75	3.15	4.28
-0.75	3.25	4.06
-0.75	3.90	4.37
-0.75	4.50	5.00
-0.75	5.00	5.95
-0.75	5.50	6.28
-0.75	6.00	5.22
-0.75	6.50	5.14
-0.75	7.00	4.80
-0.75	7.50	5.11
-0.75	7.85	4.46
-0.75	8.00	4.45
-0.75	8.50	4.28
-0.75	8.60	4.06
-0.75	9.25	4.37
-0.75	9.85	5.00
0.00	2.15	4.18
0.00	2.50	4.21
0.00	2.65	3.97
0.00	3.15	5.84
0.00	3.25	7.17
0.00	4.00	8.03
0.00	4.50	5.73
0.00	5.50	4.64
0.00	6.00	5.08
0.00	6.50	4.57
0.00	7.00	4.57
0.00	7.50	4.18
0.00	7.85	4.21
0.00	8.00	3.95
0.00	8.50	5.84
0.00	8.60	7.17
0.00	9.35	8.03
0.00	9.85	5.73
0.75	2.15	4.12
0.75	2.65	4.34
0.75	5.50	4.69
0.75	6.00	4.83
0.75	6.50	5.66
0.75	7.00	4.70

X in.	Y in.	Stanton Number $x10^3$
0.75	7.50	4.12
0.75	8.00	4.34
1.50	6.00	5.27
1.50	6.50	4.78
1.50	7.00	4.85
1.50	7.50	4.69
1.50	8.00	4.70
1.50	8.50	6.38
2.25	6.00	4.85
2.25	6.50	4.80
2.25	7.00	4.21
2.25	7.50	4.43
2.25	8.00	4.82
2.25	8.50	3.53
3.00	6.00	5.16
3.00	6.50	5.84
3.00	7.00	5.00
3.00	7.50	4.71
3.00	8.00	4.40
3.00	8.50	3.74
3.75	5.50	4.98
3.75	6.00	5.87
3.75	6.50	5.92
3.75	7.00	5.91
3.75	7.50	4.54
3.75	8.00	4.17
4.50	5.00	5.63
4.50	5.50	6.55
4.50	6.00	6.74
4.50	6.50	6.53
4.50	7.00	5.56
4.50	7.50	4.71
5.25	4.00	6.44
5.25	4.50	6.15
5.25	5.50	5.18
5.25	6.00	5.83
5.25	6.50	4.89
6.00	2.50	4.55
6.00	3.00	4.69
6.00	4.00	6.48
6.00	4.50	6.55
6.00	4.50	6.02
6.00	5.00	6.56

X in.	Y in.	Stanton Number $x10^3$
6.00	5.50	5.33
6.75	-0.85	5.08
6.75	-0.35	4.98
6.75	0.00	4.55
6.75	0.15	4.22
6.75	0.50	3.66
6.75	1.00	4.47
6.75	1.50	4.90
6.75	2.00	5.38
6.75	2.50	5.26
6.75	3.00	5.35
6.75	3.50	4.98
6.75	4.00	5.33
6.75	4.50	5.08
6.75	5.00	4.98
6.75	5.35	4.55
6.75	5.50	4.22
6.75	5.85	3.66
6.75	6.35	4.47
6.75	6.85	4.90
6.75	7.35	5.38
7.25	-0.85	5.28
7.25	-0.35	4.69
7.25	0.00	4.66
7.25	0.50	4.93
7.25	0.90	5.84
7.25	1.00	5.06
7.25	1.50	5.07
7.25	2.00	5.11
7.25	3.00	5.91
7.25	3.50	5.65
7.25	4.50	5.28
7.25	5.00	4.69
7.25	5.35	4.66
7.25	5.85	4.93
7.25	6.25	5.84
7.25	6.35	5.06
7.25	6.85	5.07
7.25	7.35	5.11

Table A-15b Tabulated Data for Rough-Wall Model

Airfoil Surface Data for Rough Wall Model

$\beta_1 = 54^0$ N = 219 Re = 2.230×10^5

(Data applies to Figure 48a and Figure 48b)

SPAN %	$\frac{S}{S_{tot(r)}}$ %	Stanton Number x10^3
10	-100	3.79
30	-100	4.13
50	-100	3.63
50	-100	3.97
70	-100	4.28
90	-100	4.92
10	-90	4.70
30	-90	4.60
50	-90	4.31
50	-90	4.46
70	-90	4.82
90	-90	5.24
10	-80	4.25
30	-80	4.24
50	-80	4.12
50	-80	3.56
70	-80	4.40
90	-80	4.78
10	-70	3.83
30	-70	3.73
50	-70	3.57
50	-70	3.61
70	-70	3.67
90	-70	4.22
10	-60	3.28
30	-60	3.32
50	-60	3.21
50	-60	3.17
70	-60	3.26
90	-60	3.91
10	-50	3.11
30	-50	3.05
50	-50	2.98
50	-50	2.94
70	-50	2.81
90	-50	3.76
10	-40	3.08
30	-40	3.25
50	-40	2.97
50	-40	2.95
70	-40	3.32
90	-40	3.51
10	-30	3.06
20	-30	3.15
40	-30	3.10
50	-30	3.10
60	-30	3.04
70	-30	2.99
80	-30	3.17
90	-30	3.17
10	-20	3.46
20	-20	3.62
30	-20	3.38
40	-20	3.42
50	-20	3.26
50	-20	3.30
60	-20	3.27
70	-20	3.15
80	-20	3.21
90	-20	3.37
10	-15	3.58
20	-15	3.66
30	-15	3.70
40	-15	3.59
50	-15	3.46
60	-15	3.31
70	-15	3.32
80	-15	3.46
90	-15	3.73
10	-10	3.28
20	-10	3.59
30	-10	3.80
40	-10	3.58
60	-10	3.42
70	-10	3.44
90	-10	3.54
10	-5	3.16
20	-5	2.99
30	-5	2.98
40	-5	2.88
60	-5	2.87
70	-5	2.77
80	-5	2.86
90	-5	2.91
10	0	6.15
20	0	5.65
30	0	6.22
40	0	5.79
50	0	5.44
60	0	5.05
70	0	5.37
80	0	5.01
90	0	5.50
10	5	11.65
20	5	9.22
40	5	7.01
60	5	4.63
80	5	4.67
90	5	3.58
10	10	9.00
20	10	7.68
30	10	7.72
60	10	5.41
70	10	5.15
80	10	4.33
10	15	8.78
30	15	6.65
50	15	5.79
50	15	5.56
70	15	5.25
90	15	4.42
10	20	7.28
20	20	7.44
30	20	6.78
40	20	7.30
50	20	6.35
50	20	5.62
60	20	5.74
70	20	5.10
80	20	4.96
90	20	5.08
30	25	5.95
50	25	7.00
50	25	5.73
70	25	5.12
90	25	5.30
10	35	4.71
20	35	5.88
30	35	5.17
40	35	5.29
50	35	5.63
50	35	4.76
60	35	4.32
70	35	4.41
80	35	4.55
90	35	6.68
10	45	6.37
20	45	5.06
30	45	4.49
40	45	4.79
50	45	4.75
50	45	4.62
60	45	4.76
70	45	4.29
80	45	4.76
90	45	7.58
10	55	5.83
20	55	5.08
40	55	4.21
50	55	4.03
50	55	4.40
60	55	3.82
70	55	3.78
90	55	8.38
15	60	5.16
25	60	4.28
35	60	3.95
65	60	3.50
75	60	4.15
85	60	7.68
10	65	5.77
20	65	4.26
30	65	3.78
40	65	3.51
50	65	3.70
50	65	3.26
60	65	3.34
70	65	3.68
80	65	5.15
90	65	7.78
15	70	4.75
25	70	3.92
35	70	3.50
65	70	3.64
75	70	4.63
85	70	6.92
10	75	5.14
20	75	4.28
40	75	3.35
50	75	3.02
50	75	3.26
60	75	3.20
70	75	3.71
90	75	6.98
15	80	4.67
25	80	3.94
35	80	3.32
65	80	3.74
75	80	5.58
85	80	6.70
10	85	4.75
20	85	4.18
30	85	3.59
40	85	3.46
50	85	3.30
50	85	3.20
60	85	3.29
70	85	4.32
80	85	6.90
90	85	7.08
15	90	5.02
25	90	3.97
35	90	3.23
65	90	3.76
75	90	5.67
85	90	7.14
10	95	4.11
30	95	3.51
40	95	3.28
50	95	3.44
50	95	3.61
60	95	3.14
70	95	4.55
80	95	6.48
90	95	7.70

Table A-16a Tabulated Data for Rough-Wall Model

Endwall Data for Rough Wall Model

$\beta_1 = 54^o$ N = 219 Re = 2.230×10^5

(Data applies to Figure 48c)

See Figure 20 for X-Y Origin

X in.	Y in.	Stanton Number $x10^3$
-0.75	2.15	4.97
-0.75	2.50	4.30
-0.75	2.65	4.48
-0.75	3.15	4.13
-0.75	3.25	4.14
-0.75	3.90	3.93
-0.75	4.50	4.31
-0.75	5.00	4.80
-0.75	5.50	5.12
-0.75	5.85	4.30
-0.75	6.00	4.81
-0.75	6.50	4.98
-0.75	7.00	4.66
-0.75	7.50	4.97
-0.75	8.00	4.48
-0.75	8.50	4.13
-0.75	8.60	4.14
-0.75	9.25	3.93
-0.75	9.85	4.31
0.00	2.15	4.29
0.00	2.50	4.14
0.00	2.65	3.83
0.00	3.15	5.28
0.00	3.25	6.34
0.00	4.00	7.02
0.00	4.50	5.23
0.00	5.50	4.38
0.00	6.00	4.64
0.00	6.50	4.41
0.00	7.00	4.47
0.00	7.50	4.29
0.00	7.85	4.14
0.00	8.00	3.83
0.00	8.50	5.28
0.00	8.60	6.34
0.00	9.35	7.02
0.00	9.86	5.23
0.75	2.15	4.06
0.75	2.65	4.09
0.75	5.50	4.79
0.75	6.00	4.50
0.75	6.50	4.63
0.75	7.00	4.28

X in.	Y in.	Stanton Number $x10^3$
0.75	7.50	4.06
0.75	8.00	4.09
1.50	6.00	4.72
1.50	6.50	4.49
1.50	7.00	4.25
1.50	7.50	4.08
1.50	8.00	3.88
1.50	8.50	5.37
2.25	6.00	4.41
2.25	6.50	4.29
2.25	7.00	3.65
2.25	7.50	3.64
2.25	8.00	3.72
2.25	8.50	3.54
3.00	6.00	4.62
3.00	6.50	4.81
3.00	7.00	4.17
3.00	7.50	3.89
3.00	8.00	4.11
3.00	8.50	3.98
3.75	5.50	4.78
3.75	6.00	5.01
3.75	6.50	5.00
3.75	7.00	5.18
3.75	7.50	4.46
3.75	8.00	3.92
4.50	5.00	5.29
4.50	5.50	5.52
4.50	6.00	6.29
4.50	6.50	5.67
4.50	7.00	5.33
4.50	7.50	4.73
5.25	4.00	5.89
5.25	4.50	6.31
5.25	5.50	6.02
5.25	6.00	5.84
5.25	6.50	5.22
6.00	2.50	4.99
6.00	3.00	5.25
6.00	4.00	6.71
6.00	4.50	6.68
6.00	4.50	6.44
6.00	5.00	6.95

X in.	Y in.	Stanton Number $x10^3$
6.00	5.50	5.93
6.75	-0.85	5.48
6.75	-0.35	5.63
6.75	0.00	5.23
6.75	0.15	4.94
6.75	0.50	4.37
6.75	1.00	4.97
6.75	1.50	5.40
6.75	2.00	6.13
6.75	2.50	5.78
6.75	3.00	6.16
6.75	3.50	5.68
6.75	4.00	5.85
6.75	4.50	5.48
6.75	5.00	5.63
6.75	5.35	5.23
6.75	5.50	4.94
6.75	5.85	4.37
6.75	6.35	4.97
6.75	6.85	5.40
6.75	7.35	6.13
7.25	-0.85	5.32
7.25	-0.35	4.96
7.25	0.00	5.07
7.25	0.50	5.32
7.25	0.90	5.77
7.25	1.00	5.61
7.25	1.50	5.43
7.25	2.00	5.73
7.25	3.00	5.94
7.25	3.50	5.67
7.25	4.50	5.32
7.25	5.00	4.96
7.25	5.35	5.07
7.25	5.85	5.32
7.25	6.25	5.77
7.25	6.35	5.61
7.25	6.85	5.43
7.25	7.35	5.73

Table A-16b Tabulated Data for Rough-Wall Model

Airfoil Surface Data for Rough Wall Model

$\beta_1 = 54^o$ N = 299 Re = 3.029×10^5

(Data applies to Figure 49a and Figure 49b)

SPAN %	$\frac{S}{S_{tot(r)}}$ %	Stanton Number $x10^3$
10	-100	3.72
30	-100	4.09
50	-100	3.67
50	-100	4.07
70	-100	4.26
90	-100	4.91
10	-90	4.55
30	-90	4.55
50	-90	4.34
50	-90	4.43
70	-90	4.61
90	-90	5.38
10	-80	4.10
30	-80	4.26
50	-80	4.07
50	-80	3.31
70	-80	4.35
90	-80	4.66
10	-70	3.80
30	-70	3.69
50	-70	3.92
50	-70	3.93
70	-70	3.63
90	-70	4.29
10	-60	3.23
30	-60	3.31
50	-60	3.21
50	-60	3.26
70	-60	3.30
90	-60	4.02
10	-50	3.00
30	-50	2.99
50	-50	2.90
50	-50	2.85
70	-50	2.80
90	-50	3.67
10	-40	2.98
30	-40	3.08
50	-40	2.78
50	-40	2.74
70	-40	3.09
90	-40	3.43
10	-30	2.84
20	-30	2.96
40	-30	2.80
50	-30	2.79
60	-30	2.78
70	-30	2.86
80	-30	3.00
90	-30	3.11
10	-20	3.13
20	-20	3.34
30	-20	3.12
40	-20	3.06
50	-20	2.83
50	-20	2.90
60	-20	2.86
70	-20	3.00
80	-20	2.95
90	-20	2.98
10	-15	3.20
20	-15	3.42
30	-15	3.33
40	-15	3.34
50	-15	3.03
60	-15	2.99
70	-15	2.95
80	-15	3.07
90	-15	3.17
10	-10	3.00
20	-10	3.60
30	-10	3.61
40	-10	3.49
60	-10	3.47
70	-10	3.12
90	-10	3.13
10	-5	3.34
20	-5	3.48
30	-5	3.65
40	-5	3.48
60	-5	3.60
70	-5	3.07
80	-5	3.38
90	-5	3.11
10	0	5.84
20	0	5.48
30	0	5.63
40	0	5.38
50	0	5.09
60	0	5.07
70	0	4.82
80	0	4.72
90	0	5.14
10	5	13.64
20	5	9.79
40	5	7.38
60	5	4.73
80	5	4.23
90	5	3.46
10	10	9.14
20	10	8.23
30	10	8.57
60	10	5.50
70	10	5.00
80	10	4.44
10	15	9.09
30	15	6.83
50	15	5.72
50	15	6.10
70	15	5.29
90	15	4.37
10	20	7.28
20	20	7.43
30	20	6.61
40	20	7.84
50	20	6.55
50	20	5.44
60	20	5.54
70	20	4.98
80	20	4.60
90	20	4.99
30	25	6.00
50	25	5.51
50	25	5.68
70	25	4.83
90	25	5.25
10	35	4.72
20	35	5.61
30	35	5.19
40	35	5.18
50	35	5.55
50	35	4.68
60	35	4.46
70	35	4.32
80	35	4.48
90	35	6.73
10	45	6.81
20	45	5.07
30	45	4.29
40	45	4.75
50	45	4.60
50	45	4.46
60	45	4.70
70	45	4.00
80	45	4.61
90	45	7.24
10	55	6.06
20	55	5.06
40	55	3.97
50	55	4.02
50	55	4.20
60	55	3.70
70	55	3.59
90	55	7.90
15	60	5.18
25	60	4.05
35	60	3.80
65	60	3.38
75	60	3.98
85	60	6.79
10	65	5.56
20	65	4.28
30	65	3.52
40	65	3.40
50	65	3.42
50	65	3.11
60	65	3.09
70	65	3.56
80	65	4.80
90	65	7.61
15	70	4.71
25	70	3.84
35	70	3.35
65	70	3.53
75	70	4.31
85	70	6.81
10	75	5.09
20	75	4.25
40	75	3.20
50	75	2.92
50	75	3.07
60	75	3.03
70	75	3.56
90	75	6.45
15	80	4.71
25	80	3.81
35	80	3.15
65	80	3.58
75	80	5.36
85	80	6.61
10	85	4.92
20	85	4.06
30	85	3.52
40	85	3.26
50	85	3.21
50	85	3.06
60	85	3.30
70	85	4.05
80	85	6.48
90	85	6.69
15	90	5.02
25	90	4.06
35	90	3.07
65	90	3.57
75	90	5.42
85	90	7.27
10	95	4.07
30	95	3.44
40	95	3.16
50	95	3.42
50	95	3.60
60	95	3.18
70	95	4.39
80	95	6.28
90	95	7.48

Table A-17a Tabulated Data for Rough-Wall Model

Endwall Data for Rough Wall Model

$\beta_1 = 54^0$ N = 299 Re = 3.029×10^5

(Data applies to Figure 49c)

See Figure 20 for X-Y Origin

X in.	Y in.	Stanton Number $x10^3$
-0.75	2.15	5.12
-0.75	2.50	4.52
-0.75	2.65	4.64
-0.75	3.15	4.16
-0.75	3.25	4.18
-0.75	3.90	3.99
-0.75	4.50	4.46
-0.75	5.00	5.36
-0.75	5.50	5.47
-0.75	5.85	4.52
-0.75	6.00	5.07
-0.75	6.50	5.19
-0.75	7.00	4.89
-0.75	7.50	5.12
-0.75	8.00	4.64
-0.75	8.50	4.16
-0.75	8.60	4.18
-0.75	9.25	3.99
-0.75	9.85	4.46
0.00	2.15	4.29
0.00	2.50	4.18
0.00	2.65	3.82
0.00	3.15	5.26
0.00	3.25	6.45
0.00	4.00	7.28
0.00	4.50	5.41
0.00	5.50	4.50
0.00	5.85	4.18
0.00	6.00	4.82
0.00	6.50	4.53
0.00	7.00	4.46
0.00	7.50	4.29
0.00	8.00	3.82
0.00	8.50	5.26
0.00	8.60	6.45
0.00	9.35	7.28
0.00	9.85	5.41
0.75	2.15	4.11
0.75	2.65	4.26
0.75	5.50	4.95
0.75	6.00	4.61
0.75	6.50	5.12
0.75	7.00	4.61

X in.	Y in.	Stanton Number $x10^3$
0.75	7.50	4.11
0.75	8.00	4.26
1.50	6.00	5.08
1.50	6.50	4.50
1.50	7.00	4.53
1.50	7.50	4.08
1.50	8.00	3.98
1.50	8.50	5.83
2.25	6.00	4.60
2.25	6.50	4.42
2.25	7.00	3.80
2.25	7.50	3.71
2.25	8.00	3.99
2.25	8.50	3.64
3.00	6.00	4.73
3.00	6.50	4.98
3.00	7.00	4.29
3.00	7.50	4.07
3.00	8.00	4.29
3.00	8.50	4.02
3.75	5.50	4.85
3.75	6.00	5.23
3.75	6.50	5.25
3.75	7.00	5.61
3.75	7.50	4.65
3.75	8.00	4.19
4.50	5.00	5.40
4.50	5.50	5.93
4.50	6.00	6.70
4.50	6.50	6.24
4.50	7.00	5.89
4.50	7.50	4.78
5.25	4.00	6.31
5.25	4.50	6.43
5.25	5.50	5.95
5.25	6.00	6.20
5.25	6.50	5.26
6.00	2.50	4.77
6.00	3.00	5.15
6.00	4.00	6.95
6.00	4.50	7.01
6.00	4.50	6.61
6.00	5.00	7.00

X in.	Y in.	Stanton Number $x10^3$
6.00	5.50	5.71
6.75	-0.85	5.72
6.75	-0.35	5.57
6.75	0.00	5.27
6.75	0.15	4.92
6.75	0.50	4.38
6.75	1.00	5.20
6.75	1.50	5.45
6.75	2.00	6.18
6.75	2.50	5.94
6.75	3.00	6.14
6.75	3.50	5.58
6.75	4.00	5.90
6.75	4.50	5.72
6.75	5.00	5.57
6.75	5.35	5.27
6.75	5.50	4.92
6.75	5.85	4.38
6.75	6.35	5.20
6.75	6.85	5.45
6.75	7.35	6.18
7.25	-0.85	5.22
7.25	-0.35	5.03
7.25	0.00	5.22
7.25	0.50	5.30
7.25	0.90	5.81
7.25	1.00	5.41
7.25	1.50	5.40
7.25	2.00	5.49
7.25	3.00	6.02
7.25	3.50	5.62
7.25	4.50	5.22
7.25	5.00	5.03
7.25	5.35	5.22
7.25	5.85	5.30
7.25	6.25	5.81
7.25	6.35	5.41
7.25	6.85	5.40
7.25	7.35	5.49

Table A-17b Tabulated Data for Rough-Wall Model

Airfoil Surface Data for Rough Wall Model

$\beta_1 = 54^o$ N = 397 Re = 4.027×10^5

(Data applies to Figure 50a and Figure 50b)

SPAN %	$\frac{S}{S_{tot(r)}}$ %	Stanton Number $x10^3$
10	-100	3.33
30	-100	3.94
50	-100	3.25
50	-100	3.77
70	-100	4.05
90	-100	4.47
10	-90	4.39
30	-90	4.44
50	-90	3.81
50	-90	4.34
70	-90	4.52
90	-90	5.04
10	-80	4.05
30	-80	4.24
50	-80	3.86
50	-80	2.91
70	-80	4.38
90	-80	4.51
10	-70	3.71
30	-70	3.63
50	-70	3.41
50	-70	3.52
70	-70	3.64
90	-70	4.20
10	-60	3.23
30	-60	3.20
50	-60	3.18
50	-60	3.00
70	-60	3.42
90	-60	3.97
10	-50	3.00
30	-50	3.04
50	-50	2.75
50	-50	2.83
70	-50	2.82
90	-50	3.56
10	-40	2.96
30	-40	2.97
50	-40	2.70
50	-40	2.55
70	-40	3.02
90	-40	3.45
10	-30	2.73
20	-30	2.86
40	-30	2.80
50	-30	2.72
60	-30	2.70
70	-30	2.81
80	-30	2.97
90	-30	3.05
10	-20	2.90
20	-20	2.88
30	-20	3.02
40	-20	2.67
50	-20	2.74
50	-20	2.62
60	-20	2.65
70	-20	2.93
80	-20	2.69
90	-20	2.95
10	-15	2.87
20	-15	2.75
30	-15	3.07
40	-15	2.72
50	-15	2.76
60	-15	2.64
70	-15	2.79
80	-15	2.74
90	-15	3.12
10	-10	2.44
20	-10	2.70
30	-10	3.01
40	-10	2.60
60	-10	2.68
70	-10	2.71
90	-10	2.89
10	-5	2.81
20	-5	2.72
30	-5	2.97
40	-5	2.55
60	-5	2.47
70	-5	2.47
80	-5	2.42
90	-5	2.54
10	0	5.27
20	0	4.41
30	0	5.31
40	0	4.49
50	0	4.12
60	0	4.21
70	0	4.23
80	0	3.83
90	0	4.68
10	5	12.72
20	5	8.85
40	5	6.14
60	5	4.84
80	5	4.20
90	5	3.49
10	10	8.14
20	10	7.51
30	10	7.80
60	10	5.70
70	10	5.11
80	10	4.59
10	15	8.36
30	15	6.19
50	15	5.82
50	15	5.63
70	15	5.49
90	15	4.38
10	20	6.29
20	20	6.84
30	20	6.59
40	20	7.22
50	20	5.88
50	20	5.35
60	20	5.73
70	20	5.00
80	20	4.73
90	20	4.96
30	25	5.65
50	25	5.49
50	25	5.20
70	25	4.81
90	25	5.45
10	35	4.45
20	35	4.98
30	35	4.92
40	35	4.88
50	35	4.86
50	35	4.38
60	35	4.45
70	35	4.04
80	35	4.59
90	35	6.75
10	45	6.17
20	45	4.85
30	45	4.01
40	45	4.39
50	45	4.33
50	45	4.36
60	45	4.55
70	45	3.89
80	45	4.64
90	45	7.84
10	55	5.60
20	55	4.45
40	55	3.68
50	55	3.65
50	55	3.75
60	55	3.45
70	55	3.46
90	55	7.69
15	60	4.91
25	60	3.64
35	60	3.50
65	60	3.15
75	60	3.95
85	60	6.86
10	65	5.18
20	65	3.98
30	65	3.20
40	65	3.12
50	65	3.14
50	65	2.86
60	65	2.87
70	65	3.61
80	65	4.78
90	65	7.48
15	70	4.50
25	70	3.59
35	70	3.25
65	70	3.41
75	70	4.68
85	70	6.59
10	75	4.74
20	75	3.96
40	75	3.09
50	75	2.72
50	75	2.82
60	75	2.88
70	75	3.68
90	75	6.45
15	80	4.37
25	80	3.61
35	80	3.06
65	80	3.55
75	80	5.56
85	80	6.27
10	85	4.65
20	85	3.77
30	85	3.24
40	85	3.12
50	85	3.09
50	85	3.00
60	85	3.23
70	85	4.14
80	85	6.42
90	85	6.64
15	90	4.56
25	90	3.74
35	90	2.95
65	90	3.57
75	90	5.37
85	90	6.83
10	95	3.70
30	95	3.31
40	95	2.95
50	95	3.31
50	95	3.32
60	95	3.07
70	95	4.30
80	95	5.93
90	95	7.11

Table A-18a Tabulated Data for Rough-Wall Model

Endwall Data for Rough Wall Model

$\beta_1 = 54^o$ N = 397 Re = 4.027×10^5

(Data applies to Figure 50c)

See Figure 20 for X-Y Origin

X in.	Y in.	Stanton Number $x10^3$
-0.75	2.15	4.72
-0.75	2.50	4.16
-0.75	2.65	4.31
-0.75	3.25	3.83
-0.75	3.35	3.89
-0.75	3.90	3.77
-0.75	4.50	4.27
-0.75	5.00	5.22
-0.75	5.50	5.34
-0.75	6.00	4.76
-0.75	6.50	4.87
-0.75	7.00	4.57
-0.75	7.50	4.72
-0.75	7.85	4.16
-0.75	8.00	4.31
-0.75	8.50	3.89
-0.75	8.60	3.83
-0.75	9.25	3.77
-0.75	9.85	4.27
0.00	2.15	4.00
0.00	2.50	3.83
0.00	2.65	3.63
0.00	3.15	4.80
0.00	3.25	6.14
0.00	4.00	6.83
0.00	4.50	5.10
0.00	5.50	4.29
0.00	6.00	4.66
0.00	6.50	4.25
0.00	7.00	4.29
0.00	7.50	4.00
0.00	7.85	3.83
0.00	8.00	3.63
0.00	8.50	4.80
0.00	8.60	6.14
0.00	9.35	6.83
0.00	9.85	5.10
0.75	2.15	3.87
0.75	2.65	3.98
0.75	5.50	4.74
0.75	6.00	4.43
0.75	6.50	4.99
0.75	7.00	4.39

X in.	Y in.	Stanton Number $x10^3$
0.75	7.50	3.87
0.75	8.00	3.98
1.50	6.00	4.80
1.50	6.50	4.38
1.50	7.00	4.34
1.50	7.50	3.92
1.50	8.00	3.87
1.50	8.50	5.43
2.25	6.00	4.34
2.25	6.50	4.02
2.25	7.00	3.60
2.25	7.50	3.53
2.25	8.00	3.99
2.25	8.50	3.45
3.00	6.00	4.45
3.00	6.50	4.85
3.00	7.00	4.18
3.00	7.50	4.00
3.00	8.00	4.11
3.00	8.50	3.84
3.75	5.50	4.46
3.75	6.00	4.75
3.75	6.50	4.99
3.75	7.00	5.41
3.75	7.50	4.44
3.75	8.00	3.99
4.50	5.00	5.06
4.50	5.50	5.89
4.50	6.00	6.16
4.50	6.50	6.39
4.50	7.00	5.47
4.50	7.50	4.60
5.25	4.00	5.79
5.25	4.50	5.84
5.25	5.50	5.30
5.25	6.00	5.85
5.25	6.50	4.70
6.00	2.50	4.10
6.00	3.00	4.37
6.00	4.00	5.41
6.00	4.50	6.03
6.00	4.50	6.17
6.00	5.00	5.77

X in.	Y in.	Stanton Number $x10^3$
6.00	5.50	5.01
6.75	-0.85	4.42
6.75	-0.35	4.60
6.75	0.00	4.40
6.75	0.15	4.01
6.75	0.50	3.60
6.75	1.00	4.29
6.75	1.50	4.64
6.75	2.00	4.93
6.75	2.50	4.95
6.75	3.00	5.03
6.75	3.50	4.56
6.75	4.00	4.85
6.75	4.50	4.42
6.75	5.00	4.60
6.75	5.35	4.40
6.75	5.50	4.01
6.75	5.85	3.60
6.75	6.35	4.29
6.75	6.85	4.64
6.75	7.35	4.93
7.25	-0.85	4.60
7.25	-0.35	4.20
7.25	0.00	4.19
7.25	0.50	4.62
7.25	0.90	4.95
7.25	1.00	4.30
7.25	1.50	4.57
7.25	2.00	4.55
7.25	3.00	5.02
7.25	3.50	4.80
7.25	4.50	4.60
7.25	5.00	4.20
7.25	5.35	4.19
7.25	5.85	4.62
7.25	6.25	4.95
7.25	6.35	4.30
7.25	6.85	4.57
7.25	7.35	4.55

Table A-18b Tabulated Data for Rough-Wall Model